The Quest for Electrocatalytic Nitrogen Fixation with a Molecular Catalyst and What We Learned Along the Way

Thesis by

Trevor James Del Castillo

In Partial Fulfillment of the Requirements for

the degree of

Doctor of Philosophy

CALIFORNIA INSTITUTE OF TECHNOLOGY

Pasadena, California

2018

(Defended April 23, 2018)

ACKNOWLEDGEMENTS

In very brief treatment for so many wonderful people:

I'd like to thank my advisor Jonas for giving me a place in his lab and teaching me so many things, I can honestly say it has been both an honor and a great pleasure conducting research with you all these years.

In that vein I would also like to acknowledge Adam (Veige) my undergraduate advisor, friend, and the one who started me down this path.

I am particularly thankful to several group members who tolerated, advised, and taught me a great deal either directly or indirectly when I was first starting at Caltech; Jon Rittle, John Anderson, Sid Creutz, Hill Harman, Dan Suess, Sam MacMillan, Charles McCrory, and David Lacy.

For brevity I won't write out all of the Peters group members I overlapped with, suffice it to say that you know who you are and thank you each for being an amazing group of colleagues and friends. Particular thanks to Trixia Buscagan, Nik Thompson, and Kareem Hannoun who I shared office space with for most of my tenure.

I had the distinct pleasure of collaborating directly with Nik, Ben Matson, and Matt Chalkley on various projects discussed throughout my thesis, you are all great scientists and some of my favorite people to discuss chemistry with (especially over drinks).

Special thanks to the people who keep me sane and make it all seem worthwhile:

The Lake House bunch: featuring David Paul Walton, Jenna Bush, Ben Matson, Mark Nesbit, JingXin Liang, and Stella with special guest appearances by Noah Duffy, Nick Cowper, Liz O'Brien, Tanvi Ratani, Richard Mosesso and many more (coming soon to a theater near you).

Our amazing garage band the 818's (Beau Pritchett, Mark Nesbit, Ben Matson, and occasionally Paul Walton (you were the Young to our Crosby, Stills & Nash))

My group of pick-up soccer friends; what started on a lark with some Caltech people (perhaps most notably Gaël Ung and Josh Buss who I haven't mentioned yet but who have also been great sources of chemistry insight and friendship over the years) has grown steadily over the last four years to one of my most cherished pastimes and a great group of people largely not associated with Caltech who I would not have met otherwise.

My beloved adopted family (in no particular order): Evan, Mike, Owen, Bert, Brandon, James, Lauren, Gene, Isabelle, Patrick, and others too beloved to mention here.

My even more beloved biological family: my invaluable sister Lisa who taught me to read and so is ultimately sort of responsible for all of this, my dad who taught me to laugh and to think, and my mom who taught me to break on through to the other side; as well as my vast extended family.

ABSTRACT

Substrate selectivity in reductive multi-electron/proton catalysis with small molecules such as N_2, CO_2, and O_2 is a major challenge for catalyst design, especially where the competing hydrogen evolution reaction (HER) is thermodynamically and kinetically competent. A further significant and unmet challenge is to develop molecular catalysts, and conditions, compatible with electrocatalytic N_2 reduction (N_2RR). Progress in this area could have both fundamental and practical benefits, including access to informative in situ mechanistic studies via electrochemical techniques, and an electrochemical means to translate solar or otherwise derived chemical currency (H^+/e^-) into NH_3. This report details research into the mechanism and operating principles underlying the N_2RR efficacy of a tris(phosphine)borane Fe complex (P_3^BFe). Insights are provided into enabling chemical properties of this platform, into relevant catalytic intermediates, and into the importance and potential utility of controlling the direct interaction of acid and reductant sources, culminating in the first demonstration of electrocatalytic N_2RR with a molecular catalyst.

This report details the synthesis of a molecular Co complex analogous to the featured P_3^BFe-N_2 complex that also generates superstoichiometric yields of NH_3 (>200% NH_3 per Co-N_2 precursor) *via* the direct reduction of N_2 with protons and electrons. Comparison of the P_3^BFe-N_2 complex with this structurally related Co-N_2 and other Fe-N_2 species shows how remarkably sensitive the N_2 reduction performance of potential pre-catalysts are. These studies enable consideration of structural and electronic effects that are likely relevant to N_2 conversion activity, including π-basicity, charge state, and geometric flexibility.

Kinetic studies of N_2RR by P_3^BFe reveal first-order rate dependence on P_3^BFe catalyst concentration, consistent with a single-site catalyst model. Freeze-quench Mössbauer spectroscopy under turnover conditions reveals an iron-borohydrido-hydride complex as a likely resting state of the P_3^BFe catalyst system when KC_8 and $HBAr^F_4$ are employed as acid and reductant sources. However, it is also shown that P_3^BFe achieves both significantly improved efficiency for NH_3 formation (up to 72% for e^- delivery) and an unusually high turnover number for a synthetic molecular catalyst (84 equiv NH_3 per Fe site), when employing a significantly weaker combination of reductant (Cp^*_2Co) and acid ($[Ph_2NH_2][OTf]$ or $[PhNH_3][OTf]$). Further freeze-quench Mössbauer spectroscopy under turnover conditions suggests a change in the rate of key elementary steps; formation of the previously characterized off-path iron-borohydrido-hydride resting state is also suppressed. Theoretical and experimental studies are presented that highlight the possibility of protonated metallocenes as discrete PCET reagents under these (and related) catalytic conditions, offering a plausible rationale for the increased efficiency at reduced driving force of the P_3^BFe catalyst.

Inclusion of $Cp^*_2Co^+$ as a co-catalyst in controlled potential electrolysis experiments leads to improved yields of NH_3. The data presented provide what is to our knowledge the first unambiguous demonstration of electrocatalytic nitrogen fixation by a molecular catalyst (up to 6.7 equiv NH_3 per Fe at −2.1 V vs $Fc^{+/0}$). While the electrocatalysis is modest in terms of turnover, the comparatively favorable Faradaic efficiencies for NH_3 (up to 31%) highlight the value of studying molecular N_2RR catalysts to define design criteria for selective N_2RR

electrocatalysis. Our collective results contribute to a growing body of evidence that metallocenes may play multiple roles during reductive catalysis. While they can behave as single electron transfer (SET) reagents in the reductive protonation of small molecule substrates, ring-functionalized metallocenes, previously considered as intermediates of background HER, can also play a critical role in productive substrate bond-forming steps.

PUBLISHED CONTENT AND CONTRIBUTIONS

Del Castillo, T. J.; Thompson, N. B.; Suess, D. L.; Ung, G.; Peters, J. C.; *Inorg. Chem.*, **2015**, 54, 9256-9262. **DOI:** 10.1021/acs.inorgchem.5b00645

T.J.D.C. participated in the conception of the project, performed chemical synthesis and reaction chemistry, assisted in the analysis of all data, and wrote portions of the manuscript.

Del Castillo, T.; Thompson, N.; Peters, J. C.; *J. Am. Chem. Soc.*, **2016**, *138*, 5341-5350. **DOI:** 10.1021/jacs.6b01706

T.J.D.C. participated in the conception of the project, performed chemical synthesis and reaction chemistry, assisted in the analysis of all data, and wrote portions of the manuscript.

Chalkley, M.; Del Castillo, T.; Matson, B.; Roddy, J.; Peters, J. C.; *ACS Central Science*, **2017**, 3, 217-223. **DOI:** 10.1021/acscentsci.7b00014

T.J.D.C. participated in the conception of the project, performed chemical synthesis and reaction chemistry, assisted in the analysis of all data, and wrote portions of the manuscript.

Chalkley, M.; Del Castillo, T.; Matson, B.; Peters, J. C.; *J. Am. Chem. Soc.*, **2018**, accepted. **DOI:** 10.1021/jacs.8b02335

T.J.D.C. participated in the conception of the project, performed chemical synthesis and reaction chemistry, assisted in the analysis of all data, and wrote portions of the manuscript.

TABLE OF CONTENTS

LIST OF FIGURES

Number *Page*

LIST OF SCHEMES

Number *Page*

LIST OF TABLES

Number *Page*

ABBREVIATIONS

Atm - Atmosphere

Avg - Average

BAr^{F}_{4} - $B(3,5\text{-}C_6H_3(CF_3)_2)_4$

BDE - Bond Dissociation Enthalpy

BDFE - Bond Dissociation Free-Energy

C - Constant

ca - circa

calc - Calculated

Cp - Cyclopentadienyl

Cp* - Pentamethylcyclopentadienyl

CP_3 - $(o\text{-}^{i}Pr_2P(C_6H_4))_3C$-

CV - cyclic voltammogram

DFT - Density Functional Theory

DME - 1,2-dimethoxyethane

e^- - Electron

EPR - Electron paramagnetic resonance

eq - Equation

equiv - Equivalents

E^o - Reduction potential

$Fc^{+/0}$ - Ferrocene/Ferrocenium couple

GC - gas chromatography

G - Gauss

g - Gram

g_n - Electron g-factor

GC - Gas chromatography

GHz - Gigahertz

H - Enthalpy

HIPT - hexa-isopropyl-terphenyl

HOMO - Highest-Occupied Molecular Orbital

Hz - Hertz

iPr - isopropyl

IR - Infrared

K - Kelvin

K_{eq} - Equilibrium constant

L - Generic neutral dative ligand

LUMO - Lowest-Unoccupied Molecular Orbital

kcal - Kilocalorie

M - Concentration in molarity

max - Maximum

Me - Methyl

mg - Milligram

MHz - Megahertz

mL - Milliliter

mM - Millimolar

mm - Millimeter

mV - Millivolt

mmol - Millimole

MO - Molecular orbital

mol - Mole

n - generic number

nm - nanometer

NMR - Nuclear magnetic resonance

N_xH_y - Generic nitrogenous ligand with x N atoms and y H atoms

NNH_x - Generic nitrogenous ligand with 2 N atoms and x H atoms

o - ortho

OTf - Triflate (OSO_2CF_3)

P_3^B - $(o\text{-}^iPr_2P(C_6H_4))_3B$-

P_3^C - $(o\text{-}^iPr_2P(C_6H_4))_3C$-

P_3^{Si} - $(o\text{-}^iPr_2P(C_6H_4))_3Si$-

Ph - Phenyl

pK_a - Acid dissociation constant

R - Generic organic group

RT - Room temperature

S – Entropy

SiP_3 - $(o\text{-}^iPr_2P(C_6H_4))_3Si$-

TBA - Tetra-n-butyl ammonium

tBu - tert-Butyl

TEMPO - 2,2,6,6-tetramethylpiperidine-N-oxide

THF - Tetrahydrofuran

TMS - Trimethylsilyl

TPB - $(o\text{-}^iPr_2P(C_6H_4))_3B$-

UV-vis – Ultraviolet-visible

V - Volt

XRD - X-ray diffraction

N_α - Proximal nitrogen atom of a bound N_2 ligand

N_β - Terminal nitrogen atom of a bound N_2 ligand

γ - High frequency electromagnetic radiation

Q - Mössbauer quadrupole splitting

δ - chemical shift or Mössbauer isomer shift

° - Degree

°C - Degrees Celsius

ε - Extinction coefficient in units of $M^{-1}\,cm^{-1}$

η_x - Hapticity of order x

λ - Wavelength

λ_{max} - Wavelength of local maximum intensity

μ - Bridging

μA - Microamps

ν_{xy} - Vibrational frequency between atoms x and y

Σ - Summation

σ - Sigma symmetry orbital or interaction

σ* - Sigma symmetry antibonding interaction

π - Pi symmetry orbital or interaction

π* - Pi symmetry antibonding interaction

$\tau_{1/2}$ - Half-life

Å - Angstrom

12-C-4 - 12-crown-4

^{1}H - Hydrogen-1

^{2}H - Hydrogen-2

^{11}B - Boron-11

^{13}C - Carbon-13

^{15}N - Nitrogen-15

^{31}P - Phosphorus-31

2-MeTHF - 2-Methyl-tetrahydrofuran

def2-xxx - Basis sets for DFT

TPSS, etc. - DFT functional

HER – Hydrogen Evolution Reaction

N_2RR – Nitrogen Reduction Reaction

C h a p t e r 1

INTRODUCTION

Introductory remarks often begin, predictably, with an introduction to a subject matter. In this instance however I would like to begin with an introduction to the style and purpose of the document to follow, before setting the stage for our players (e.g., nitrogen gas and electricity). In preparing to write this thesis I am forced to address the question of purpose. Keeping in mind that I find myself in a fortunate and perhaps atypical state in which the vast majority of my five years[1] of research at Caltech has found its way into the published literature in the form of peer-reviewed journal articles. What purpose then is my thesis to serve, that is not already served by a perusal of my published works? After some deliberation on this question I have come across the following thoughts: i. almost every project which concludes in publication also encompasses some experimental results which, though of potential interest to a specialized reader, are not suited to publication (usually due to a lack of concrete interpretation or in some cases due to only a tangential relation to the main conclusion(s) of the project) in a thesis these results might be given light ii. as this paragraph surely gives evidence to, I have a tendency to elaborate and even to editorialize, habits which are rightly suppressed in compositions for the scientific literature iii. one component of research, which I believe is of great value, especially to researchers at the beginning of their career, is an accounting of the thought process (dare I say method?) that leads to scientific discovery. Of these thoughts the first is an obvious "correct" answer to the dilemma of purpose, the second is something of a metaphorical carrot (a treat to myself which might

encourage me in the writing process, though perhaps to the detriment of any reader brave enough to wade through my rambling), and the third, to my current thinking, may be the most valuable information that I might provide to my most likely future audience, which is to say some few overzealous new students to join Jonas' group in the next five or so years. I have settled on the following approach then, with each chapter (excluding this first) I shall recount a project, this will involve the reproduction of a manuscript describing scientific discovery, experimentation, and conclusions; I shall endeavor where possible to include additional experimental results and interpretation; additionally I shall begin each chapter with an account (to be set in italics) of one or more processes that contributed to the work discussed, which will hopefully contain useful lessons for new researchers. The sorts of lessons which might be conveyed in a candid discussion with one's advisor or colleague but that are generally not included in a published report.[2]

1.1 Background

The reduction of nitrogen (N_2) to ammonia (NH_3) (a reaction referred to herein both as nitrogen fixation and the nitrogen reduction reaction, abbreviated N_2RR) is a critical reaction for sustaining life on this planet.[3] This transformation is known to be effected biologically by nitrogenase enzymes and synthetically in a number of chemical systems, including the massive-scale industrial hydrogenation of N_2 mediated by the Haber-Bosch process.[4] In the Haber-Bosch process, H_2 and N_2 gas are dissociatively adsorbed at the surface of an Fe-based heterogeneous catalyst to give surface bound hydrides and nitrides, these surface bound species recombine to form sequential N-H bonds, ultimately giving rise to NH_3, (Scheme 1.1).[5]

Scheme 1.1: Mechanism (above) and net reaction (middle) of N_2 fixation by the Haber-Bosch process and the net reaction of N_2 fixation by nitrogenase (bottom) showing limiting 1:1 stoichiometry of H_2 production (vide infra).

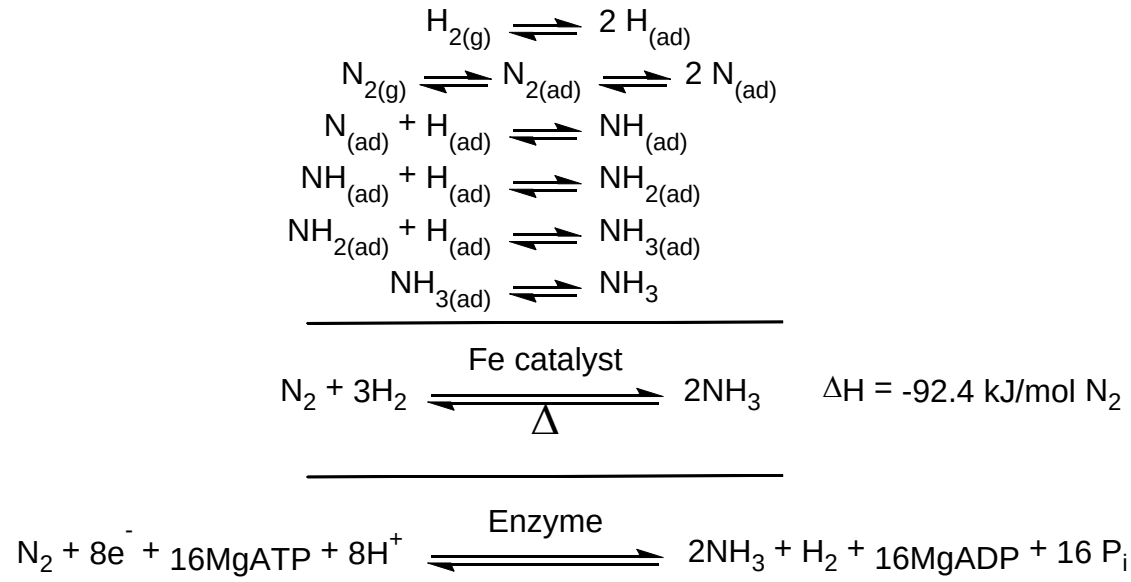

Despite this reaction being exothermic (ΔH = -46.2 kJ/mol of NH_3), the Haber-Bosch process requires forcing conditions to attain reasonable rates of NH_3 production, (typical Haber-Bosch reactor operating conditions: temperatures ≥200°C and pressures ≥400 atm).[6] This industrial process is sufficiently energy intensive, and performed on such a massive scale, as to constitute ~2% of the global energy demand.[7] The biological N_2 to NH_3 transformation as performed by nitrogenase enzymes is known to occur at ambient temperature and 1 atm of N_2 (Scheme 1.1).[8] Although considering the consumption of 16 equiv Mg(ATP) per molecule of N_2 fixed (two Mg(ATP) per reducing equivalent) in this process as well as the generation of at least some H_2 (1 equiv of H_2 produced per equiv of N_2 fixed has been demonstrated as a limiting stoichiometry[4,9]) the energetic efficiency of the processes may in fact be similar. Frustratingly, intimate understanding of the mechanism(s) of nitrogen

fixation as performed in biological systems, has remained elusive; presenting an ongoing opportunity for the inorganic and organometallic communities to expound a basic understanding of nitrogenous coordination chemistry and reactivity.

Some (of the many) notable advances in this field, prior to the beginning of the work described in this thesis,[10] include coordination, cleavage, or functionalization of N_2 or NxHy ligands relevant to nitrogen fixation at Mo,[11,12] W,[11] Fe,[13,14] Ti,[15] Zr,[16] V,[17] and Co[18] metal centers. Additionally, rare examples of direct conversion of N_2 to NH_3 by molecular systems have been demonstrated. For instance the treatment of Fe[19] and Co[20] dinitrogen compounds with acid has been shown to liberate modest yields of NH_3 ($\leq$ 0.21 mol NH_3/ mol complex), while Chatt et al. demonstrated that the treatment of a W dinitrogen compound with acid has yielded stoichiometric yields of NH_3 (~2.0 mol NH_3/ mol complex),[21] Chirik et. al. have also demonstrated the generation of ~15% NH_3 from a Zr dinitrogen complex in the presence of H_2 at elevated temperatures.[22] Interestingly, a mere handful of examples of complexes capable of mediating the catalytic conversion of N_2 to NH_3 in the presence of acid and electron sources have been reported, all utilizing complexes of W, Mo, or Fe.

Building on the early work by Chatt et al. (vide supra) that demonstrated the ability of phosphine ligated W-N_2 complexes to yield stoichiometric NH_3 upon treatment with acid[21] (a reaction in which the W(0) metal center is presumably oxidized to W(VI) degradation products in order to provide the requisite 6 e^-), Pickett and Talarmin demonstrated the conversion of *trans*-[$W(N_2)_2(dppe)_2$] (dppe = bis(diphenylphsophino)ethane) to *trans*-[$W(NNH_2)TsO(dppe)_2]^+$ (NNH_2 = hydrazido(2-), TsO = p-toluenesulfonate) upon treatment with p-toluenesulfonic acid, and further showed that *trans*-[$W(NNH_2)TsO(dppe)_2]^+$ could be

reduced by a mercury pool electrode at -2.6 V (vs Fc/Fc^+) in the presence of N_2 to regenerate *trans*-$[W(N_2)_2(dppe)_2]$ (85-95% yield) with concomitant generation of NH_3 (22-24% yield) establishing cyclic (though not catalytic) conversion of N_2 to NH_3 by W with protons and reducing equivalents (Scheme 1.2).[23]

In later work Schrock et. al. demonstrated that a triamidoamine Mo system, $[HIPTN_3N]Mo(N_2)$ ($[HIPTN_3N]3-$ = $[\{3,5\text{-}(2,4,6\text{-}(^iPr)_3C_6H_2)_2C_6H_3NCH_2CH_2\}_3N]^{3-}$) (Figure 1.1, **A**) could mediate the catalytic conversion of N_2 to NH_3 when treated with [2,6-lutidinium][BAr^F_4] over ~6 hours in the presence of $(Cp^*)_2Cr$ at room temperature (~7.5 equiv NH_3 produced per Mo).[24]

Scheme 1.2: Cyclic electrosynthesis of NH_3 from N_2 by a W system

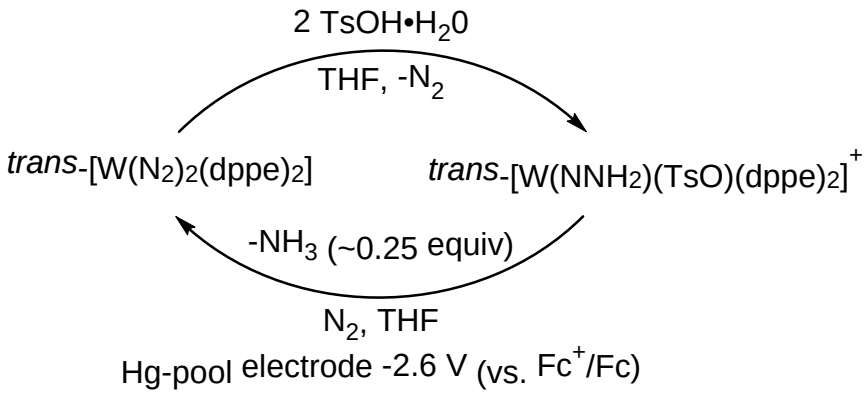

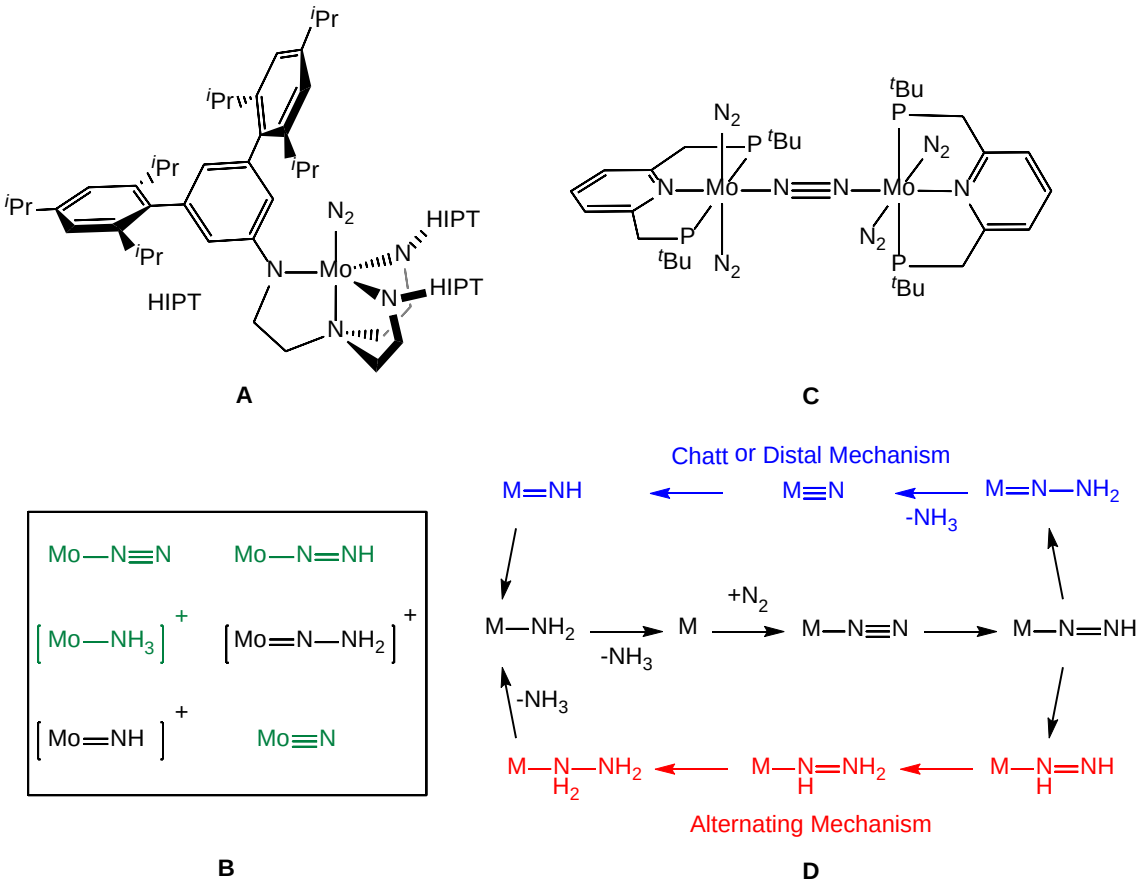

Figure 1.1: [HIPTN$_3$N]Mo(N$_2$) (**A**) and six independently synthesized [HIPTN$_3$N]Mo-N$_x$H$_y$ ligand complexes (**B**), complexes in green were shown to catalyze N$_2$ to NH$_3$ conversion. The [Mo(N$_2$)$_2$(PNP)]$_2$(μ-N$_2$) pincer complex (**C**) was also reported to catalyze N$_2$ to NH$_3$ conversion. **D** schematically shows the Chatt or distal vs. alternating mechanisms for sequential protonation and reduction of N$_2$ bound at a single metal center to generate 2 equiv NH3, each step represents delivery of one proton and one electron to the nitrogenous ligand, it should be noted that in addition to these mechanisms hybrid pathways are also possible.

A particularly interesting feature of this research was the ability to isolate and characterize six proposed intermediates (Figure 1.1, **B**), and to demonstrate catalytic competency from four of these, which strongly suggests that this reaction follows a Chatt[11] (or "distal") type mechanism (Figure 1.1, **D**). Nishibayashi et al. later reported a PNP-ligated Mo system (Figure 1.1, **C**) capable of generating 12 equiv of NH_3 from N_2 per Mo metal center, in this case utilizing [2,6-lutidinium][OTf] (OTf = trifluoromethanesulfonate) and the weaker reductant Cp_2Co, also at room temperature.[25]

Scheme 1.3: Catalytic N_2 conversion to NH_3 by $[Na(12\text{-crown-}4)_2][(P_3^B)Fe(N_2)]$ (**A**) and $[K(Et_2O)_{0.5}][(P_3^C)Fe(N_2)]$ (**B**)

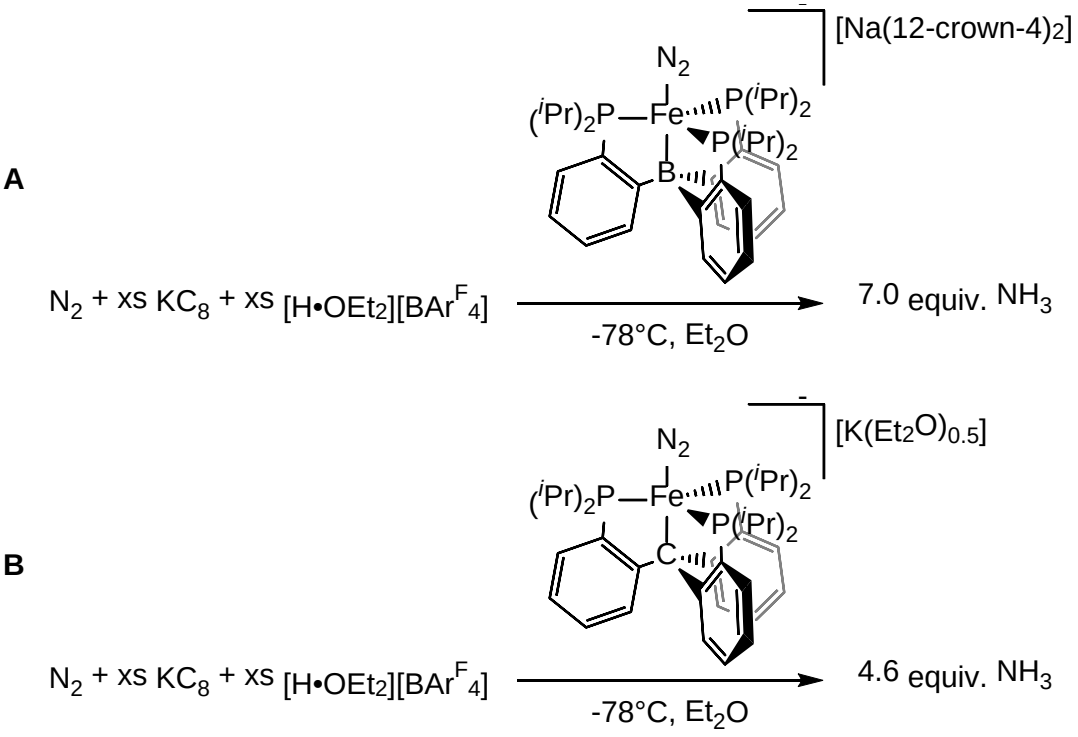

More recently, our group has reported that a tris(phosphine)borane ligated Fe complex, $[Na(12\text{-crown-}4)_2][(P_3^B)Fe(N_2)]$ (P_3^B = tris[2-(diisopropylphosphino)phenyl]borane), is capable of catalytically converting N_2 to NH_3 upon treatment with KC_8 and $[H{\cdot}OEt_2][BAr^F{}_4]$ at -78°C (~7 equiv NH_3 generated per Fe, Scheme 1.3, **A**).[26] Similar reactivity can be observed for the structurally related tris(phosphine)alkyl complex $[K(Et_2O)_{0.5}][(P_3^C)Fe(N_2)]$, which is also competent for catalytic N_2 to NH_3 conversion when treated with KC_8 and $[H{\cdot}OEt_2][BAr^F{}_4]$ at -78°C (~4.6 equiv NH_3 generated per Fe, Scheme 1.3, **B**).[27]

A key structural feature of the $(P_3^B)Fe$ and $(P_3^C)Fe$ systems is flexibility of the M-axial ligand interaction, which is postulated to facilitate N_2 fixation by allowing the metal center to sample geometries ranging from trigonal bipyramidal to tetrahedral, in turn giving access to d-orbital manifolds that stabilize the alternately π-basic or π-acidic nitrogenous ligands that may be encountered during catalysis (Figure 1.2). For example the Fe center in $[Na(12\text{-crown-}4)_2][(P_3^B)Fe(N_2)]$adopts a trigonal bipyramidal geometry (Figure 1.2, **A**) providing available filled d_{xz} and d_{yz} orbitals for π back donation into the N_2 π* orbitals, facilitating N_2 binding and activation. Whereas in the imide complex $(P_3^B)Fe(NAr)$ (Figure 1.2, **B**), the Fe center adopts approximate tetrahedral geometry to facilitate M-N multiple bonding with empty d_{xz} and d_{yz} orbitals.[28]

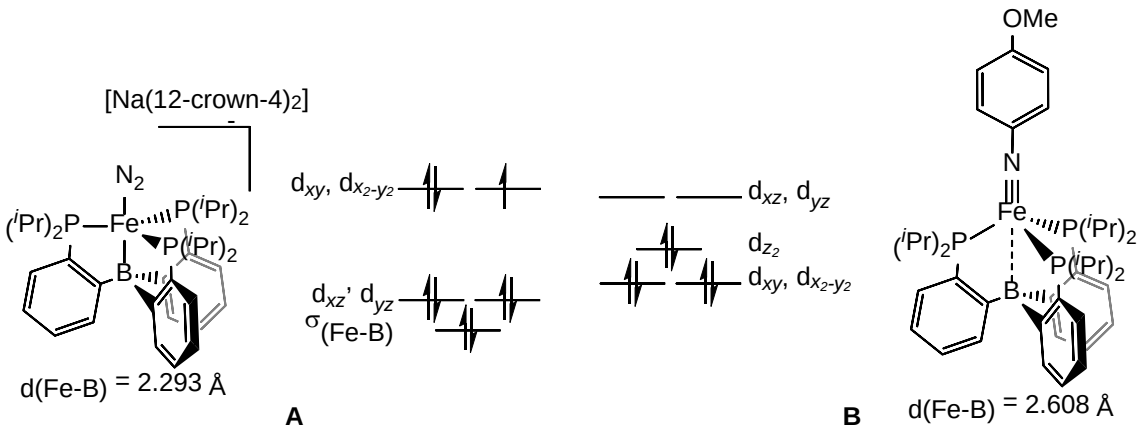

Figure 1.2: Qualitative ligand field splitting diagrams for TPB ligated Fe complexes adopting trigonal bipyramidal geometry (**A**) or pseudo-tetrahedral geometry (**B**) to stabilize π acidic and π basic ligands respectively. Flexibility of the Fe-B interaction is critical in facilitating this geometric variability.

Thus at the beginning of this research (and indeed still today) there remain many interesting questions relating to N_2RR. Questions of particular interest that will be (at least in part) addressed in the following chapters include: i) what mechanisms allow N_2RR (for instance at a single metal center) in turn what chemical properties of a catalyst enable or enhance this reactivity ii) how can selectivity for N_2RR over hydrogen evolution be accomplished iii) can electrocatalytic N_2RR be demonstrated by a molecular catalyst considering how few catalysts are known for this chemistry?

1.2 REFERENCES

[1] I do not count my first half year at Caltech (before I joined Jonas' group) to my research total bringing my count down from five and one half years (total residency time).

[2] To this end I may need to attribute some idea or innovation to an individual other than myself, that is to say one of my many wonderful colleagues and collaborators. As my understanding of the origin of ideas within a group of close collaborators and also my memory are not infallible, I shall try to be vague in these cases to avoid offering affront.

[3] Burgess, B. K.; Lowe, D. J. *Chem. Rev.* **1996**, *96*, 2983–3012.

[4] Fryzuk, M. D.; Johnson, S. A. *Coord. Chem. Rev.* **2000**, *200*, 379–409.

[5] Ertl, G. *J. Vac. Sci. Technol. A Vacuum, Surfaces, Film.* **1983**, *1*, 1247.

[6] Crossland, J. L.; Tyler, D. R. *Coord. Chem. Rev.* **2010**, *254*, 1883–1894.

[7] Erisman, J. W.; Sutton, M. A.; Winiwarter, W. et al. *Nat. Geosci.* **2008**, *1*, 636–639.

[8] Hoffman, B. M.; Dean, D. R.; Seefeldt, L. C. *Acc. Chem. Res.* **2009**, *42*, 609–619.

[9] Simpson, F. B.; Burris, R. H. *Science* **1984**, *224*, 1095–1097.

[10] The discussion here treats with the state of the art of nitrogen fixation at the time this thesis work began, circa 2013, thus setting the stage for the earlier projects discussed in the first chapters, more recent developments and citation appear throughout the later chapters with additional discussion.

[11] (a) Chatt, J.; Dilworth, J. R.; Richards, R. L. *Chem. Rev.* **1978**, *78*, 589–625. (b) Chatt, J.; Heath, G. A.; Richards, R. L. *J. Chem. Soc. Dalt. Trans.* **1974**, 2074–2082.

[12] (a) Yandulov, D. V; Schrock, R. R.; Rheingold, A. L.; Ceccarelli, C.; Davis, W. M. *Inorg. Chem.* **2003**, *42*, 796–813. (b) Hebden, T. J.; Schrock, R. R.; Takase, M. K.; Müller, P. *Chem. Commun. (Camb).* **2012**, *48*, 1851–1853.

[13] (a) Saouma, C. T.; Lu, C. C.; Peters, J. C. *Inorg. Chem.* **2012**, *51*, 10043–10054. (b) Rodriguez, M. M.; Bill, E.; Brennessel, W. W.; Holland, P. L. *Science* **2011**, *334*, 780–783. (c) Moret, M.-E.; Peters, J. C. *J. Am. Chem. Soc.* **2011**, *133*, 18118–18121. (d) Yuki, M.; Tanaka, H.; Sasaki, K.; Miyake, Y.; Yoshizawa, K.; Nishibayashi, Y. *Nat. Commun.* **2012**, *3*, 1254. (e) Field, L. D.; Li, H. L.; Magill, A. M. *Inorg. Chem.* **2009**, *48*, 5–7. (f) Li, Y.; Li, Y.; Wang, B.; Luo, Y.; Yang, D.; Tong, P.; Zhao, J.; Luo, L.; Zhou, Y.; Chen, S.; Cheng, F.; Qu, J. *Nat. Chem.* **2013**, *5*, 320–326. (g) Lee, Y.; Mankad, N. P.; Peters, J. C. *Nat. Chem.* **2010**, *2*, 558–565.

[14] Betley, T. A; Peters, J. C. *J. Am. Chem. Soc.* **2003**, *125*, 10782–10783.

[15] (a) Duchateau, R.; Gambarotta, S.; Beydoun, N.; Bensimon, C. *J. Am. Chem. Soc.* **1991**, *113*, 8986. (b) Nikiforov, G. B.; Vidyaratne, I.; Gambarotta, S.; Korobkov, I. *Angew. Chem. Int. Ed. Engl.* **2009**, *48*, 7415–7419. (c) Hanna, T. E.; Lobkovsky, E.; Chirik, P. J. *Organometallics* **2009**, *28*, 4079–4088.

[16] (a) Pun, D.; Lobkovsky, E.; Chirik, P. J. *J. Am. Chem. Soc.* **2008**, *130*, 6047–6054. (b) Chirik, P. J. *Dalton Trans.* **2007**, 16–25.

[17] (a) Smythe, N. C.; Schrock, R. R.; Muller, P.; Weare, W. W. *Inorg. Chem.* **2006**, *45*, 9197–9205. (b) Vidyaratne, I.; Crewdson, P.; Lefebvre, E.; Gambarotta, S. *Inorg. Chem.* **2007**, *46*, 8836–8842.

[18] (a) Betley, T. A; Peters, J. C. *J. Am. Chem. Soc.* **2003**, *125*, 10782–10783. (b) Ding, K.; Brennessel, W. W.; Holland, P. L. *J. Am. Chem. Soc.* **2009**, *131*, 10804–10805. (c) Koerner, V; Huttner, G; Vogel, S; et al. *Chem. Ber./Recueil,* **1997**, *130*, 489–492. (d) Vogel, S.; Barth, A.; Huttner, G.; Klein, T.; Zsolnai, L.; Kremer, R. *Angew. Chem. Int. Ed. Engl.* **1991**, *30*, 303–304. (e) Bowman, A. C.; Milsmann, C.; Atienza, C. C. H.; Lobkovsky, E.; Wieghardt, K.; Chirik, P. J. *J. Am. Chem. Soc.* **2010**, *132*, 1676–1684.

[19] Crossland, J. L.; Tyler, D. R. *Coord. Chem. Rev.* **2010**, *254*, 1883–1894.

[20] Yamamoto, A.; Miura, Y.; Ito, T.; Chen, H.; Iri, K.; Ozawa, F.; Miki, K.; Sei, T.; Tanaka, N.; Kasai, N. *Organometallics* **1983**, *2*, 1429–1436.

[21] Chatt, J.; Pearman, A. J.; Richards, R. L. *Nature* **1975**, *253*, 39–40.

[22] Pool, J. A.; Lobkovsky, E.; Chirik, P. J. *Nature* **2004**, *427*, 527–530.

[23] Pickett, C. J.; Talarmin, J. *Nature* **1985**, *317*, 652–653.

[24] Yandulov, D. V; Schrock, R. R. *Science* **2003**, *301*, 76–78.

[25] Arashiba, K.; Miyake, Y.; Nishibayashi, Y. *Nat. Chem.* **2010**, *3*, 120–125.

[26] Anderson, J. S.; Rittle, J.; Peters, J. C. *Nature* **2013**, *501*, 84–87.

[27] Creutz, S. E.; Peters, J. C. *J. Am. Chem. Soc.* **2014**, *136*, 1105–1115.

[28] Moret, M.-E.; Peters, J. C. *Angew. Chem. Int. Ed. Engl.* **2011**, *50*, 2063–2067.

C h a p t e r 2

EVALUATING MOLECULAR COBALT COMPLEXES FOR THE CONVERSION OF N_2 TO NH_3

Reproduced in part with permission from:

Del Castillo, T. J.; Thompson, N. B.; Suess, D. L.; Ung, G.; Peters, J. C.; *Inorg. Chem.*, **2015**, 54, 9256-9262. **DOI:** 10.1021/acs.inorgchem.5b00645

The story I choose to relate for the following chapter does not center on project conception but rather on data interpretation and the value of presenting one's work to others, for instance at a conference. The idea to perform a structure-function study comparing Fe to Co complexes given the (at that time) recently discovered catalytic activity of the P_3^B and P_3^C Fe platforms was fairly obvious. Once that idea is hit upon there is a veritable step-by-step program of experiment design available in the form of the previous work on Fe. However, once the data is collected (all of the characterization metrics relating to the Co congeners and the comparative catalytic activity, or lack thereof) we must ask what can we conclude from this data. In short what lesson can we learn? I had much of the following data in hand for some time with no real idea how to structure it into a story with a meaningful conclusion before presenting it at a poster session at an ACS national meeting. It was during this meeting, on running through my poster for the fourth or fifth time as I recall, that I finally noticed that the P_3^BCo system outperformed the P_3^{Si}Fe system in comparative NH_3 yield despite having a less activated (as far as IR stretches go to inform on bond activation in any

event) fully reduced N_2-bound state. This seems like an obvious conclusion to draw, but at the time my thinking was so centered on the importance of axial ligand flexibility as a hypothesis for why P_3^BFe yielded more NH_3 than $P_3^{Si}Fe$ that I had lost sight of another equally valid hypothesis, that yield across the Fe series simply tracked with N_2 stretching frequency, which this Co study provided evidence against. That conclusion, which only occurred to me in the process of explaining my entire project to a researcher with no familiarity with our work, ended up forming one of the bones of the following chapter.

2.1 Introduction

The conversion of dinitrogen (N_2) to ammonia (NH_3) is integral for life.[1] Despite extensive study, there are many unanswered questions regarding the rational design of molecular N_2-to-NH_3 conversion catalysts. It may be that the ability of a complex to activate terminally bound N_2 (as reported by the N—N stretching frequency) relates to the propensity of that complex to functionalize the N_2 moiety. For example, $HCo(N_2)(PPh_3)_3$ ($\nu_{(N\text{-}N)}$ = 2088 cm^{-1}) quantitatively releases N_2 upon treatment with acid, with no evidence of N_2 functionalization;[2,3] however, if this cobalt complex is deprotonated to generate the more activated complex $[(PPh_3)_3Co(N_2)][Li(Et_2O)_3]$ ($\nu_{(N\text{-}N)}$ = 1900 cm^{-1}), treatment with acid does produce some NH_3 and N_2H_4 (0.21 and 0.22 equivalents respectively).[3] Extensive efforts have been made to study the activation and functionalization of N_2 bound to metal centers of varying electronic properties.[4] In some cases, systems have been shown to activate bound N_2 to the extent that the N—N bond is fully cleaved.[5] In other cases, it has been shown that treatment of strongly activated N_2 complexes with acid or H_2 leads to reduced nitrogenous products.[2,3,4] However, this guiding principle alone has been insufficient to design many synthetic species capable of the catalytic conversion of N_2 to

NH_3.[6-8] In this regard it is prudent to study the few systems known to catalyze this reaction with an emphasis on identifying those properties critical to the observed N_2 reduction activity.

We have recently reported that a tris(phosphino)borane-ligated Fe complex is capable of catalyzing the conversion of N_2 to NH_3 at -78 °C.[7] We have postulated that the success of this system in activating N_2 stoichiometrically and mediating its catalytic conversion to NH_3 may arise from a highly flexible Fe-B interaction.[9,10] Such flexibility, trans to the N_2 binding site, may allow a single Fe center to access both trigonal bipyramidal and pseudo-tetrahedral coordination geometries, alternately stabilizing π-acidic or π-basic nitrogenous moieties sampled along an N_2 fixation pathway.[4d,11] Consistent with this hypothesis, we have studied isostructural (P_3E)-ligated Fe systems and found a measurable dependence of activity on the identity of the E atom, with the least flexible E = Si system furnishing divergently low NH_3 yields and the more flexible E = C or B systems affording moderate yields of NH_3.[7,8] However, the lower NH_3 production by the E = Si precursor may alternatively be attributed to other factors. Potential factors include (i) a lesser degree of N_2 activation than that observed in the E = C or B species (*vide infra*); (ii) faster poisoning of the E = Si system, for example by more rapid formation of an inactive terminal hydride;[7,8] (iii) faster degradation of the E = Si system, for example by dechelation of the ligand.

To complement our previous ligand modification studies, we chose to alter the identity of the transition metal. Moving from Fe to Co predictably modulates the π-basicity and electronic configuration of the metal center while maintaining the ligand environment. In principle, this allows the extrication of electronic effects, such as π-backbonding, from

structural features, such as geometric flexibility, *via* comparison of the Fe and Co systems. We therefore sought to explore the N_2 reduction activity of Co complexes of TPB (TPB = [*o*-(^{i}Pr$_2$P)C$_6$H$_4$]$_3$B), SiP_3 (SiP_3 = [*o*-(^{i}Pr$_2$P)C$_6$H$_4$]$_3$Si), and CP_3 (CP_3 = [*o*-(^{i}Pr$_2$P)C$_6$H$_4$]$_3$C). While correlating NH_3 yields with molecular structure is no doubt informative in terms of understanding the behavior of nitrogen fixing systems, correlation does not imply causation and the results described herein should be read with that in mind.

2.2 Results and Discussion

The previously reported[12] (TPB)Co(N_2) complex (Scheme 2.1, **1**) provided a logical entry point to study the N_2 chemistry of (TPB)Co complexes. The cyclic voltammogram of **1** in THF displays a quasi-reversible reduction wave at -2.0 V vs. Fc/Fc^+ and a feature corresponding to an oxidation process at -0.2 V vs. Fc/Fc^+ (Figure 2.1). These features are reminiscent of the cyclic voltammogram of (TPB)Fe(N_2), which shows a reduction event at -2.2 V vs. Fc/Fc^+ and an oxidation event at -1.5 V vs. Fc/Fc^+.[10]

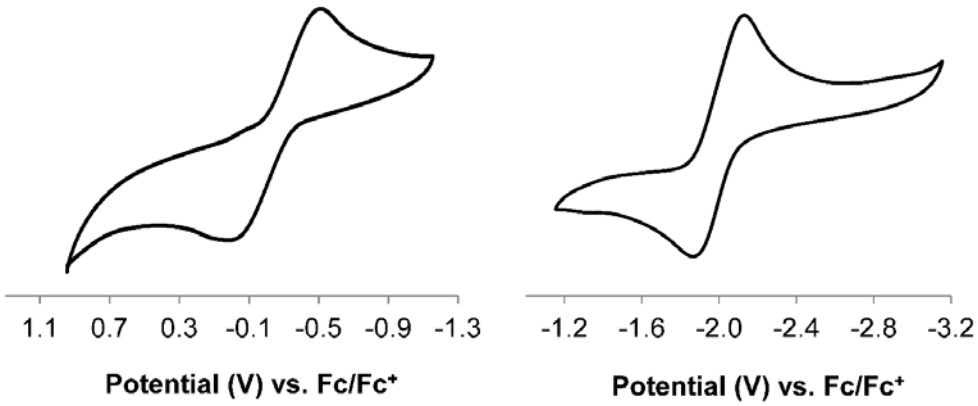

Figure 2.1: Cyclic voltammagram of (TPB)Co(N_2) (**1**) scanning oxidatively (left) and reductively (right) at 100 mV/sec in THF with 0.1 M $TBAPF_6$ electrolyte.

Scheme 2.1. Chemical oxidation and reduction of (TPB)Co(N_2).

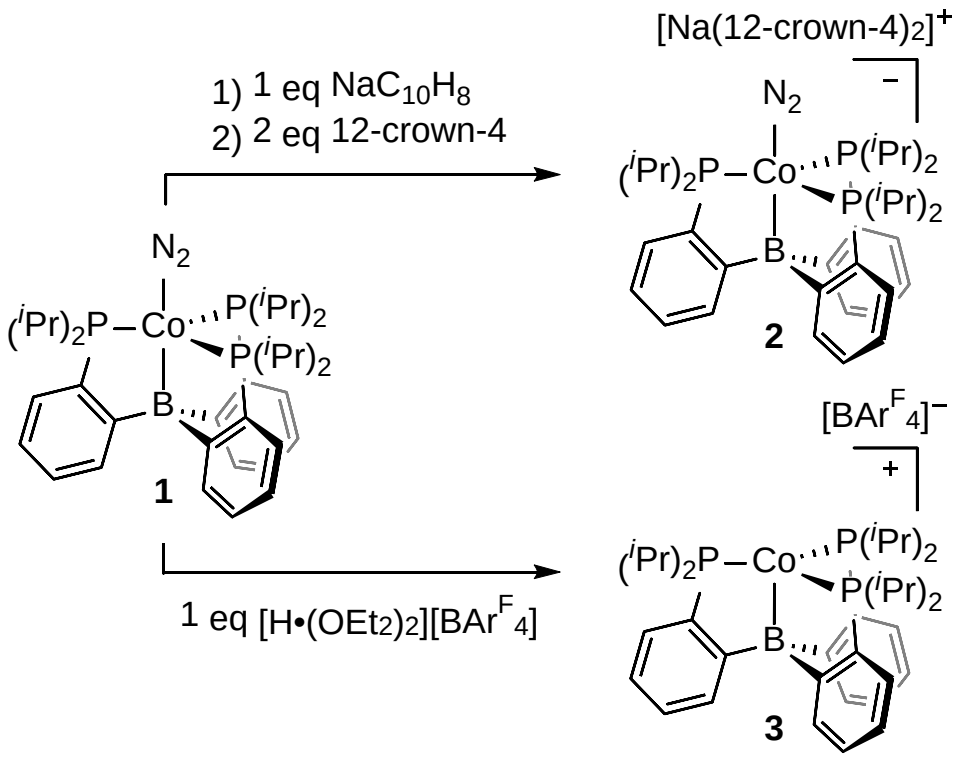

Treatment of **1** with 1 equivalent of $NaC_{10}H_8$ followed by 2 equivalents of 12-crown-4 (12-c-4) generates diamagnetic [Na(12-c-4)$_2$)][(TPB)Co(N_2)] as red crystals (Scheme 2.1, **2**). The $\nu_{(N\text{-}N)}$ stretch of **2** is lower in energy than that of **1** (Table 2.1) and the solid-state structure of **2** (Figure 2.2, left) displays contracted Co-N, Co-B, and Co-P distances compared to **1**, consistent with increased backbonding to each of these atoms. The one-electron oxidation of **1** can be achieved by addition of 1 equivalent of [H•(OEt$_2$)$_2$][BAr^F_4] at low temperature followed by warming, which generates red-purple [(TPB)Co][BAr^F_4] (Scheme 2.1, **3**, BAr^F_4 = tetrakis(3,5-bistrifluoromethylphenyl)borate). The structure of **3** (Figure 2.2, right) confirms that [(TPB)Co][BAr^F_4] does not bind N_2 in the solid state. The lack of dinitrogen binding at room temperature for **3** is consistent with the behavior of the isostructural Fe complex, [(TPB)Fe][BAr^F_4].[13] SQUID magnetometry measurements

indicate that **3** is high spin (S = 1) in the solid state with no evidence for spin crossover (Figure 2.3).

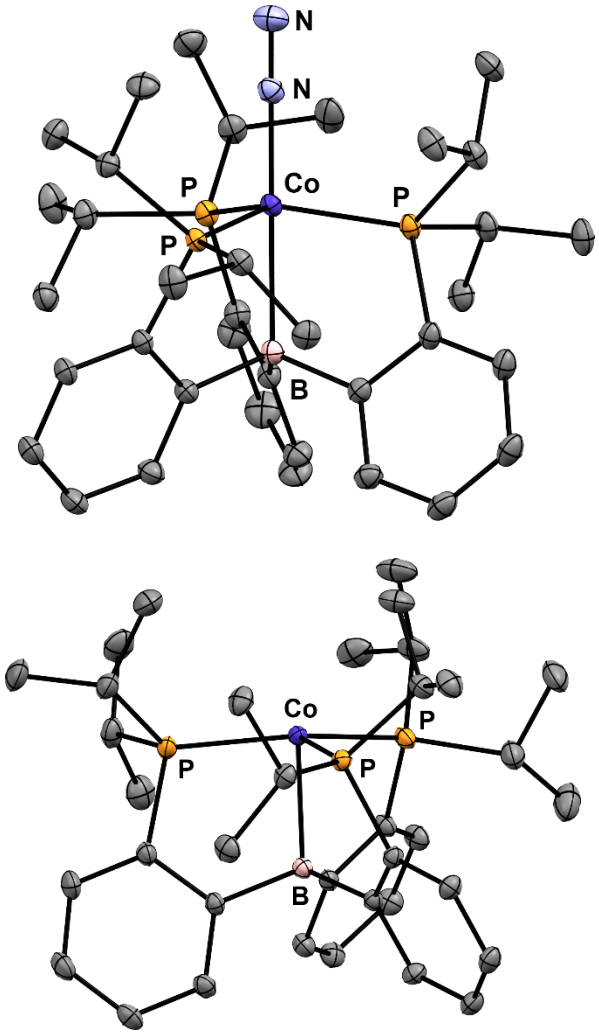

Figure 2.2. Solid-state crystal structures of **2** (top) and **3** (bottom; also see SI). Thermal ellipsoids shown at 50% probability. Countertions, solvent molecules, and H atoms omitted for clarity.

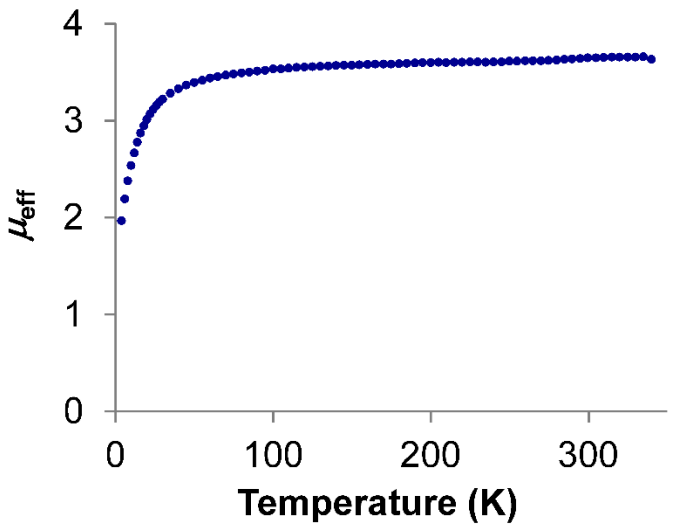

Figure 2.3. Temperature dependence of the magnetic susceptibility of [(TPB)Co][BAr^F_4] (**3**) as measured by SQUID magnetometry.

The synthesis of (SiP_3)Co(N_2) (**4**) has been reported previously.[14] The isoelectronic alkyl species, (CP_3)Co(N_2) (**5**), was obtained in 83% yield as a deep red solid from the reaction of CP_3H, $CoCl_2$•$(THF)_{1.5}$, and MeMgCl under an N_2 atmosphere (Scheme 2.2). Complex **5** ($\nu_{(N\text{-}N)}$ = 2057 cm^{-1}) is diamagnetic, possesses C_3 symmetry in solution, and binds N_2 as confirmed by a solid-state structure. The cyclic voltammogram of **5** in THF displays a quasi-reversible oxidation wave at -1.1 V vs. Fc/Fc^+ (Figure 2.4, left). Treatment of **5** with 1 equivalent of [Fc][BAr^F_4] at low temperature allowed for the isolation of the one electron oxidation product, [(CP_3)Co(N_2)][BAr^F_4] (**6,** $\nu_{(N\text{-}N)}$ = 2182 cm^{-1}), in 86% yield after recrystallization (Scheme 2.2). The coordinated N_2 ligand of **6** is labile and can be displaced under vacuum (Figure 2.4, middle) to generate a vacant or possibly solvent-coordinated [(CP_3)Co(L)]$^+$ species. The EPR spectrum of **6** at 80 K under N_2 is consistent with an S = ½ species (Figure 2.4, right).

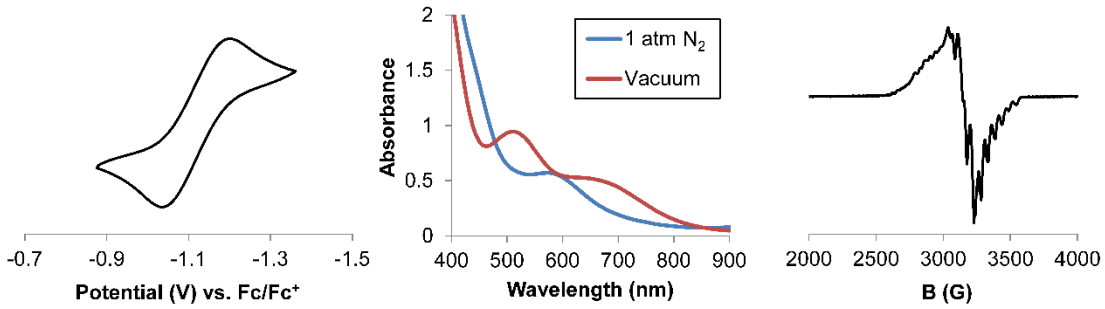

Figure 2.4: (left) Cyclic voltammagram of $(CP_3)Co(N_2)$ (**5**) scanning oxidatively at 100 mV/sec in THF with 0.1 M $TBAPF_6$ electrolyte. (middle) UV-vis spectra of **6** under 1 atm N_2 (solid line) and under static vacuum (dotted line: after three freeze-pump-thaw cycles). Spectra were collected on a 1 mM solution of **6** in THF at 298 K. (right) X-band EPR spectrum of **6** collected under 1 atm N_2 in 2-Me-THF at 80 K. No low-field features were detected.

Scheme 2.2. Synthesis and oxidation of $(CP_3)Co(N_2)$

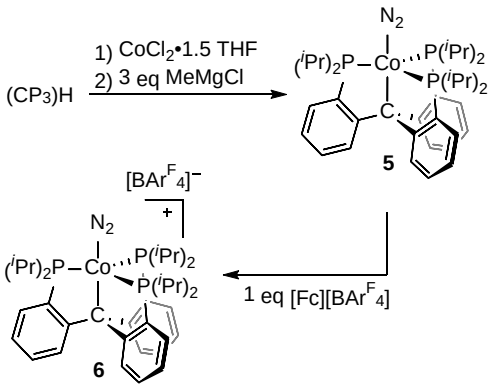

Consideration of the M-E interatomic distances presented in Table 2.1 reveals that the (TPB)Co platform exhibits a significant degree of flexibility of the M-B interaction, similar to that observed for the (TPB)Fe platform. Within each platform the M-B distance varies by > 0.16 Å between the neutral halide (Table 2.1, G and H) and anionic N_2 complexes (B and J). Likewise, the M-C interaction among $(CP_3)Co$ complexes exhibits flexibility

comparable to the analogous Fe series. For both platforms the M-C distance increases by ~0.07 Å upon one electron reduction of the cationic N_2 complexes (Table 2.1, F to E and K to L).

Table 2.1. Select Characterization Data for (P_3E)M Complexes (M = Co, Fe; E = B, C, Si)

Entry	Complex	M—E (Å)	$\nu_{(N\text{-}N)}$ (cm^{-1})[f]
A[a]	(TPB)Co(N_2) (**1**)	2.319(1)	2089
B	[(TPB)Co(N_2)]$^-$ (**2**)	2.300(3)	1978
C	[(TPB)Co]$^+$ (**3**)	2.256(2)	—
D[b]	(SiP_3)Co(N_2) (**4**)	2.2327(7)	2063
E	(CP_3)Co(N_2) (**5**)	2.135(4)	2057
F	[(CP_3)Co(N_2)]$^+$ (**6**)	2.054(2)	2182
G[a]	(TPB)CoBr	2.4629(8)	—
H[c]	(TPB)FeBr	2.458(5)	—
I[c]	(TPB)Fe(N_2)	—	2011
J[c]	[(TPB)Fe(N_2)]$^-$	2.293(3)	1905
K[d]	[(CP_3)Fe(N_2)]$^+$	2.081(3)	2128
L[d]	(CP_3)Fe(N_2)	2.152(3)	1992
M[d]	[(CP_3)Fe(N_2)]$^-$	2.165(2)	1905
N[e]	[(SiP_3)Fe(N_2)]$^-$	2.236(1)	1920

[a]from ref. 12 [b]from ref. 14 [c]from ref. 10 [d]from ref. 8 [e]from ref. 15 [f]IR from solid-state samples.

A comparison of the trends in interatomic metrics between the isoelectronic $\{(TPB)Co(N_2)\}^n$ and $\{(CP_3)Co(N_2)\}^n$ redox series reveals divergent geometric behavior. Upon reduction from **1** to **2**, the Co-B distance decreases by 0.02 Å, resulting in a significant decrease in the pyramidalization about Co ($\Delta\tau$ = 0.13).[16] The opposite is true for the reduction of **6** to **5**, which results in an increase in the Co-C distance and an increase in the pyramidalization ($\Delta\tau$ = -0.13). A plausible rationale is that the Z-type borane ligand in (TPB)Co complexes enforces a trigonal bipyramidal geometry upon reduction, by drawing the Co atom into the P_3 plane with an attractive Co-B interaction. The X-type alkyl ligand in $(CP_3)Co$ complexes instead causes a distortion away from a trigonal pyramidal geometry upon reduction, with a comparatively repulsive Co-C interaction forcing the Co above the P_3 plane.

The reactivity of these $(P_3E)Co$ complexes with sources of protons and electrons in the presence of N_2 was investigated. In analogy to the $[Na(12\text{-}c\text{-}4)_2][(TPB)Fe(N_2)]$ complex, treatment of a suspension of **2** in Et_2O at -78 °C with excess $[H{\bullet}(OEt_2)_2][BAr^F{}_4]$ followed by excess KC_8 under an atmosphere of N_2 leads to the formation of 2.4 ± 0.3 equivalents of NH_3 (240% per Co, average of six iterations with independent NH_3 yields of 2.3, 2.1, 2.2, 2.5, 2.8, 2.2 equiv, Table 2.2, A). Yields of NH_3 were determined by the indophenol method;[17] no hydrazine was detected by a standard UV-vis quantification method.[18] We acknowledge that these results are close to a stoichiometric yield of NH_3, and include the results of individual experiments here to demonstrate that the yields are reproducibly above 2.1 equivalents. While modest with respect to establishing *bona fide* catalysis, these yields are consistently greater than 200% NH_3 normalized to Co in **2** and represent an order of

Table 2.2. Ammonia Generation from N_2 Mediated by Co Precursors[a]

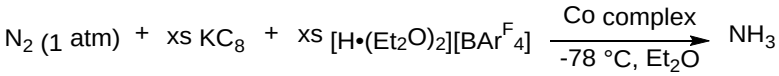

Entry	Co complex	NH_3 equiv/Co
A	[(TPB)Co(N_2)][Na(12-c-4)$_2$] (**2**)	2.4 ± 0.3[b]
B	(TPB)Co(N_2) (**1**)	0.8 ± 0.3
C	[(TPB)Co][$BAr^F{}_4$] (**3**)	1.6 ± 0.2
D	(TPB)CoBr	0.7 ± 0.4
E	(SiP_3)Co(N_2) (**4**)	<0.1
F	(CP_3)Co(N_2) (**5**)	0.1 ± 0.1
G	[($NArP_3$)CoCl][BPh_4]	<0.1
H	(PBP)Co(N_2)	0.4 ± 0.2
I	Co(PPh_3)$_2$$I_2$	0.4 ± 0.1
J	$CoCp_2$	0.1 ± 0.1
K	$Co_2(CO)_8$	<0.1

[a]Co precursors at -78 °C under an N_2 atmosphere treated with an Et_2O solution containing 47 equiv [H•(OEt_2)$_2$][$BAr^F{}_4$] followed by an Et_2O suspension containing 60 equiv KC_8. Yields are reported as an average of 3 iterations; data for individual experimental iterations presented in Supporting Information. [b]Average of 6 iterations.

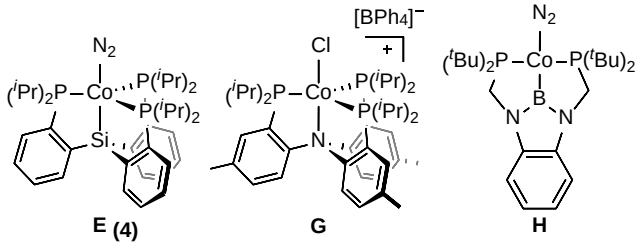

magnitude improvement over the only previous report of N_2 to NH_3 conversion mediated by well-defined Co complexes (NH_3 yield ≤0.21 equiv per Co-N_2 *vide supra*).[3,19]

Notably, no NH_3 is formed when either **2**, $[H•(OEt_2)_2][BAr^F{}_4]$, or KC_8 is omitted from the standard conditions, indicating that all three components are necessary for NH_3 production. In an effort to study the fate of **2** under the reaction conditions, we treated **2** with 10 equiv $[H•(OEt_2)_2][BAr^F{}_4]$ and 12 equiv KC_8, and observed signs of ligand decomposition by ^{31}P NMR (see SI). If the observed reactivity indeed represents modest catalysis, ligand decomposition under the reaction conditions provides a plausible rationale for the limited turnover number. As a control, free TPB ligand was subjected to the standard conditions as a precatalyst, leading to no detectable NH_3 production.

Interestingly, though anionic **2** and cationic **3** both generated substantial NH_3 under the standard conditions, submitting neutral **1** to these conditions provided attenuated yields of NH_3, comparable to the yields obtained with (TPB)CoBr (Table 2.2, B-D). Furthermore, complexes **4** and **5**, which are isoelectronic to **2**, are not competent for the reduction of N_2 with protons and electrons, producing ≤0.1 equivalents of NH_3 and no detectable hydrazine under identical conditions (Table 2.2, E and F). This result appears to underscore the importance of the nature of the M-E interaction in facilitating N_2 fixation by $(P_3E)M$ complexes.

To further explore the generality of N_2 conversion activity for Co complexes under these conditions, we screened a number of additional Co species. We targeted, for instance, a Co complex of the tris(phosphino)amine ligand, $NArP_3$ ($NArP_3$ = $[2\text{-}(^iPr_2P)\text{-}4\text{-}(CH_3)\text{-}C_6H_3]_3N$).[20] Synthesis of a $(NArP_3)Co$ complex completes a family of tris(phosphino) Co complexes featuring L, X and Z type axial donors. $[(NArP_3)CoCl][BPh_4]$ (Table 2.2, G)

was isolated as purple crystals in 90% yield from the reaction of the $NArP_3$ ligand with $CoCl_2$ and $NaBPh_4$. An X-ray diffraction study revealed a pseudo-tetrahedral geometry at the Co center, with minimum interaction with the apical N of the ligand (d = 2.64 Å). As expected for tetrahedral Co(II), $[(NArP_3)CoCl][BPh_4]$ is high-spin $S = 3/2$, with a solution magnetic moment of 3.97 μ_B in CD_2Cl_2 at 23 °C. We also tested the known bis(phosphino)boryl Co-N_2 complex[21] (Table 2.2, H), as well as various other common Co complexes (Table 2.2, I-K). Interestingly, of all the Co precursors subjected to the standard conditions, only (TPB)-ligated Co complexes generated >0.5 equivalents of NH_3 per metal center. At this point, we can begin to delineate the structural/electronic factors correlated to NH_3 production by $(P_3E)M$ complexes.

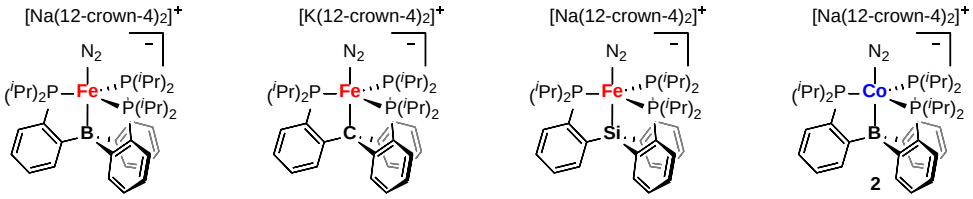

$\nu_{(N\text{-}N)}$ (cm^{-1}) [a]	1905	1905	1920	1978
$E_{1/2}$ (V vs. Fc/Fc^+) [b]	-2.19	-2.55	-2.20	-2.00
NH_3 equiv/M	7.0 ± 1.0	3.5 ± 0.3	0.8 ± 0.4	2.4 ± 0.3

Figure 2.5. Vibrational spectroscopy, electrochemistry, and catalytic competence data for select $[(P_3E)M(N_2)]^-$ complexes. Data for M = Fe, E = B is from refs. 7 and 10; data for M = Fe, E = C is from ref. 8; data for M = Fe, E = Si is taken refs. 8 and 15; and data for M = Co, E = B is from this work. [a]IR from solid state samples [b]Oxidation potentials determined by cyclic voltammetry in THF. Note: NH_3 yields based on the addition of ~ 50 equiv $[H•(OEt_2)_2][BAr^F{}_4]$ and ~ 60 equiv KC_8 in Et_2O (see refs. provided for specific details).

Among $(P_3E)Fe$ complexes, NH_3 production appears to be correlated both with flexibility of the M-E interaction and with degree of N_2 activation; more flexible and more activating platforms providing greater yields of NH_3. Moving from Fe to Co, the degrees of N_2

activation are systematically lower, which is expected due to the decreased spatial extent of the Co 3*d* orbitals (due to increased Z_{eff}).[22] Nevertheless, NH_3 production is still correlated among these $(P_3E)Co$ complexes with N_2 activation. However, comparing the Fe to the Co complexes demonstrates that, in an absolute sense, the degree of N_2 activation is not predictive of the yield of NH_3 (Figure 2.5). For example, $[Na(12\text{-}c\text{-}4)_2][(SiP_3)Fe(N_2)]$ shows a higher degree of N_2 activation than **2**, yet **2** demonstrates higher N_2-to-NH_3 conversion activity. The relative activity of these two complexes *is* predicted, on the other hand, by the flexibility of the M-E interactions trans to bound N_2. Indeed, among the factors considered here, only M-E interaction flexibility appears to predict the comparatively high N_2 conversion activity of **2**.

The potential at which the anionic states of the complexes depicted in Figure 2.5 are achieved do not follow a clear trend regarding their relative N_2 conversion activity. However, a comparison of the Fe and Co systems does demonstrate that the accessibility of highly reduced, *anionic* $[(P_3E)M(N_2)]^-$ complexes is favorably correlated to NH_3 production. It may be the case that the relative basicity of the β-N atom (N_β) plays an important role in N_2 conversion activity, with anionic species being appreciably more basic. Considering complexes **2** and **5**, neutral **5** affords <5% NH_3 per Co-N_2 subunit under the standard reaction conditions whereas the isoelectronic and isostructural, yet anionic, **2** produces >200% NH_3 (Table 2.2). The enhanced basicity of N_β in the anion would in turn favor protonation to produce a "$Co(N_2H)$" intermediate relative to other reaction pathways. We have performed calculations (DFT; see SI for details) to compare the theoretically predicted electrostatic potential maps of **2** and **5**. As shown in Figure 2.6, N_β in anionic **2** shows a far greater degree of negative charge relative to the same atom in neutral **5**.

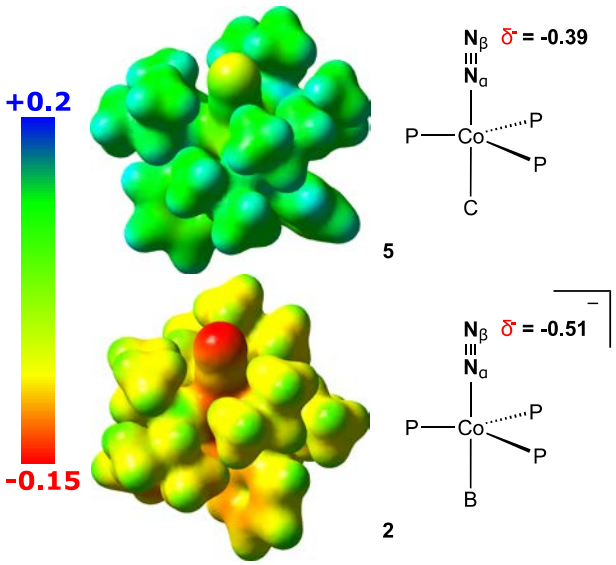

Figure 2.6. Electrostatic potential maps of anionic **2** and neutral **5** (isovalue = 0.015, color map in Hartrees), and atomic charges for N_β.

2.3 Conclusion

We have demonstrated the ability of a molecular Co-dinitrogen complex to facilitate the conversion of N_2 to NH_3 at -78 °C in the presence of proton and electron sources (2.4 equivalents of NH_3 generated per Co center on average). Prior to this report, the only well-defined molecular systems (including nitrogenase enzymes) capable of directly mediating the catalytic conversion of N_2 to NH_3 contained either Mo or Fe. While the measured NH_3 production by the featured cobalt complex is very modest with respect to catalysis, the yields measured do consistently indicate that some degree of catalysis is viable. The propensity of the $(P_3E)M$ complexes we have studied to perform productive nitrogen fixation does not appear to depend solely on the ability of the precursor complex to activate N_2. The observations collected herein indicate that anionic charge, and hence basicity of the bound N_2 ligand, in addition to flexibility of the M-E interaction trans to the bound N_2 ligand, correlate with more favorable NH_3 production. Of course, correlation does not

presume causation and the factors that lead to different NH_3 yields may be numerous. While some of the design features important to consider in catalysts of the $(P_3E)M(N_2)$ type have been highlighted here, other factors, including comparative rates of H_2 evolution and catalyst degradation/poisoning rates, warrant further studies.

2.4 Experimental

General considerations. All manipulations were carried out using standard Schlenk or glovebox techniques under an N_2 atmosphere. Solvents were deoxygenated and dried by thoroughly sparging with N_2 followed by passage through an activated alumina column in a solvent purification system by SG Water, USA LLC. Nonhalogenated solvents were tested with sodium benzophenone ketyl in tetrahydrofuran in order to confirm the absence of oxygen and water. Deuterated solvents were purchased from Cambridge Isotope Laboratories, Inc., degassed, and dried over activated 3-Å molecular sieves prior to use.

$[H(OEt_2)_2][BAr^F{}_4]$,[23] KC_8,[24] (TPB)Co(N_2),[12] (TPB)CoBr,[12] (SiP_3)Co(N_2),[14] $NArP_3$,[20] (PBP)Co(N_2),[21] CP_3H,[8] and Co(PPh_3)$_2I_2$[25] were prepared according to literature procedures. All other reagents were purchased from commercial vendors and used without further purification unless otherwise stated. Et_2O for NH_3 generation reactions was stirred over Na/K ($\geq$ 2 hours) and filtered before use.

Physical Methods. Elemental analyses were performed by Midwest Microlab, LLC (Indianapolis, IN). ^1H and ^{13}C chemical shifts are reported in ppm relative to tetramethylsilane, using ^1H and ^{13}C resonances from residual solvent as internal standards. ^{31}P chemical shifts are reported in ppm relative to 85% aqueous H_3PO_4. Solution phase magnetic measurements were performed by the method of Evans.[26] IR measurements were obtained as solutions or thin films formed by evaporation of solutions using a Bruker Alpha

Platinum ATR spectrometer with OPUS software. Optical spectroscopy measurements were collected with a Cary 50 UV-vis spectrophotometer using a 1-cm two-window quartz cell. Electrochemical measurements were carried out in a glovebox under an N_2 atmosphere in a one compartment cell using a CH Instruments 600B electrochemical analyzer. A glassy carbon electrode was used as the working electrode and platinum wire was used as the auxiliary electrode. The reference electrode was $Ag/AgNO_3$ in THF. The ferrocene couple (Fc/Fc^+) was used as an internal reference. THF solutions of electrolyte (0.1 M tetra-*n*-butylammonium hexafluorophosphate, $TBAPF_6$) and analyte were also prepared under an inert atmosphere. X-band EPR spectra were obtained on a Bruker EMX spectrometer.

X-ray diffraction studies were carried out at the Caltech Division of Chemistry and Chemical Engineering X-ray Crystallography Facility on a Bruker three-circle SMART diffractometer with a SMART 1K CCD detector. Data was collected at 100K using Mo Kα radiation (λ = 0.71073 Å). Structures were solved by direct or Patterson methods using SHELXS and refined against *F*2 on all data by full-matrix least squares with SHELXL-97. All non-hydrogen atoms were refined anisotropically. All hydrogen atoms were placed at geometrically calculated positions and refined using a riding model. The isotropic displacement parameters of all hydrogen atoms were fixed at 1.2 (1.5 for methyl groups) times the U_{eq} of the atoms to which they are bonded.

[Na(12-crown-4)$_2$][(TPB)Co(N$_2$)] (2). To a -78 ˚C solution of (TPB)CoBr (70.5 mg, 0.0967 mmol) in THF (2 mL) was added a freshly prepared solution of $NaC_{10}H_8$ (23.5 mg $C_{10}H_8$, 0.222 mmol) in THF (3 mL). The solution was brought to room temperature and allowed to stir for six hours. Addition of 12-crown-4 (51.1 mg, 0.290 mmol) and removal of solvent *in vacuo* provided a dark red solid. Et_2O was added and subsequently removed

in vacuo. The residue was suspended in C_6H_6 and filtered and the solids were washed with C_6H_6 (2 x 2 mL) and pentane (2 x 2 mL) to furnish a red solid (68.8 mg, 0.0660 mmol, 68%). Single crystals were grown by vapor diffusion of pentane onto a THF solution of the title compound that had been layered with Et_2O. ^{1}H NMR (400 MHz, THF-d_8) δ 7.41 (3H), 6.94 (3H), 6.66 (3H), 6.44 (3H), 3.64 (32H), 2.29 (br), 1.37 (6H), 1.20 (6H), 0.93 (6H), -0.26 (6H). ^{11}B NMR (128 MHz, THF-d_8) δ 9.32. ^{31}P NMR (162 MHz, THF-d_8) δ 62.03. IR (thin film, cm^{-1}): 1978 (N_2). Anal. Calcd. for $C_{52}H_{86}BCoN_2NaO_8P_3$: C, 59.32; H, 8.23; N, 2.66. Found: C, 59.05; H, 7.99; N, 2.47.

[(TPB)Co][BAr$^F_4$] (3). To a -78 ˚C solution of (TPB)Co(N_2) (**1**) (91.5 mg, 0.135 mmol) in Et_2O (2 mL) was added solid [H(OEt_2)$_2$][BAr$^F_4$] (134.0 mg, 0.132 mmol). The reaction was brought to room temperature and vented to allow for the escape of H_2. The purple-brown solution was stirred for 1 hr. The solution was layered with pentane (5 mL) and stored at -35 ˚C to furnish red-purple single crystals of the title compound (162.9 mg, 0.0952 mmol, 82%) which were washed with pentane (3 x 2 mL). ^{1}H NMR (400 MHz, C_6D_6) δ 26.25, 23.80, 8.64, 8.44 ([BAr$^F_4$]), 7.88 ([BAr$^F_4$]), 6.33, -2.16, -3.68. UV-Vis (Et_2O, nm {L cm^{-1} mol^{-1}}): 585 {1500}, 760 {532}. Anal. Calcd. for $C_{68}H_{66}B_2CoF_{24}P_3$: C, 53.99; H, 4.40. Found: C, 53.94; H, 4.51.

(CP_3)Co(N_2) (5). (CP_3)H (100 mg, 0.169 mmol) and $CoCl_2$ • 1.5 THF (40 mg, 0.169 mmol) were mixed at room temperature in THF (10 mL). This mixture was allowed to stir for one hour, yielding a homogeneous cyan solution. This solution was chilled to -78 ˚C, and a solution of MeMgCl in tetrahydrofuran (0.5 M, 0.560 mmol) was added in three 370 μL portions over three hours. The mixture was allowed to warm slowly to room temperature, and then was concentrated to *ca.* 1 mL. 1,4-dioxane (2 mL) was added, and

the resultant suspension was stirred vigorously for at least 2 hours before filtration. The filtrate was concentrated to a tacky red-brown solid, which was extracted with 1:1 C_6H_6 : pentane (10 mL), filtered over celite and lyophilized to yield the product as a red powder (96 mg, 0.141 mmol, 83%). Crystals suitable for X-ray diffraction were grown via slow evaporation of a pentane solution. ^{1}H NMR (300 MHz, C_6D_6) δ 7.28 (br, 3H), 6.82 (m, 9H), 2.82 (oct., -C*H*, 3H), 2.09 (sept., -C*H*, 3H), 1.49 (m, 18H), 1.06 (dd, -CHC*H*$_3$, 9H), 0.30 (dd, -CHC*H*$_3$, 9H). ^{31}P{^{1}H} (121 MHz, C_6D_6): δ 47.39. IR (thin film, cm^{-1}): 2057 (N_2). Anal. Calcd. for $C_{37}H_{54}CoN_2P_3$: C, 65.48; H, 8.02; N, 4.13. Found: C, 64.14; H, 8.36; N, 4.03.

[(CP$_3$)Co(N$_2$)][BAr$^F_4$] (6). **5** (75 mg, 0.11 mmol) and [Cp$_2$Fe][BAr$^F_4$] (122 mg, 0.12 mmol) were dissolved separately in diethyl ether (ca. 3 mL each) and the ethereal solutions were cooled to -78˚C. The chilled solution of [Cp$_2$Fe][BAr$^F_4$] was added dropwise to the solution of **5**, and the resultant mixture was allowed to stir at low temperature for one hour. At this point, the mixture was allowed to warm to room temperature before filtration over celite and concentration to *ca.* 2 mL. The concentrated filtrate was layered with pentane, and placed in a freezer at -35˚C to induce crystallization. Decanting the mother liquor off crystalline solids and washing thoroughly with pentane yields [(CP$_3$)Co(N$_2$)][BAr$^F_4$] (**6**) as dark green-brown crystals (147 mg, 0.095 mmol, 86%). Crystals suitable for X-ray diffraction were grown by slow diffusion of pentane vapors into an ethereal solution of **6** at -35˚C. μ_{eff} (5:1 d$_8$-toluene:d$_8$-THF, Evans' method, 23 °C): 3.49 μ_B. ^{1}H NMR (300 MHz, C_6D_6) δ 17.22, 9.94, 8.24 ([BAr$^F_4$]), 7.72 ([BAr$^F_4$]), 3.13, 2.57, 1.5 – -2 (br, m), –3.68. IR (cm^{-1}): 2182 (N_2, thin film), 2180 (N_2, solution). Elemental analysis shows low values for N consistent with a labile N_2 ligand, Anal. Calcd. for $C_{69}H_{66}BCoF_{24}N_2P_3$: C, 53.75; H,

4.31; N, 1.82. Found: C, 53.86; H, 4.31; N, 0.27. Note: The magnetic moment for **6** in solution may be complicated by some degree of solvent exchange for N_2 at the cobalt center as described in the text.

[(NArP$_3$)CoCl][BPh$_4$]. THF (5 mL) was added to a solid mixture of NArP$_3$ (58 mg, 91.2 mmol), $CoCl_2$ (12 mg, 92.4 mmol) and $NaBPh_4$ (31 mg, 90.6 mmol). The reaction was stirred for 4 hours at room temperature during which the color evolved from yellow to green to purple. The solvent was removed *in vacuo* and the residue was taken up in dichloromethane. The suspension was filtered over a plug of Celite and the filtrate was dried yielding a purple powder (86 mg, 82.1 mmol, 90%). Single crystals were grown by slow evaporation of a saturated solution of [(NArP$_3$)CoCl][BPh$_4$] in diethyl ether/dichloromethane (1:2 v:v). ^{1}H NMR (CD_2Cl_2, 300 MHz) δ 177.77, 37.50, 23.78, 13.48, 12.96, 7.37, 7.08, 6.92, 4.41, 1.50, -3.60, -9.81; UV-Vis (THF, nm {L cm^{-1} mol^{-1}}): 564 {452}, 760 {532}; μ_{eff} (CD_2Cl_2, Evans' method, 23 °C): 3.97 μ_B. Anal. Calcd. for $C_{63}H_{80}BClCoNP_3$: C, 72.10; H, 7.68; N, 1.33. Found: C, 71.97; H, 7.76; N, 1.30.

Ammonia Quantification. A Schlenk tube was charged with HCl (3 mL of a 2.0 M solution in Et_2O, 6 mmol). Reaction mixtures were vacuum transferred into this collection flask. Residual solid in the reaction vessel was treated with a solution of [Na][O-*t*-Bu] (40 mg, 0.4 mmol) in 1,2-dimethoxyethane (1 mL) and sealed. The resulting suspension was allowed to stir for 10 min before all volatiles were again vacuum transferred into the collection flask. After completion of the vacuum transfer, the flask was sealed and warmed to room temperature. Solvent was removed in vacuo, and the remaining residue was dissolved in H_2O (1 mL). An aliquot of this solution (20 μL) was then analyzed for the

presence of NH_3 (present as $[NH_4][Cl]$) by the indophenol method.[17] Quantification was performed with UV−vis spectroscopy by analyzing absorbance at 635 nm.

Standard NH_3 Generation Reaction Procedure with [(TPB)Co(N_2)][Na(12-crown-4)$_2$] (2). [(TPB)Co(N_2)][Na(12-crown-4)$_2$] (2.2 mg, 0.002 mmol) was suspended in Et_2O (0.5 mL) in a 20 mL scintillation vial equipped with a stir bar. This suspension was cooled to −78 °C in a cold well inside of a N_2 glovebox. A solution of $[H{\cdot}(OEt_2)_2][BAr^F{}_4]$ (95 mg, 0.094 mmol) in Et_2O (1.5 mL) similarly cooled to −78 °C was added to this suspension in one portion with stirring. Residual acid was dissolved in cold Et_2O (0.25 mL) and added subsequently. This mixture was allowed to stir 5 minutes at −78 °C, before being transferred to a precooled Schlenk tube equipped with a stir bar. The original reaction vial was washed with cold Et_2O (0.25 mL) which was added subsequently to the Schlenk tube. KC_8 (16 mg, 0.119 mmol) was suspended in cold Et_2O (0.75 mL) and added to the reaction mixture over the course of 1 minute. The Schlenk tube was then sealed, and the reaction was allowed to stir for 40 min at −78 °C before being warmed to room temperature and stirred for 15 min.

2.5 REFERENCES

1 Smil, V. *Enriching the Earth*; MIT Press: Cambridge, 2001.

2 Hidai, M.; Takahashi, T.; Yokotake, I.; Uchida, Y. *Chem. Lett.* **1980**, 645.

3 Yamamoto, A.; Miura, Y.; Ito, T.; Chen, H.; Iri, K.; Ozawa, F.; Miki, K.; Sei, T.; Tanaka, N.; Kasai, N. *Organometallics* **1983**, *2*, 1429.

4 (a) Fryzuk, M. D. *Acc. Chem. Res.* **2009**, *42*, 127. (b) Schrock, R. R. *Angew. Chem. Int. Ed.* **2008**, *47*, 5512. (c) Chirik, P. J. *Dalton Trans.* **2007**, 16. (d) Peters, J. C.; Mehn, M. P. In *Activation of Small Molecules: Organometallic and Bioinorganic Perspectives*; Tolman, W. B., Ed.; Wiley-VCH: New York, 2006; pp 81–119. (e) Crossland, J. L.; Tyler, D. R. *Coord. Chem. Rev.* **2010**, *254*, 1883. (f) Chatt, J.; Dilworth,

J. R.; Richards, R. L. *Chem. Rev.* **1978**, *78*, 589. (g) Siedschlag, R. B.; Bernales, V.; Vogiatzis, K. D.; Planas, N.; Clouston, L. J.; Bill, E.; Gagliardi, L.; Lu, C. C. *J. Am. Chem. Soc.* **2015**, *137*, 4638.

5 (a) Laplaza, C. E.; Cummins, C. C. *Science* **1995**, *268*, 861. (b) Zanotti-Gerosa, A.; Solari, E.; Giannini, L.; Floriani, C.; Chiesi-Villa, A.; Rizzoli, C. *J. Am. Chem. Soc.* **1998**, *120*, 437. (c) Nikiforov, G. B.; Vidyaratne, I.; Gambarotta, S.; Korobkov, I. *Angew. Chem. Int. Ed.* **2009**, *48*, 7415. (d) Vidyaratne, I.; Crewdson, P.; Lefebvre, E.; Gambarotta, S. *Inorg. Chem.* **2007**, *46*, 8836. (e) Clentsmith, G. K. B.; Bates, V. M. E.; Hitchcock, P. B.; Cloke, F. G. N. *J. Am. Chem. Soc.* **1999**, *121*, 10444. (f) Hebden, T. J.; Schrock, R. R.; Takase, M. K.; Müller, P. *Chem. Commun.* **2012**, *48*, 1851. (g) Rodriguez, M. M.; Bill, E.; Brennessel, W. W.; Holland, P. L. *Science* **2011**, *334*, 780. (h) Curley, J. J.; Cook, T. R.; Reece, S. Y.; Müller, P.; Cummins, C. C. *J. Am. Chem. Soc.* **2008**, *130*, 9394. (i) Fryzuk, M. D.; Kozak, C. M.; Bowdridge, M. R.; Patrick, B. O.; Rettig, S. J. *J. Am. Chem. Soc.* **2002**, *124*, 8389.

6 (a) Yandulov, D. V.; Schrock, R. R. *Science* **2003**, *301*, 76. (b) Schrock, R. R. *Angew. Chem. Int. Ed.* **2008**, *47*, 5512. (c) Arashiba, K.; Miyake, Y.; Nishibayashi, Y. *Nat. Chem.* **2010**, *3*, 120. (d) Kuriyama, S.; Arashiba, K.; Nakajima, K.; Tanaka, H.; Kamaru, N.; Yoshizawa, K.; Nishibayashi, Y. *J. Am. Chem. Soc.* **2014**, *136*, 9719. (e) Ung, G.; Peters, J. C. *Angew. Chem. Int. Ed.* **2015**, *54*, 532.

7 Anderson, J. S.; Rittle, J.; Peters, J. C. *Nature* **2013**, *501*, 84.

8 Creutz, S. E.; Peters, J. C. *J. Am. Chem. Soc.* **2014**, *136*, 1105.

9 Moret, M.-E.; Peters, J. C. *J. Am. Chem. Soc,* **2011**, *133*, 18118.

10 Moret, M.-E.; Peters, J. C. *Angew. Chem. Int. Ed.* **2011**, *50*, 2063.

11 For a recent review see: Hoffman, B. M.; Lukoyanov, D.; Yang, Z.-Y.; Dean, D. R.; Seefeldt, L. C. *Chem. Rev.* **2014**, *114*, 4041.

12 Suess, D. L. M.; Tsay, C.; Peters, J. C. *J. Am. Chem. Soc.* **2012**, *134*, 14158.

13 Anderson, J. S.; Moret, M.-E.; Peters, J. C. *J. Am. Chem. Soc.* **2013**, *135*, 534.

14 Whited, M. T.; Mankad, N. P.; Lee, Y.; Oblad, P. F.; Peters, J. C. *Inorg. Chem.* **2009**, *48*, 2507.

15 Lee, Y.; Mankad, N. P.; Peters, J. C. *Nat. Chem.* **2010**, *2*, 558.

16 Vela, J.; Cirera, J.; Smith, J. M.; Lachicotte, R. J.; Flaschenriem, C. J.; Alvarez, S.; Holland, P. L. *Inorg. Chem.* **2007**, *46*, 60.

17 Weatherburn, M. W. *Anal. Chem.* **1967**, *39*, 971.

18 Watt, G. W.; Chrisp, J. D. *Anal. Chem.* **1952**, *24*, 2006.

19 There is an additional early report of the generation of one equivalent of NH_3 by a Co-porphyrin complex under an N_2 containing atmosphere upon treatment with sodium borohydride (see Fleischer, E. B.; Krishnamurthy, M. *J. Am. Chem. Soc.* **1972**, *94*, 1382). However a later study firmly concluded that the NH_3 detected under these conditions was not derived from N_2 (see Chatt, J.; Elson, C. M.; Leigh, G. J. *J. Am. Chem. Soc.* **1973**, *95*, 2408).

20 MacBeth, C. E.; Harkins, S. B.; Peters, J. C. *Can. J. Chem.* **2005**, *83*, 332.

21 Lin, T.-P.; Peters, J. C. *J. Am. Chem. Soc.* **2013**, *135*, 15310.

22 Miessler, G. L.; Tarr, D. A. *Inorganic Chemistry*, 4th ed. Prentice Hall: New York, 2011; pp 37–43.

23 Brookhart, M.; Grant, B.; Volpe Jr., A. F. *Organometallics* **1992**, *11*, 3920–3922.

24 Wietz, I. S.; Rabinovitz, M. J. *J. Chem. Soc., Perkin Trans.* **1993**, *1*, 117.

25 Cotton, F. A.; Faut, O. D.; Goodgame, D. M. L.; Holm, R. H. *J. Am. Chem. Soc.* **1961**, *83*, 1780.

26 Evans, D. F. *J. Chem. Soc.* **1959**, 2003.

Chapter 3

A SYNTHETIC SINGLE-SITE FE NITROGENASE: HIGH TURNOVER, FREEZE-QUENCH ^{57}FE MÖSSBAUER DATA, AND A HYDRIDE RESTING STATE

Reproduced in part with permission from:

Del Castillo, T.; Thompson, N.; Peters, J. C.; *J. Am. Chem. Soc.*, **2016**, *138,* 5341-5350.

DOI: 10.1021/jacs.6b01706

Thinking back on this study the thing I remember most is that, prior to collecting all of the data presented here and the many months of experimentation Nik and I produced during this period, there was an additional four or so months during which time we worked extensively on a methodology to prepare very pure sodium tetrakis(3,5-bistrifluoromethylphenyl)borate ($NaBAr^F_4$) and in turn very pure acid $[H(OEt_2)_2][BAr^F_4]$ on a large scale. This methodology (which is presented in the supplementary information for this chapter) will turn out to be something of an unsung hero throughout the rest of my thesis as the high purity level allowed us to obtain higher turnover numbers, in turn enabling kinetic probes and in situ spectroscopy by freeze-quenching (presented in the following chapter), as well as allowing all of the electrochemistry presented in chapter five in which $NaBAr^F_4$ is employed as an ether soluble electrolyte. The lesson of course is that it can be well worth the effort to obtain very pure starting materials, though as with all things this should be balanced against the

scope and direction of one's specific project. As I've always found balance-two-things advice a little thin I will add, err on the side of spending too much time obtaining pure starting materials.

3.1 Introduction

The fixation of molecular nitrogen (N_2) into ammonia (NH_3) is a transformation of fundamental importance to both biology and industry,[1] a fact which has prompted mechanistic study of the few known systems capable of catalyzing this reaction. The industrial Haber-Bosch process has been the subject of exhaustive investigation, resulting in a detailed mechanistic understanding in large part supported by surface spectroscopic studies on model systems.[2] The nitrogenase family of enzymes provides an example of catalytic N_2 conversion under ambient conditions and has also been studied extensively. While many questions remain unanswered regarding the mechanism of nitrogenase, a great deal of kinetic and reactivity information has been collected.[3] Additionally, important insights have been provided by protein crystallography, X-ray emission spectroscopy, and site-mutagenesis studies, as well as in situ freeze-quench ENDOR and EPR spectroscopy.[4,5]

Hypotheses underpinning the mechanisms of both of these systems are bolstered by synthetic model chemistry and efforts to develop molecular N_2 conversion catalysts.[6] This search has yielded systems capable of the catalytic reduction of N_2 to hydrazine (N_2H_4),[7] tris(trimethylsilyl)amine,[8] and a few examples of the direct catalytic fixation of N_2 to NH_3 (Chart 1).[8g,9,10,11,12] While a wealth of mechanistic information for the original Mo catalyst system developed by Schrock has been derived from stoichiometric studies and theory,[13,14]

in situ spectroscopic studies during catalysis were not reported. These synthetic catalysts operate under heterogeneous conditions and are likely to generate mixtures of intermediate species that are both diamagnetic and paramagnetic, making it challenging to reliably determine speciation under turnover. This latter limitation is also true of biological nitrogenases. While CW and pulsed-EPR techniques can and have been elegantly applied,[5] such studies are inherently limited in that species/intermediates not readily observable by these techniques will go unnoticed.

Chart 1: Synthetic catalysts for nitrogen fixation with maximum observed yields of NH_3[a]

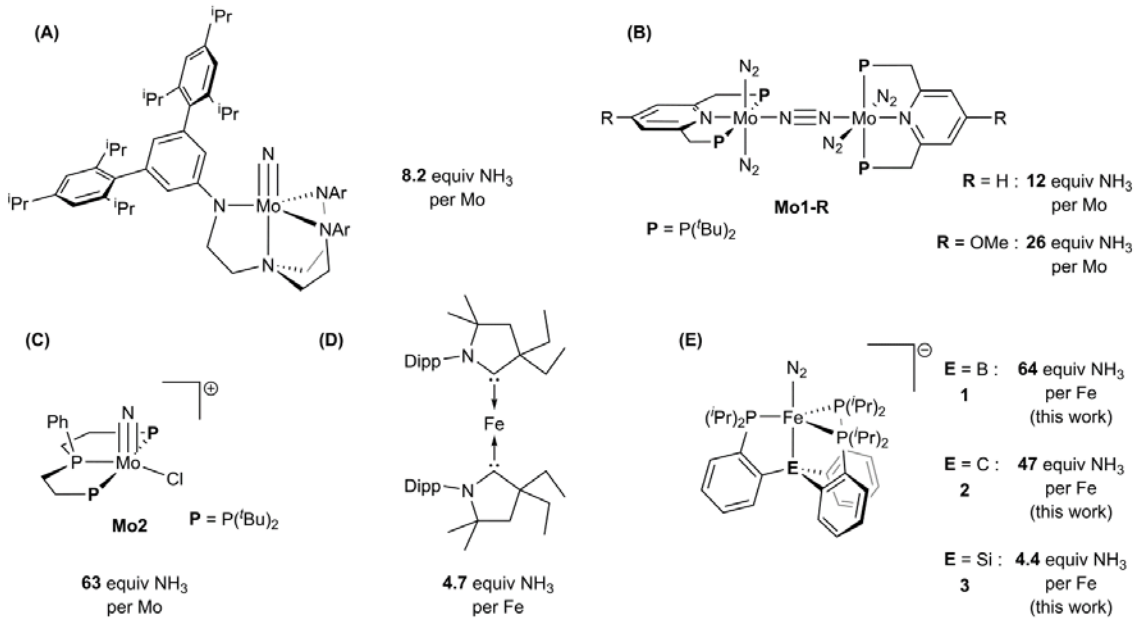

[a](A) See reference 9a. (B) See references 10. (C) See reference 11. (D) See reference 8g. (E) See references 12. Note that NH_3 equivalents shown represent the highest single-run values that have been reported for the various catalysts shown; direct cross-comparisons of Fe and Mo catalyst performance are tenuous due to the different reaction conditions used.

Iron is the only transition metal that is essential in the cofactor for nitrogenase function, and this fact has motivated a great deal of recent interest in Fe-N_2 model chemistry.[15] In recent years we have focused on a family of Sacconi-type tetradentate ligands, P_3^E, in which three phosphine donors are bonded to a central atom through an *ortho*-phenylene linker (E = B, Si, C). We have shown that P_3^EM (M = Fe, Co) complexes promote the binding and activation of N_2, as well as the functionalization of bound N_2 with various electrophiles.[16,17,18] Moreover, we discovered that P_3^BFe (P_3^B = tris(*o*-diisopropylphosphinophenyl)borane) and P_3^CFe (P_3^C = tris(*o*-diisopropylphosphinophenyl)methyl) complexes mediate the catalytic reduction of N_2 to NH_3 at low temperature using a strong acid—$[H(OEt_2)_2][BAr^F_4]$ ($HBAr^F_4$)—and a strong reductant—potassium graphite (KC_8) (Chart 1, D).[12] One unique aspect of these Fe-based systems is their suitability for in situ spectroscopic study by freeze-quench ^{57}Fe Mössbauer spectroscopy. In principle, this technique enables observation of the total Fe speciation as frozen snapshots during turnover.[19] For single-site Fe nitrogenase mimics of the type we have developed, analysis of such data is far simpler than in a biological nitrogenase where many iron centers are present.[20]

For the most active P_3^BFe catalyst system, many P_3^BFe-N_xH_y model complexes that may be mechanistically relevant (e.g., Fe^+, Fe-N_2^-, Fe=NNH_2^+, Fe-NH_3^+) have now been independently generated and characterized, including by ^{57}Fe Mössbauer spectroscopy, and these data facilitate interpretation of the freeze-quench Mössbauer data reported here. In combination with chemical quenching methods that we present to study the dynamics of product formation, it becomes possible to attempt to correlate the species observed spectroscopically with the N_2 fixing activity to gain a better understanding of the overall

catalytic system. Such a strategy complements the studies of model complexes and stoichiometric reactions steps that we have previously undertaken and offers a fuller mechanistic picture. While many questions remain, this approach to studying N_2-to-NH_3 conversion mediated by synthetic iron catalysts is a mechanistically powerful one.

Here we undertake tandem spectroscopy/activity studies using the P_3^E (E = B, C, Si) Fe catalyst systems and report the following: (i) two of these Fe-based catalysts (E = B, C) are unexpectedly robust under the reaction conditions, demonstrating comparatively high yields of NH_3 that are nearly an order of magnitude larger than in initial reports at lower acid/reductant loadings; (ii) based on electrochemical measurements the dominant catalysis by the P_3^BFe system likely occurs at the formal P_3^BFe-N_2/P_3^BFe-N_2^- couple, corroborated by demonstrating catalysis with Na/Hg and electrolytic N_2-to-NH_3 conversion in a controlled-potential bulk electrolysis; (iii) the P_3^BFe system shows first order rate dependence on iron catalyst concentration and zero order dependence on acid concentration; (iv) kinetic competition between rates of N_2 versus H^+ reduction are a key factor in determining whether productive N_2-to-NH_3 conversion is observed; and (v) a metal hydride-borohydride species is a resting state of the P_3^BFe catalysis system.

3.2 Results and Discussion

3.2.1. Increased turnover of Fe-catalyzed N_2 fixation and evidence for catalysis at the P_3^BFe-N_2/P_3^BFe-N_2^- couple. Following our initial discovery that the addition of excess $HBAr^F_4$ and KC_8 to the anionic dinitrogen complex $[P_3^B Fe(N_2)][(12\text{-crown-}4)_2Na]$ (**1**) at low temperature in Et_2O under an atmosphere of N_2 furnishes catalytic yields of NH_3, we pursued the optimization of this system for NH_3 yield (Eqn. 1).

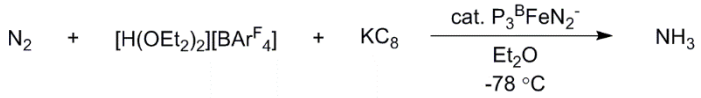

(1)

Under our initially reported conditions (in Et_2O at -78 °C with 48 equiv $HBAr^F_4$ and 58 equiv KC_8) the catalysis furnishes 7.0 ± 1.0 equiv of NH_3 per Fe atom, corresponding to 44% of added protons being delivered to N_2 to make NH_3. Initial attempts at optimization showed that neither the overall concentration of the reactants nor the mole ratio of the catalyst substantially altered the yield of NH_3 with respect to proton equivalents.

We have since examined whether the post-reaction material retained any catalytic competence when more substrate was delivered. We found that if, after stirring at -78 °C for 1 hour the reaction mixture was frozen (at -196 °C), delivered additional substrate, and then thawed to -78 °C, significantly more NH_3 was formed. Iterating this reloading process several times resulted in a steady increase in the total yield of NH_3 per Fe atom (Figure 3.1), demonstrating that some active catalyst remains at -78 °C, even after numerous turnovers. This result implies that the yield of NH_3 is limited by competitive consumption of substrate in a hydrogen evolving reaction (HER).

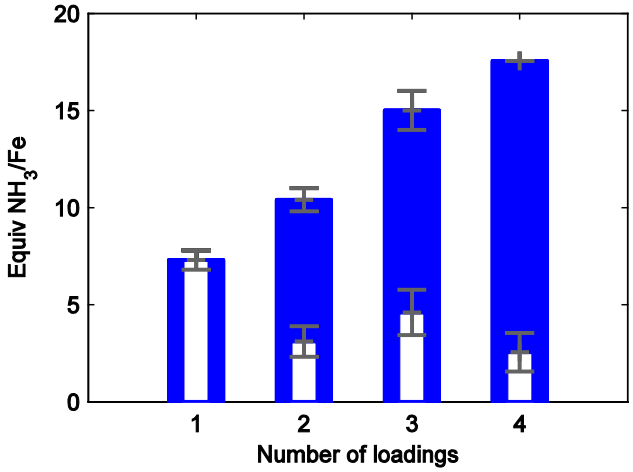

Figure 3.1: Yields of NH_3 obtained using $P_3^BFe\text{-}N_2^-$ **1** from successive reloading of $HBAr^F_4$ and KC_8 to reactions maintained at ≤ -70 °C in Et_2O. Blue bars denote total observed yields and white inset bars denote the average increase in total yield from the final loading of substrate. Each loading corresponds to 48 equiv $HBAr^F_4$ and 58 equiv KC_8 relative to Fe. Data presented are averages of two experiments.

The apparent stability of at least some of the catalyst at low temperature suggested that it may be possible to observe higher turnover numbers if the catalyst is delivered more substrate at the beginning of the reaction. Indeed, as shown in Table 3.1, addition of increasing equivalents of $HBAr^F_4$ and KC_8 to **1** at low temperature furnished steadily increasing yields of NH_3 relative to catalyst, with a current maximal observed yield of 64 equivalents of NH_3 per Fe atom (average of 59 ± 6 over 9 iterations, Table 3.1, Entries 1–5) at 1500 equiv acid loading. This yield is nearly an order of magnitude larger than that reported at the original acid loading of 48 equiv. We note that the yields of NH_3 under these conditions are highly sensitive to the purity of the acid source, unsurprising given the high acid substrate loading relative to catalyst (~1500 equiv $HBAr^F_4$). To obtain reproducible yields, we have developed a tailored protocol for the synthesis of sufficiently pure

$NaBAr^F{}_4/HBAr^F{}_4$, which is detailed in the Supporting Information. It is also important to ensure good mixing and a high gas-liquid interfacial surface area to enable proper mass transfer in the heterogeneous reaction mixture.

Having discovered that $P_3{}^BFe\text{-}N_2^-$ **1** is a significantly more robust catalyst than originally appreciated, we investigated the activity of the alkyl N_2 anion $[P_3{}^CFe\text{-}N_2][(Et_2O)_{0.5}K]$ (**2**) toward N_2 fixation at higher substrate loading. Significantly higher yields of NH_3 per Fe are also attainable using **2** as a catalyst, albeit with roughly 2/3 the activity of **1** (Table 3.1, Entries 6–10). As a point of comparison, we also submitted the silyl congener $[P_3{}^{Si}Fe\text{-}N_2][(12\text{-crown-}4)_2Na]$ (**3**) ($P_3{}^{Si}$ = tris(*o*-diisopropylphosphinophenyl)silyl) to these conditions and observed dramatically lowered yields of NH_3, consistent with earlier reports (Table 3.1, Entries 11,12). Although the $P_3{}^{Si}Fe\text{-}N_2^-$ system **3** displays worse selectivity for NH_3 formation vs. HER than **1** (*vide infra*), **3** still demonstrates catalytic yields of NH_3 under sufficiently high substrate loading (up to 4 equiv NH_3 per Fe, Table 3.1 Entry 12).

Table 3.1 also contains data for catalytic trials with the borohydrido-hydrido complex $(P_3{}^B)(\mu\text{-}H)Fe(H)(N_2)$ (**4-N_2**) as a catalyst in mixed Et_2O/toluene solvent. In the presence of admixed toluene **4-N_2** is observed to be partially soluble and demonstrates competence as a catalyst (Table 3.1, Entry 14); in the absence of toluene **4-N_2** shows poor solubility and lower than catalytic yields of NH_3 were observed under the originally reported catalytic conditions (0.50 ± 0.1 equiv NH_3 per Fe).[12a] The significance of these observations is discussed below (section 2.4).

The efficiency of NH_3 production with respect to acid substrate decreases under increasingly high turnover conditions for these iron systems. Our understanding of the HER

kinetics (*vide infra*) rationalizes this phenomenon in that under comparatively low catalyst loading (which engenders higher turnover) the background HER should be increasingly competitive, thereby reducing N_2-fixing efficiency. The product of the reaction (NH_3) may also act as an inhibitor of catalysis. To test this latter possibility, catalytic runs with 150 equiv $HBAr^F_4$ and 185 equiv KC_8 in the presence of **1** were conducted with the inclusion of 25 equiv of NH_3 (Table 3.1, Entry 15). The fixed N_2 yield of this reaction is substantially lower than the comparable experiment without added NH_3 (Table 3.1, Entry 3). One contributing cause for NH_3 inhibition is that it sequesters $HBAr^F_4$ as $[NH_4][BAr^F_4]$; however, the yield of NH_3 observed in Entry 15 is suppressed compared to an experiment with only 100 equiv $HBAr^F$. This observation indicates that NH_3 inhibits the catalytic reaction, and that the degree of inhibition is more substantial than stoichiometric leveling of the acid strength.

Table 3.1. NH_3 Generation from N_2 Mediated by Synthetic Fe Catalysts[a]

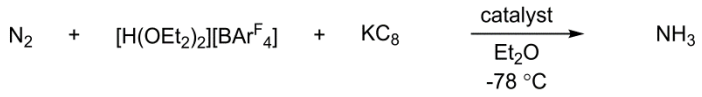

Entry	Catalyst	[Fe] (mM)	$HBAr^F_4$ equiv	KC_8 equiv	Variation	Equiv NH_3/Fe	% Yield NH_3/H^+
1	**1**	1.3	48	58	—	7.3 ± 0.5	45 ± 3
2	**1**	0.64	96	58	—	12 ± 1	38 ± 3
3	**1**	0.43	150	185	—	17.4 ± 0.2	35.6 ± 0.4
4	**1**	0.08	720	860	—	43 ± 4	18 ± 2
5	**1**	0.04	1500	1800	—	59 ± 6	12 ± 1
6[b]	**2**	1.0	37	40	$[HBAr^F_4]$ = 31 mM	4.6 ± 0.8	36 ± 6
7	**2**	0.56	110	120	—	11.3 ± 0.9	31 ± 2
8	**2**	0.28	220	230	—	14 ± 3	19 ± 4
9	**2**	0.08	750	810	—	19 ± 4	7 ± 2
10	**2**	0.04	1500	1600	—	36 ± 7	7 ± 1
11[c]	**3**	0.58	48	58	$[HBAr^F_4]$ = 31 mM	0.8 ± 0.5	5 ± 3
12	**3**	0.04	1500	1800	—	3.8 ± 0.8	0.8 ± 0.2
13	**4-N_2**[d]	-	150	185	3% toluene	1.1 ± 0.1	2.4 ± 0.3
14	**4-N_2**	0.44	150	185	25% toluene	5.6 ± 0.9	12 ± 2
15	**1**	0.41	150	185	25 equiv NH_3 added	6.4 ± 0.1	13.2 ± 0.2
16	**1**	0.41	150	0	1900 equiv 10 wt% Na/Hg	5.0 ± 0.2	10.3 ± 0.5

[a]Fe precursor, $HBAr^F_4$, KC_8, and Et_2O sealed in a vessel at -196 °C under an N_2 atmosphere followed by warming to -78 °C and stirring at -78 °C. Unless noted otherwise, $[HBAr^F_4]$ = 63 mM. Yields are reported as an average of at least 2 iterations; data for individual experimental iterations are presented in the Supporting Information. [b]Data taken from reference 12b. [c]Data taken from reference 12a. [d]Not fully soluble under reaction conditions.

We also sought to establish the minimum reducing potential required to drive catalysis with $P_3^BFe\text{-}N_2^-$ **1**. We have shown in previous work that **1** reacts favorably with $HBAr^F_4$ in Et_2O at -78 °C along a productive N_2 fixation pathway.[18] In brief, **1** can be doubly protonated in Et_2O at -78 °C to generate $P_3^BFe{=}NNH_2^+$ (Eqn. 2). If only stoichiometric acid is present, **1** is instead unproductively oxidized to $P_3^BFe\text{-}N_2$ (Eqn. 3). We have only observed net oxidation in the reaction of the neutral $P_3^BFe\text{-}N_2$ state with $HBAr^F_4$ in Et_2O to produce $P_3^BFe^+$ (Eqn. 4).

$$\mathbf{1} + \text{xs } HBAr^F_4 \rightarrow P_3^BFe{=}NNH_2^+ \quad (2)$$

$$\mathbf{1} + HBAr^F_4 \rightarrow P_3^BFe\text{-}N_2 + 0.5\ H_2 \quad (3)$$

$$P_3^BFe\text{-}N_2 + HBAr^F_4 \rightarrow P_3^BFe^+ + 0.5\ H_2 \quad (4)$$

These observations suggest that N_2 fixing catalysis likely occurs at the $P_3^BFe\text{-}N_2/P_3^BFe\text{-}N_2^-$ redox couple (-2.2 V vs Fc/Fc^+), but not at the $P_3^BFe^+/P_3^BFe\text{-}N_2$ couple (-1.5 V vs Fc/Fc^+). We have explored this hypothesis via cyclic voltammetry (CV) experiments. Figure 3.2 shows electrochemical data for $P_3^BFe^+$ dissolved in Et_2O at -45 °C under 1 atm N_2 in the presence of 0.1 M $NaBAr^F_4$ as a soluble electrolyte to create a modestly conductive ethereal solution.[21] The blue trace shows the expected irreversible $P_3^BFe^+/P_3^BFe\text{-}N_2$ couple centered around ~ -1.7 V and the $P_3^BFe\text{-}N_2/P_3^BFe\text{-}N_2^-$ couple at -2.2 V, as previously reported.[17a] The red trace shows the electrochemical behavior of $P_3^BFe^+$ in the presence of 5 equiv $HBAr^F_4$. The data reveal a sharp plateaued increase in current coincident with the $P_3^BFe\text{-}N_2/P_3^BFe\text{-}N_2^-$ redox couple, and very little increase in

current at the $P_3^BFe^+/P_3^BFe\text{-}N_2$ couple. The onset of an apparent catalytic response at the $P_3^BFe\text{-}N_2/P_3^BFe\text{-}N_2^-$ couple intimates that electrocatalysis may be feasible, and that chemical reductants with weaker reduction potentials than KC_8 may also be competent for N_2-to-NH_3 conversion catalyzed by $P_3^BFe\text{-}N_2^-$. Also, the potential of the apparent catalytic response does not shift from the $P_3^BFe\text{-}N_2/P_3^BFe\text{-}N_2^-$ couple in the absence of acid, indicating that this reduction precedes the first protonation event.

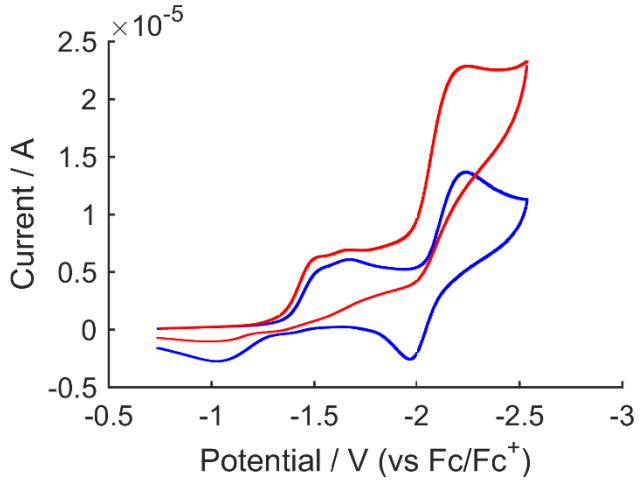

Figure 3.2: Cyclic voltammetry of $[P_3^BFe][BAr^F{}_4]$ in the presence of 0 (blue trace) and 5 (red trace) equiv $HBAr^F{}_4$, collected in Et_2O with 0.1 M $NaBAr^F{}_4$ electrolyte at -45 °C using a glassy carbon electrode and referenced to the Fc/Fc^+ couple. Scan rate is 100 mV/s.

To determine whether electrolytic N_2-to-NH_3 conversion contributes to the catalytic feature observed in the CV data, a controlled-potential bulk electrolysis of $P_3^BFe^+$ and 10 equiv $HBAr^F{}_4$ in Et_2O at -45 °C under 1 atm N_2 in the presence of 0.1 M $NaBAr^F{}_4$ electrolyte with a reticulated vitreous carbon working electrode was performed. The electrolysis was held at -2.6 V (vs Fc/Fc^+) for 4.6 hours, after which time 5.85 C of charge

had been passed. Product analysis revealed the formation of NH_3 (18% faradaic efficiency) as well as H_2 (58% faradaic efficiency). The amount of NH_3 generated in this experiment corresponds to 0.5 equiv with respect to Fe and 14% yield with respect to acid. When the experiment was performed at higher acid loading (50 equiv), the NH_3 yield increased substantially (2.2 equiv per Fe; 25% faradaic efficiency; electrolysis held at -2.3 V in this instance with 8.39 C charge passed over 16.5 hrs). While these yields of NH_3 with respect to Fe do not demonstrate formal turnover, they do suggest that electrocatalytic N_2-to-NH_3 conversion by this iron system may be feasible. That the NH_3 yield increases with increased acid correlates well with our results in the chemical system. Studies to more thoroughly explore the electrocatalytic N_2-to-NH_3 conversion behavior of P_3^BFe-species are underway.

The electrochemical data presented in Figure 3.2 also suggest that chemical reductants with weaker reduction potentials than KC_8 may be competent for N_2-to-NH_3 conversion catalysis by **1**. Consistent with this notion we find that catalytic yields of NH_3 (5 equiv per Fe) are obtainable using **1** in the presence of 150 equiv $HBAr^F_4$ and 1900 equiv 10 wt% Na/Hg amalgam under ~1 atm N_2 at -78 °C in Et_2O (Table 3.1, Entry 16; a larger excess of 10 wt% Na/Hg amalgam was employed to compensate for the lower surface area of the reagent). This result demonstrates that the catalysis is not unique to the presence of either potassium or graphite. KC_8 is a stronger reductant than is needed for N_2-to-NH_3 conversion, but shows more favorable selectivity for N_2 reduction relative to H_2 generation than other reductants we have thus far canvassed.

3.2.2 Kinetics of ammonia and hydrogen formation. To better understand the competing NH_3- and H_2-forming reactions that occur during catalysis, we measured the time profiles of product formation using the most active catalyst, P_3^BFe-N_2^- **1**. Our method

for quenching catalytic NH_3 production uses rapid freeze-quenching of reactions to -196 °C, followed by addition of *tert*-butyllithium (^{t}BuLi), and subsequent annealing to -78 °C. Employing this method allows for the measurement of NH_3 production as a function of time. The time courses of NH_3 formation obtained for the previously reported substrate loading (blue trace)[12a] as well as a higher substrate loading (red trace) are shown in Figure 3.3.

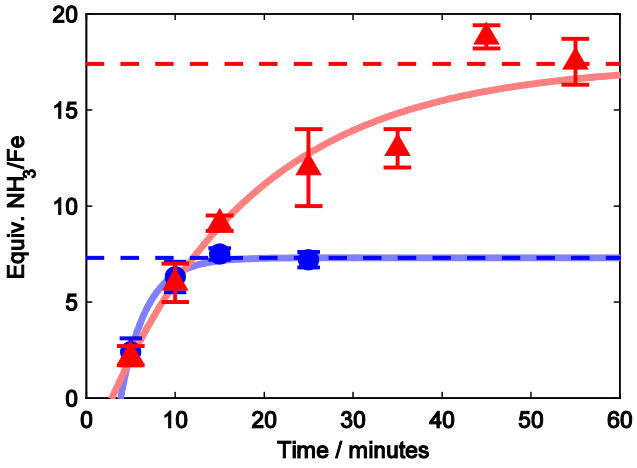

Figure 3.3: Time profiles of the formation of NH_3 from N_2 using **1** as a catalyst at -78 °C under previously reported reaction conditions (blue circles, 0.64 mM **1**, 48 equiv $HBAr^F_4$, 58 equiv KC_8) and higher-turnover conditions (red triangles, 0.43 mM **1**, 150 equiv $HBAr^F_4$, 185 equiv KC_8). Dashed lines show expected final yields from the corresponding entries in Table 3.1 (Entries 1 and 3). Each point represents an average of two experiments; data for the individual experimental iterations are presented in the Supporting Information. Solid lines are provided as guides for the eye only.

Under both substrate loadings shown in Figure 3.3, the reaction proceeds to completion at -78 °C. Furthermore, under the higher-turnover conditions (with 150 equiv $HBAr^F_4$ and 185 equiv KC_8, Figure 3.3, red triangles) the reaction proceeds to completion over ~45 min, a time-scale that enables us to measure the dependence of $d[NH_3]/dt$ on the concentrations of the soluble reagents—**1** and $HBAr^F_4$—via the method of initial rates. As shown in Figure 3.4 (left), an initial rates analysis demonstrates that the reaction is first order in [Fe], which is consistent with the involvement of a monomeric $P_3{}^BFe$ species in the turnover-limiting step for NH_3 formation. Comparing conditions ranging from 15 mM to 250 mM [$HBAr^F_4$] revealed no significant correlation between initial [$HBAr^F_4$] and initial NH_3 production rate; for instance, there is no measurable difference in the amount of NH_3 produced after five minutes. This observation suggests zero-order rate dependence on acid concentration, which is borne out by the initial rates analysis (Figure 3.4, right).

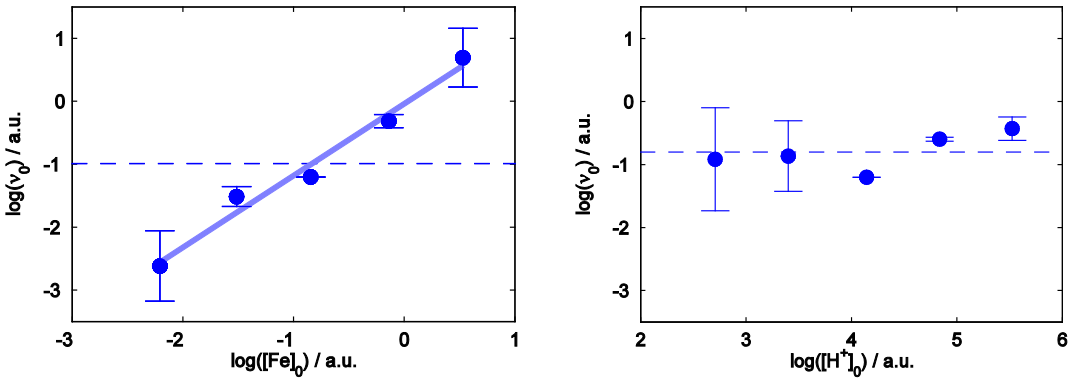

Figure 3.4: Log-log plots of the initial rate of NH_3 formation (υ_0) versus initial concentrations of soluble reagents. (Left) υ_0 versus $[Fe]_0$ for a range of [**1**] from 0.11–1.7 mM. The dashed line shows a constant function fit to the mean of the data, while the solid trend line shows the result of least squares linear regression ($\log(\upsilon_0) = (-0.04 \pm 0.1) + (1.1 \pm 0.1) \cdot \log([\mathbf{1}]_0)$, r^2 = 0.98). (Right) υ_0 versus $[HBAr^F{}_4]_0$ for a range of $[HBAr^F{}_4]$ from 15–250 mM. The dashed line shows a constant function fit to the mean of the data (RMSE = 0.3), which is not statistically different from the result of a least squares linear regression (RMSE = 0.3). Data for individual experimental iterations and discussion of initial rates estimates are presented in the Supporting Information.

These data provide an estimate of initial turnover frequency (TOF, determined as moles of NH_3 produced per minute per Fe atom) of this catalyst system of 1.2 ± 0.1 min^{-1}. While the TOF of this catalyst is not directly comparable to other N_2-to-NH_3 conversion catalysts due to differences in conditions and substrate, it is notable that **1** under the conditions used here furnishes a substantially higher TOF than the other synthetic systems in Chart 1 for which data is available (Table 3.2), despite operating over 100 °C lower in temperature (albeit with the benefit of a stronger reductant). MoFe nitrogenase purified from *Klebsiella pneumoniae* exhibits a TOF of approximately 80 min^{-1},[22] nearly two orders

of magnitude larger than the present synthetic Fe system, while operating at room temperature.

Table 3.2. Comparison of NH_3 Generating Reactions[a]

Catalyst	Temperature (°C)	Maximum yield[d]	TOF (min^{-1})	Efficiency (%)
Mo1-H[a]	25	12	0.14	31
Mo2[b]	25	63	0.26	35
1[c]	-78	64	1.2	12

Data for **Mo1-H** and **Mo2** are from reference 11 and depictions of the compounds are presented in Chart 1. [a]Conditions: 2,6-lutidinium trifluoromethanesulfonate and cobaltocene in toluene. [b]Conditions: 2,4,6-trimethylpyridinium trifluoromethanesulfonate and decamethylcobaltocene in toluene. [c]Conditions: $HBAr^F_4$ and KC_8 in diethyl ether. [d] Expressed in NH_3 equivalents.

To determine potential HER activity of $P_3^BFe\text{-}N_2^-$ **1**, we measured the time course of $H_{2(g)}$ formation from $HBAr^F_4$ and KC_8 in the absence and presence of **1**, under catalytically relevant conditions. As shown in Figure 3.5, the initial rate of $H_{2(g)}$ evolution at -78 °C is enhanced by the presence of **1**. The Fe-catalyzed HER is > 85% complete within the first hour with a final yield of ~40% (blue trace).[23] Quantifying the NH_3 produced in this reaction (34% yield based on $HBAr^F_4$) accounts for 74% of the acid added. We also confirm that there is significant background HER from $HBAr^F_4$ and KC_8 (black trace), as expected. We conclude that both catalyzed and background HER are competing with NH_3 formation in the catalyst system.

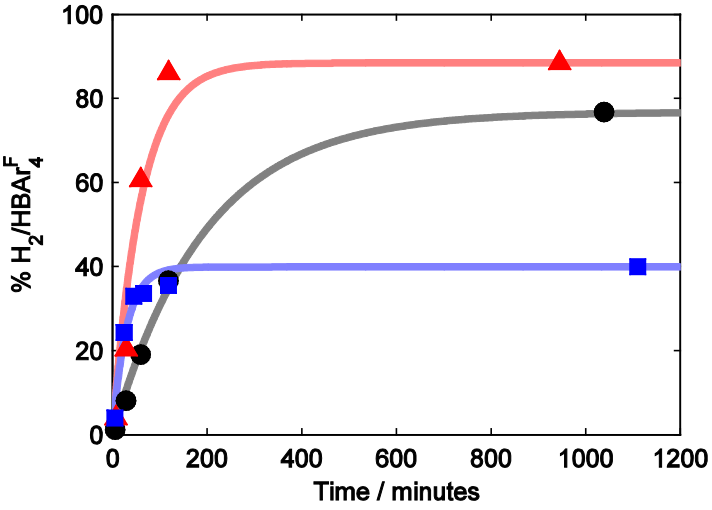

Figure 3.5: Time profiles of the formation of H_2 from $HBAr^F_4$ and KC_8 in Et_2O at -78 °C. Data is presented for the reaction of these reagents alone (black circles) as well as in the presence of **1** (blue squares) and **3** (red triangles). Each time course was collected continuously from a single experiment. Solid lines are provided as guides for the eye only.

As a point of comparison, we also measured the rate of H_2 evolution in the presence of $P_3^{Si}Fe\text{-}N_2^-$ (**3**). As shown in Figure 3.5, **3** also catalyzes HER, with an initial rate that is comparable to **1**. However, in this case, H_2 evolution approaches completion over two hours, resulting in a final measured yield of 88%. This is consistent with the low N_2-fixing activity of **3**; in the absence of a competitive NH_3-producing reaction, **3** catalyzes the reduction of protons to H_2. Understanding the fundamental differences that give rise to the divergent selectivity of these Fe catalysts is an important goal in the context of designing selective N_2 reduction catalysts.

3.2.3 Spectroscopic characterization of Fe speciation under turnover. Considering the relatively slow rate of NH_3 formation ascertained from low-temperature

quenching experiments, we sought to determine the Fe speciation under turnover using the $P_3^BFe\text{-}N_2^-$ catalyst **1**. By rapidly freeze-quenching reaction mixtures using ^{57}Fe-enriched **1** as a catalyst, time-resolved Mössbauer spectra can be obtained reflective of catalysis.[24]

Table 3.3. Mössbauer parameters for P_3^BFe complexes[a]

Compound	*S*	Conditions	δ (mm s^{-1})	ΔE_Q (mm s^{-1})
$P_3^BFe^+$ [b]	3/2	Frozen solution, 50 mT	0.75	2.55
$P_3^BFe\text{-}N_2H_4^+$	3/2	Frozen solution, 50 mT	0.7	2.30
$P_3^BFe\text{-}NH_3^+$	3/2	Frozen solution, zero field	0.68	1.94
$P_3^BFe\text{-}NH_2$	3/2	Frozen solution, zero field	0.60	1.47
$P_3^BFe\text{-}N_2$ [b]	1	Frozen solution, 50 mT	0.56	3.34
$P_3^BFe\text{-}N_2^-$ [b]	1/2	Frozen solution, 50 mT	0.40	0.99
$P_3^BFe\text{-}NNH_2^+$ [b]	1/2	Frozen solution, 50 mT	0.35	1.02
$P_3^BFe\text{-}NAd^+$	1/2	Powder, 50 mT	0.15	1.31
$(P_3^B)(\mu\text{-}H)Fe(H)(N_2)$	0	Frozen solution, zero field	0.21	1.44
$(P_3^B)(\mu\text{-}H)Fe(H)(H_2)$	0	Frozen solution, zero field	0.19	1.55
$P_3^BFe\text{-}NAd$	0	Powder, zero field	0.04	1.40

[a]All data were collected at 80 K under the conditions noted; external magnetic fields applied in parallel mode. [b]Data taken from reference 18.

The Mössbauer parameters of some independently synthesized P_3^BFe species that may be relevant to the present catalysis have been measured and are collected in Table 3.3. Mössbauer isomer shifts (δ) can often be used to assign the relative oxidation state of structurally related compounds,[16b,25] yet in this series of P_3^BFe compounds there is a poor correlation between δ and formal oxidation state assignments (e.g. $Fe\text{-}N_2^-$ and $Fe{=}NNH_2^+$ species have nearly identical isomer shifts). This fact reflects the high degree of covalency present in these $P_3^BFe\text{-}N_xH_y$ complexes, skewing classical interpretations of the Mössbauer data; the degree of true oxidation/reduction at the iron centers in $P_3^BFe\text{-}N_xH_y$ species is buffered by strong covalency with the surrounding ligand field.[26,27] We do, however, find a useful linear correlation ($r^2 = 0.90$) between the measured ground spin states (S) of $P_3^BFe\text{-}N_xH_y$ compounds and δ (Figure 3.6),[28] providing an empirical relationship that guides analysis of Mössbauer spectra obtained from catalytic reactions. Ground spin states can be reliably correlated with the type of N_xH_y ligand, and possibly the presence of hydride ligands, coordinated to a P_3^BFe center. This knowledge, combined with freeze-quench Mössbauer data, enables us to predict with some confidence the type(s) of Fe species that are present in a spectrum obtained after freeze-quenching during turnover.

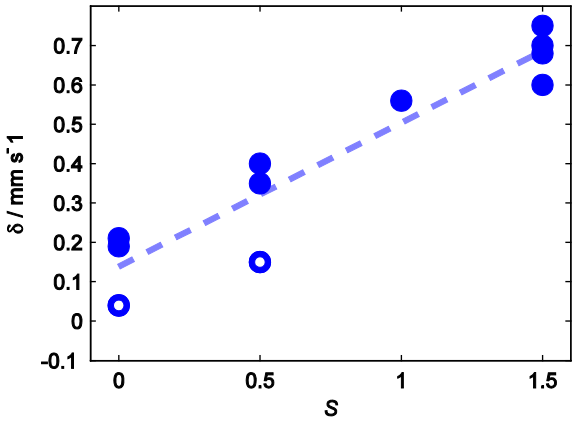

S	$\delta_{predicted}$ (mm s^{-1})
0	0.1 ± 0.1
1/2	0.3 ± 0.1
1	0.5 ± 0.2
3/2	0.7 ± 0.2

Figure 3.6: A plot of δ versus ground spin-state *S* for the compounds listed in Table 3.3 (blue circles), along with a linear least-squares fit to the data (dotted line, r^2 = 0.90). The isomer shifts of the P_3^BFe-NAd$^{0/1+}$ are highlighted by open circles.[28] The table to the right lists the expectation values for δ based on *S* computed from the linear fit (ranges reported as 95% confidence interval).

Figure 3.7 shows time-resolved Mössbauer spectra of freeze-quenched catalytic reaction mixtures of P_3^BFe-N_2^- anion **1** with 48 equiv of $HBAr^F_4$ and 58 equiv of KC_8. Figure 3.7A shows the spectrum of catalyst **1** as a 0.64 mM solution in THF, which features a sharp, asymmetric quadrupole doublet at 80 K in the presence of a 50 mT external magnetic field. Figure 3.7B shows the spectrum of a catalytic reaction mixture freeze-quenched after 5 minutes of stirring, revealing the major Fe species (blue, representing ca. 60% of all Fe) present during active turnover to have parameters δ = 0.16 ± 0.2 mm s^{-1} and ΔE_Q = 1.63 ± 0.03 mm s^{-1}, which, within the error of the simulation, is consistent with the diamagnetic borohydrido-hydrido species (P_3^B)(μ-H)Fe(H)(L) (**4-L**), where L = N_2 or H_2.[29] This observation correlates well with the previously reported result that **4-N_2** is produced from the reaction of **1** with smaller excesses of $HBAr^F_4$ and KC_8.[12a] Further corroborating this assignment, data collected at liquid He temperature with a small applied magnetic field

suggest that this species is a non-Kramer's spin system,[30] and should be $S = 0$ given the observed correlation between δ and S (*vide supra*). Also present in Figure 3.7B is a minor component (~8%, shown in white) with parameters $\delta = 0.02 \pm 0.2$ mm s^{-1} and $\Delta E_Q = 0.97 \pm 0.2$ mm s^{-1}, and a broad residual absorbance centered at $\delta \approx 0.9$ mm s^{-1} encompassing a width of ~2 mm s^{-1} (representing ca. 20-30% of all Fe in the sample, shown in grey). Due to the broadness of the latter resonance ($\Gamma \approx 1$ mm s^{-1}), this feature could not be accurately modeled. Nevertheless, the signal is consistent with several known $S = 3/2$ P_3^BFe species. For example, the vacant cation, $P_3^BFe^+$, and the cationic species $P_3^BFe\text{-}N_2H_4^+$ and $P_3^BFe\text{-}NH_3^+$, are $S = 3/2$ species and give rise to quadrupole doublets that lie within the envelope of this broad signal (Table 3.3, Entries 1–3).[31] The utility of freeze-quench ^{57}Fe Mössbauer spectroscopy is evident; in a single spectral snapshot the presence of P_3^BFe-components with varied spin states including $S = 0$, 1/2, 1, and 3/2 are observed.

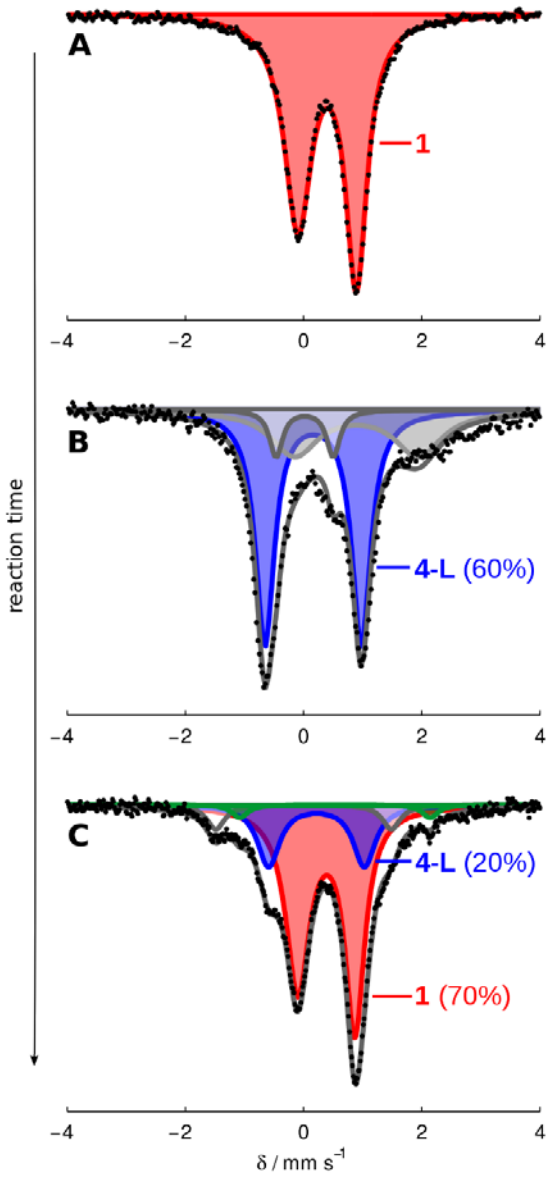

Figure 3.7: Frozen solution Mössbauer spectra collected at 80 K in the presence of a 50 mT parallel magnetic field. (A) Spectrum of **1** (0.64 mM in THF); (B) a catalytic mixture (Et_2O, 0.64 mM **1**, 48 equiv $HBAr^F_4$, 58 equiv KC_8) freeze-quenched after 5 minutes of stirring at -78 °C; (C) a catalytic mixture (Et_2O, 0.64 mM **1**, 48 equiv $HBAr^F_4$, 58 equiv KC_8) freeze-quenched after 25 minutes of stirring at -78 °C. Data are presented as black points and simulations as solid grey lines with components plotted as solid areas underneath the curve. For parameters of individual components see the SI.

Figure 3.7C shows that the primary Fe species present after 25 minutes of reaction time is the starting catalyst **1** (shown in red, representing ca. 70% of all Fe in the sample). Also present is ca. 20% of the species we assign as **4-L** ($\delta = 0.22 \pm 0.2$ mm s^{-1} and $\Delta E_Q = 1.62 \pm 0.03$ mm s^{-1}, shown in blue), < 5% of the neutral dinitrogen complex, $P_3^BFe\text{-}N_2$ (green), and ~7% of an as-yet unknown species with parameters $\delta = 0.00 \pm 0.02$ mm s^{-1} and $\Delta E_Q = 2.97 \pm 0.06$ mm s^{-1} (white). Thus, as acid substrate is consumed in the reaction to produce NH_3 and H_2, the mixture of Fe species shown in Figure 3.7B at an early time point evolves back to the starting material **1**. A slight residual excess of KC_8 is needed to ensure recovery of the active catalyst. These data help rationalize the results of the substrate reloading experiments (*vide supra*).

The increasingly low Fe concentrations used to achieve the highest yields of NH_3 reported here make the collection of well-resolved Mössbauer spectra under such conditions challenging. Nonetheless, we repeated freeze-quench experiments for one set of higher-turnover conditions (Figure 3.8). Although in this case the Fe speciation at intermediate times appears more complex, these data exhibit the same gross behavior shown in Figure 3.7; under active turnover the major Fe species present is consistent with hydride **4-L** (≥ 50%, average parameters $\delta = 0.20 \pm 0.2$ mm s^{-1} and $\Delta E_Q = 1.49 \pm 0.09$ mm s^{-1}, Figure 3.8A,B[32]), and as the extent of reaction increases significant amounts of $P_3^BFe\text{-}N_2^-$ **1** reform (Figure 3.8C[33]).

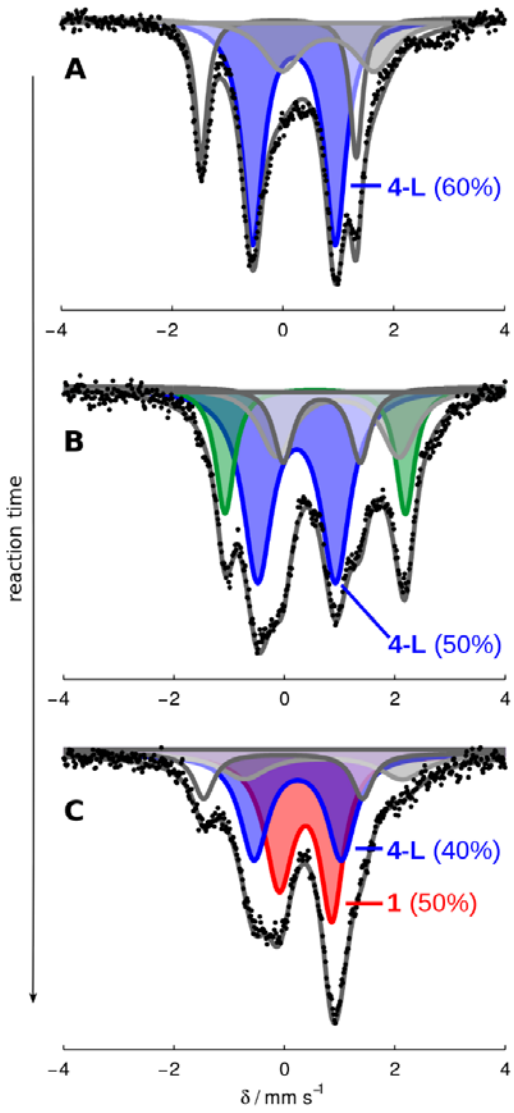

Figure 3.8: Frozen solution Mössbauer spectra collected at 80 K in the presence of a 50 mT parallel magnetic field. (A) A catalytic mixture (Et_2O, 0.43 mM **1**, 150 equiv $HBAr^F_4$, 185 equiv KC_8) freeze-quenched after 5 minutes of stirring at -78 °C; (B) a catalytic mixture (Et_2O, 0.43 mM **1**, 150 equiv $HBAr^F_4$, 185 equiv KC_8) freeze-quenched after 10 minutes of stirring at -78 °C; (C) a catalytic mixture (Et_2O, 0.43 mM **1**, 150 equiv $HBAr^F_4$, 185 equiv KC_8) freeze-quenched after 25 minutes of stirring at -78 °C. Data presented as black points, simulations as solid grey lines with components plotted as solid areas underneath the curve. For parameters of individual components, see SI.

3.2.4 Precatalyst activity of (P_3^B)(μ-H)Fe(H)(N_2) (4-N_2) and identification of a catalyst resting state. The observations presented in section 2.3 suggest that hydride **4-L** builds up as the major Fe-containing species during active turnover and appears to be converted back to the active catalyst **1** when catalysis is complete. We previously observed that this species can form under conditions that model the catalytic conditions (10 equiv acid / 12 equiv reductant) and our initial thinking that **4-N_2** may be a catalyst deactivation product was guided by the poor activity of isolated **4-N_2** as a precatalyst under the standard conditions (generating only 0.5 ± 0.1 equiv NH_3 per Fe at 50 equiv acid / 60 equiv reductant).[12a] However, in that initial report we also noted that isolated **4-N_2** is not solubilized under the catalytic conditions. Therefore, in light of the current in situ spectroscopy, and the observation that **4-N_2** liberated some NH_3 under the original conditions, we wondered whether its insolubility may be what is responsible for its comparative low activity as an isolated precursor. If **4-N_2** is brought into solution, or formed in solution during turnover, it may exhibit activity. To test this hypothesis we explored the activity of **4-N_2** under modified catalytic conditions where a toluene/Et_2O mixture (which improves the solubility of **4-N_2**) was employed as the solvent. In this case we find that **4-N_2** serves as a viable precatalyst (Table 3.1, Entries 13, 14). We suppose then that under the standard conditions (in pure Et_2O), if **4-L** is generated in solution during catalysis, it should be able to react productively so long as it does not irreversibly precipitate, which may be slow at -78 °C. Accordingly, we have observed that the Mössbauer spectrum of a sample taken from a standard catalytic mixture as described in section 2.3 can be filtered at low temperature and still displays substantial **4-L**.

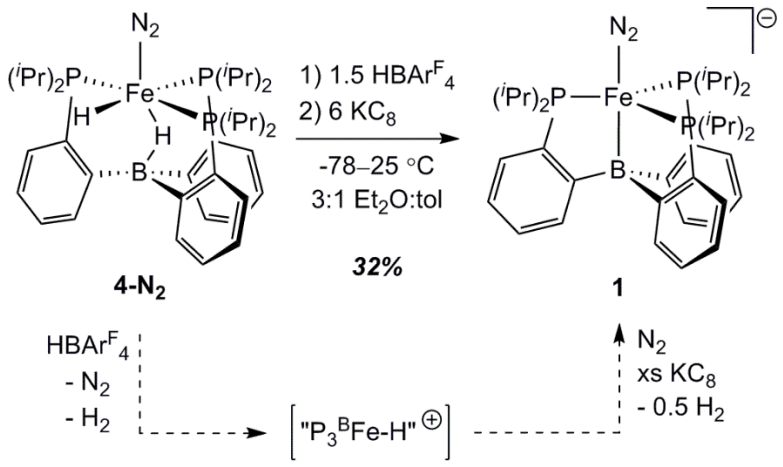

Scheme 3.1: Stoichiometric conversion of **4-N_2** into **1** under catalytically relevant conditions. A proposed reaction pathway is shown along the dashed arrows. "$P_3^BFe\text{-}H^+$" is a plausible intermediate of this conversion but has not been thoroughly characterized.

These results suggest the feasibility of the stoichiometric transformation of hydride **4-L** into N_2 anion **1** under catalytically relevant conditions. In a previous report, we showed that **4-N_2** is stable for short periods to either $HBAr^F_4$ or KC_8 in Et_2O at room temperature, again noting its insolubility under these conditions.[12a] Given the results above, we have reinvestigated this reactivity in Et_2O/toluene mixtures. Thus the reaction of **4-N_2** with 1 equiv of $HBAr^F_4$ in 6:1 *d*$_8$-toluene:Et_2O results in consumption of the starting material along with the appearance of several new, paramagnetically-shifted ^{1}H NMR resonances. We hypothesize that protonolysis of either the terminal or bridging hydride moieties in **4-N_2** produces a cationic "$P_3^BFe\text{-}H^+$" species, which may then be reduced to liberate 0.5 equiv of H_2 and re-enter the catalytic manifold of $\{P_3^BFe\text{-}N_2\}^n$ species under an N_2 atmosphere. Indeed, the sequential addition of 1.5 equiv of $HBAr^F_4$ followed by 6 equiv of KC_8 to **4-N_2** at -78 °C in 3:1 Et_2O:toluene produces substantial amounts of **1** (32% yield, unoptimized;

Scheme 3.1). This stoichiometric reactivity provides support for the idea that as **4-L** is formed under the standard reaction conditions it can react with acid and reductant to produce the starting catalyst **1**, consistent with the observations provided in section 2.3.

Given that (i) **4-L** appears to be the predominant Fe-containing species observed by freeze-quench Mössbauer spectroscopy under turnover conditions at early time points, (ii) that this species serves as a competent precatalyst when solubilized, and (iii) **4-N_2** can be synthetically converted to **1** by $HBAr^F_4$ and KC_8, we conclude that **4-L** is a major resting state of the catalysis. This conclusion does not require **4-L** to be an "on path" intermediate; we instead think **4-L** is more likely a resting state that ties up the catalyst, but one that reversibly leaks into the on-path catalytic cycle in which **1** is ultimately protonated.

The observation of a hydride resting state for this synthetic Fe catalyst may have additional relevance in the context of biological nitrogen fixation, where the intermediacy of metal hydride species has been proposed on the basis of spectroscopic data obtained during turnover.[5] It has further been proposed that the reductive elimination of hydrides as H_2 may be a requisite component of N_2 binding to the nitrogenase active-site cofactor,[22,34,35] giving rise to obligate H_2 evolution in the limiting stoichiometry of N_2 conversion to NH_3.[36] The results described here directly implicate the relevance of a synthetic iron hydride species to a system capable of catalytic N_2-to-NH_3 conversion. This in turn motivates complimentary model reactivity studies on iron hydride species such as **4-L**, targets whose relevance might otherwise be overlooked.

3.2.5 Summary of mechanistically relevant observations.

To help collect the information presented here and in related studies of the P_3^BFe-system, Scheme 3.2 provides a mechanistic outline for the key iron species and plausible transformations we think are most relevant to the catalytic N_2-to-NH_3 conversion cycle catalyzed by $P_3^BFeN_2^-$ **1**. The complexes shown in blue, along with their respective spin states *S*, have been thoroughly characterized. Also, the net conversions between complexes that are indicated by solid blue arrows have been experimentally demonstrated. Those complexes depicted in black have not (as yet) been experimentally detected.

Several results are worth underscoring. (i) We have characterized the S = 3/2, substrate-free state $P_3^BFe^+$, and shown that it binds N_2 upon electron loading, generating S = 1 $P_3^BFe\text{-}N_2$ or S = ½ $P_3^BFe\text{-}N_2^-$ depending on reducing equivalents provided.[12a,17] $P_3^BFe^+$ is competent for catalytic N_2-to-NH_3 conversion,[12a] and facilitates this conversion electrolytically as established herein. (ii) The most reduced state, $P_3^BFe\text{-}N_2^-$ **1**, can be doubly protonated at low temperature to generate $P_3^BFe{=}N\text{-}NH_2^+$, a distal pathway intermediate.[18] This S = 1/2 species features a short Fe-N multiple bond (~1.65 Å). Its diamagnetic relative, $P_3^{sSi}Fe{=}N\text{-}NH_2^+$, has very recently been structurally characterized.[37] (iii) The $P_3^BFe{=}N\text{-}NH_2^+$ intermediate anneals (in the absence of reductant) to generate significant amounts of $P_3^BFe\text{-}NH_3^+$;[12a,18] (iv) $P_3^BFe\text{-}NH_3^+$ can also be generated by protonation of $P_3^BFe\text{-}NH_2$, and reductive displacement of NH_3 from $P_3^BFe\text{-}NH_3^+$ under N_2 regenerates $P_3^BFe\text{-}N_2^-$.[12a]

Also worth emphasizing is that diamagnetic $P_3^{Si}Fe{=}N\text{-}NH_2^+$ can be reduced at low temperature to S = 1/2 $P_3^{Si}Fe{=}N\text{-}NH_2$, and this species in the presence of additional acid and reductant evolves to a mixture of $P_3^{Si}Fe\text{-}N_2H_4^+$ and $P_3^{Si}Fe\text{-}NH_3^+$.[37] $P_3^{Si}Fe\text{-}N_2H_4^+$, and

also $P_3^BFe\text{-}N_2H_4^+$, readily disproportionate the bound N_2H_4 to generate the corresponding NH_3 adducts $P_3^{Si}Fe\text{-}NH_3^+$ and $P_3^BFe\text{-}NH_3^+$,[12a,16b] each of which evolves NH_3 upon reduction to regenerate (under N_2) $P_3^BFe\text{-}N_2^-$ **1** and $P_3^{Si}Fe\text{-}N_2^-$, respectively. The reaction pathway observed for $P_3^{Si}Fe{=}N\text{-}NH_2^+$, more readily studied than for $P_3^BFe{=}N\text{-}NH_2^+$ because $P_3^{Si}Fe{=}N\text{-}NH_2^+$ can be isolated in pure form, highlights the possibility of a hybrid crossover mechanistic pathway wherein a distal intermediate ($Fe{=}N\text{-}NH_2$) traverses to an alternating intermediate ($Fe\text{-}N_2H_4$) that may then be converted to NH_3, possibly via disproportionation.[18,37]By demonstrating first-order rate dependence on the concentration of $P_3^BFe\text{-}N_2^-$, [**1**], the present study remains consistent with our hypothesis that a single-site mechanism is likely operative during N_2-to-NH_3 conversion catalysis. The direct observation of both **1** and its neutral form $P_3^BFe\text{-}N_2$ in catalytic mixtures by freeze-quench Mössbauer spectroscopy lends further credence to this idea.

A plausible pathway for the formation of the putative resting state species **4-L** would be hydrogenation of $P_3^BFe\text{-}N_2$ by evolved H_2 side-product during catalysis. This process has been demonstrated independently at room temperature in benzene.[29] Follow-up control experiments in d_8-toluene, however, suggest that this reaction is not kinetically competent at -78 °C. One alternative pathway for the formation of **4-L** during catalysisis via bimolecular H-atom transfer from the unobserved intermediate $P_3^BFe\text{-}N_2H$ (e.g., 2 $P_3^BFe\text{-}N_2H \rightarrow$ **4-L** + $P_3^BFe\text{-}N_2$), a process that could compete with productive protonation to generate $P_3^BFe{=}N\text{-}NH_2^+$. Efforts are ongoing to find conditions under which $P_3^BFe\text{-}N_2H$ can be generated, characterized, and studied.

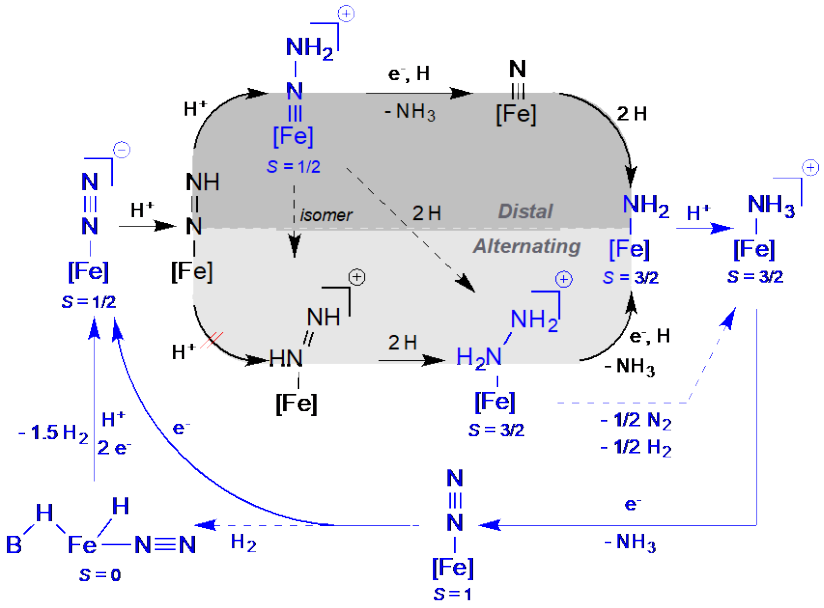

Scheme 3.2: Possible catalytic scenarios for N_2-to-NH_3 conversion by **1**. [Fe] = P_3^BFe. Thoroughly characterized species and their respective ground spin states *S* are shown in blue, while as yet undetected species are shown in black. Blue arrows indicate known pathways that are likely kinetically competent (solid) at -78 °C. Dashed arrows are likely incompetent at -78 °C.

3.3 Conclusion

In the present study we have shown that N_2-fixing catalyst systems with P_3^EFe (E = B, C, Si) species give rise to high yields of NH_3 if supplied with sufficient acid and reductant. These yields (for E = B and C) compare very favorably to the most active known Mo catalysts and are almost an order of magnitude greater than the yields presented in our previous reports. While we do not rule out some degree of catalyst degradation at -78 °C, these iron catalysts are unexpectedly robust and it is possible that the lower efficiency of catalysis at higher turnover is in part due to build-up of NH_3 product, which is an inhibitor.

We have also provided new mechanistic insights for reactions with catalyst $P_3^BFe\text{-}N_2^-$ **1**, such as the observation that catalysis proceeds at -78 °C, the demonstration of first-order rate dependence on catalyst concentration, the demonstration of zeroth-order rate dependence on $HBAr^F_4$ concentration, and the observation that **1** catalyzes HER as well as NH_3 formation. Preliminary electrochemistry data suggests that catalysis by the P_3^BFe system can be driven at the formal $P_3^BFe\text{-}N_2$/ $P_3^BFe\text{-}N_2^-$ couple around -2.2 V vs Fc/Fc^+, consistent with Na/Hg also serving as a viable reductant for catalytic turnover. Cyclic voltammetry and controlled potential electrolysis of $P_3^BFe^+$ at -45 °C demonstrate that electrolytic N_2 reduction is possible.

The present study has also demonstrated the utility of coupling in situ freeze-quench ^{57}Fe Mössbauer spectroscopy with kinetic analysis of product formation as a powerful tool for the mechanistic study of Fe-catalyzed N_2 fixation. To date, no synthetic molecular N_2-to-NH_3 conversion catalyst system had been studied spectroscopically under active turnover conditions. Our freeze-quench Mössbauer results suggest that **4-L** is a resting state of the overall catalysis; this hydride species, which we previously posited to be primarily a catalyst sink, can instead reenter the catalytic pathway via its conversion to catalytically active $P_3^BFe\text{-}N_2^-$ **1**. This observation underscores the importance of understanding metal hydride reactivity in the context of Fe-mediated nitrogen fixation. It may be that HER activity provides a viable strategy for recovering catalytically active states from the unavoidable generation of iron hydride intermediates.

3.4 REFERENCES

[1] Smil, V. *Enriching the Earth*. Cambridge: MIT Press, 2001.

[2] (a) Ertl, G. *J. Vac. Sci. Technol. A* **1983**, *1*, 1247. (b) Ertl, G. *Angew. Chem. Int. Ed.* **2008**, *47*, 3524.

[3] Burgess, B. K.; Lowe, D. J. *Chem. Rev.* **1996**, *96*, 2983.

[4] (a) Howard, J. B.; Rees, D. C. *Chem. Rev*. **1996**, *96*, 2965. (b) Einsle, O.; Tezcan, F. A.; Andrade, S. L. A.; Schmid, B.; Yoshida, M.; Howard, J. B.; Rees, D. C. *Science* **2002**, *297*, 1696. (c) Spatzal, T.; Aksoyoglu, M.; Zhang, L.; Andrade, S. L. A.; Schleicher, E.; Weber, S.; Rees, D. C.; Einsle, O. *Science* **2011**, *334*, 940. (d) Kowalska, J.; DeBeer, S. *Biochim. Biophys. Acta-Molecular Cell Research* **2015**, *1853*, 1406.

[5] Hoffman, B. M.; Lukoyanov, D.; Yang, Z.-Y.; Dean, D. R.; Seefeldt, L. C. *Chem. Rev.* **2014**, *114*, 4041.

[6] (a) Chatt, J.; Leigh, G. J. *Chem. Soc. Rev.* **1972**, *1*, 121. (b) Khoenkhoen, N.; de Bruin, B.; Reek, J. N. H.; Dzik, W. I. *Eur. J. Inorg. Chem.* **2015**, *4*, 567.

[7] Bazhenova, T. A.; Shilov, A. E. *Coord. Chem. Rev*. **1995**, *144*, 69.

[8] (a) Shiina, K. *J. Am. Chem. Soc.* **1972**, *94*, 9266. (b) Komori, K.; Oshita, H.; Mizobe, Y.; Hidai, M. *J. Am. Chem. Soc.* **1989**, *111*, 1939. (c) Tanaka, H.; Sasada, A.; Kouno, T.; Yuki, M.; Miyake, Y.; Nakanishi, H.; Nishibayashi, Y; Yoshizawa, K. *J. Am. Chem. Soc.* **2011**, *133*, 3498. (d) Yuki, M.; Tanaka, H.; Sasaki, K.; Miyake, Y.;Yoshizawa, K.; Nishibayashi, Y. *Nat. Commun.* **2012**, *3*, 1254. (e) Ogawa, T.; Kajita, Y.; Wasada-Tsutsui, Y; Wasada, H; Masuda, H. *Inorg. Chem.* **2013**, *52*, 182. (f) Liao, Q.; Saffon-Merceron, N.; Mézailles, N. *Angew. Chem. Int. Ed.* **2014**, *53*, 14206. (g) Ung, G.; Peters, J. C. *Angew. Chem. Int. Ed.* **2015**, *54*, 532. (h) Siedschlag, R. B.; Bernales, V.; Vogiatzis, K. D.; Planas, N.; Clouston, L. J.; Bill, E.; Gagliardi, L.; Lu, C. C. *J. Am. Chem. Soc.* **2015**, 137, 4638.

[9] (a) Yandulov, D. V.; Schrock, R. R. *Science* **2003**, *301*, 76. (b) Ritleng, V.; Yandulov, D. M.; Weare, W. W.; Schrock, R. R.; Hock, A. S.; Davis, W. M. *J. Am. Chem. Soc.* **2004**, *126*, 6150.

[10] (a) Arashiba, K.; Miyake, Y.; Nishibayashi, Y. *Nat. Chem.* **2011**, *3*, 120. (b) Tanka, H.; Arashiba, K.; Kuriyama, S.; Sasada, A.; Nakajima, K.; Yoshizawa, K.; Nishibayashi, K. *Nat. Commun.* **2014**, *5*, 3737. (c) Kuriyama, S.; Arashiba, K.; Nakajima, K.; Tanaka, H.; Kamaru, N.; Yoshizawa, K.; Nishibayashi, Y. *J. Am. Chem. Soc.* **2014**, *136*, 9719.

[11] Arashiba, K.; Kinoshita, E.; Kuriyama, S.; Eizawa, A.; Nakajima, K.; Tanaka, H.; Yoshizawa, K.; Nishibayashi, Y. *J. Am. Chem. Soc.* **2015**, *137*, 5666.

[12] (a) Anderson, J. S.; Rittle, J.; Peters, J. C. *Nature* **2013**, *501*, 84. (b) Creutz, S.; Peters, J. C. *J. Am. Chem. Soc.* **2014**, *136*, 1105. (c) Del Castillo, T. J.; Thompson, N. B.; Suess, D. L. M.; Ung, G.; Peters, J. C. *Inorg. Chem.* **2015**, *54*, 9256.

[13] Schrock, R. R. *Angew. Chem. Int. Ed.* **2008**, *47*, 5512.

[14] For theoretical work regarding the (PNP)Mo system developed by Nishibayashi, see references 10b,c and also Tian, Y.-H.; Pierpont, A. W.; Batista, E. R. *Inorg. Chem.* **2014**, *53*, 4177.

[15] See for example: (a) McWilliams, S. F.; Holland, P. L. *Acc. Chem. Res.* **2015**, *48*, 2059-2065. (b) Field, L. D.; Li, H. L.; Dalgarno, S. J.; Turner, P. *Chem. Commun.* **2008**, 1680-1682. (c) Crossland, J. L.; Tyler, D. R. *Coord. Chem. Rev.* **2010**, *254*, 1883-1894. (d) Peters, J. C.; Mehn, M. P. Bio-Organometallic Approaches to Nitrogen Fixation. In *Activation of Small Molecules*; Tolman, W. B., Ed.; Wiley-VCH: Weinheim, Germany; 2006, p 81. (e) Hendrich, M. P.; Gunderson, W.; Behan, R. K.; Green, M. T.; Mehn, M. P.; Betley, T. A.; Lu, C. C.; Peters, J. C. *Proc. Natl. Acad. Sci. U. S. A.* **2006**, *103*, 17107-17112. (f) Grubel, K.; Brennessel, W. W.; Mercado, B. Q.; Holland, P. L. *J. Am. Chem. Soc.* **2014**, *136*, 16807.

[16] (a) Mankad, N. P.; Whited, M. T.; Peters, J. C. *Angew. Chem. Int. Ed.* **2007**, *46*, 5768. (b) Lee, Y.; Mankad, N. P.; Peters, J. C. *Nature Chem.* **2010**, *2*, 558.

[17] (a) Moret, M.-E.; Peters, J. C. *Angew. Chem. Int. Ed.* **2011**, *50*, 2063. (b) Moret, M.-E.; Peters, J. C. *J. Am. Chem. Soc.* **2011**, *133*, 18118. (c) Anderson, J. S.; Moret, M.-E.; Peters, J. C. *J. Am. Chem. Soc.* **2013**, *135*, 534.

[18] Anderson, J. S.; Cutsail III, G.; Rittle, J.; Connor, B.; Gunderson, W.; Zhang, L.; Hoffman, B.; Peters, J. C. *J. Am. Chem. Soc.* **2015**, *137*, 7803.

[19] (a) Krebs, C.; Price, J. C.; Baldwin, J.; Saleh, L.; Green, M. T.; Bollinger, J. M. *Inorg. Chem.* **2005**, *44*, 742. (b) Krebs, C; Bollinger, J. M. *Photosynth. Res.* **2009**, *102*, 295.

[20] (a) McLean, P. A.; Papaefthymiou, V.; Orme-Johnson, W. H.; Münck, E. *J. Biol. Chem.* **1987**, *262*, 12900. (b) Yoo, S. J.; Angove, H. C.; Papaefthymiou, V.; Burgess, B. K.; Münck, E. *J. Am. Chem. Soc.* **2000**, *122*, 4926.

[21] Data were not collected at -78 °C due to lower solubility of $NaBAr^{F}{}_{4}$ at that temperature.

[22] Lowe, D. J.; Thorneley, R. N. F. *Biochem. J.* **1984**, *224*, 877.

[23] This represents a lower limit of the H_2 produced due to leakage using a set-up that enables quantification of H_2 and NH_3 in a single experiment.

[24] (a) Daifuku, S. L.; Al-Afyouni, M. H.; Snyder, B. E. R.; Kneebone, J. L.; Neidig, M. L. *J. Am. Chem. Soc.* **2014**, *136*, 9132. (b) Daifuku, S. L.; Kneebone, J. L.; Snyder, B. E. R.; Neidig, M. L. *J. Am. Chem. Soc.* **2015**, *137*, 11432.

[25] Berry, J. F.; Bill, E.; Bothe, E.; DeBeer, S.; Mienert, B.; Neese, F.; Wieghardt, K. *Science* **2006**, *312*, 1937.

[26] Lee, Y.; Peters, J. C. *J. Am. Chem. Soc.* **2011**, *133*, 4438.

[27] Ye, S.; Bill, E.; Neese, F. Inorg. Chem. 2016, ASAP, DOI: 10.1021/acs.inorgchem.5b02908.

[28] If the adamantyl imide species $P_3{}^{B}Fe\text{-}NAd^{0/1+}$ are excluded from the series of data collected in Figure 3.6, the correlation improves significantly ($r^2 = 0.96$). The isomer shifts of these imides appear to be systematically reduced by ca. 0.1-0.2 mm s^{-1} from the trend exhibited by the rest of the compounds in Table 3.3.

[29] Fong, H.; Moret, M.-E.; Lee, Y.; Peters, J. C. *Organometallics* **2013**, *32*, 3053.

[30] Münck, E. *Methods Enzymol.* **1978**, *54*, 346.

[31] Although the low isomer shift of the minor component present in Figure 3.7B is suggestive of a diamagnetic ground state, its identity is presently unknown.

[32] Also present in Figure 3.8A: ca. 20% of the species with parameters δ = -0.03 ± 0.04 mm s^{-1} and ΔE_Q = 2.88 ± 0.09 mm s^{-1} that is present in Figure 3.7C (white), and ca. 20% of a broad residual signal consistent with an unresolved quartet species (grey). Also present in Figure 3.8B: ca. 20% of neutral $P_3^BFe\text{-}N_2$ (green); ca. 15% of a sharply resolved species with parameters δ = 0.68 mm s^{-1} and ΔE_Q = 1.40 mm s^{-1} (white) that is consistent with a quartet species such as $P_3^BFe\text{-}NH_2$; ca. 20% of a broad residual signal consistent with an unresolved quartet species (grey).

[33] Also present in Figure 3.8C: ca. 10% of the species with parameters δ = -0.03 ± 0.04 mm s^{-1} and ΔE_Q = 2.88 ± 0.09 mm s^{-1} that is present in Figure 3.7C and 3.8A (white), and ca. 15% of a broad residual signal consistent with an unresolved quartet species (grey).

[34] (a) Lowe, D. J.; Thorneley, R. N. F. *Biochem. J.* **1984**, *224*, 887, (a) Lowe, D. J.; Thorneley, R. N. F. *Biochem. J.* **1984**, *224*, 895, (a) Lowe, D. J.; Thorneley, R. N. F. *Biochem. J.* **1984**, *224*, 903.

[35] Lukoyanov, D.; Yang, Z.-Y.; Khadka, N.; Dean, D. R.; Seefeldt, L. C.; Hoffman, B. M. *J. Am. Chem. Soc.* 2**015**, *137*, 3610.

[36] (a) Rivera-Ortiz, J. M.; Burris, R. H. *J. Bacteriol.* **1975**, *123*, 537. (b) Simpson, F. B.; Burris, R. H. *Science* **1984**, *224*, 1095.

[37] Rittle, J.; Peters, J. C.; *J. Am. Chem. Soc.* 2**016**, *online ASAP,* DOI: 10.1021/jacs.6b01230.

Chapter 4

CATALYTIC N_2-TO-NH_3 CONVERSION BY FE AT LOWER DRIVING FORCE: A PROPOSED ROLE FOR METALLOCENE-MEDIATED PCET

Reproduced in part with permission from:

Chalkley, M.; Del Castillo, T.; Matson, B.; Roddy, J.; Peters, J. C.; *ACS Central Science*, **2017**, 3, 217-223. **DOI:** 10.1021/acscentsci.7b00014

This was one of my favorite projects that I worked on at Caltech and there are actually two potentially valuable lessons to take away from it. The first is that one should generally follow one's advisor's advice (at least eventually), not only will this streamline future conversations with one's advisor, but also, occasionally, the ideas will even be worth pursuing on their own merit. Prior to this project the idea of finding a new combination of acid and reductant that would work with the P_3^BFe catalyst to drive N_2RR had been kicked around the lab as a target essentially as long as I was with the group and no one had taken it up. Finally, Jonas had a small group of my colleagues and I assembled in his office and he said something to the effect of "I want this done, who's willing to do it?" I was in between interesting leads at the time so I raised my hand. The following research ended up being perhaps the most fruitful of my graduate career and ultimately unlocked my long-held dream of observing electrocatalytic N_2RR with the P_3^BFe catalyst. The other take away is about not being afraid to jump to conclusions; even if the reason for the conclusion is wrong it might still be a good idea. When I first got the data that decamethylcobaltocene could serve as a chemical

reductant for N_2RR with the P_3^BFe catalyst we thought that this reaction must not be going through the anionic $P_3^BFeN_2^-$ state. The reason we thought this was because we didn't know the potential of the $P_3^BFeN_2^{0/-}$ couple under the relevant conditions and thought decamethylcobaltocene wouldn't be sufficiently reducing to access $P_3^BFeN_2^-$. That thinking turned out to be wrong, but for a time we had a new paradigm that went against our previous hypothesis that this reduced state was critical for N_2RR. That was the line of thinking that got us talking about PCET. By the time we found out that decamethylcobaltocene is, in fact, sufficiently reducing to access the $P_3^BFeN_2^-$ anion after all, that good idea (that we might have a different mechanism at work which might involve the metallocene as more than a reductant) was firmly entrenched. So far we still think we ended up at the right hypothesis for the (initially) wrong reasons.

4.1 Introduction

The reduction of N_2 to NH_3 is critical for life and is performed on a massive scale both industrially and biologically.[1] The high stability of the N≡N triple bond necessitates catalysts and high-energy reagents/conditions to achieve the desired transformation.[2] Synthetic studies of catalytic N_2-to-NH_3 conversion by model complexes are of interest to constrain hypotheses concerning the mechanism/s of biological (or industrial) N_2-fixation and to map fundamental catalyst design principles for multi-electron reductive transformations.[3,4] Interest in Fe model systems that catalyze N_2-to-NH_3 conversion has grown in part due to the postulate that one or more Fe centers in the FeMo-cofactor of FeMo-nitrogenase may serve as the site of N_2 binding and activation during key bond-breaking and -making steps.[5] Previous examples of synthetic molecular Fe catalysts that mediate N_2-to-NH_3 conversion operate with high driving force, relying on a very strong

acid (pK_a ca. 0) and reductant ($E° < -3.0$ V vs $Fc^{+/0}$).[6,7,8,9] In contrast, several Mo catalysts have been shown to facilitate N_2-to-NH_3 conversion with significantly lower driving force.[10,11,12,13] There is thus interest in exploring the viability of Fe-mediated catalytic N_2-to-NH_3 conversion under less forcing conditions from a practical perspective, and to continue assessing these systems as functional models of biological nitrogenases, in which 8 ATP are consumed per NH_3 formed leading to a driving force of 58 kcal/mol.[2]

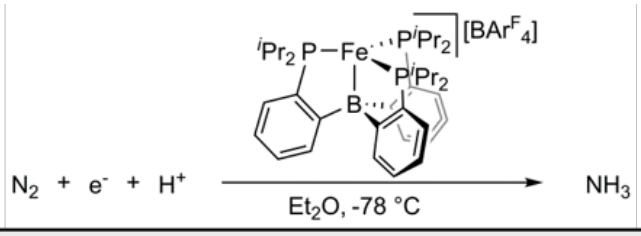

e^- (E^0 vs $Fc^{+/0}$)	H^+ (pK_a in THF)	$\Delta\Delta H_f$ (kcal/mol)
Cp^*_2Co (-1.96 V)	$[PhNH_3][OTf]$ (7.8)	62
Cp^*_2Co (-1.96 V)	$[Ph_2NH_2][OTf]$ (4.1)	77
KC_8 (≤ -3.0 V)	$HBAr^F_4$ (ca. 0)	≥ 156

Figure 4.1. Summary of conditions used for catalytic N_2-to-NH_3 conversion by $P_3{}^BFe^+$ highlighting the estimated enthalpic driving force ($\Delta\Delta H_f$).[14,15,16,17,18,19]

Herein we demonstrate that catalytic conversion of N_2 to NH_3 by $P_3{}^BFe^+$ ($P_3{}^B$ = tris(*o*-diisopropylphosphinophenyl)borane) can be achieved with a significantly lower driving force by coupling Cp^*_2Co with $[Ph_2NH_2]^+$ or $[PhNH_3]^+$ (Figure 4.1). Such conditions additionally afford unusually high selectivity and catalytic turnover for NH_3.[20] Moreover, we note the use of milder reagents as reductant (E^0; eq 1) and acid (pK_a) engenders a higher effective bond dissociation enthalpy ($BDE_{effective}$; eq 1).15,[21] This may in turn afford access

to proton-coupled electron transfer (PCET) pathways (e.g., $FeN_2 + H\cdot \rightarrow FeN_2H$) in addition to electron transfer (ET)/proton transfer (PT) pathways, thus enhancing overall catalytic efficiency. Theoretical considerations, including DFT calculations, and experimental details are discussed that suggest the viability of a decamethylcobaltocene-mediated PCET pathway in this system; by extension we suggest metallocene-mediated (e.g., Cp^*_2Cr) PCET pathways may be operative in previously studied Mo and Fe N_2-fixing systems that use metallocene reductants.[10-13,20]

$$BDE_{effective} = 1.37(pK_a) + 23.06(E^0) + C_H \quad (1)$$

Various observations of P_3^BFe complexes in the presence of acids and reductants suggested that this system might be capable of N_2-to-NH_3 conversion with lower driving force than that originally reported. Accordingly, we had observed that the treatment of $P_3^BFeN_2^-$ with KC_8 and weaker acids ($pK_a > 0$) led to greater than stoichiometric NH_3 formation (e.g., under unoptimized conditions [2,6-dimethylanilinium][OTf] afforded 2.1 equiv NH_3 per Fe).[22] Similarly, the treatment of $P_3^BFeN_2^-$ with $[H(OEt_2)_2][BAr^F_4]$ ($HBAr^F_4$, BAr^F_4 = tetrakis(3,5-bis(trifluoromethyl)phenyl)borate) and weaker reductants led to modest yields of NH_3. For example, under unoptimized conditions we had observed that decamethylcobaltocene (Cp^*_2Co) and $HBAr^F_4$ afforded 0.6 equiv NH_3 per Fe.[22,23] Most recently, an apparent catalytic response was observed during a cyclic voltammetry experiment at the $P_3^BFeN_2^{0/-}$ couple (−2.1 V vs $Fc^{+/0}$) upon addition of excess $HBAr^F_4$ under an N_2 atmosphere. Electrolytic NH_3 generation by $P_3^BFe^+$ was observed at −2.4 V vs $Fc^{+/0}$ in Et_2O,[23] and Na/Hg (−2.4 V vs $Fc^{+/0}$ in THF)[16] could instead be used for N_2-to-NH_3

conversion catalysis (albeit less selectively and with low turnover). Finally, mixing $P_3^BFe^+$ with Cp^*_2Co in Et_2O at −78 °C under N_2 generates some $P_3^BFeN_2^-$ as observed by X-band EPR and Mössbauer spectroscopy (see SI), suggesting that Cp^*_2Co is in principle a sufficiently strong reductant to trigger catalysis by $P_3^BFe^+$.

4.2 Results and Discussion

Treatment of $P_3^BFe^+$ with Cp^*_2Co and $[Ph_2NH_2][OTf]$, $[Ph_2NH_2][BAr^F_4]$, or $[PhNH_3][OTf]$ in Et_2O at −78 °C under an N_2 atmosphere affords catalytic yields of NH_3 (Table 4.1). Notably, the highest selectivity for NH_3 obtained among this series (72% at standard substrate loading; Entry 1) is significantly improved compared to all previously described (molecular) Fe catalysts for N_2-to-NH_3 conversion.[20,24] Tripling the initial substrate loading (Entry 2) nearly triples the NH_3 production with only modest loss in efficiency for NH_3 (63%). Preliminary attempts to further increase the initial substrate loading have led to substantially decreased efficiency (Entry 3). However, substrate reloading experiments (Entries 4 and 5) maintain greater than 50% efficiency for NH_3 overall; a turnover number for NH_3 generation via two reloadings has been achieved as high as 89 in a single run (84 ± 8; Entry 5). This is an unusually high turnover number for a molecular N_2-to-NH_3 conversion catalyst under any conditions.[20,25]

The use of the more soluble acid $[Ph_2NH_2][BAr^F_4]$ (Entry 6) provides significantly lower, but still catalytic, yields of NH_3. This more soluble acid presumably increases background reactivity with Cp^*_2Co (see SI). Perhaps more significantly, $[PhNH_3][OTf]$ is a considerably weaker acid than $[Ph_2NH_2][OTf]$ (Figure 4.1), but still provides substantial catalytic yields of NH_3 (Entries 7 and 8) and at efficiencies that compare well with those

obtained previously using $HBAr^F_4$ and KC_8 despite a difference in driving force of nearly 100 kcal/mol.23

Table 4.1. N_2-to-NH_3 Conversion with P_3^EM Complexes (M = Fe, Co)

	Catalyst	Cp^*_2Co (equiv)	Acid (equiv)	Equiv NH_3/Fe	% Yield NH_3/e^-
1	$P_3^BFe^+$	54	108[b]	12.8 ± 0.5	72 ± 3
2	$P_3^BFe^+$	162	322[b]	34 ± 1	63 ± 2
3	$P_3^BFe^+$	322	638[b]	26.7 ± 0.9	25 ± 1
4[a]	$P_3^BFe^+$	[162]x2	[322]x2[b]	56 ± 9	52 ± 9
5[a]	$P_3^BFe^+$	[162]x3	[322]x3[b]	84 ± 8	52 ± 5
6	$P_3^BFe^+$	54	108[c]	8 ± 1	42 ± 6
7	$P_3^BFe^+$	54	108[d]	7 ± 1	38 ± 7
8	$P_3^BFe^+$	162	322[d]	16 ± 3	29 ± 4
9	$P_3^{Si}FeN_2$	54	108[b]	1.2 ± 0.1	6 ± 1
10	$P_3^BCoN_2^-$	54	108[b]	1.1 ± 0.4	6 ± 2
11	$P_3^{Si}CoN_2$	54	108[b]	0 ± 0	0 ± 0

The catalyst, acid, Cp^*_2Co, and Et_2O were sealed in a vessel at −196 °C under an N_2 atmosphere followed by warming to −78 °C and stirring. Yields are reported as an average of at least 2 runs; for individual experiments see SI. [a]For these experiments the reaction was allowed to proceed for 3 hours at −78 °C before cooling to −196 °C and furnished with additional substrate and solvent [b]$[Ph_2NH_2][OTf]$. [c]$[Ph_2NH_2][BAr^F_4]$. [d]$[PhNH_3][OTf]$.

We also screened several related phosphine-ligated Fe–N_2 and Co–N_2 complexes[26,27] under the new standard reaction conditions with $[Ph_2NH_2][OTf]$ and Cp^*_2Co (Entries 9–11) but found that none of these other systems were competent catalysts. While we anticipate other catalyst systems for N_2-to-NH_3 conversion may yet be found that function

under the conditions described herein,20 certain features of the P_3^BFe system correlate with unusually productive catalysis.27

Also significant is that when $P_3^BFe^+$ is loaded with 322 equiv $[Ph_2NH_2][OTf]$ and 162 equiv Cp^*_2Co in Et_2O at −78 °C, modest levels of N_2H_4 are detected (< 1 equiv per Fe; see SI).9,20 We had previously reported that catalytic N_2 reduction with KC_8 and $HBAr^F_4$ yielded no detectable hydrazine, but observed that if hydrazine was added at the outset of a catalytic run, it was consumed.6 When 5 equiv of N_2H_4 were added at the beginning of a catalytic run (again with 322 equiv $[Ph_2NH_2][OTf]$ and 162 equiv Cp^*_2Co), only 0.22 equiv of N_2H_4 (4.4% recovery) remained after workup. This result indicates that liberated hydrazine can also be reduced or disproportionated under the present conditions. That N_2H_4 is detected to any extent in the absence of initially added N_2H_4 under these conditions indicates that a late N–N cleavage mechanism to produce NH_3 (e.g., alternating or hybrid cross-over) is accessible.4,28 A recent report by Ashley and coworkers describes a phosphine-supported Fe system for which catalytic hydrazine formation is kinetically dominant.20 Whether such a pathway is kinetically dominant in this system is as yet unclear.23,29

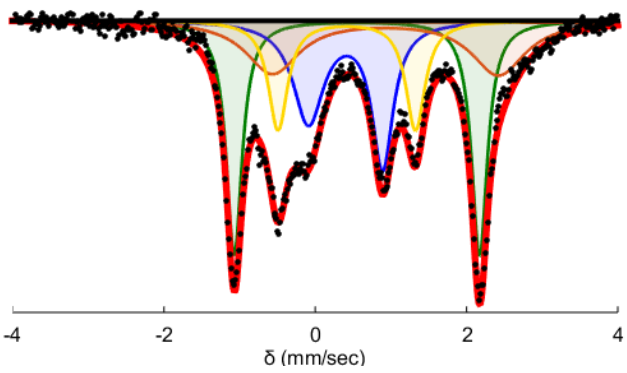

Figure 4.2. Mössbauer spectrum at 80 K with 50 mT applied parallel field of a freeze-quenched catalytic reaction (54 equiv Cp^*_2Co, 108 equiv $[Ph_2NH_2][OTf]$, 1 equiv $P_3^B[^{57}Fe]^+$) after five minutes of reaction time.

The P_3^BFe speciation under turnover conditions was probed via freeze-quench Mössbauer spectroscopy.23 The Mössbauer spectrum of a catalytic reaction mixture after five minutes of reaction time (Figure 4.2) reveals the presence of multiple species featuring well-resolved sets of quadrupole doublets. The spectrum is satisfactorily simulated with $P_3^BFeN_2$ (δ = 0.55 mm/sec, ΔE_Q = 3.24 mm/sec, 32%; Figure 4.2 green), $P_3^BFeN_2^-$ (δ = 0.40 mm/sec, ΔE_Q = 0.98 mm/sec, 26%; Figure 4.2 blue),23,[30] an unknown, likely P_3^B metallated Fe species (δ = 0.42 mm/sec, ΔE_Q = 1.84 mm/sec, 18%; Figure 4.2 yellow), and a final species that is modeled with δ = 0.96 mm/sec and ΔE_Q = 3.10 mm/sec (24%; Figure 4.2 orange). The broad nature of this last signal and its overlap with other features in the spectrum prevents its precise assignment, but its high isomer shift and large quadrupole splitting are suggestive of a tetrahedral, S = 2 Fe(II) complex.[31,32] The Mössbauer spectrum of a catalytic reaction mixture after 30 minutes was also analyzed (see SI). The spectrum still shows $P_3^BFeN_2$ (53%), the same unknown P_3^BFe species (18%), and again a tetrahedral, high-spin Fe(II) component (22%). However, $P_3^BFe^+$ is now present (δ = 0.75

mm/sec, ΔE_Q = 2.55 mm/sec, 8%) and $P_3^BFeN_2^-$ is no longer observed. The reloading experiments described above provide strong evidence that "P_3^BFe" species represent an "active catalyst" population; interpretation of the relative speciation via spectroscopy should hence bear on the mechanism of the overall catalysis.

The appearance of a presumed high-spin (S = 2), tetrahedral Fe(II) species during catalysis (ca. 25%) might arise via dechelation of a phosphine arm. This species could represent an off-path state, or a downstream deactivation product. Interestingly, under the present catalytic conditions we do not observe the borohydrido-hydrido species P_3^B(μ-H)Fe(H)(L) (L = N_2 or H_2); this species was postulated to be an off-path resting state during N_2-to-NH_3 conversion catalysis using $HBAr^F_4$ and KC_8 and was the major component observed at early times (ca. 60% at 5 min).23 It therefore appears that a larger fraction of the "P_3^BFe" species are in a catalytically on-path state at early reaction times under these new catalytic conditions.

Additionally, the presence of a significant degree of $P_3^BFeN_2^-$ (Figure 4.2) at an early time point is distinct from conditions with $HBAr^F_4$ and KC_8.23 This observation is consistent with the notion that protonation of $P_3^BFeN_2^-$ is slowed under the present conditions, likely as a result of the insolubility of the triflate salt [Ph_2NH_2][OTf] and its attenuated acidity relative to $HBAr^F_4$.17,18,33 Clearly, differences in the rates of key elementary steps under the new conditions described here may lead to new mechanistic scenarios for N_2-to-NH_3 conversion.

The improved catalytic efficiency at significantly lower driving force warrants additional consideration. When using $HBAr^F_4$ and KC_8 we have previously suggested that protonation of $P_3^BFeN_2^-$, which itself can be generated by reduction of $P_3^BFeN_2$, to produce

P_3^BFe-N=NH is a critical first step; P_3^BFe-N=NH can then be trapped by acid to produce spectroscopically observable P_3^BFe=N-NH_2^+.29 These steps, shown in eq 2a-b, represent an ET-PT pathway. A PT-ET pathway, where $P_3^BFeN_2$ is sufficiently basic to be protonated to generate P_3^BFe-N=NH^+ as a first step, followed by ET, is also worth considering (eq 3a-b). A direct PCET pathway (eq 4) where H-atom delivery to $P_3^BFeN_2$ occurs, thus obviating the need to access either $P_3^BFeN_2^-$ or P_3^BFe-N=NH^+, needs also to be considered.

$$P_3^BFeN_2 + e^- \rightarrow P_3^BFeN_2^- \quad (2a)$$

$$P_3^BFeN_2^- + H^+ \rightarrow P_3^BFe\text{-}N{=}NH \quad (2b)$$

$$P_3^BFeN_2 + H^+ \rightarrow P_3^BFe\text{-}N{=}NH^+ \quad (3a)$$

$$P_3^BFe\text{-}N{=}NH^+ + e^- \rightarrow P_3^BFe\text{-}N{=}NH \quad (3b)$$

$$P_3^BFeN_2 + H\cdot \rightarrow P_3^BFe\text{-}N{=}NH \quad (4)$$

Initial PT to $P_3^BFeN_2$ to generate P_3^BFe-N=NH^+ (eq 3a) is unlikely under the present conditions due to the high predicted acidity of P_3^BFe-N=NH^+ (pK_a = −3.7; estimated via DFT; see SI); efficient generation of such a species seems implausible for acids whose pK_a's are calculated at 1.4 ($Ph_2NH_2^+$) and 6.8 ($PhNH_3^+$) in Et_2O (Table 4.2). We note that [Ph_2NH_2][OTf] does not react productively with $P_3^BFeN_2$ at -78 °C in Et_2O, as analyzed by Mössbauer spectroscopy.

Table 4.2. Calculated pK_a Values and BDEs of Selected Species[a]

Species	pK_a	BDE[b]
$Ph_2NH_2^+$	1.4[c]	-
$PhNH_3^+$	6.8	-
Lutidinium	14.5	-
endo-Cp*Co(η^4-C_5Me_5H)$^+$	16.8	31
exo-Cp*Co(η^4-C_5Me_5H)$^+$	16.8	31
endo-Cp*Cr(η^4-C_5Me_5H)$^+$	17.3	37
exo-Cp*Cr(η^4-C_5Me_5H)$^+$	12.1	30
P_3^BFe-N=NH$^+$	-3.7	-
P_3^BFe-N=NH	38.7	35
P_3^BFe=N-NH_2^+	14.4	51
P_3^BFe=N-NH_2	-	47
[HIPTN_3N]Mo-N=NH	-	51

[a]Calculations were performed using the M06-L[34] functional with a def2-TZVP basis set on Fe and a def2-SVP basis set on all other atoms[35] (see SI). [b]In kcal/mol. [c]pK_a values were calculated in Et_2O and reported relative to $(Et_2O)_2H^+$.

Focusing instead on the PCET pathway (eq 4), the DFT-calculated $BDE_{N\text{-}H}$ for P_3^BFe-N=NH (35 kcal/mol; Table 4.2; see SI for details)[36] is larger than the effective BDE21 of either Cp*$_2$Co/$Ph_2NH_2^+$ or Cp*$_2$Co/$PhNH_3^+$ (25 and 31 kcal/mol, respectively). This suggests that PCET (eq 4) is plausible on thermodynamic grounds. Given that we have employed Cp*$_2$Co in this study, and that this and also Cp_2Co and Cp*$_2$Cr have been effective in other N_2-fixing molecular catalyst systems,[10,11,12,13,20] we have explored via DFT several putative metallocene-derived PCET reagents. Independent studies of H_2 evolution from cobaltocene have invoked a protonated cobaltocene intermediate.[37,38,39] The observation of a background H_2 evolution reaction (HER) when employing

metallocene reductants, but in the absence of an N_2-to-NH_3 conversion catalyst, suggests that metallocene protonation is kinetically competent.[10,40] Based on the analysis we describe below, we propose that protonated metallocenes may serve as discrete and highly active H· sources for PCET.

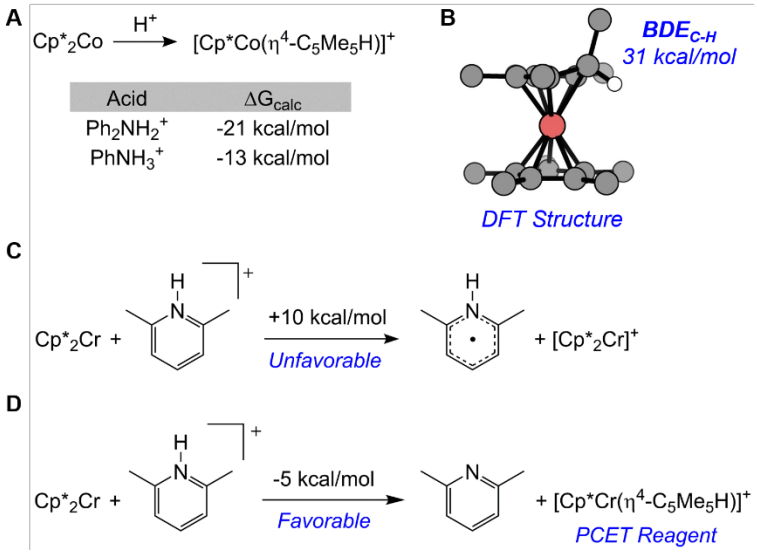

Figure 4.3. (A) Calculated free-energy changes for the protonation of Cp^*_2Co. (B) DFT optimized structure of *endo*-$Cp^*Co(\eta^4\text{-}C_5Me_5H)^+$ (methyl protons omitted for clarity). (C) The unfavorable reduction of 2,6-lutidinium by Cp^*_2Cr with the calculated free energy change. (D) The favorable protonation of Cp^*_2Cr by lutidinium with the calculated free energy change.

We find that the formation of *endo*- and *exo*-$Cp^*Co(\eta^4\text{-}C_5Me_5H)^+$ are predicted to be thermodynamically favorable via protonation of Cp^*_2Co by either $Ph_2NH_2^+$ or $PhNH_3^+$ (−21 and −13 kcal/mol, respectively; Figure 4.3A).[41,42] We have calculated the $BDE_{C\text{-}H}$'s for both *endo*- and *exo*-$Cp^*Co(\eta^4\text{-}C_5Me_5H)^+$ as 31 kcal/mol (Figure 4.3B; Table 4.2), indicating that they should be among the strongest PCET reagents accessible in this catalyst cocktail. Indeed, they would be among the strongest PCET reagents known.21

We anticipate these species would be extremely unstable in solution and hence difficult to detect in situ, but via trapping in the solid state by rapid precipitation we have isolated a species whose EPR data and chemical behavior are consistent with {Cp*Co(η^4-C_5Me_5H)}{OTf}. Accordingly, slow addition of a toluene solution of Cp*$_2$Co at -78 °C to triflic acid (HOTf) leads to the instantaneous precipitation of a purple solid that can be isolated at low temperature. The purple solid can be characterized at 77 K by powder EPR spectroscopy via its highly structured signal. By contrast, at this temperature S = ½ Cp*$_2$Co does not display a discernable EPR signal (see SI). The new signal shows strong Co hyperfine coupling and significant g-anisotropy, consistent with a new S = ½ cobalt species (Figure 4.4). Furthermore, the resulting EPR signal is slightly perturbed when this purple solid is instead generated from the reaction between deuterated triflic acid (DOTf) and Cp*$_2$Co (see SI), suggesting that the acidic proton is directly associated with the new Co species and consistent with its assignment as a protonated decamethylcobaltocene species. Close inspection of these spectra indicate they likely represent a mixture of two signals arising from similar Co-containing complexes. This observation is fully consistent with the presence of both *endo*- and *exo*-Cp*Co(η^4-C_5Me_5H)$^+$, as is to be expected given they are predicted to be nearly isoenergetic. Allowing the purple precipitate to warm to room temperature either as a solid or a stirred suspension in toluene leads to the formation of H_2 and Cp*$_2$Co$^+$ (see SI).

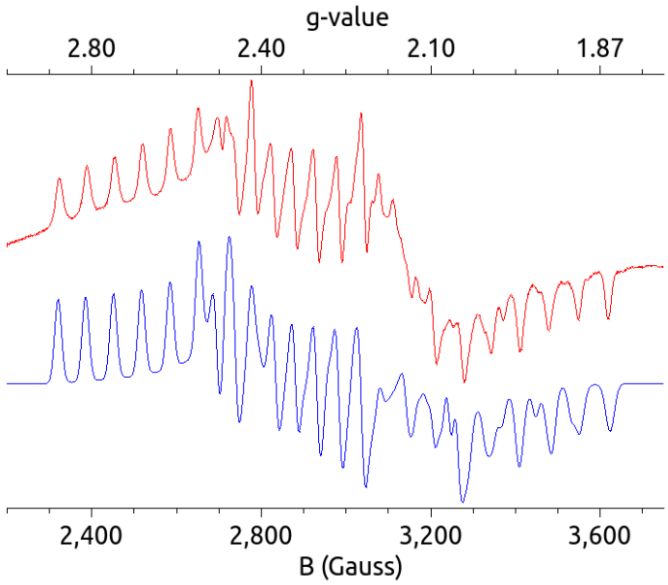

Figure 4.4. X-band 77 K powder EPR spectrum (red) and simulation (blue) of the isolated purple precipitate (assigned as *endo*- and *exo*-Cp*Co(η^4-C_5Me_5H)$^+$) from reaction between Cp^*_2Co and HOTf at -78 °C (see SI for simulation parameters).

To better understand the potential role of PCET in N_2-to-NH_3 conversion catalysis by P_3^BFe, we have additionally calculated the N–H bond strengths (Table 4.2) of several early stage candidate intermediates, including the aforementioned P_3^BFe-N=NH (35 kcal/mol), P_3^BFe=N-NH_2^+ (51 kcal/mol), and P_3^BFe=N-NH_2 (47 kcal/mol). We conclude that PCET from Cp*Co(η^4-C_5Me_5H)$^+$ to generate intermediates of these types is thermodynamically favorable in each case.[43] To generate the first and most challenging intermediate (eq 5), the enthalpic driving force for PCET is estimated at ~4 kcal/mol (ΔG_{calc} = −9 kcal/mol). This driving force, and hence the plausibility of PCET steps, increases sharply as further downstream Fe-N_xH_y intermediates are considered.[44,45,46,47]

$P_3^BFeN_2 + Cp^*Co(\eta^4\text{-}C_5Me_5H)^+$

$$\rightarrow P_3^BFe\text{-}N{=}NH + Cp^*_2Co^+ \quad (5)$$

Given the prevalence of metallocene reductants in N_2-to-NH_3 (or -N_2H_4) conversion,[10,11,12,13,20] especially for the well-studied Mo catalyst systems, it is worth considering metallocene-mediated PCET more generally. For instance, a role for ET/PT steps (or conversely PT/ET) in N_2-to-NH_3 conversion catalyzed by [HIPTN$_3$N]Mo (HIPTN$_3$N = [(3,5-(2,4,6-^{i}Pr$_3$C$_6$H$_2$)$_2$C$_6$H$_3$NCH$_2$CH$_2$)$_3$N]$^{3-}$, a bulky triamidoamine ligand) has been frequently posited.[48,49,50,51,52] But PCET steps may play a critical role, too. In the latter context, we note reports from Schrock and coworkers that have shown both acid and reductant are required to observe productive reactivity with [HIPTN$_3$N]MoN$_2$. These observations are consistent with PCET to generate [HIPTN$_3$N]Mo-N=NH.52 A PCET scenario has been discussed in this general context of N_2-to-NH_3 conversion, where a lutidinyl radical intermediate formed via ET from Cp*$_2$Cr has been suggested as a PCET reagent that can be generated in situ.[40,53] However, our own calculations predict that the lutidinyl radical should not be accessible with Cp*$_2$Cr as the reductant (ΔG_{calc} = +10 kcal/mol; Figure 4.3C).[54,55,56] We instead propose protonation of Cp*$_2$Cr by the lutidinium acid as more plausible (ΔG_{calc} = −5.3 kcal/mol; Figure 4.3D) to generate a highly reactive decamethylchromocene-derived PCET reagent.

While N–H bond strengths have not been experimentally determined for the [HIPTN$_3$N]Mo-system, using available published data we deduce the N–H bond of [HIPTN$_3$N]Mo-N=NH to be ca. 49 kcal/mol and we calculate it via DFT (truncated HIPTN$_3$N; see SI) as 51 kcal/mol.[57] The $BDE_{N\text{-}H}$ for this Mo diazenido species is hence

much larger than we predict for P_3^BFe-N=NH (35 kcal/mol), perhaps accounting for its higher stability.52 A PCET reaction between *endo*-Cp*Cr(η^4-C_5Me_5H)$^+$ (BDE_{calc} = 37 kcal/mol) and [HIPTN_3N]MoN_2 to generate [HIPTN_3N]Mo-N=NH and Cp*$_2$Cr$^+$ would be highly exergonic. Furthermore, we predict a similarly weak $BDE_{C\text{-}H}$ for Cp-protonated cobaltocene, CpCo(η^4-C_5H_6)$^+$ (BDE_{calc} = 35 kcal/mol). These considerations are consistent with the reported rapid formation of [HIPTN_3N]Mo-N=NH using either Cp*$_2$Cr or Cp_2Co in the presence of lutidinium acid.[58]

4.3 Conclusion

To close, we have demonstrated catalytic N_2-to-NH_3 conversion by $P_3^BFe^+$ at a much lower driving force (nearly 100 kcal/mol) than originally reported via combination of a weaker reductant (Cp*$_2$Co) and acid ([Ph_2NH_2][OTf] or [Ph_3NH][OTf]). Significantly improved efficiency for NH_3 formation is observed (up to 72% at standard substrate loading), and by reloading additional substrate at low temperature a turnover number that is unusually high for a synthetic molecular catalyst (84 ± 8 equiv NH_3 per Fe) has been achieved. Freeze-quench Mössbauer spectroscopy under turnover conditions reveals differences in the speciation of P_3^BFe compared to previous studies with $HBAr^F_4$ and KC_8, suggesting changes in the rates of key elementary steps. Using DFT calculations we have considered the viability of a decamethylcobaltocene-mediated PCET pathway as an additional or alternative scenario to previously formulated ET-PT and PT-ET pathways. Based on our calculations, we propose that protonated metallocenes should serve as discrete, very reactive PCET reagents in N_2-to-NH_3 conversion catalysis. Furthermore, we present preliminary experimental data that suggest protonated decamethylcobaltocene can be accessed synthetically and that such a species may be a potent PCET reagent. Indeed,

the achievement of high efficiency for N_2-to-NH_3 conversion by both P_3^BFe and various Mo catalysts that benefit from metallocene reductants raises the intriguing possibility that metallocene-based PCET reactivity is a potentially widespread and overlooked mechanism. Efforts are underway to experimentally probe such pathways.

4.4 REFERENCES

[1] Smil, V. *Enriching the Earth*. Cambridge: MIT Press, 2001.

[2] Ham, C. J. M. van der; Koper, M. T. M.; Hetterscheid, D. G. H. Challenges in Reduction of Dinitrogen by Proton and Electron Transfer. *Chem. Soc. Rev.* **2014**, *43*, 5183–5191.

[3] Shaver, M. P.; Fryzuk, M. D. Activation of Molecular Nitrogen: Coordination, Cleavage and Functionalization of N2 Mediated By Metal Complexes. *Adv. Synth. Catal.* **2003**, *345*, 1061–1076.

[4] MacLeod, K. C.; Holland, P. L. Recent Developments in the Homogeneous Reduction of Dinitrogen by Molybdenum and Iron. *Nat Chem* **2013**, *5*, 559–565.

[5] Hoffman, B. M.; Lukoyanov, D.; Yang, Z.-Y.; Dean, D. R.; Seefeldt, L. C. Mechanism of Nitrogen Fixation by Nitrogenase: The Next Stage. *Chem. Rev.* **2014**, *114*, 4041–4062.

[6] Anderson, J. S.; Rittle, J.; Peters, J. C. Catalytic Conversion of Nitrogen to Ammonia by an Iron Model Complex. *Nature* **2013**, *501*, 84–87.

[7] Creutz, S. E.; Peters, J. C. Catalytic Reduction of N2 to NH3 by an Fe–N2 Complex Featuring a C-Atom Anchor. *J. Am. Chem. Soc.* **2014**, *136*, 1105–1115.

[8] Ung, G.; Peters, J. C. Low-Temperature N_2 Binding to Two-Coordinate L_2Fe^0 Enables Reductive Trapping of $L_2FeN_2^-$ and NH_3 Generation. *Angew. Chem. Int. Ed.* **2015**, *54*, 532–535.

[9] Kuriyama, S.; Arashiba, K.; Nakajima, K.; Matsuo, Y.; Tanaka, H.; Ishii, K.; Yoshizawa, K.; Nishibayashi, Y. Catalytic Transformation of Dinitrogen into Ammonia and Hydrazine by Iron-Dinitrogen Complexes Bearing Pincer Ligand. *Nat. Commun.* **2016**, *7*, 12181.

[10] Yandulov, D. V.; Schrock, R. R. Catalytic Reduction of Dinitrogen to Ammonia at a Single Molybdenum Center. *Science* **2003**, *301*, 76–78.

[11] Arashiba, K.; Miyake, Y.; Nishibayashi, Y. A Molybdenum Complex Bearing PNP-Type Pincer Ligands Leads to the Catalytic Reduction of Dinitrogen into Ammonia. *Nat. Chem.* **2011**, *3*, 120–125.

[12] Kuriyama, S.; Arashiba, K.; Nakajima, K.; Tanaka, H.; Kamaru, N.; Yoshizawa, K.; Nishibayashi, Y. Catalytic Formation of Ammonia from Molecular Dinitrogen by Use of Dinitrogen-Bridged Dimolybdenum–Dinitrogen Complexes Bearing PNP-Pincer Ligands: Remarkable Effect of Substituent at PNP-Pincer Ligand. *J. Am. Chem. Soc.* **2014**, *136*, 9719–9731.

[13] Arashiba, K.; Kinoshita, E.; Kuriyama, S.; Eizawa, A.; Nakajima, K.; Tanaka, H.; Yoshizawa, K.; Nishibayashi, Y. Catalytic Reduction of Dinitrogen to Ammonia by Use of Molybdenum–Nitride Complexes Bearing a Tridentate Triphosphine as Catalysts. *J. Am. Chem. Soc.* **2015**, *137*, 5666–5669.

[14] The enthalpic driving force ($\Delta\Delta H_f$) has been estimated here by taking $3*(BDE_{H\cdot} - BDE_{effective})$, where BDE is bond dissociation enthalpy. This allows for an evaluation of the driving force for a given reaction with respect to that for a hypothetical N_2-to-NH_3 conversion catalyst that uses H_2 as the proton and electron source. This is achieved by using Bordwell's equation (with the assumption that $S(X^{\cdot}) = S(XH)$; see SI) and literature values for p*K*a, redox potential, the enthalpy of reaction for $H^+ + e^- \rightarrow H^{\cdot}$ (C_H = 66 kcal/mol in THF), and the energy of $H^{\cdot}$ in THF (52 kcal/mol).

[15] Bordwell, F. G.; Cheng, J. P.; Harrelson, J. A. Homolytic Bond Dissociation Energies in Solution from Equilibrium Acidity and Electrochemical Data. *J. Am. Chem. Soc.* **1988**, *110*, 1229–1231.

[16] Connelly, N. G.; Geiger, W. E. Chemical Redox Agents for Organometallic Chemistry. *Chem. Rev.* **1996**, *96*, 877–910.

[17] Garido, G.; Rosés, M.; Ràfols, C.; Bosch, E. Acidity of Several Anilinium Derivatives in Pure Tetrahydrofuran. *J. Sol. Chem.* **2008**, *37,* 689-700.

[18] Kaljurand, I.; Kütt, A.; Sooväli, L.; Rodima, T.; Mäemets, V.; Leito, I.; Koppel, I. A. Extension of the Self-Consistent Spectrophotometric Basicity Scale in Acetonitrile to a Full Span of 28 pKa Units: Unification of Different Basicity Scales. *J. Org. Chem.* **2005**, *70*, 1019–1028.

[19] Cappellani, E. P.; Drouin, S. D.; Jia, G.; Maltby, P. A.; Morris, R. H.; Schweitzer, C. T. Effect of the Ligand and Metal on the pK_a Values of the Dihydrogen Ligand in the Series of Complexes $[M(H_2)H(L)_2]^+$, M = Fe, Ru, Os, Containing Isosteric Ditertiaryphosphine Ligands, L. *J. Am. Chem. Soc.* **1994**, *116*, 3375–3388.

[20] While initiating our studies we became aware of a phosphine-supported Fe system that catalyzes N_2-to-N_2H_4 conversion using Cp^*_2Co and $[Ph_2NH_2][OTf]$ with efficiency as high as 72% for e^- delivery to N_2: Hill, P. J.; Doyle, L. R.; Crawford, A. D.; Myers, W. K.; Ashley, A. E. Selective Catalytic Reduction of N2 to N2H4 by a Simple Fe Complex. *J. Am. Chem. Soc.* **2016**, *138*, 13521–13524.

[21] Warren, J. J.; Tronic, T. A.; Mayer, J. M. Thermochemistry of Proton-Coupled Electron Transfer Reagents and its Implications. *Chem. Rev.* **2010**, *110*, 6961-7001.

[22] Anderson, J. S. *Catalytic conversion of nitrogen to ammonia by an iron model complex. Ph.D. Thesis, California Institute of Technology, September 2013.*

[23] Del Castillo, T. J.; Thompson, N. B.; Peters, J. C. A Synthetic Single-Site Fe Nitrogenase: High Turnover, Freeze-Quench ^{57}Fe Mössbauer Data, and a Hydride Resting State. *J. Am. Chem. Soc.* **2016**, *138*, 5341–5350.

[24] Previously reported molecular Fe catalysts for N_2-to-NH_3 conversion utilize KC_8 and $HBAr^F_4$ and achieve NH_3 selectivities ≤ 45% with respect to their limiting reagent (see refs 6-9) at a similar reductant loading. Lower selectivities are observed with higher loading (see refs 6 and 23).

[25] In catalytic runs performed with labeled $[Ph_2{}^{15}NH_2][OTf]$ under an atmosphere of natural abundance $^{14}N_2$ the production of exclusively $^{14}NH_3$ is observed, demonstrating that the NH_3 formed during catalysis is derived from N_2 and not degradation of the acid (see SI).

[26] Whited, M. T.; Mankad, N. P.; Lee, Y.; Oblad, P. F.; Peters, J. C. Dinitrogen Complexes Supported by Tris(phosphino)silyl Ligands. *Inorg. Chem.* **2009**, *48*, 2507–2517.

[27] Del Castillo, T. J.; Thompson, N. B.; Suess, D. L. M.; Ung, G.; Peters, J. C. Evaluating Molecular Cobalt Complexes for the Conversion of N_2 to NH_3. *Inorg. Chem.* **2015**, *54*, 9256–9262.

[28] Rittle, J.; Peters, J. C. An Fe-N_2 Complex That Generates Hydrazine and Ammonia via Fe=NNH_2: Demonstrating a Hybrid Distal-to-Alternating Pathway for N_2 Reduction. *J. Am. Chem. Soc.* **2016**, *138*, 4243–4248.

[29] Anderson, J. S.; Cutsail, G. E.; Rittle, J.; Connor, B. A.; Gunderson, W. A.; Zhang, L.; Hoffman, B. M.; Peters, J. C. Characterization of an Fe≡N–NH_2 Intermediate Relevant to Catalytic N_2 Reduction to NH_3. *J. Am. Chem. Soc.* **2015**, *137*, 7803–7809.

[30] The presence of $P_3^BFeN_2^-$ was confirmed by freeze-quench EPR spectroscopy experiments (see SI). The asymmetry observed in the Mössbauer lineshapes is characteristic of this species. A redox equilibrium between $P_3^BFeN_2^{0/-}$ and $Cp^*_2Co^{+/0}$ is also observed in the reaction of $P_3^BFe^+$ with excess Cp^*_2Co in the absence of acid (see SI).

[31] The distinct properties of tetrahedral, high spin Fe(II) leads to high isomer shifts (0.9-1.3) and large quadrupole splittings (> 2.5) that are characteristic of these types of species: E. Münck, in *Physical Methods in Bioinorganic Chemistry: Spectroscopy and Magnetism* (Ed.: L. Que Jr.), University Science Books, Sausalito, CA, **2000**, pp. 287-320.

[32] Daifuku, S. L.; Kneebone, J. L.; Snyder, B. E. R.; Neidig, M. L. Iron(II) Active Species in Iron–Bisphosphine Catalyzed Kumada and Suzuki–Miyaura Cross-Couplings of Phenyl Nucleophiles and Secondary Alkyl Halides. *J. Am. Chem. Soc.* **2015**, *137*, 11432–11444.

[33] Hamashima, Y.; Somei, H.; Shimura, Y.; Tamura, T.; Sodeoka, M. Amine-Salt-Controlled, Catalytic Asymmetric Conjugate Addition of Various Amines and Asymmetric Protonation. *Org. Lett.* **2004**, *6*, 1861–1864.

[34] Zhao, Y.; Truhlar, D. G. A New Local Density Functional for Main-Group Thermochemistry, Transition Metal Bonding, Thermochemical Kinetics, and Noncovalent Interactions. *J. Chem, Phys.* **2006**, *125*, 194101: 1-18.

[35] Weigend, F.; Ahlrichs, R. Balanced Basis Sets of Split Valence, Triple Zeta Valence and Quadruple Zeta Valence Quality for H to Rn: Design and Assessment of Accuracy. *Phys. Chem. Chem. Phys.* **2005**, *7*, 3297–3305.

[36] Experimental $BDE_{N\text{-}H}$'s for related species ($P_3^{Si}Fe\text{-}C{=}NH^+$, $P_3^{Si}Fe\text{-}C{=}NH$, $P_3^{Si}Fe\text{-}C{=}N(Me)H^+$, $P_3^{Si}Fe\text{-}C{=}N(Me)H$, and $P_3^{Si}Fe\text{-}N{=}N(Me)H^+$) have been measured and are in good agreement with the $BDE_{N\text{-}H}$ values calculated using the DFT methods described in this work (see SI for full details): Rittle, J.; Peters, J. C. *manuscript submitted for publication.*

[37] Koelle, U.; Infelta, P. P.; Graetzel, M. Kinetics and Mechanism of the Reduction of Protons to Hydrogen by Cobaltocene. *Inorg. Chem.* **1988**, *27*, 879–883.

[38] Pitman, C. L.; Finster, O. N. L.; Miller, A. J. M. Cyclopentadiene-Mediated Hydride Transfer from Rhodium Complexes. *Chem. Commun.* **2016**, *52*, 9105–9108.

[39] Quintana, L. M. A.; Johnson, S. I.; Corona, S. L.; Villatoro, W.; Goddard, W. A.; Takase, M. K.; VanderVelde, D. G.; Winkler, J. R.; Gray, H. B.; Blakemore, J. D. Proton–hydride Tautomerism in Hydrogen Evolution Catalysis. *PNAS* **2016**, *113*, 6409–6414.

[40] Munisamy, T.; Schrock, R. R. An Electrochemical Investigation of Intermediates and Processes Involved in the Catalytic Reduction of Dinitrogen by [HIPTN$_3$N]Mo (HIPTN$_3$N = (3,5-(2,4,6-I-Pr$_3$C$_6$H$_2$)$_2$C$_6$H$_3$NCH$_2$CH$_2$)$_3$N). *Dalton Trans.* **2011**, *41*, 130–137.

[41] Efforts to instead optimize a metal hydride species, $[Cp^*_2Co\text{-}H]^+$, led to hydride transfer to the ring system. Nevertheless, reactive transition metal hydride radical cations are also known to exhibit PCET behavior.

[42] Hu, Y.; Shaw, A. P.; Estes, D. P.; Norton, J. R. Transition-Metal Hydride Radical Cations. *Chem. Rev.* **2016**, *116*, 8427–8462

[43] The dissolution equilibria and kinetics of the insoluble reagents used complicate analysis of the kinetics of individual ET, PT, and PCET steps. However, the low activation barriers ($G^{\ddagger} < 9$ kcal/mol) calculated for all proposed PCET reactions are consistent with these reactions being kinetically accessible (see SI for full details).

[44] Studies have shown that the Marcus cross-relation holds quite well for many PCET reactions. This is indicative of a substantial correlation between thermodynamic driving force and reaction kinetics; it is, however, unclear whether the proposed reactivity would demonstrate such behavior.

[45] Roth, J. P.; Yoder, J. C.; Won, T.-J.; Mayer, J. M. Application of the Marcus Cross Relation to Hydrogen Atom Transfer Reactions. *Science* **2001**, *294*, 2524–2526.

[46] Mayer, J. M.; Rhile, I. J. Thermodynamics and Kinetics of Proton-Coupled Electron Transfer: Stepwise vs. Concerted Pathways. *Biochimica et Biophysica Acta (BBA) - Bioenergetics* **2004**, *1655*, 51–58.

[47] Hammes-Schiffer, S. Theoretical Perspectives on Proton-Coupled Electron Transfer Reactions. *Acc. Chem. Res.* **2001**, *34*, 273-281.

[48] Studt, F.; Tuczek, F. Energetics and Mechanism of a Room-Temperature Catalytic Process for Ammonia Synthesis (Schrock Cycle): Comparison with Biological Nitrogen Fixation. *Angew. Chem. Int. Ed.* **2005**, *44*, 5639-5642.

[49] Reiher, M.; Le Guennic, B.; Kirchner, B. Theoretical Study of Catalytic Dinitrogen Reduction under Mild Conditions. *Inorg. Chem.* **2005**, *44*, 9640–9642.

[50] Studt, F.; Tuczek, F. Theoretical, Spectroscopic, and Mechanistic Studies on Transition-Metal Dinitrogen Complexes: Implications to Reactivity and Relevance to the Nitrogenase Problem. *J. Comput. Chem.* **2006**, *27*, 1278–1291.

[51] Thimm, W.; Gradert, C.; Broda, H.; Wennmohs, F.; Neese, F.; Tuczek, F. Free Reaction Enthalpy Profile of the Schrock Cycle Derived from Density Functional Theory Calculations on the Full [MoHIPTN$_3$N] Catalyst. *Inorg. Chem.* **2015**, *54*, 9248–9255.

[52] Yandulov, D. V.; Schrock, R. R. Studies Relevant to Catalytic Reduction of Dinitrogen to Ammonia by Molybdenum Triamidoamine Complexes. *Inorg. Chem.* **2005**, *44*, 1103–1117.

[53] Pappas, I.; Chirik, P. J. Catalytic Proton Coupled Electron Transfer from Metal Hydrides to Titanocene Amides, Hydrazides and Imides: Determination of Thermodynamic Parameters Relevant to Nitrogen Fixation. *J. Am. Chem. Soc.* **2016**, *138*, 13379–13389.

[54] Although our calculations for a hypothetical lutidinyl radical predict a weak N–H bond ($BDE_{N\text{-}H}$ ~ 35 kcal/mol), the oxidation potential of this species is calculated to be −1.89 V vs $Fc^{+/0}$ in THF (see SI). Experimental determination of this reduction potential for calibration has been contentious; however, our calculated reduction potential is similar to that previously calculated for pyridinium in aqueous media (−1.37 V vs SCE).

[55] Yan, Y.; Zeitler, E. L.; Gu, J.; Hu, Y.; Bocarsly, A. B. Electrochemistry of Aqueous Pyridinium: Exploration of a Key Aspect of Electrocatalytic Reduction of CO_2 to Methanol. *J. Am. Chem. Soc.* **2013**, *135*, 14020–14023.

[56] Keith, J. A.; Carter, E. A. Theoretical Insights into Pyridinium-Based Photoelectrocatalytic Reduction of CO_2. *J. Am. Chem. Soc.* **2012**, *134*, 7580–7583.

[57] It has been reported that [HIPTN$_3$N]MoN$_2^-$/[HIPTN$_3$N]Mo-N=NH is in equilibrium with DBU/DBUH$^+$ (DBU = 1,8-diazabicyclo[5.4.0]undec-7-ene; pK_a = 18.5 in THF; see refs 7c-d). Taken with the reported reduction potential of [HIPTN$_3$N]MoN$_2$ ($E_{1/2}$ = −1.81 V vs $Fc^{+/0}$ in THF, see ref 52), the experimental BDE can be approximated with the Bordwell equation and the enthalpy of reaction for $H^+ + e^- \rightarrow H^\cdot$ (see refs 15 and 19).

[58] In addition to lutidinium salts, $[Et_3NH][OTf]$ has been shown to affect the formation of $[HIPTN_3N]Mo\text{-}N{=}NH$ from $[HIPTN_3N]MoN_2$ in the presence of metallocene reductants (see ref 52).

Chapter 5

FE-MEDIATED NITROGEN FIXATION WITH A METALLOCENE MEDIATOR: EXPLORING PK_A EFFECTS AND DEMONSTRATING ELECTROCATALYSIS

Reproduced in part with permission from:

Chalkley, M.; Del Castillo, T.; Matson, B.; Peters, J. C.; *J. Am. Chem. Soc.*, **2018**, accepted.

DOI: 10.1021/jacs.8b02335

We've reached the final chapter of our tale. I'm afraid I don't have a particular message to accompany this project, perhaps it is still too fresh for me to have formed an impression of it. I'll relate here that, as I've alluded to, demonstrating electrocatalytic N_2RR was one of the very first targets I latched onto when I started my research with Jonas. The idea seemed optimistic (to say the least) at the time and even until almost the end of my fifth year I didn't think I would see this result in my time at Caltech. I suppose something can be said here for persistence in pursuing a goal, but probably the better message is that while it is important to work towards big, overarching targets it is also important to be open to things you discover along the way.

5.1 Introduction

There has been substantial recent progress in the development of soluble, well-defined molecular catalysts for N_2-to-NH_3 conversion, commonly referred to as the nitrogen

reduction reaction (N_2RR).[1] Nevertheless, a significant and unmet challenge is to develop molecular catalysts, and conditions, compatible with electrocatalytic N_2RR. Progress in this area could have both fundamental and practical benefits, including access to informative in situ mechanistic studies via electrochemical techniques, and an electrochemical means to translate solar or otherwise derived chemical currency (H^+/e^-) into NH_3. The latter goal, which has been the subject of numerous studies using heterogeneous catalysts, is key to the long-term delivery of new ammonia synthesis technologies for fertilizer and/or fuel.[2]

Many soluble coordination complexes are now known that electrocatalytically mediate the hydrogen evolution reaction (HER),[3] the carbon dioxide reduction reaction (CO_2RR),[4] and the oxygen reduction reaction (O_2RR).[5] The study of such systems has matured at a rapid pace in recent years, coinciding with expanded research efforts towards solar-derived fuel systems. In this context, it is noteworthy how little corresponding progress has been made towards the discovery of soluble molecular catalysts that mediate electrocatalytic N_2RR. To our knowledge, only two prior systems address this topic directly.[6,7,8]

More than three decades ago, Pickett and coworkers reported that a Chatt-type tungsten-hydrazido(2−) complex could be electrochemically reduced to release ammonia (and trace hydrazine), along with some amount of a reduced tungsten-dinitrogen product; the latter species serves as the source of the tungsten-hydrazido(2−) complex (via its protonation by acid).[6a] By cycling through such a process, an electrochemical, but not an electrocatalytic, synthesis of ammonia was demonstrated. Indeed, efforts to demonstrate electrocatalysis with this and related systems instead led to substoichiometric NH_3 yields.[6c]

An obvious limitation to progress in electrochemical N_2RR by molecular systems concerns the small number of synthetic N_2RR catalysts that have been available for study; it is only in the past five years that sufficiently robust catalyst systems have been identified to motivate such studies. In addition, the conditions that have to date been employed to mediate N_2RR have typically included non-polar solvents, such as heptane, toluene, and diethyl ether (Et_2O), that are not particularly well-suited to electrochemical studies owing to the lack of compatible electrolytes.[1]

Nevertheless, several recent developments, including ones from our lab, point to the likelihood that iron (and perhaps other) molecular coordination complexes may be able to mediate electrocatalytic N_2RR in organic solvent. Specifically, our lab recently reported that a tris(phosphine)borane iron complex, $P_3^BFe^+$, that is competent for catalytic N_2RR with chemical reductants, can also mediate electrolytic N_2-to-NH_3 conversion,[6d] with the available data (including that presented in this study) pointing to bona fide electrocatalysis in Et_2O.

Focusing on the $P_3^BFe^+$ catalytic N_2RR system, a development germane to the present study was its recently discovered compatibility with reagents milder than those that had been originally employed.[1c] Thus, decamethylcobaltocene (Cp^*_2Co) and diphenylammonium acid are effective for N_2RR catalysis; these reagents give rise to fast, and also quite selective (> 70% vs HER), N_2RR catalysis at low temperature and pressure in ethereal solvent. In addition, based on preliminary spectroscopic evidence and density functional theory (DFT) predictions, it appears that a protonated metallocene species, $Cp^*(\eta^4\text{-}C_5Me_5H)Co^+$, may be an important intermediate of N_2RR catalysis under such conditions. Indeed, we have suggested that $Cp^*(\eta^4\text{-}C_5Me_5H)Co^+$ may serve as a proton-

coupled-electron-transfer (PCET) donor ($BDE_{C–H}$(calc) = 31 kcal mol^{-1}), thereby mediating net H-atom transfers to generate N–H bonds during N_2RR.[9] The presence of a metallocene mediator might, we therefore reasoned, enhance N_2RR during electrocatalysis.

We present here a study of the effect of pK_a on the selectivity of $P_3^BFe^+$ for N_2RR vs HER. By using substituted anilinium acids, we are able to vary the acid pK_a over 9 orders of magnitude and find that the selectivity is highly correlated with the pK_a. In our efforts to investigate the origin of the observed pK_a effect, we found, to our surprise, that in stoichiometric reactions, the catalytically competent anilinium triflate acids are unable to faciltate productive N–H bond formation with early-stage N_2-fixation intermediates. We therefore hypothesize that the formation of a protonated metallocene species, Cp*(η^4-C_5Me_5H)Co^+, plays a critical role in N–H bond-forming reactions, either via PCET, PT, or a combination of both during N_2RR catalysis. DFT studies support this hypothesis and also establish that the observed pK_a correlation with N_2RR selectivity can be explained by the varying ability of the acids to protonate Cp^*_2Co. The suggested role of this protonated metallocene intermediate in N–H bond forming reactions led us to test the effect of $Cp^*_2Co^+$ as an additive in the electrolytic synthesis of NH_3 mediated by $P_3^BFe^+$. We find that the addition of co-catalytic $Cp^*_2Co^+$ enhances the yield of NH_3 without decreasing the Faradaic efficiency (FE), and furnishes what is to our knowledge the first unambiguous demonstration of electrocatalytic N_2RR mediated by a soluble, molecular coordination complex.

5.2 Results and Discussion

5.2.1 pK_a Studies.

In our recent study on the ability of $P_3^BFe^+$ to perform N_2RR with Cp^*_2Co as the chemical reductant,[9] we found that there was a marked difference in efficiency for NH_3 generation with diphenylammonium triflate ([Ph_2NH_2][OTf]) versus anilinium triflate ([$PhNH_3$][OTf]). In that study, we posited that this difference could arise from several possibilities, including the differential solubility, sterics, or pK_a's of these acids.[9]

To investigate the last possibility, we have studied the efficiency of the catalysis by quantifying the NH_3 and H_2 produced when using substituted anilinium acids with different pK_a values (Table 5.1). The table is organized in increasing acid strength, from [$^{4\text{-}OMe}$PhNH$_3$][OTf] as the weakest acid to the perchlorinated derivative ([$^{per\text{-}Cl}$PhNH$_3$][OTf]) as the strongest. Importantly, good total electron yields (85.8 ± 3.3) were obtained in all cases. As can be seen from the table, the NH_3 efficiencies are found to be strongly correlated with pK_a.[10]

In particular, a comparison of the efficiency for NH_3 with the pK_a of the anilinium acid used gives rise to four distinct activity regimes (Table 5.1, Figure 5.1). One regime that is completely inactive for N_2RR, but active for HER, is defined by the weakest acid, [$^{4\text{-}OMe}$PhNH$_3$][OTf] (pK_a = 8.8).[11] A gradual increase in observed NH_3 yields, coupled with a decrease in H_2 yield, comprises a second regime, in which the acid is strengthened from [$PhNH_3$][OTf] (pK_a = 7.8), to [$^{2,6\text{-}Me}$PhNH$_3$][OTf] (pK_a = 6.8), to [$^{2\text{-}Cl}$PhNH$_3$][OTf] (pK_a = 5.6). Yet stronger acids, [$^{2,5\text{-}Cl}$PhNH$_3$][OTf] (pK_a = 4.3), [$^{2,6\text{-}Cl}$PhNH$_3$][OTf] (pK_a = 3.4), and [$^{2,4,6\text{-}Cl}$PhNH$_3$][OTf] (pK_a = 2.1), constitute another, most active N_2RR regime, one in which the H_2 yields are nearly invariant.[12] The highest selectivity for N_2RR (~ 78%) was observed

using [$^{2,5\text{-Cl}}$PhNH$_3$][OTf] as the acid. A final regime of very low N_2RR activity is encountered with [$^{\text{per-Cl}}$PhNH$_3$][OTf] (pK_a = 1.3) as the acid. We suspect this last acid undergoes unproductive

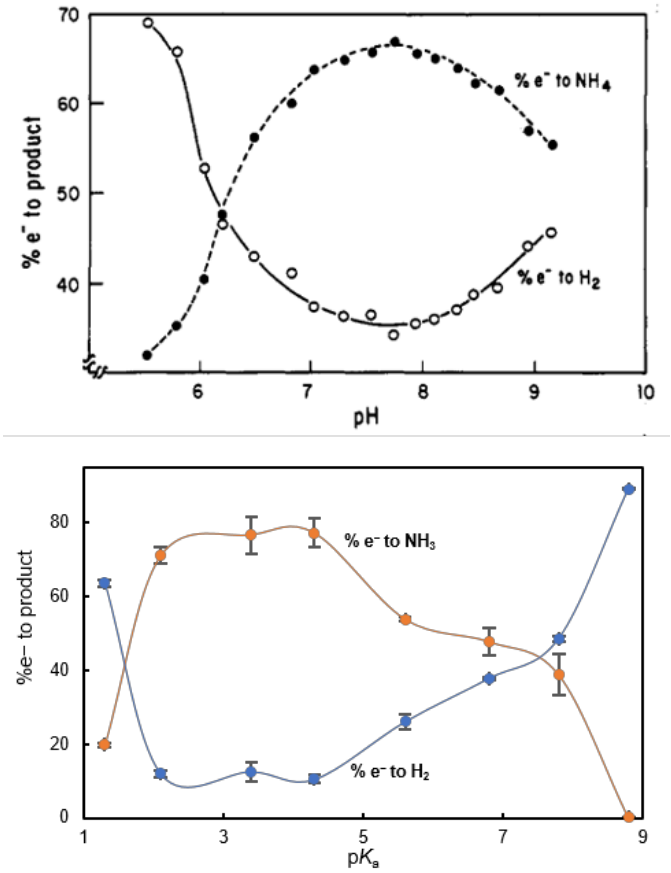

Figure 5.1. (top) Percentage of electrons being used to form NH_3 or H_2 at different pH values by the FeMo-nitrogenase in *A. vinelandii*. Reprinted with permission from Pham, D. N.; Burgess, B. K. *Biochemistry* **1993**, *32*, 13725. Copyright 1993 American Chemical Society. (bottom) Percentage of electrons being used to form NH_3 or H_2 at different pK_a values by $P_3{}^{B}Fe^{+}$.

Table 5.1. Literature and calculated pK_a values and efficiencies observed in catalytic N_2-to-NH_3 conversion

	pK_a^{exp} (THF)[10]	pK_a^{calc} (298 K)[a]	pK_d^{calc} (195 K)[b]	Equiv of NH_3/Fe	% yield of NH_3/e^-	% yield of H_2/e^-[c]
$[^{4\text{-OMe}}PhNH_3][OTf]$	8.8	9.6	15.7	0.04 ± 0.01	0.2 ± 0.1	89.1 ± 0.2
$[PhNH_3][OTf]$	7.8	7.7	13.8	7.3 ± 0.1	40.4 ± 0.5	48.6 ± 0.7
$[^{2,6\text{-Me}}PhNH_3][OTf]$	6.8	7.3	13.2	8.6 ± 0.7	47.5 ± 4.0	37.8 ± 0.2
[Cp*(*exo*-η^4-C_5Me_5H)Co][OTf]	N/A	9.2	11.8	—	—	—
$[^{2\text{-Cl}}PhNH_3][OTf]$	5.6	5.6	6.0	10.7 ± 0.1	53.9 ± 0.4	26.1 ± 1.9
$[^{2,5\text{-Cl}}PhNH_3][OTf]$	4.3	4.0	5.0	13.9 ± 0.7	77.5 ± 3.8	10.5 ± 1.1
$[^{2,6\text{-Cl}}PhNH_3][OTf]$	3.4	3.4	3.4	13.8 ± 0 .9	76.7 ± 4.9	12.6 ± 2.5
$[^{2,4,6\text{-cl}}PhNH_3][OTf]$	2.1	2.7	1.8	12.8 ± 0.4	70.9 ± 2.2	12.0 ± 0.8
$[^{\text{per-Cl}}PhNH_3][OTf]$	1.3	0.8	0.4	3.6 ± 0.1	19.9 ± 0.5	63.5 ± 1.1

$[^{4\text{-OMe}}PhNH_3][OTf]$ = 4-methoxyanilinium triflate, $[PhNH_3][OTf]$ = anilinium triflate, $[^{2,6\text{-Me}}PhNH_3][OTf]$ = 2,6-dimethylanilinium triflate, $[^{2\text{-Cl}}PhNH_3][OTf]$ = 2-chloroanilinium triflate, $[^{2,5\text{-Cl}}PhNH_3][OTf]$ = 2,5-dichloroanilinium triflate, $[^{2,6\text{-Cl}}PhNH_3][OTf]$ = 2,6-dichloroanilinium triflate, $[^{2,4,6\text{-Cl}}PhNH_3][OTf]$ = 2,4,6-trichloroanilinium triflate, $[^{\text{per-Cl}}PhNH_3][OTf]$ = 2,3,4,5,6-pentachloroanilinium triflate. [a]Acidities calculated at 298 K in THF and referenced to the known literature value for $[^{2,6\text{-Cl}}PhNH_3][OTf]$. [b] All species calculated as the ion-paired OTf^- species in Et_2O at 195 K and referenced to the known literature value for $[^{2,6\text{-Cl}}PhNH_3][OTf]$ in THF.

reduction via ET, thereby short-circuiting N_2RR. The only other N_2RR system for which this type of acid-dependent correlation has been systematically studied is the enzyme MoFe-nitrogenase.[13,14] As shown in Figure 5.1, the N_2RR vs HER activity of $P_3^BFe^+$ as a function of acid strength, is, in broad terms, similar to the behavior of the enzyme[13] across a wide pH range.

In a previous study of Cp^*_2Co-mediated N_2RR by $P_3^BFe^+$,[9] we identified that $P_3^BFeN_2^-$ forms under the catalytic conditions. Earlier studies on the reactivity of $P_3^BFeN_2^-$ with an excess of soluble acids, including HOTf and $[H(OEt_2)_2][BAr^F_4]$ ($HBAr^F_4$, BAr^F_4 = tetrakis(3,5- bis(trifluoromethyl)phenyl)borate)), at −78 °C in Et_2O, established rapid formation of the doubly protonated species, $P_3^BFeNNH_2^+$.[15] Recent computational work from our group suggests that, under catalytic conditions with a soluble acid, different efficiencies for N_2RR (versus HER) by P_3^EFe catalysts (E = B, C, Si) are likely correlated to the rate of formation and consumption of early N_2RR intermediates (i.e., P_3^EFeNNH and $P_3^EFeNNH_2^{+/0}$).[16] Thus, we were interested in the reactivity of these anilinium triflate acids with $P_3^BFeN_2^-$, reasoning they may show differential efficiency in the formation of $P_3^BFeNNH_2^+$.

To our surprise, a freeze-quench EPR spectrum of the reaction of excess $[^{2,6\text{-}Cl}PhNH_3][OTf]$ (high N_2RR efficiency regime) at −78 °C in Et_2O with $P_3^BFeN_2^-$ does not show any $P_3^BFeNNH_2^+$. Also, freeze-quench Mössbauer analysis shows the formation of the oxidized products $P_3^BFeN_2$ and $P_3^BFe^+$, but nothing assignable to $P_3^BFeNNH_2^+$ (see SI for relevant spectra). Analysis of such a reaction for NH_3 or N_2H_4 after warming shows no fixed-N products. The observation of exclusive oxidation, rather than productive N–H bond formation, is analogous to what is observed upon addition of 1 equiv of a soluble acid

(HBAr$^{F}_{4}$ or HOTf) to $P_3^BFeN_2^-$. We have previously suggested that if unstable P_3^BFeNNH is formed (eq 1) without excess acid to trap it (to form more stable $P_3^BFeNNH_2^+$, eq 2), then it can decay bimolecularly with the loss of 1/2 H_2 to form $P_3^BFeN_2$ (eq 3).

$$P_3^BFeN_2^- + H^+ \rightarrow P_3^BFeNNH \quad (1)$$

$$P_3^BFeNNH + H^+ \rightarrow P_3^BFeNNH_2^+ \quad (2)$$

$$P_3^BFeNNH \rightarrow P_3^BFeN_2 + 1/2\ H_2 \quad (3)$$

The low solubility of the anilinium triflate acids studied herein, in excess (50 equiv) and under the catalytically relevant conditions (1 mL Et_2O, −78 °C), likely leads to a similar scenario; consequently, P_3^BFeNNH that is generated is not efficiently captured by excess acid, leading instead to bimolecular H_2 loss. In accord with this idea, a freeze-quench EPR spectrum of the addition of 50 equiv of [$^{2,6\text{-Cl}}PhNH_3$][BAr$^{F}_{4}$], a far more ether soluble derivative of the same anilinium, to $P_3^BFeN_2^-$ shows $P_3^BFeNNH_2^+$ formation, and the detection of fixed-N products upon warming (0.20 ± 0.04 eq. NH_3 per Fe).

These observations must next be reconciled with the seemingly contradictory observation that comparatively efficient N_2RR catalysis is observed when [$^{2,6\text{-Cl}}PhNH_3$][OTf], and other anilinium triflate acids, are employed under catalytic conditions. For example, [Ph_2NH_2][OTf] leads to better efficiency for NH_3 formation versus [Ph_2NH_2][BAr$^{F}_{4}$] (72 ± 3% and 42 ± 6%, respectively). A key difference between the stoichiometric reactions described above, and the catalytic reaction, is the presence of Cp^*_2Co in the latter.

We have suggested that Cp^*_2Co can be protonated under the catalytic reaction conditions, to form $Cp^*(\eta^4\text{-}C_5Me_5H)Co^+$,[9] which may then play a role in N–H bond forming steps.[17] The results presented here (and below) suggest that such a mechanism is

not only plausible, but is likely necessary, to explain the observed catalytic results with anilinium triflate acids. Given the effect of pK_a on the efficiency for N_2RR, we now hypothesize that this effect can arise from the relative energetics and rates of Cp*$_2$Co protonation by the different anilinium triflate acids.

5.2.2 Computational Studies.

To investigate the kinetics and thermodynamics of Cp*$_2$Co protonation by anilinium triflate acids we turned to a computational study. DFT-D$_3$[18] calculations were undertaken at the TPSS/def2-TZVP(Fe); def2-SVP[19] level of theory, as used previously for studies of this $P_3^BFe^+$ system.[20] The free energy of H^+ exchange (ΔG_a) was calculated for all of the anilinium acids used (representative example shown in eq 4), and also for Cp*(*exo*-η^4-C_5Me_5H)Co^+, in Et_2O at 298 K. These free energies were then used to determine the acid pK_a's, with inclusion of a term to reference them to the literature pK_a value for [$^{2,6\text{-Cl}}$PhNH$_3$][OTf] at 298 K in THF (eq 5).

$$PhNH_2 + {}^{2,6\text{-Cl}}PhNH_3^+ \rightarrow PhNH_3^+ + {}^{2,6\text{-Cl}}PhNH_2 \quad (4)$$

$$pK_a(PhNH_3^+) = -\Delta G_a/(2.303\times RT) + pK_a({}^{2,6\text{-Cl}}PhNH_3^+) \quad (5)$$

Because we presume that variable triflate hydrogen bonding effects (0.5-10 kcal mol^{-1}) are likely to be important under the catalytic conditions (low temperature and low polarity solvent), we additionally calculated the free energy for net HOTf exchange reactions (ΔG_d) at 195 K in Et_2O (representative example shown in eq 6). The free energies of these reactions can then be used to determine a pK_d, referenced to the pK_a value for [$^{2,6\text{-Cl}}$PhNH$_3$][OTf] at 298 K in THF, for ease of comparison (eq 7). Hereafter, we use these pK_d values for discussion, but note that use of the pK_a values instead does not substantively alter the conclusions drawn.

$PhNH_2 + [^{2,6\text{-}Cl}PhNH_3][OTf] \rightarrow$

$[PhNH_3][OTf] + {}^{2,6\text{-}Cl}PhNH_2$ (6)

$pK_d([PhNH_3][OTf]) = -\Delta G_d/(2.303\times RT) + pK_a(^{2,6\text{-}Cl}PhNH_3^+)$ (7)

Calculations of the pK_d of all of the relevant species (Table 5.1) shows that the pK_d of [Cp*(*exo*-η^4-C_5Me_5H)Co][OTf] (pK_d^{calc} = 11.8; Table 5.1) falls within the range of the anilinium acids studied ($0.4 \leq pK_d^{calc} \leq 15.7$), suggesting there should be a significant acid dependence on the kinetics and thermodynamics of Cp^*_2Co protonation. To better elucidate the differences in Cp^*_2Co protonation between the acids studied, we investigated the kinetics of protonation for three acids, $[^{2,6\text{-}Cl}PhNH_3][OTf]$ (high selectivity; pK_d^{calc} = 3.4), $[^{2,6\text{-}Me}PhNH_3][OTf]$ (modest selectivity; pK_d^{calc} = 13.2), and $[^{4\text{-}OMe}PhNH_3][OTf]$ (poor selectivity; pK_d^{calc} = 15.8).

Transition states for Cp^*_2Co protonation were located for all three acids. To confirm that these transition states accurately reflect proton transfer, internal reaction coordinates (IRC) were followed to determine the reactant (IRC-A) and product (IRC-B) minima (Figure 5.2). These minima represent hydrogen bonded arrangements of the reactants and products. Protonation is found to have only a moderate barrier ($\Delta G^{\ddagger}$ in kcal mol^{-1}) in all three cases: ($[^{4\text{-}OMe}PhNH_3][OTf]$, +4.5; $[^{2,6\text{-}\ Me}PhNH_3][OTf]$, +3.8; $[^{2,6\text{-}Cl}PhNH_3][OTf]$, +1.3).

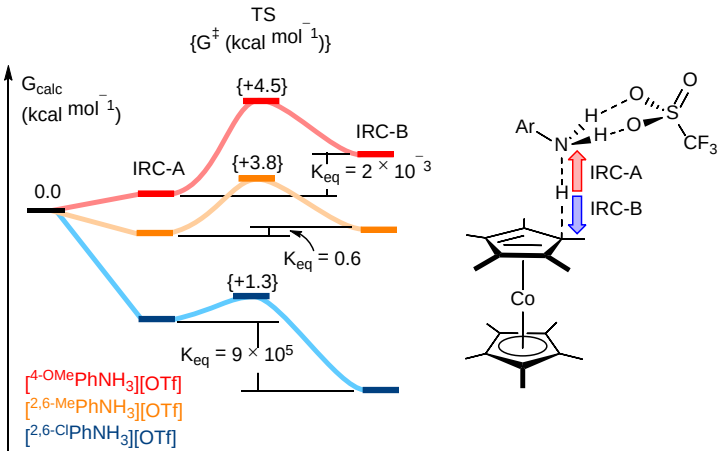

Figure 5.2. The kinetics and thermodynamics of protonation of Cp*$_2$Co for three acids from different catalytic efficiency regimes ([$^{4\text{-OMe}}$PhNH$_3$][OTf] = poor selectivity]; [$^{2,6\text{-Me}}$PhNH$_3$][OTf] = modest selectivity; [$^{2,6\text{-Cl}}$PhNH$_3$][OTf] = high selectivity).

This suggests that Cp*$_2$Co protonation is kinetically accessible in all cases, in agreement with the experimental observation of background HER with each of these acids (see SI).

The small differences in rate, and the large variance in the equilibrium constant K_{eq} defined in eq 8, points to a significant difference in the population of protonated metallocene, [Cp*(*exo*-η^4-C$_5$Me$_5$H)Co][OTf], for these anilinium acids during catalysis.

$$K_{eq} = \frac{[{}^{R}PhNH_2\text{–}Cp^{*}(exo\text{–}\eta^4\text{–}C_5Me_5H)Co^{+}]}{[{}^{R}PhNH_3^{+}\text{–}Cp^{*}_2Co]} \quad (8)$$

We reason that the low solubility of the anilinium triflate acids, and the low catalyst concentration (2.3 mM P$_3^B$Fe), leads to a scenario in which the interaction between the acid and the Cp*$_2$Co, the latter being present in excess relative to the iron catalyst (measured solubility of Cp*$_2$Co at −78 °C in Et$_2$O is ~ 6 mM, see SI), significantly affects the overall kinetics of productive N–H bond formation. As such, the difference in [Cp*(*exo*-η^4-C$_5$Me$_5$H)Co][OTf] concentration and formation rate should relate to, and likely dominate,

the origin of the observed pK_a effect. This explanation, rather than one that involves differences in rates for the direct interaction of a given $P_3^BFeN_xH_y$ species with an anilinium acid, better captures the collected data available.[21]

[Cp*(*exo*-η^4-C_5Me_5H)Co][OTf], characterized by a very weak C–H bond, should be a strong PCET donor, and we presume it serves such a role under the catalytic conditions being discussed herein.[22] Its reactions with $P_3^BFeN_xH_y$ intermediates may occur in a synchronous fashion, akin to HAT, or in an asynchronous fashion more akin to a PT-ET reaction.[23] While many $P_3^BFeN_xH_y$ intermediates may, at least in part, be generated via PCET with [Cp*(*exo*-η^4-C_5Me_5H)Co][OTf],[24] available experimental data point to a critical role for such a reaction via trapping of the highly reactive first fixed intermediate, P_3^BFeNNH (**Figure 5.3**), before it can bimolecularly release H_2 (eq 3). We hence investigated this reaction in more detail.

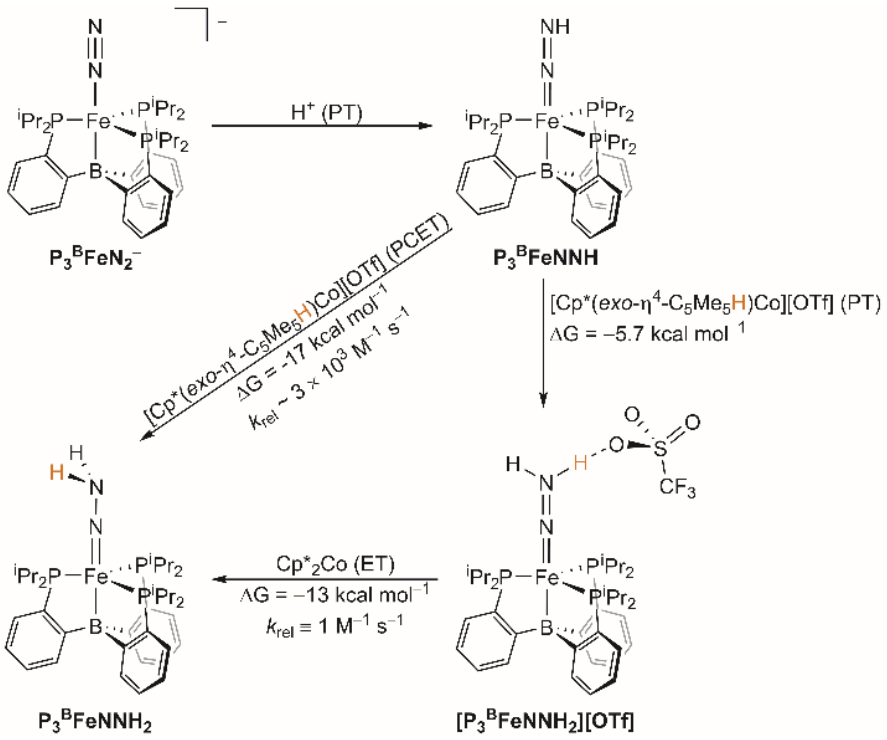

Figure 5.3. The calculated thermodynamics and kinetics of synchronous PCET and asynchronous PCET (PT-ET), between P_3^BFeNNH and [Cp*(*exo*-η^4-C_5Me_5H)Co][OTf] to generate $P_3^BFeNNH_2$. Note: k_{rel} for ET is defined as 1 M^{-1} s^{-1}.

Both a synchronous PCET (ΔG_{PCET} = −17.3 kcal mol^{-1}; eq 9) and an asynchronous PCET path (ΔG_{PT} = −5.7 kcal mol^{-1}, ΔG_{ET} = −11.6 kcal mol^{-1}; eq 10 and 11), are predicted to be thermodynamically favorable.

P_3^BFeNNH + [Cp*(*exo*-η^4-C_5Me_5H)Co][OTf] →

$P_3^BFeNNH_2$ + [Cp*$_2$Co][OTf] (9)

P_3^BFeNNH + [Cp*(*exo*-η^4-C_5Me_5H)Co][OTf] →

[$P_3^BFeNNH_2$][OTf] + Cp*$_2$Co (10)

[$P_3^BFeNNH_2$][OTf] + Cp*$_2$Co →

$P_3^BFeNNH_2$ + [Cp*$_2$Co][OTf] (11)

To evaluate the kinetics of these reactions the Marcus theory expressions[25] and the Hammes-Schiffer method[26] were used to approximate relative rates of bimolecular ET and PCET. We find that there is a slight kinetic preference for the fully synchronous PCET reaction ($k_{rel}^{PCET} \sim 3 \times 10^3\ M^{-1}s^{-1}$) compared to the fully asynchronous PT-ET reaction ($k_{rel}^{PT\text{-}ET} \approx k_{rel}^{ET} \equiv 1\ M^{-1}\ s^{-1}$; Figure 5.3).[27]

The above discussion leads to the conclusion that the efficiency for NH_3 formation in this system is coupled to the kinetics and/or thermodynamics of the reaction between the anilinium triflate acid and the Cp^*_2Co reductant. This conclusion is counterintuitive, as the protonation of Cp^*_2Co is also the requisite first step for background HER.[28] The fact that a key HER intermediate can be intercepted and used for productive N_2RR steps is an important design principle for such catalysis. Similar design strategies are currently being used to repurpose molecular cobalt HER catalysts for the reduction of unsaturated substrates.[29]

Efforts are often undertaken to suppress background reactivity between acid and reductant in catalytic N_2RR systems.[1a-b] We were hence particularly interested to explore whether the inclusion of a metallocene co-catalyst, in this case Cp^*_2Co, might improve the yield, and/or the Faradaic efficiency (FE), for N_2RR versus HER, in controlled potential electrolysis (CPE) experiments with $P_3^BFe^+$ under N_2.

5.2.3 Electrolysis Studies.

To set the context for this section of the present study, we had shown previously that ~ 2.2 equiv NH_3 (per Fe) could be generated via controlled potential electrolysis (CPE; −2.3 V vs $Fc^{+/0}$) at a reticulated vitreous carbon working electrode, using $P_3^BFe^+$ as the (pre)catalyst in the presence of $HBAr^F_4$ (50 equiv) at −45 °C under an atmosphere of N_2.

This yield of NH_3 corresponded to a ~ 25% FE which, while modest in terms of overall chemoselectivity, compares very favorably to FE's most typically reported for heterogeneous electrocatalysts for N_2RR that operate below 100 °C (< 2%).[2,30]

To further explore the possibility of using $P_3^BFe^+$ as an electrocatalyst for N_2RR, various conditions were surveyed to determine whether enhanced yields of NH_3 could be obtained from CPE experiments. For example, various applied potentials were studied (ranging from −2.1 to −3.0 V vs $Fc^{+/0}$), the concentrations of $P_3^BFe^+$ and $HBAr^F_4$ were varied, the ratio of acid to catalyst was varied, and the rate at which acid was delivered to the system was varied (e.g., initial full loadings, batch-wise additions, reloadings, or continuous slow additions). None of these studies led to substantial improvement in N_2RR; in all cases, < 2.5 equiv of NH_3 was obtained per $P_3^BFe^+$. Attempts to vary the ratio of the electrode surface area to the working compartment solution volume, either by employing smaller cell geometries or by using different morphologies of glassy carbon as the working electrode (e.g., reticulated porous materials of different pore density or plates of different dimensions), also failed to provide substantial improvement in NH_3 yield. The replacement of $HBAr^F_4$, the original acid used in our electrolysis studies,[6d] by 50 equiv of $[Ph_2NH_2][OTf]$ led to similar yields of NH_3 (Table 5.2, entry 1).

We next investigated the effect of $Cp^*_2Co^+$ as an additive on the electrolysis/electrocatalysis. Traces of relevant cyclic voltammograms (Figure 5.4A and 5.4B) collected with glassy carbon as the working electrode in Et_2O under glovebox atmosphere N_2 at −35 °C are provided. Background traces including only $[Ph_2NH_2][OTf]$ are present in both panels (gray traces). $Cp^*_2Co^+$ (panel A, yellow trace), $Cp^*_2Co^+$ with the addition of ten equiv of $[Ph_2NH_2][OTf]$ (panel A, green trace), $P_3^BFe^+$ (panel B, dark blue

trace), $P_3^BFe^+$ with the addition of ten equiv of $[Ph_2NH_2][OTf]$ (panel B, light blue trace), and $P_3^BFe^+$ with the addition of one equiv of $Cp^*_2Co^+$ and ten equiv of $[Ph_2NH_2][OTf]$ (both panels, red trace).

Table 5.2. Yields and Faradaic Efficiencies of NH_3 from CPE Experiments with $P_3^BFe^+$

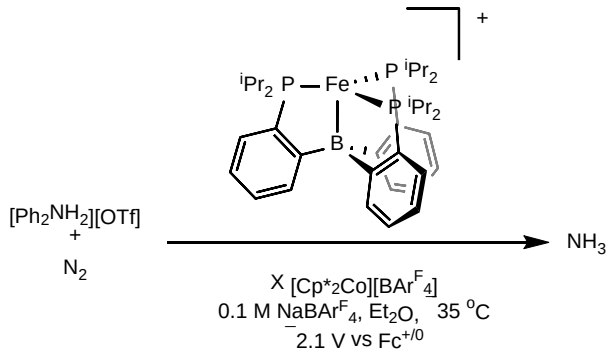

Entry	Equiv $Cp^*_2Co^+$	Equiv NH_3 (per Fe)	Equiv NH_3 (per Co)	NH_3 FE (%)
1	0	2.6 ± 0.3[d]	—	24 ± 5
2[a]	0	2.6 ± 0.6	—	18 ± 1
3	1	4.0 ± 0.6	4.0 ± 0.6	28 ± 5
4	5	4.0 ± 0.6[d]	0.8 ± 0.1	25 ± 3
5[a]	5	5.5 ± 0.9[e]	1.1 ± 0.2	19 ± 1
6	10	4 ± 1	0.4 ± 0.1	24 ± 7
7[b]	5	1.9 ± 0.2	0.4 ± 0.1	10 ± 1
8[c]	5	0.9 ± 0.4	0.2 ± 0.1	6 ± 3

All CPE experiments conducted at −2.1 V vs $Fc^{+/0}$ with 0.1 M $NaBAr^F_4$ in Et_2O as solvent at −35 °C under an N_2 atmosphere, featuring a glassy carbon plate working electrode, $Ag^{+/0}$ reference couple isolated by a CoralPor™ frit referenced externally to $Fc^{+/0}$, and a solid sodium auxiliary electrode. Working and auxiliary chambers separated by a sintered glass frit. See SI for further experimental details, controls, and additional data. Averages represent two runs unless noted. [a]After initial electrolysis with 50 equiv $[Ph_2NH_2][OTf]$, an additional 50 equiv $[Ph_2NH_2][OTf]$ in 0.1 M $NaBAr^F_4$ Et_2O solution

was added to the working chamber, via syringe through a rubber septum, followed by additional CPE at −2.1 V vs $Fc^{+/0}$. The listed Equiv NH_3 (per Fe) for these runs is the total yield after both electrolysis experiments are completed. [b]$[^{2,6\text{-Cl}}PhNH_3][OTf]$ employed as the acid. [c]$[PhNH_3][OTf]$ employed as the acid. [d]Average of three runs. [e]Average of five runs.

The cyclic voltammogram of $Cp^*_2Co^+$ is shown in panel **A** (yellow trace), displaying the reversible $Cp^*_2Co^{+/0}$ couple at −2.0 V. The addition of $[Ph_2NH_2][OTf]$ to $Cp^*_2Co^+$ causes an increase in current at this potential, consistent with HER

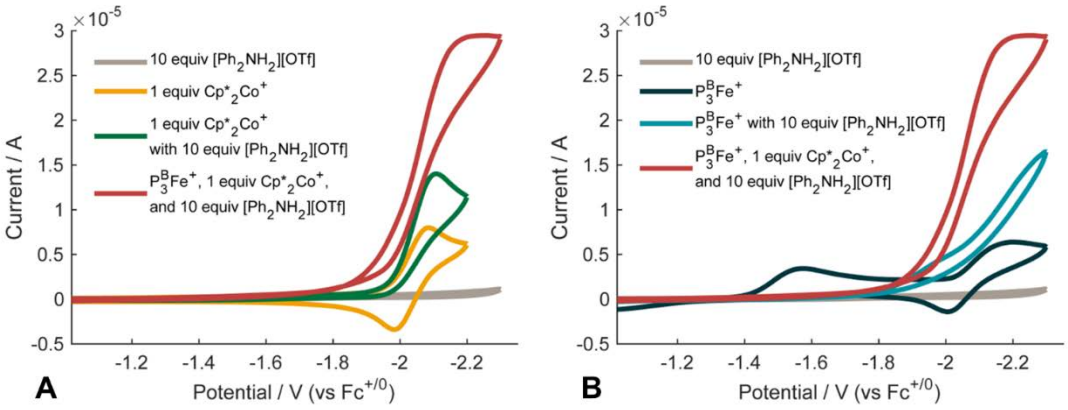

Figure 5.4. A) Cyclic voltammograms of 10 equiv $[Ph_2NH_2][OTf]$ (gray trace), 1 equiv $[Cp^*_2Co][BAr^F_4]$ ($Cp^*_2Co^+$) (yellow trace), 1 equiv $Cp^*_2Co^+$ with 10 equiv $[Ph_2NH_2][OTf]$ (green trace), and $P_3{}^BFe^+$ with 1 equiv of $Cp^*_2Co^+$ and 10 equiv $[Ph_2NH_2][OTf]$ (red trace). **B**) Cyclic voltammograms of 10 equiv $[Ph_2NH_2][OTf]$ (gray trace), $P_3{}^BFe^+$ (dark blue trace), $P_3{}^BFe^+$ with 10 equiv $[Ph_2NH_2][OTf]$ (light blue trace), and $P_3{}^BFe^+$ with 1 equiv of $Cp^*_2Co^+$ and 10 equiv $[Ph_2NH_2][OTf]$ (red trace). All spectra are collected in 0.1 M $NaBAr^F_4$ solution in Et_2O at −35 °C using a glassy carbon working electrode, and externally referenced to the $Fc^{+/0}$ couple. Scan rate is 100 mV/s.

catalyzed by $Cp^*_2Co^+$ (panel **A**, green trace).

Panel B provides the cyclic voltammogram of $P_3^BFe^+$ in the absence (dark blue trace, showing previously assigned and quasi-reversible $P_3^BFeN_2^{0/-}$ couple at ~ −2.1 V) and in the presence (light blue trace) of $[Ph_2NH_2][OTf]$.[31] The latter is indicative of modest HER and N_2RR. Also evident upon the addition of acid is the disappearance of a wave corresponding to the $P_3^BFe^{+/0}$ couple at ~ −1.6 V. This wave, in the absence of acid, is broad and shows a large peak-to-peak separation, likely due to the presence of both $P_3^BFe^+$ and $P_3^BFeN_2^+$ in solution at −35 °C. The addition of a large excess of $[Ph_2NH_2][OTf]$ presumably results in triflate binding (to generate P_3^BFeOTf, thereby attenuating the waves associated with the reduction of $P_3^BFe^+$ and $P_3^BFeN_2^+$). The red trace of Panel A is reproduced in Panel B to illustrate the marked increase in current observed when $Cp^*_2Co^+$ is added.

CPE studies were undertaken to characterize the reduction products associated with the red trace at ~ −2.1 V vs $Fc^{+/0}$. These studies employed a glassy carbon plate electrode, a $Ag^{+/0}$ reference electrode that was isolated by a CoralPor™ frit and referenced externally $Fc^{+/0}$ redox couple, and a solid sodium auxiliary electrode. The latter was used to avoid excessive, non-productive redox cycling between the working and auxiliary chambers.[32] Unless otherwise noted, CPE experiments were performed at −2.1 V versus $Fc^{+/0}$, with 0.1 M $NaBAr^F_4$ as the ether-soluble electrolyte, under a glovebox N_2 atmosphere at −35 °C. The electrolysis was continued until the current had dropped to 1% of the initial current measured, or until 21.5 hours had passed. The Supporting Information provides additional details.

CPE experiments were conducted with the inclusion of 0, 1, 5, and 10 equiv of $Cp^*_2Co^+$ with respect to $P_3^BFe^+$, using excess $[Ph_2NH_2][OTf]$ as the acid. In the absence of added $Cp^*_2Co^+$, a significant amount of NH_3 was generated (2.6 ± 0.3 equiv per Fe, entry 1), consistent with the previous finding that, in the presence of a strong acid, $P_3^BFe^+$ can electrolytically mediate N_2-to-NH_3 conversion.[6d] Notably, when a CPE experiment that did not include $Cp^*_2Co^+$ was reloaded with additional acid after electrolysis and electrolyzed again, the total yield of NH_3 (2.6 ± 0.6 equiv NH_3 per Fe, entry 2) did not improve.

We found that inclusion of 1.0 equiv of $Cp^*_2Co^+$ enhanced the NH_3 yield, by a factor of ~ 1.5 (Table 5.2, entry 3) without decreasing the FE. The data provide a total yield, with respect to both Fe and Co, that confirm modest, but still unequivocal, N_2RR electrocatalysis. In single run experiments, the highest NH_3 yield in the absence of $Cp^*_2Co^+$ was 2.8 equiv, compared with 4.4 equiv in the presence of 1 equiv of $Cp^*_2Co^+$. Conversely, the lowest single run NH_3 yield in the absence of $Cp^*_2Co^+$ was 2.3 equiv, compared with 3.5 equiv in the presence of 1 equiv of $Cp^*_2Co^+$.

Increasing the amount of added $Cp^*_2Co^+$ did not affect the NH_3 yield (entry 4). However, the addition of a second loading of $[Ph_2NH_2][OTf]$ following the first electrolysis (entry 5), followed by additional electrolysis, led to an improved yield of NH_3, suggesting that some active catalyst is still present after the first run.[6d,9] Even higher $Cp^*_2Co^+$ loading did not lead to higher NH_3 yields (entry 6).

CPE of $P_3^BFe^+$ in the presence of $Cp^*_2Co^+$ was also explored with other acids. Replacing $[Ph_2NH_2][OTf]$ in these experiments with $[^{2,6\text{-}Cl}PhNH_3][OTf]$ led to lower yields of NH_3, and with $[PhNH_3][OTf]$ even lower yields of NH_3 were observed (entries 7 and 8 respectively). The lower, but nonzero, yield of NH_3 provided by $[PhNH_3][OTf]$ in these

CPE experiments is consistent with chemical trials employing various acids (vide supra) and can be rationalized by the relative pK_a of the acids (Table 5.1). The intermediate yield of NH_3 provided by [$^{2,6\text{-Cl}}$PhNH$_3$][OTf] in these CPE experiments is less consistent with simple pK_a considerations, suggesting that additional factors are at play, perhaps including the relative stability of the acid or conjugate base to electrolysis.

To probe whether electrode-immobilized iron might contribute to the N_2RR electrocatalysis, X-ray photoelectron spectroscopy (XPS) was used to study the electrode. After a standard CPE experiment with $P_3^BFe^+$, 5 equiv of Cp*$_2$Co$^+$, and 50 equiv [Ph_2NH_2][OTf], the electrode was removed, washed with fresh 0.1 M NaBAr$^F_4$ Et_2O solution, then fresh Et_2O, and probed by XPS. A *very low* coverage of Fe (< 0.3 atom % Fe) was detected in the post-electrolysis material; no Fe was detected on a segment of the electrode which was not exposed to the electrolytic solution. This observation implies a detectable but likely small degree of degradation of $P_3^BFe^+$ over the course of a 15 hour CPE experiment. Worth noting is that no Co was detected on the post-electrolysis electrode. This may be consistent with the known stability of metallocenes and the recently discovered stability of protonated-Cp* ligands on Rh.[33]

To test whether the small amount of deposited Fe material might be catalytically active for N_2RR, following a standard CPE experiment the electrode was removed from the cold electrolysis solution, washed with fresh 0.1 M NaBAr$^F_4$ Et_2O at −35 °C (the electrode itself was maintained at −35 °C at all times), and then used for an additional CPE experiment, under identical conditions except that $P_3^BFe^+$ was excluded. This CPE experiment yielded no detectable NH_3. The charge passed, and H_2 yield, were very similar to a "no $P_3^BFe^+$" control experiment conducted with a freshly cleaned electrode (See SI for

further details). Accordingly, a CPE experiment in the absence of $P_3^BFe^+$ demonstrated that $Cp^*_2Co^+$ serves as an effective electrocatalyst for HER with $[Ph_2NH_2][OTf]$ as the acid source, but does not catalyze the N_2RR reaction (0% FE for NH_3, 75% FE for H_2; see SI). This background HER, and the observed catalytic response to the addition of $[Ph_2NH_2][OTf]$ at the $Cp^*_2Co^{+/0}$ couple, provides circumstantial evidence for the formation of a protonated decamethylcobaltocene intermediate, $Cp^*(\eta^4\text{-}C_5Me_5H)Co^+$, on a timescale similar to that of the N_2RR mediated by $P_3^BFe^+$.

To probe whether the sodium auxiliary electrode used in the CPE experiments might play a non-innocent role as a chemical reductant, a standard CPE experiment with $P_3^BFe^+$, 5 equiv $Cp^*_2Co^+$, and 50 equiv $[Ph_2NH_2][OTf]$ was assembled, but was left to stir at −35 °C for 43 hours without an applied potential bias. This experiment yielded 0.3 equiv NH_3 (relative to Fe), suggesting that background N_2RR due to the sodium auxiliary electrode is very minor.

To ensure the NH_3 produced was derived from the N_2 atmosphere during these electrolysis experiments, as opposed to degradation of the anilinium acid used, a standard CPE experiment using $P_3^BFe^+$, 5 equiv $Cp^*_2Co^+$, and 50 equiv of $[Ph_2{}^{15}NH_2][OTf]$ was performed. Only $^{14}NH_3$ product was detected.

We also sought to compare the chemical N_2RR catalysis efficiency of the $P_3^BFe^+$ catalyst under conditions similar to those used for electrocatalysis. Hence, chemical catalysis with $P_3^BFe^+$, employing Cp^*_2Co as a reductant and $[Ph_2NH_2][OTf]$ as the acid at −35 °C instead of the more typical temperature of −78 °C, in a 0.1 M $NaBAr^F_4$ Et_2O solution, afforded lower yields of NH_3 (1.8 ± 0.7 equiv of NH_3 per Fe) than the yields observed via electrolysis with $Cp^*_2Co^+$ as an additive. The lower yields of NH_3 in these

chemical trials, compared with our previously reported conditions (12.8 ± 0.5 equiv of NH_3 per Fe at −78 °C),[9] may be attributable to increased competitive HER resulting from a more solubilizing medium (0.1 M $NaBAr^F{}_4$ Et_2O vs pure Et_2O) and a higher temperature (−35 °C vs −78 °C).[9] These results suggest that an electrochemical approach to NH_3 formation can improve performance, based on selectivity for N_2RR, of a molecular catalyst under comparable conditions.

5.3 Conclusion

Herein we described the first systematic pK_a studies on a synthetic nitrogen fixation catalyst and find a strong correlation between pK_a and N_2RR vs HER efficiency. Chemical studies reveal that, on their own, the anilinium triflate acids employed in the catalysis are unable to generate the N–H bonds of early-stage N_2RR intermediates such as $P_3{}^BFeNNH_2{}^+$. We propose that the insolubility of these triflate acids prevents the sufficiently rapid proton transfer necessary to capture the critical but unstable first fixed intermediate, $P_3{}^BFeNNH$. Under catalytic conditions, we believe that the presence of the metallocene reductant ($Cp^*{}_2Co$) is essential, as this species can be protonated in situ to form $Cp^*(\eta^4\text{-}C_5Me_5H)Co^+$, which in turn is effective in N–H bond formation with early intermediates. This leads to the intriguing conclusion that an intermediate of the background HER pathway is redirected for productive N_2RR chemistry during catalysis.

DFT studies illustrate that the pK_a effect on the N_2RR efficiency may be explained by the variation in the kinetics and thermodynamics of $Cp^*{}_2Co$ protonation by the different acids. Investigation of the reactivity of $Cp^*(\textit{exo}\text{-}\eta^4\text{-}C_5Me_5H)Co^+$ with the $P_3{}^BFeNNH$ intermediate revealed that PCET reactivity, either synchronous or asynchronous, is favorable and may proceed with only a small barrier, suggesting that $P_3{}^BFeNNH$ can be

rapidly trapped by Cp*(*exo*-η^4-C_5Me_5H)Co^+. We suspect Cp*(η^4-C_5Me_5H)Co^+ is likely involved in a variety of N–H bond forming reactions during the overall catalysis, including reactions with late-stage nitrogen fixation intermediates.

Despite the fact that $Cp^*_2Co^+$ itself catalyzes HER under the conditions employed for electrocatalytic N_2RR, we found that its inclusion in CPE experiments containing $P_3^BFe^+$ and acid under an N_2 atmosphere led to modest improvements in the overall catalytic yield of NH_3. This system represents what is to our knowledge the first unambiguous example of electrocatalytic N_2RR mediated by a soluble, molecular coordination complex.

5.4 REFERENCES

[1] (a) Yandulov, D. V.; Schrock, R. R. *Science* **2003,** *301*, 76. (b) Arashiba, .; Miyake, Y.; Nishibayashi, Y. *Nat. Chem.* **2010,** *3*, 120. (c) Anderson, J. S.; Rittle, J.; Peters, J. C. *Nature* **2013,** *501*, 84. (d) Imayoshi, R.; Tanaka, H.; Matsuo, Y.; Yuki, M.; Nakajima, K.; Yoshizawa, K.; Nishibayashi, Y. *Angew. Chem. Int. Ed.* **2015**, *21*, 8905.

(e) Ung, G.; Peters, J. C. *Angew. Chem. Int. Ed.* **2015**, *54*, 532. (f) Kuriyama, S.; Arashiba, K.; Nakajima, K.; Matsuo, Y.; Tanaka, H.; Ishii, K.; Yoshizawa, K.; Nishibayashi, Y. *Nat. Commun.* **2016,** *7*, 12181. (g) Hill, P. J.; Doyle, L. R.; Crawford, A. D.; Myers, W. K.; Ashley, A. E. *J. Am. Chem. Soc.* **2016**, *138*, 13521. (h) Buscagan, T. M.; Oyala, P. H.; Peters, J. C. *Angew. Chem. Int. Ed.* **2017**, *56*, 6921. (i) Wickramasinghe, L. A.; Ogawa, T.; Schrock, R. R.; Müller, P. *J. Am. Chem. Soc.* **2017,** *139*, 9132. (j) Fajardo Jr., J.; Peters, J. C. *J. Am. Chem. Soc.* **2017**, *139*, 16105.

[2] (a) Shipman, M. A.; Symes, M. D. *Catal. Today* **2017,** *286*, 57. (b) Kyriakou, V.; Garagounis, I.; Vasileiou, E.; Vourros, A.; Stoukides, M. *Catal. Today* **2017,** *286*, 2.

[3] (a) McKone, J. R.; Marinescu, S. C.; Brunschwig, B. S.; Winkler, J. R.; Gray, H. B. *Chem. Sci.* **2014,** *5*, 865. (b) Bullock, R. M.; Appel, A. M.; Helm, M. L. *Chem. Commun.* **2014,** *50*, 3125.

[4] (a) Benson, E. E.; Kubiak, C. P.; Sathrum, A. J.; Smieja, J. M. *Chem. Soc. Rev.* **2009,** *38*, 89. (b) Appel, A. M.; Bercaw, J. E.; Bocarsly, A. B.; Dobbek, H.; DuBois, D. L.; Dupuis, M.; Ferry, J. G.; Fujita, E.; Hille, R.; Kenis, P. J. A.; Kerfeld, C. A.; Morris, R. H.; Peden, C. H. F.; Portis, A. R.; Ragsdale, S. W.; Rauchfuss, T. B.; Reek, J. N. H.; Seefeldt, L. C.; Thauer, R. K.; Waldrop, G. L. *Chem. Rev.* **2013,** *113*, 6621. (c) Francke, R.; Schille, B.; Roemelt, M. *Chem. Rev.* **2018,** *DOI: 10.1021/acs.chemrev.7b00459*.

[5] Zhang, W.; Lai, W.; Cao, R. *Chem. Rev.* **2017,** *117*, 3717.

[6] (a) Pickett, C. J.; Talarmin, J. *Nature* **1985,** *317*, 652. (b) Al-Salih, T. I.; Pickett, C. J. *J. Chem. Soc. Dalton Trans.* **1985**, 1255. (c) Pickett, C. J.; Ryder, K. S.; Talarmin, J. *J. Chem. Soc. Dalton Trans.* **1986**, 1453. (d) Del Castillo, T. J.; Thompson, N. B.; Peters, J. C. *J. Am. Chem. Soc.* **2016,** *138*, 5341.

[7] In this context, a recent report in which the bioelectrosynthesis of ammonia by nitrogenase is coupled to H_2 oxidation is also noteworthy: Milton, R. D.; Cai, R.; Abdellaoui, S.; Leech, D.; De Lacey, A. L.; Pita, M.; Minteer, S. D. *Angew. Chem. Int. Ed.* **2017,** *56*, 2680.

[8] Very recently there was a report of electrolytic NH_3 synthesis by Cp_2TiCl_2. Although rates and Faradaic efficiencies are discussed, no yields of NH_3 are reported: Jeong, E.-Y.; Yoo, C.-Y.; Jung, C. H.; Park, J. H.; Park, Y. C.; Kim, J.-N.; Oh, S.-G.; Woo, Y.; Yoon, H. C. *ACS Sustainable Chem. Eng.* **2017**, *5*, 9662.

[9] Chalkley, M. J.; Del Castillo, T. J.; Matson, B. D.; Roddy, J. P.; Peters, J. C. *ACS Cent. Sci.* **2017,** *3*, 217.

[10] In some cases, the pK_a of a particular anilinium acid was already known in THF in which case this value was used. In cases where the pK_a has not been reported in THF a literature procedure was used to appropriately convert the pK_a from the solvent in which it was measured into a value for THF. See SI for details.

[11] Consistent with this observation is that efforts to use other weak, non-anilinium acids such as benzylammonium triflate (pK_a in THF of 13.2) and collidinium triflate (pK_a in THF of 11.2) also led to no observed NH_3 formation.

[12] These results are also consistent with our previous observation of $[Ph_2NH_2][OTf]$ (pK_a in THF of 3.2) yielding 72 ± 3 % NH_3. See reference 9.

[13] Pham, D. N.; Burgess, B. K. *Biochemistry* **1993,** *32*, 13275.

[14] In some other reports on N_2RR by molecular catalysts, efficiencies for NH_3 have been reported for several acids, but typically these acids span only a small pK_a range, electron yields are inconsistent, and variations are not explained. For a representative example, see Reference 1b.

[15] Anderson, J. S.; Cutsail III, G. E.; Rittle, J.; Connor, B. A.; Gunderson, W. A.; Zhang, L.; Hoffman, B. M.; Peters, J. C. *J. Am. Chem. Soc.* **2015,** *137*, 7803.

[16] Matson, B. D.; Peters, J. C. *ACS Catal.* **2018,** *8*, 1448.

[17] Recent results on a Cr–N_2 species also support the role of PCET in the formation of early-stage N_2 fixation intermediates in the presence of collidinium triflate and a cobaltocene: Kendall, A. J.; Johnson, S. I.; Bullock, R. M.; Mock, M. T. *J. Am. Chem. Soc.* **2018**, *140*, 2528.

[18] Grimme, S.; Antony, J.; Ehrlich, S.; Krieg, H. *J. Chem. Phys.* **2010**, *132*, 154104.

[19] (a) Tao, J.; Perdew, J. P.; Staroverov, V. N.; Scuseria, G. E. *Phys. Rev. Lett.* **2003,** *91*, 146401. (b) Weigend, F.; Ahlrichs, R. *Phys. Chem. Chem. Phys.* **2005,** *7*, 3297.

[20] For the $P_3^BFeN_xH_y$ and related systems, this combination of functional and basis sets is able to reproduce not only crystallographic details, but also experimentally measured singlet-triplet gaps, reduction potentials, and N–H BDFE's, as described in reference 16.

[21] In all cases where the basicity of $P_3^BFeN_xH_y$ intermediates has been evaluated, they are predicted to be readily protonated by the anilinium triflate acids employed (see SI for details).

[22] DFT calculations suggest that almost all of the $P_3^BFeN_xH_y$ intermediates on the N_2RR pathway have N–H bonds stronger than the C–H bond in Cp*(*exo*-η^4-C_5Me_5H)Co^+, suggesting that, at least thermodynamically, the formation of these N–H bonds by PCET is favorable. See reference 16.

[23] The reactivity of ring-functionalized Cp* rings has been discussed previously in the context of electrocatalytic HER by 4d and 5d metals, but via a mechanism involving hydride transfer, rather than via PCET. See: (a) Pitman, C. L.; Finster, O. N. L.; Miller, A. J. M. *Chem. Commun.* **2016**, *52*, 9105. (b) Quintana, L. M. A.; Johnson, S. I.; Corona, S. L.; Villatoro, W.; Goddard, W. A.; Takase, M. K.; VanderVelde, D. G.; Winkler, J. R.; Gray, H. B.; Blakemore, J. D. *Proc. Natl. Acad. Sci.* **2016**, *113*, 6409. (c) Peng, Y.; Ramos-Garcés, M. V.; Lionetti, D.; Blakemore, J. D. *Inorg. Chem.* **2017**, *56*, 10824.

[24] Productive N–H bond formation via PCET with models of late-stage N_2 fixation intermediates (i.e., M≡N or M–NH_2) has been observed previously: (a) Scepaniak, J. J.; Young, J. A.; Bontchev, R. P.; Smith, J. M. *Angew. Chem. Int. Ed.* **2009**, *48*, 3158. (b) Pappas, I.; Chirik, P. J. *J. Am. Chem. Soc.* **2015**, *137*, 3498. (c) MacLeod, K. C.; McWilliams, S. F.; Mercado, B. Q.; Holland, P. L. *Chem. Sci.* **2016**, *7*, 5736. (d) Lindley, B. M.; Bruch, Q. J.; White, P. S.; Hasanayn, F.; Miller, A. J. M. *J. Am. Chem. Soc.* **2017**, *139*, 5305.

[25] Marcus, R. A. *J. Chem. Phys.* **1956**, *24*, 966.

[26] Iordanova, N.; Decornez, H.; Hammes-Schiffer, S. *J. Am. Chem. Soc.* **2001**, *123*, 3723.

[27] We have assumed a PT-ET mechanism in which ET is rate limiting based on significantly lower reorganization energies and barriers for PT compared to ET. See SI for full description.

[28] Koelle, U.; Infelta, P. P.; Graetzel, M. *Inorg. Chem.* **1988,** *27*, 879.

[29] Call, A.; Casadevall, C.; Acuna-Pares, F.; Casitas, A.; Lloret-Fillol, J. *Chem. Sci.* **2017**, *8*, 4739.

[30] Very recently there has been a study of electrocatalytic N_2RR under ambient conditions in ionic liquids with Fe nanoparticles that reports FE's for NH_3 as high as 60%: Zhou, F.; Azofra, L. M.; Ali, M.; Kar, M.; Simonov, A. N.; McDonnell-Worth, C.; Sun, C.; Zhang, X.; MacFarlane, D. R. *Energy Environ. Sci.* **2017**, *10*, 2516.

[31] We believe that the quasi-reversible nature of the electrochemical couple results from a high reorganization energy, but the couple is fully chemically reversible: Moret, M.-E.; Peters, J. C. *Angew. Chem. Int. Ed.* **2011**, *50*, 2063.

[32] Due to the extensive diffusion between the working and auxiliary chambers, production of an oxidation product which can diffuse to the working electrode and be re-reduced at −2.1 V vs $Fc^{+/0}$ leads to excessive, nonproductive redox cycling between chambers over the course of the lengthy CPE experiments. Sodium metal as an electrode material provides a suitable solution to this technical challenge, as the product of its oxidation (Na^+) is stable to the CPE conditions.

Appendix 1

SUPPLEMENTARY INFORMATION FOR CHAPTER 2: EVALUATING MOLECULAR COBALT COMPLEXES FOR THE CONVERSION OF N_2 TO NH_3

Reproduced in part with permission from:

Del Castillo, T. J.; Thompson, N. B.; Suess, D. L.; Ung, G.; Peters, J. C.; *Inorg. Chem.*, **2015**, 54, 9256-9262. **DOI:** 10.1021/acs.inorgchem.5b00645

A1.1 General considerations:

All manipulations were carried out using standard Schlenk or glovebox techniques under an N_2 atmosphere. Solvents were deoxygenated and dried by thoroughly sparging with N_2 followed by passage through an activated alumina column in a solvent purification system by SG Water, USA LLC. Nonhalogenated solvents were tested with sodium benzophenone ketyl in tetrahydrofuran in order to confirm the absence of oxygen and water. Deuterated solvents were purchased from Cambridge Isotope Laboratories, Inc., degassed, and dried over activated 3-Å molecular sieves prior to use.

$[H(OEt_2)_2][BAr^F{}_4]$,[1] KC_8,[2] (TPB)Co(N_2),[3] (TPB)CoBr,[3] (SiP_3)Co(N_2),[4] $NArP_3$,[5] (PBP)Co(N_2),[6] CP_3H,[7] and Co(PPh_3)$_2I_2$[8] were prepared according to literature procedures. All other reagents were purchased from commercial vendors and used without further purification unless otherwise stated. Et_2O for NH_3 generation reactions was stirred over Na/K ($\geq$ 2 hours) and filtered before use.

Physical Methods:

Elemental analyses were performed by Midwest Microlab, LLC (Indianapolis, IN). ^{1}H and ^{13}C chemical shifts are reported in ppm relative to tetramethylsilane, using ^{1}H and ^{13}C resonances from residual solvent as internal standards. ^{31}P chemical shifts are reported in ppm relative to 85% aqueous H_3PO_4. Solution phase magnetic measurements were performed by the method of Evans.[9] IR measurements were obtained as solutions or thin films formed by evaporation of solutions using a Bruker Alpha Platinum ATR spectrometer with OPUS software. Optical spectroscopy measurements were collected with a Cary 50 UV-vis spectrophotometer using a 1-cm two-window quartz cell. Electrochemical measurements were carried out in a glovebox under an N_2 atmosphere in a one compartment cell using a CH Instruments 600B electrochemical analyzer. A glassy carbon electrode was used as the working electrode and platinum wire was used as the auxiliary electrode. The reference electrode was $Ag/AgNO_3$ in THF. The ferrocene couple (Fc/Fc^+) was used as an internal reference. THF solutions of electrolyte (0.1 M tetra-*n*-butylammonium hexafluorophosphate, $TBAPF_6$) and analyte were also prepared under an inert atmosphere. X-band EPR spectra were obtained on a Bruker EMX spectrometer.

X-ray Crystallography:

X-ray diffraction studies were carried out at the Caltech Division of Chemistry and Chemical Engineering X-ray Crystallography Facility on a Bruker three-circle SMART diffractometer with a SMART 1K CCD detector. Data was collected at 100K using Mo Kα radiation (λ = 0.71073 Å). Structures were solved by direct or Patterson methods using SHELXS and refined against *F*2 on all data by full-matrix least squares with SHELXL-97. All non-hydrogen atoms were refined anisotropically. All hydrogen atoms were placed at geometrically calculated positions and refined using a riding model. The isotropic displacement parameters of all hydrogen atoms were fixed at 1.2 (1.5 for methyl groups) times the U_{eq} of the atoms to which they are bonded.

Notes specific to individual structures:

The 12-crown-4 fragments are disordered for [Na(12-crown-4)$_2$][(TPB)Co(N_2)]. One 12-crown-4 (with O atoms labeled O5-O8 and O50-O80) is fully disordered over two unique positions. The other 12-crown-4 (O atoms labeled O1-O4) shows a disorder in the methyl carbons but not the oxygen atoms. In all cases, the positions of the carbons could be located in the difference map and refined anisotropically and the hydrogen atoms were placed at geometrically calculated positions as usual. The oxygen atom in one of the solvent THF molecules (O10 and O100) is disordered over two positions. The other THF molecule (with O9) shows large thermal ellipsoids, potentially indicating an unresolved disorder of this moiety. A diethylether molecule was located on an inversion center and is therefore disordered about this symmetry element. The occupancies of all disordered fragments were freely refined and the bond lengths and angles were restrained to be the

same for the disordered fragments. Hydrogen atoms were not included on any of the solvent molecules for these reasons.

The fluorine substituents on C143, C144, C152, and C168 in [(TPB)Co][BAr_4^F] are disordered by rotation about the C–C bonds to varying extents and were refined as two-part positional disorders in each case. The occupancies of the disordered fragments were freely refined and the bond lengths and angles were restrained to be the same for the disordered fragments.

One isopropyl group attached to P2 is disordered for (CP_3)Co(N_2); one methyl group (labeled C37A and C37B) is disordered over two positions. Each position was located in the difference map and refined anisotropically with hydrogen atoms calculated in the usual manner. The occupancies of the two fragments were refined freely. In addition, after refinement, the model displays large positive residual electron density located within 0.06 Å of CO1. This is likely due to unresolved disorder; attempts to include this as disorder with respect to the cobalt atom do not improve the model upon refinement. The residual electron density may also be due to poor data at high angles, as imposing a high-angle cutoff (using SHEL 100.0 0.84) during refinement reduces the residual density significantly. Importantly, the bond distances about CO1 do not change significantly when this restraint is imposed.

The isopropyl substituents on P3 are disordered for [(CP_3)Co(N_2)][BAr^F_4]. The disorder reflects simultaneous rotation of the methyl substituents about the methine carbon for

each isopropyl group, which was modeled as a two-part positional disorder. All carbons in the disordered fragments were located in the difference map and refined anisotropically, with hydrogen atoms geometrically calculated in the usual manner. In addition, the CF_3 groups attached to C16B and C18B are disordered between two positions, reflecting rotation of the CF_3 group with simultaneous rotation of the arene fragment attached to B. Both CF_3 groups were refined as two-part positional disorders. In all cases, the occupancies of disordered fragments were freely refined and the bond lengths and angles were restrained to be the same for disordered fragments of the same type.

Computational Methods:

All computations were carried out using version 3.0.2 of the ORCA program system.[10] DFT calculations employed the BP86 exchange-correlation functional. The 6-31+G* basis set[11] was used for all geometry optimizations, while single point calculations were performed at the 6-311++G**[12] level of theory. The atomic coordinates of **2** and **5** obtained from XRD studies were used as inputs for geometry optimizations at the lower level of theory, and the optimized geometries obtained in this way were used as inputs for single point calculations of the electron densities at the higher level of theory. Molecular electrostatic potentials were computed from the calculated electron densities using the orca_vpot subroutine. Atomic charges were computed using the CHELPG method developed by Breneman and Wiberg.[13] Electrostatic potential maps were visualized using version 5 of the GaussView program.[14]

A1.2 Synthetic Details:

[Na(12-crown-4)$_2$][(TPB)Co(N$_2$)] (2):

To a -78 ˚C solution of (TPB)CoBr (70.5 mg, 0.0967 mmol) in THF (2 mL) was added a freshly prepared solution of NaC$_{10}$H$_8$ (23.5 mg C$_{10}$H$_8$, 0.222 mmol) in THF (3 mL). The solution was brought to RT and allowed to stir for six hours. Addition of 12-crown-4 (51.1 mg, 0.290 mmol) and removal of solvent *in vacuo* provided a dark red solid. Et$_2$O was added and subsequently removed *in vacuo*. The residue was suspended in C$_6$H$_6$ and filtered and the solids were washed with C$_6$H$_6$ (2 x 2 mL) and pentane (2 x 2 mL) to furnish a red solid (68.8 mg, 0.0660 mmol, 68%). Single crystals were grown by vapor diffusion of pentane onto a THF solution of the title compound that had been layered with Et$_2$O. ^{1}H NMR (400 MHz, THF-*d*$_8$) δ 7.41 (3H), 6.94 (3H), 6.66 (3H), 6.44 (3H), 3.64 (32H), 2.29 (br), 1.37 (6H), 1.20 (6H), 0.93 (6H), -0.26 (6H). ^{11}B NMR (128 MHz, THF-*d*$_8$) δ 9.32. ^{31}P NMR (162 MHz, THF-*d*$_8$) δ 62.03. IR (thin film, cm^{-1}): 1978 (N$_2$). Anal. Calcd. for C$_{52}$H$_{86}$BCoN$_2$NaO$_8$P$_3$: C, 59.32; H, 8.23; N, 2.66. Found: C, 59.05; H, 7.99; N, 2.47.

[(TPB)Co][BAr$^F{}_4$] (3):

To a -78 ˚C solution of (TPB)Co(N$_2$) (**1**) (91.5 mg, 0.135 mmol) in Et$_2$O (2 mL) was added solid [H(OEt$_2$)$_2$][BAr$^F{}_4$] (134.0 mg, 0.132 mmol). The reaction was brought to RT and vented to allow for the escape of H$_2$. The purple-brown solution was stirred for 1 hr. The solution was layered with pentane (5 mL) and stored at -35 ˚C to furnish red-purple

single crystals of the title compound (162.9 mg, 0.0952 mmol, 82%) which were washed with pentane (3 x 2 mL). ^{1}H NMR (400 MHz, C_6D_6) δ 26.25, 23.80, 8.64, 8.44 ([BAr^F_4]), 7.88 ([BAr^F_4]), 6.33, -2.16, -3.68. UV-Vis (Et_2O, nm {L cm^{-1} mol^{-1}}): 585 {1500}, 760 {532}. Anal. Calcd. for $C_{68}H_{66}B_2CoF_{24}P_3$: C, 53.99; H, 4.40. Found: C, 53.94; H, 4.51.

$(CP_3)Co(N_2)$ (5):

$(CP_3)H$ (100 mg, 0.169 mmol) and $CoCl_2$ • 1.5 THF (40 mg, 0.169 mmol) were mixed at room temperature in THF (10 mL). This mixture was allowed to stir for one hour, yielding a homogeneous cyan solution. This solution was chilled to -78 ˚C, and a solution of MeMgCl in tetrahydrofuran (0.5 M, 0.560 mmol) was added in three 370 μL portions over three hours. The mixture was allowed to warm slowly to room temperature, and then was concentrated to *ca.* 1 mL. 1,4-dioxane (2 mL) was added, and the resultant suspension was stirred vigorously for at least 2 hours before filtration. The filtrate was concentrated to a tacky red-brown solid, which was extracted with 1:1 C_6H_6 : pentane (10 mL), filtered over celite and lyophilized to yield the product as a red powder (96 mg, 0.141 mmol, 83%). Crystals suitable for X-ray diffraction were grown via slow evaporation of a pentane solution. ^{1}H NMR (300 MHz, C_6D_6) δ 7.28 (br, 3H), 6.82 (m, 9H), 2.82 (oct., -C*H*, 3H), 2.09 (sept., -C*H*, 3H), 1.49 (m, 18H), 1.06 (dd, -CHC*H*$_3$, 9H), 0.30 (dd, -CHC*H*$_3$, 9H). ^{31}P{^{1}H} (121 MHz, C_6D_6): δ 47.39. IR (thin film, cm^{-1}): 2057 (N_2). Anal. Calcd. for $C_{37}H_{54}CoN_2P_3$: C, 65.48; H, 8.02; N, 4.13. Found: C, 64.14; H, 8.36; N, 4.03.

[$(CP_3)Co(N_2)$][BAr^F_4] (6):

5 (75 mg, 0.11 mmol) and $[Cp_2Fe][BAr^F_4]$ (122 mg, 0.12 mmol) were dissolved separately in diethyl ether (ca. 3 mL each) and the ethereal solutions were cooled to -78˚C. The chilled solution of $[Cp_2Fe][BAr^F_4]$ was added dropwise to the solution of **5**, and the resultant mixture was allowed to stir at low temperature for one hour. At this point, the mixture was allowed to warm to room temperature before filtration over celite and concentration to *ca.* 2 mL. The concentrated filtrate was layered with pentane, and placed in a freezer at -35˚C to induce crystallization. Decanting the mother liquor off crystalline solids and washing thoroughly with pentane yields $[(CP_3)Co(N_2)][BAr^F_4]$ (**6**) as dark green-brown crystals (147 mg, 0.095 mmol, 86%). Crystals suitable for X-ray diffraction were grown by slow diffusion of pentane vapors into an ethereal solution of **6** at -35˚C. μ_{eff} (5:1 d_8-toluene:d_8-THF, Evans' method, 23 °C): 3.49 μ_B. ^{1}H NMR (300 MHz, C_6D_6) δ 17.22, 9.94, 8.24 ($[BAr^F_4]$), 7.72 ($[BAr^F_4]$), 3.13, 2.57, 1.5 – -2 (br, m), –3.68. IR (cm^{-1}): 2182 (N_2, thin film), 2180 (N_2, solution). Elemental analysis shows low values for N consistent with a labile N_2 ligand, Anal. Calcd. for $C_{69}H_{66}BCoF_{24}N_2P_3$: C, 53.75; H, 4.31; N, 1.82. Found: C, 53.86; H, 4.31; N, 0.27. Note: The magnetic moment for **6** in solution may be complicated by some degree of solvent exchange for N_2 at the cobalt center. Freeze-pump-thaw experiments monitored by optical spectroscopy establish that the N_2 ligand is labile in solution (see Figure A1.6). Low temperature (80 K) EPR spectroscopy in a solvent of lower donicity (2-Me-THF) is consistent with a low spin, S = 1/2 species (see Figure A1.7).

$[(NArP_3)CoCl][BPh_4]$:

THF (5 mL) was added to a solid mixture of $NArP_3$ (58 mg, 91.2 mmol), $CoCl_2$ (12 mg, 92.4 mmol) and $NaBPh_4$ (31 mg, 90.6 mmol). The reaction was stirred for 4 hours at room temperature during which the color evolved from yellow to green to purple. The solvent was removed *in vacuo* and the residue was taken up in dichloromethane. The suspension was filtered over a plug of Celite and the filtrate was dried yielding a purple powder (86 mg, 82.1 mmol, 90%). Single crystals were grown by slow evaporation of a saturated solution of $[(NArP_3)CoCl][BPh_4]$ in diethyl ether/dichloromethane (1:2 v:v). ^{1}H NMR (CD_2Cl_2, 300 MHz) δ 177.77, 37.50, 23.78, 13.48, 12.96, 7.37, 7.08, 6.92, 4.41, 1.50, -3.60, -9.81; UV-Vis (THF, nm {L cm^{-1} mol^{-1}}): 564 {452}, 760 {532}; μ_{eff} (CD_2Cl_2, Evans' method, 23 °C): 3.97 μ_B. Anal. Calcd. for $C_{63}H_{80}BClCoNP_3$: C, 72.10; H, 7.68; N, 1.33. Found: C, 71.97; H, 7.76; N, 1.30.

Treatment of $[(TPB)Co(N_2)][Na(12\text{-crown-}4)_2]$ (2) with 10 equiv $[H\bullet(OEt_2)_2][BAr^F{}_4]$ and 12 equiv KC_8:

$[(TPB)Co(N_2)][Na(12\text{-crown-}4)_2]$ (10 mg, 0.01 mmol) was suspended in Et_2O (0.5 mL) in a 20 mL scintillation vial equipped with a stir bar. This suspension was cooled to −78 °C in a cold well inside of a N_2 glovebox. A solution of $[H\cdot(OEt_2)_2][BAr^F{}_4]$ (95 mg, 0.094 mmol) in Et_2O (1.5 mL) similarly cooled to −78 °C was added to this suspension in one portion with stirring. Residual acid was dissolved in cold Et_2O (0.25 mL) and added subsequently. This mixture was allowed to stir for 5 minutes. Then KC_8 (16 mg, 0.119 mmol) was suspended in cold Et_2O (0.75 mL) and added to the reaction mixture over the course of 1 minute. The vial was then sealed, and the reaction was allowed to stir for 40 min at −78 °C before being warmed to room temperature and stirred for 15 min. The

reaction mixture was then filtered and evaporated to dryness under vacuum. The resulting residue was extracted with C_6D_6 and submitted to ^{31}P NMR spectroscopy, revealing a signal consistent with uncoordinated phosphine at 10.8 ppm (Figure A1.1).

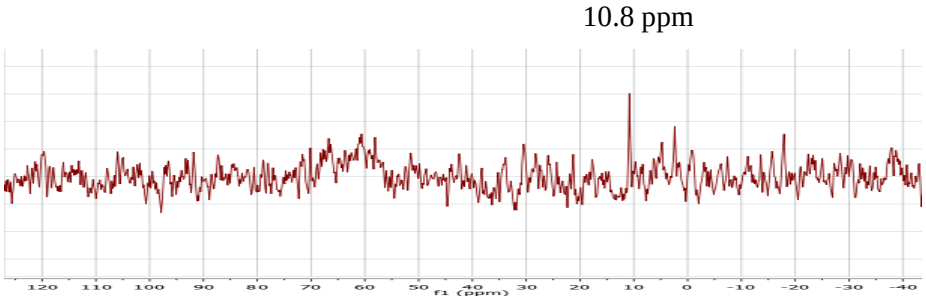

Figure A1.1: ^{31}P NMR of reaction mixture

A1.3 Ammonia Quantification:

A Schlenk tube was charged with HCl (3 mL of a 2.0 M solution in Et_2O, 6 mmol). Reaction mixtures were vacuum transferred into this collection flask. Residual solid in the reaction vessel was treated with a solution of [Na][O-*t*-Bu] (40 mg, 0.4 mmol) in 1,2-dimethoxyethane (1 mL) and sealed. The resulting suspension was allowed to stir for 10 min before all volatiles were again vacuum transferred into the collection flask. After completion of the vacuum transfer, the flask was sealed and warmed to room temperature. Solvent was removed in vacuo, and the remaining residue was dissolved in H_2O (1 mL). An aliquot of this solution (20 μL) was then analyzed for the presence of

NH_3 (present as $[NH_4][Cl]$) by the indophenol method.[15] Quantification was performed with UV−vis spectroscopy by analyzing absorbance at 635 nm.

Standard NH_3 Generation Reaction Procedure with $[(TPB)Co(N_2)][Na(12\text{-crown-}4)_2]$ (2):

$[(TPB)Co(N_2)][Na(12\text{-crown-}4)_2]$ (2.2 mg, 0.002 mmol) was suspended in Et_2O (0.5 mL) in a 20 mL scintillation vial equipped with a stir bar. This suspension was cooled to −78 °C in a cold well inside of a N_2 glovebox. A solution of $[H\cdot(OEt_2)_2][BAr^F{}_4]$ (95 mg, 0.094 mmol) in Et_2O (1.5 mL) similarly cooled to −78 °C was added to this suspension in one portion with stirring. Residual acid was dissolved in cold Et_2O (0.25 mL) and added subsequently. This mixture was allowed to stir 5 minutes at −78 °C, before being transferred to a precooled Schlenk tube equipped with a stir bar. The original reaction vial was washed with cold Et_2O (0.25 mL) which was added subsequently to the Schlenk tube. KC_8 (16 mg, 0.119 mmol) was suspended in cold Et_2O (0.75 mL) and added to the reaction mixture over the course of 1 minute. The Schlenk tube was then sealed, and the reaction was allowed to stir for 40 min at −78 °C before being warmed to room temperature and stirred for 15 min.

Table A1.1: UV-vis quantification results for standard NH_3 generation experiments with $[(TPB)Co(N_2)][Na(12\text{-crown-}4)_2]$ (**2**)

Iteration	Absorbance (635 nm)	Eq. NH_3/Co	% Yield Based on H^+

A	0.225	2.3	16
B	0.187	2.1	14
C	0.199	2.2	14
D	0.240	2.5	18
E	0.255	2.8	19
F	0.197	2.2	14
Average	0.217 ± 0.027	2.4 ± 0.3	16 ± 2

Hydrazine was not detected in the catalytic runs using a standard UV-Vis quantification method.[16]

Standard NH_3 Generation Reaction Procedure with (TPB)Co(N_2) (1):

The procedure was identical to that of the standard NH_3 generation reaction protocol with the changes noted. The precursor used was (TPB)Co(N_2) (1.3 mg, 0.002 mmol).

Table A1.2: UV-vis quantification results for standard NH_3 generation experiments with (TPB)Co(N_2) (**1**)

Iteration	Absorbance (635 nm)	Eq. NH_3/Co	% Yield Based on H^+
A	0.064	0.7	4
B	0.058	0.6	4
C	0.107	1.2	8
Average	0.076 ± 0.027	0.8 ± 0.3	5 ± 2

Standard NH_3 Generation Reaction Procedure with [(TPB)Co][BAr^F_4] (3):

The procedure was identical to that of the standard NH_3 generation reaction protocol with the changes noted. The precursor used was [(TPB)Co(N_2)][BAr^F_4] (2.3 mg, 0.002 mmol).

Table A1.3: UV-vis quantification results for standard NH_3 generation experiments with [(TPB)Co][BAr^F_4] (**3**)

Iteration	Absorbance (635 nm)	Eq. NH_3/Co	% Yield Based on H^+
A	0.092	1.4	6
B	0.122	1.8	9
C[1]	0.091	1.5	6
Average	0.107 ± 0.021	1.6 ± 0.2	7 ± 1

[1] Used 2.0 mg (0.001 mmol) of catalyst; omitted from average absorbance

Standard NH_3 Generation Reaction Procedure with (TPB)CoBr:

The procedure was identical to that of the standard NH_3 generation reaction protocol with the changes noted. The precursor used was (TPB)CoBr (1.6 mg, 0.002 mmol).

Table A1.4: UV-vis quantification results for standard NH_3 generation experiments with (TPB)CoBr

Iteration	Absorbance (635 nm)	Eq. NH_3/Co	% Yield Based on H^+

A	0.035	0.3	2
B	0.101	1.0	7
C[1]	0.088	0.7	6
Average	0.068 ± 0.047	0.7 ± 0.4	5 ± 3

[1] Used 2.0 mg (0.003 mmol) of catalyst; omitted from average absorbance

Standard NH_3 Generation Reaction Procedure with $(SiP_3)Co(N_2)$ (4):

The procedure was identical to that of the standard NH_3 generation reaction protocol with the changes noted. The precursor used was $(SiP_3)Co(N_2)$ (1.5 mg, 0.002 mmol).

Table A1.5: UV-vis quantification results for standard NH_3 generation experiments with $(SiP_3)Co(N_2)$

Iteration	Absorbance (635 nm)	Eq. NH_3/Co	% Yield Based on H^+
A	< 0.005	< 0.1	—

B	< 0.005	< 0.1	—
C	< 0.005	< 0.1	—
Average	—	< 0.1	—

Standard NH_3 Generation Reaction Procedure with $(CP_3)Co(N_2)$ (5):

The procedure was identical to that of the standard NH_3 generation reaction protocol with the changes noted. The precursor used was $(CP_3)Co(N_2)$ (1.4 mg, 0.002 mmol).

Table A1.6: UV-vis quantification results for standard NH_3 generation experiments with $(CP_3)Co(N_2)$

Iteration	Absorbance (635 nm)	Eq. NH_3/Co	% Yield Based on H^+
A	0.044	0.21	1.5
B	< 0.005	< 0.1	—
C	< 0.005	< 0.1	—
Average	0.02 ± 0.02	0.1 ± 0.1	—

Standard NH_3 Generation Reaction Procedure with $[(NArP_3)CoCl][BPh_4]$:

The procedure was identical to that of the standard NH_3 generation reaction protocol with the changes noted. The precursor used was $[(NArP_3)CoCl][BPh_4]$ (1.9 mg, 0.002 mmol).

Table A1.7: UV-vis quantification results for standard NH_3 generation experiments with $[(NArP_3)CoCl][BPh_4]$

Iteration	Absorbance (635 nm)	Eq. NH_3/Co	% Yield Based on H^+
A	< 0.005	< 0.1	—
B	< 0.005	< 0.1	—
C	< 0.005	< 0.1	—
Average	—	< 0.1	—

Standard NH_3 Generation Reaction Procedure with (PBP)Co(N_2):

The procedure was identical to that of the standard NH_3 generation reaction protocol with the changes noted. The precursor used was (PBP)Co(N_2) (1.1 mg, 0.002 mmol).

Table A1.8: UV-vis quantification results for standard NH_3 generation experiments with (PBP)Co(N_2)

Iteration	Absorbance (635	Eq. NH_3/Co	% Yield Based on

	nm)		H^+
A	0.021	0.15	1
B	0.03	0.29	2
C	0.057	0.62	4
Average	0.036 ± 0.019	0.4 ± 0.2	2 ± 1

Standard NH_3 Generation Reaction Procedure with $Co(PPh_3)_2I_2$:

The procedure was identical to that of the standard NH_3 generation reaction protocol with the changes noted. The precursor used was $Co(PPh_3)_2I_2$ (1.8 mg, 0.002 mmol).

Table A1.9: UV-vis quantification results for standard NH_3 generation experiments with $Co(PPh_3)_2I_2$

Iteration	Absorbance (635 nm)	Eq. NH_3/Co	% Yield Based on H^+
A[1]	0.036	0.3	2
B	0.036	0.3	2
C	0.046	0.4	3
Average	0.041 ± 0.007	0.4 ± 0.1	2 ± 0.4

[1] Used 2.0 mg (0.0024 mmol) of catalyst; omitted from average absorbance

Standard NH_3 Generation Reaction Procedure with $CoCp_2$:

The procedure was identical to that of the standard NH_3 generation reaction protocol with the changes noted. The precursor used was $CoCp_2$ (0.6 mg, 0.003 mmol).

Table A1.10: UV-vis quantification results for standard NH_3 generation experiments with $CoCp_2$

Iteration	Absorbance (635 nm)	Eq. NH_3/Co	% Yield Based on H^+
A	0.020	0.09	1
B	0.008	0.02	0
C	0.033	0.20	2
Average	0.020 ± 0.013	0.1 ± 0.1	1 ± 1

Standard NH_3 Generation Reaction Procedure with $Co_2(CO)_8$:

The procedure was identical to that of the standard NH_3 generation reaction protocol with the changes noted. The precursor used was $Co_2(CO)_8$ (0.4 mg, 0.001 mmol, 0.002 mmol Co) sampled as a 100 μL aliquot of a stock solution (2.0 mg $Co_2(CO)_8$ in 0.5 mL Et_2O).

Table A1.11: UV-vis quantification results for standard NH_3 generation experiments with $Co_2(CO)_8$

Iteration	Absorbance (635 nm)	Eq. NH_3/Co	% Yield Based on H^+
A	< 0.005	< 0.1	—
B	< 0.005	< 0.1	—
C	< 0.005	< 0.1	—
Average	—	< 0.1	—

NH_3 Generation Reaction of [(TPB)Co(N_2)][Na(12-crown-4)$_2$] (2) with Reductant Added First Followed by Acid:

N.B.: The following experiment was conducted to study the effect of the order of addition of reagents in the NH_3 generation reaction with **2**.

[(TPB)Co(N_2)][Na(12-crown-4)$_2$] (2.2 mg, 0.002 mmol) was suspended in Et_2O (0.5 mL) in a 20 mL scintillation vial. This suspension was cooled to −78 °C in a cold well inside of a N_2 glovebox. This suspension was transferred to a precooled Schlenk tube equipped with a stir bar. Residual solid was suspended in additional cold Et_2O (2 x 0.25 mL) and transferred subsequently. To this mixture was added a precooled suspension of KC_8 (16 mg, 0.119 mmol) in 0.5 mL Et_2O. Residual solid was suspended in additional cold Et_2O (2 x 0.25 mL) and transferred subsequently. This mixture was allowed to stir for 5 minutes at −78 °C. To this mixture was then added a similarly cooled to −78 °C solution of [H·(OEt_2)$_2$][$BAr^F{}_4$] (95 mg, 0.094 mmol) in Et_2O (1.5 mL) in one

portion with stirring. Residual acid was dissolved in cold Et_2O (0.25 mL) and added subsequently. The Schlenk tube was then sealed, and the reaction was allowed to stir for 40 min at −78 °C before being warmed to room temperature and stirred for 15 min.

Table A1.12: UV-vis quantification results for NH_3 generation experiments with [(TPB)Co(N_2)][Na(12-crown-4)$_2$] (**2**) and reductant being added first

Iteration	Absorbance (635 nm)	Eq. NH_3/Co	% Yield Based on H^+
A[1]	0.175	2.2	13
B	0.153	1.7	11
Average	—	1.9 ± 0.4	12 ± 1

[1] Used 1.9 mg (0.0018 mmol) of catalyst; omitted from average absorbance

Calibration Curves for NH_3 and N_2H_4 Quantification

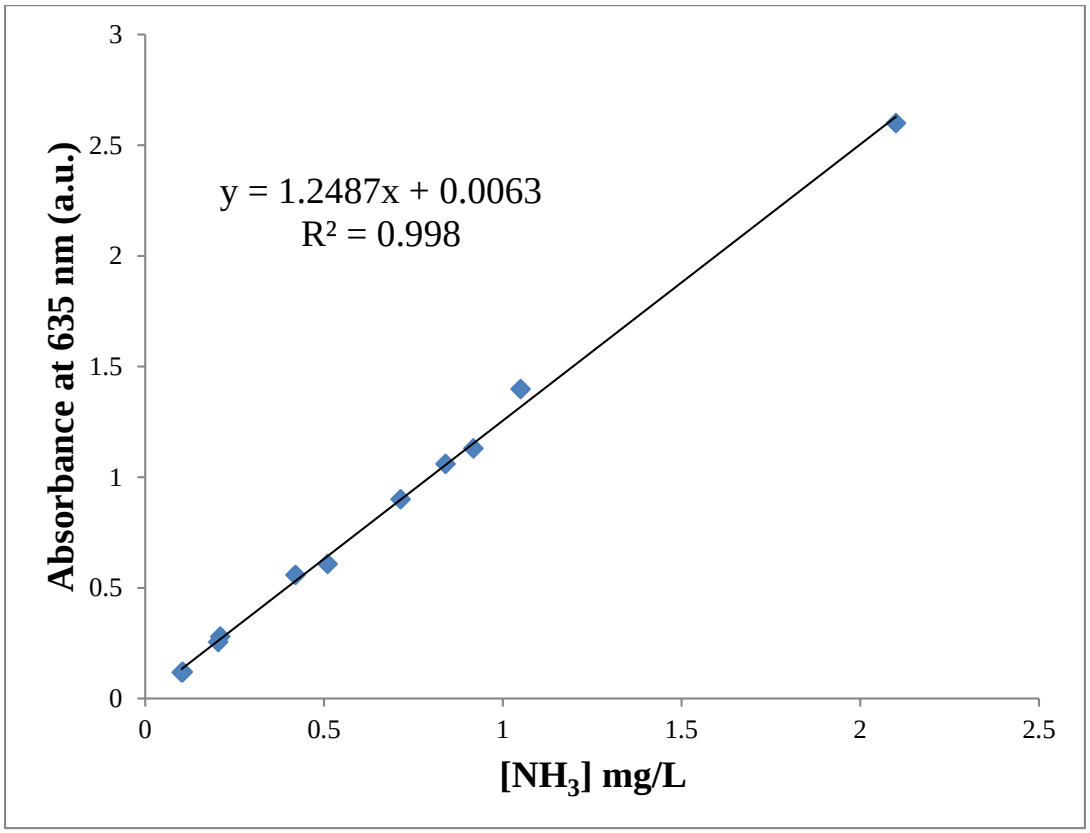

Figure A1.2: Calibration curve for NH_3 quantification by indophenol method.

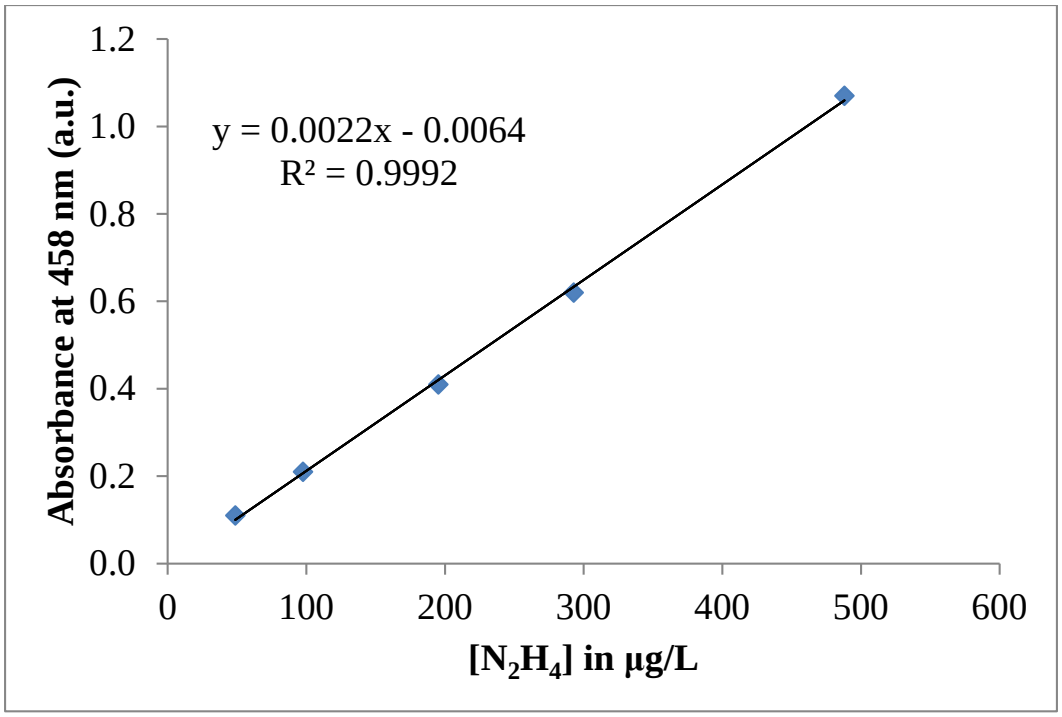

Figure A1.3: Calibration curve for UV-vis quantification of hydrazine.

A1.4 X-ray Diffraction Tables

Table A1.13: Crystal data and structure refinement for $[Na(12\text{-crown-}4)_2][(TPB)Co(N_2)]$ (**2**) and $[(TPB)Co][BAr^F{}_4]$ (**3**)

Identification code	**2**	**3**
Empirical formula	$C_{62}H_{86}BCoN_2NaO_{10.5}P_3$	$C_{68}H_{66}B_2CoF_{24}P_3$
Formula weight	1212.97	1512.67
Temperature/K	100(2)	100(2)
Crystal system	monoclinic	orthorhombic
Space group	$P2_1/n$	Pbca
a/Å	10.8142(5)	26.3920(15)
b/Å	27.5046(13)	19.7049(13)
c/Å	22.3660(10)	26.4995(19)
α/°	90	90
β/°	91.141(2)	90
γ/°	90	90

Volume/$Å^3$	6651.2(5)	13781.1(16)
Z	4	8
$\rho_{calc}g/cm^3$	1.211	1.458
μ/mm^{-1}	0.391	0.424
F(000)	2576	6176
Crystal size/mm^3	0.38 × 0.30 × 0.25	0.35 × 0.32 × 0.24
Radiation	MoKα (λ = 0.71073)	MoKα (λ = 0.71073)
2Θ range for data collection/°	3.94 to 86.26	3.72 to 64.06
Index ranges	-20 ≤ h ≤ 20, -52 ≤ k ≤ 52, -43 ≤ l ≤ 43	-39 ≤ h ≤ 39, -23 ≤ k ≤ 29, -39 ≤ l ≤ 39
Reflections collected	451328	377520
Independent reflections	49547 [R_{int} = 0.0632, R_{sigma} = 0.1797]	23962 [R_{int} = 0.0539, R_{sigma} = 0.0255]
Data/restraints/parameters	49547/1385/952	23962/1174/1007
Goodness-of-fit on F^2	1.091	1.052
Final R indexes [I>=2σ (I)]	R_1 = 0.0629, wR_2 = 0.1600	R_1 = 0.0459, wR_2 = 0.1084
Final R indexes [all data]	R_1 = 0.0999, wR_2 = 0.1797	R_1 = 0.0720, wR_2 = 0.1241
Largest diff. peak/hole / e $Å^{-3}$	1.78/-0.83	1.27/-1.34

Table A1.14: Crystal data and structure refinement for $(CP_3)Co(N_2)$ (**5**) and $[(CP_3)Co(N_2)][BAr^F{}_4]$ (**6**)

Identification code	**5**	**6**
Empirical formula	$C_{37}H_{54}CoN_2P_3$	$C_{50}H_{60}BN_2F_{24}P_3Co$
Formula weight	678.66	1541.89
Temperature/K	100(2)	100(2)
Crystal system	trigonal	orthorhombic
Space group	R-3	Pbca
a/Å	19.3720(4)	19.7869(17)
b/Å	19.3720(4)	25.670(2)
c/Å	48.1269(14)	26.680(3)
α/°	90	90
β/°	90	90
γ/°	120	90
Volume/Å^3	15641.1(8)	13552(2)
Z	18	8
ρ_{calc}g/cm^3	1.297	1.511
μ/mm^{-1}	0.660	0.421
F(000)	6516.0	6296.0
Crystal size/mm^3	0.380 × 0.330 × 0.210	0.5 × 0.3 × 0.2
Radiation	MoKα (λ = 0.71073)	MoKα (λ = 0.71073)
2Θ range for data	2.57 to 49.982°	3.014 to 69.836°

collection/°		
Index ranges	$-20 \leq h \leq 22$, $-23 \leq k \leq 23$, $-57 \leq l \leq 57$	$-31 \leq h \leq 30$, $-40 \leq k \leq 40$, $-42 \leq l \leq 22$
Reflections collected	56089	259812
Independent reflections	6124[R(int) = 0.0480]	28701[R(int) = 0.0932]
Data/restraints/parameters	6124/0/412	28701/138/1046
Goodness-of-fit on F^2	1.088	1.027
Final R indexes [I>=2σ (I)]	$R_1 = 0.0738$, $wR_2 = 0.1910$	$R_1 = 0.0747$, $wR_2 = 0.1811$
Final R indexes [all data]	$R_1 = 0.0825$, $wR_2 = 0.2046$	$R_1 = 0.1609$, $wR_2 = 0.2254$
Largest diff. peak/hole / e $Å^{-3}$	3.13/-0.82	1.42/-0.99

Table A1.15: Crystal data and structure refinement for [(NArP$_3$)CoCl][BPh$_4$]

Identification code	**[(NArP$_3$)CoCl][BPh$_4$]**
Empirical formula	C63H80BClCoNP3
Formula weight	1049.38
Temperature/K	100
Crystal system	triclinic
Space group	P-1
a/Å	10.9491(7)
b/Å	14.9096(10)
c/Å	17.8512(11)
α/°	83.935(3)
β/°	79.063(3)
γ/°	89.303(3)
Volume/Å^3	2845.1(3)
Z	2
ρ_{calc}g/cm^3	1.225
μ/mm^{-1}	0.472
F(000)	1118
Crystal size/mm^3	0.06 × 0.04 × 0.02
Radiation	MoKα (λ = 0.71073)
2Θ range for data	2.746 to 59.26

collection/°	
Index ranges	$-15 \leq h \leq 15$, $-20 \leq k \leq 20$, $-24 \leq l \leq 24$
Reflections collected	103727
Independent reflections	15990 [Rint = 0.0972, Rsigma = 0.0851]
Data/restraints/parameters	15990/0/646
Goodness-of-fit on F^2	1
Final R indexes [I>=2σ (I)]	R1 = 0.0457, wR2 = 0.0837
Final R indexes [all data]	R1 = 0.0986, wR2 = 0.0978
Largest diff. peak/hole / e Å^{-3}	0.53/-0.53

A1.5 DFT Calculations

Table A1.16: DFT Calculations

Optimized coordinates (Å) for

$(CP_3)Co(N_2)$

Co	-6.493886	11.262439	3.205589
N	-6.498954	11.321632	1.436042
N	-6.509619	11.385450	0.291428
P	-8.326503	12.522417	3.530507
P	-4.468119	12.255409	3.466626
P	-6.717203	9.021548	3.482688
C	-6.448223	11.249419	5.315842
C	-7.421986	10.199514	5.854976
C	-6.831755	12.659131	5.809506
C	-3.940694	11.432267	5.038929
C	-7.788337	13.400564	5.064772
C	-5.023737	10.903746	5.778111
C	-7.568622	8.990937	5.132867
C	-7.603117	15.265630	6.637577
H	-7.887795	16.279035	6.939901
C	-4.742746	10.136998	6.931716
H	-5.568096	9.715601	7.513927
C	-8.127028	10.359559	7.068594
H	-8.021476	11.293607	7.630781
C	-2.350013	10.456601	6.623530
H	-1.315073	10.282269	6.938001
C	-3.418954	9.904690	7.345217
H	-3.227213	9.293903	8.234740
C	-8.171005	14.688130	5.486194
H	-8.895772	15.267989	4.902966
C	-6.290306	13.242663	6.974586
H	-5.546257	12.689483	7.558133
C	-6.663915	14.537630	7.381966
H	-6.211178	14.975618	8.278356
C	-2.618218	11.224609	5.475974
H	-1.778935	11.644663	4.910620
C	-8.973486	9.348391	7.556041
H	-9.520264	9.499953	8.493350
C	-9.117028	8.151983	6.838150
H	-9.780016	7.359107	7.201788
C	-8.410860	7.978161	5.633634
H	-8.543338	7.044435	5.079921
C	-8.870946	13.927902	2.377234
H	-9.579139	14.549161	2.960254
C	-7.900856	7.939713	2.420048
H	-8.881225	8.224247	2.846787
C	-2.974980	11.978914	2.306120

H -2.138575 12.558042 2.749566
C -11.073490 12.803315 4.510635
H -11.460515 13.353930 3.634190
H -10.701499 13.537242 5.246478
H -11.933946 12.280737 4.970473
C -3.155907 14.432185 4.936140
H -2.159615 14.205199 4.513040
H -3.263170 13.874622 5.878956
H -3.168058 15.512103 5.177167
C -4.285126 14.122349 3.935571
H -5.248225 14.315181 4.440866
C -9.996182 11.777970 4.114182
H -9.674600 11.254092 5.032798
C -5.136224 6.885483 4.794468
H -5.782644 6.041163 4.502203
H -5.478636 7.259548 5.772591
H -4.112307 6.486414 4.928211
C -5.111683 8.001046 3.732927
H -4.436670 8.792666 4.106835
C -4.174136 15.079503 2.733239
H -4.366117 16.114986 3.072409
H -4.893794 14.855473 1.930931
H -3.157001 15.064980 2.302688
C -9.609634 13.412697 1.125076
H -9.843467 14.265270 0.459541
H -10.561744 12.918383 1.372599
H -8.989970 12.703071 0.551246
C -10.558264 10.713993 3.153910
H -11.275419 10.065197 3.690750
H -9.756200 10.075649 2.751813
H -11.095315 11.160582 2.300029
C -7.678939 14.805649 1.967150
H -6.977841 14.237435 1.333723
H -7.125591 15.188887 2.840252
H -8.036167 15.674064 1.381632
C -4.537403 7.491093 2.393519
H -3.454400 7.295446 2.497673
H -4.667629 8.216410 1.571018
H -5.011330 6.545616 2.083009
C -7.792465 6.401362 2.524942

H	-8.705875	5.949101	2.092706
H	-7.694497	6.030410	3.555785
H	-6.938697	6.010390	1.948296
C	-7.904811	8.352731	0.936507
H	-6.920300	8.196505	0.460825
H	-8.178301	9.409648	0.801834
H	-8.640228	7.738209	0.384056
C	-3.216013	12.483650	0.865156
H	-3.500306	13.543308	0.807540
H	-4.003415	11.894901	0.368387
H	-2.285833	12.356421	0.279678
C	-2.570856	10.495897	2.228057
H	-3.389036	9.905335	1.785547
H	-2.324313	10.056729	3.207090
H	-1.685878	10.388535	1.571978

Total Energy: -3957.61934856 E_h

(BP86/6-311++G**)

Optimized coordinates (Å) for

[(TPB)Co(N_2)]$^-$

Co	5.278117	27.030827	17.095131
P	6.125307	28.046072	18.886124
P	3.060970	26.876003	16.921108
P	6.470673	27.144088	15.217970
N	5.627731	25.347668	17.547636
B	4.817109	29.224289	16.525303
C	5.694135	28.434162	14.141827
C	6.659431	29.741719	18.371700
C	8.356512	27.596015	15.041523
H	8.852351	26.898761	15.744263
C	2.349616	28.554979	17.254355
C	5.919014	30.203287	17.243942
C	4.249169	30.366935	14.143766
H	3.613935	31.089718	14.672539
C	3.298031	29.589854	17.025977
C	2.039333	26.364325	15.342342
H	2.508052	25.411985	15.027534
C	8.632318	29.033776	15.509744
H	9.724234	29.225133	15.517654
H	8.240887	29.232546	16.516177
H	8.165162	29.763658	14.825147
C	5.776139	28.504122	12.734994

H	6.347344	27.754542	12.173135	H	7.469612	23.621753	13.990762
C	4.916069	29.360531	14.888824	C	8.994765	27.410878	13.648312
C	7.654097	30.537197	18.977000	H	8.510202	28.063279	12.900483
H	8.234583	30.154477	19.825542	H	8.967805	26.373773	13.274978
C	7.696175	27.281935	19.678655	H	10.061346	27.711202	
H	8.113875	28.047126	20.361713	13.698303			
C	6.505175	25.578416	14.108638	C	2.863843	30.916667	17.272552
H	6.911463	25.889319	13.126608	H	3.572857	31.743962	17.141225
C	5.097816	25.012789	13.875878	C	7.207457	32.308686	17.379210
H	5.149571	24.119288	13.221278	H	7.426705	33.305361	16.974755
H	4.435311	25.751866	13.395731	C	5.200391	28.462003	20.552587
H	4.640644	24.714059	14.833576	H	4.768821	27.487389	20.853188
C	8.769269	26.956916	18.629434	C	4.046442	29.450732	20.325145
H	9.662297	26.521936	19.121695	H	3.455086	29.562047	21.256355
H	9.088697	27.858071	18.080500	H	3.367768	29.136369	19.521294
H	8.389141	26.224844	17.897330	H	4.435636	30.447730	20.053591
C	5.086680	29.504431	12.026363	N	5.856363	24.255842	17.849517
H	5.132996	29.537479	10.930024	C	2.156451	25.748101	18.179342
C	6.213374	31.510860	16.783934	H	1.079237	25.995091	18.113992
H	5.686654	31.896838	15.901416	C	2.219078	27.389988	14.211139
C	7.428237	24.484391	14.686274	H	1.747463	27.013325	13.281694
H	7.051899	24.114548	15.653220	H	3.274732	27.607010	13.999641
H	8.463576	24.833229	14.841144	H	1.735394	28.347886	14.470504

C	4.325635	30.444635	12.741090	H	0.020513	27.043374	15.878152
H	3.772521	31.226887	12.204249	H	0.291949	25.313607	16.248614
C	7.366421	26.022881	20.507880	H	0.074957	25.846405	14.563890
H	6.952413	25.222948	19.873021	C	0.654345	30.165915	17.966300
H	6.643132	26.219178	21.317461	H	-0.349915	30.380368	
H	8.291398	25.631095	20.977402	18.352394			
C	7.941743	31.818806	18.473149	C	2.613088	26.022466	19.619329
H	8.737444	32.423937	18.925743	H	2.062411	25.370398	20.325778
C	2.330158	24.252065	17.843386	H	2.433085	27.070631	19.910027
H	3.384122	23.944599	17.933429	H	3.692725	25.819015	19.729581
H	1.991543	23.999396	16.823928	C	6.065299	28.994192	21.714186
H	1.738459	23.637376	18.550680	H	6.545033	29.952417	21.444344
C	1.569705	31.207822	17.738468	H	6.851377	28.295209	22.046501
H	1.280539	32.247270	17.943962	H	5.415134	29.194200	22.590266
C	1.047615	28.839125	17.714406				
H	0.337713	28.028272	17.918176	Total Energy: -3944.45818385 E_h			
C	0.527783	26.123393	15.537653	(BP86/6-311++G**)			

A1.6 Additional Characterization of Complexes

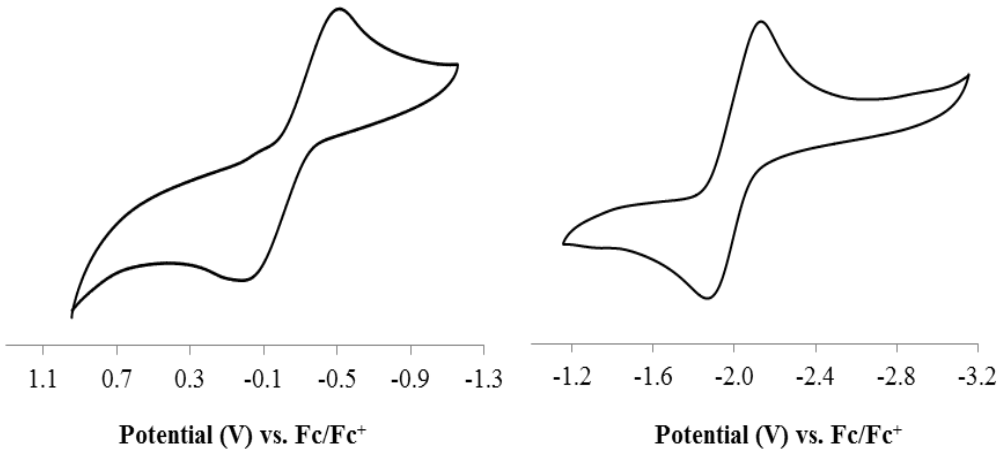

Figure A1.4: Cyclic voltammagram of (TPB)Co(N_2) (**1**) scanning oxidatively (left) and reductively (right) at 100 mV/sec in THF with 0.1 M $TBAPF_6$ electrolyte.

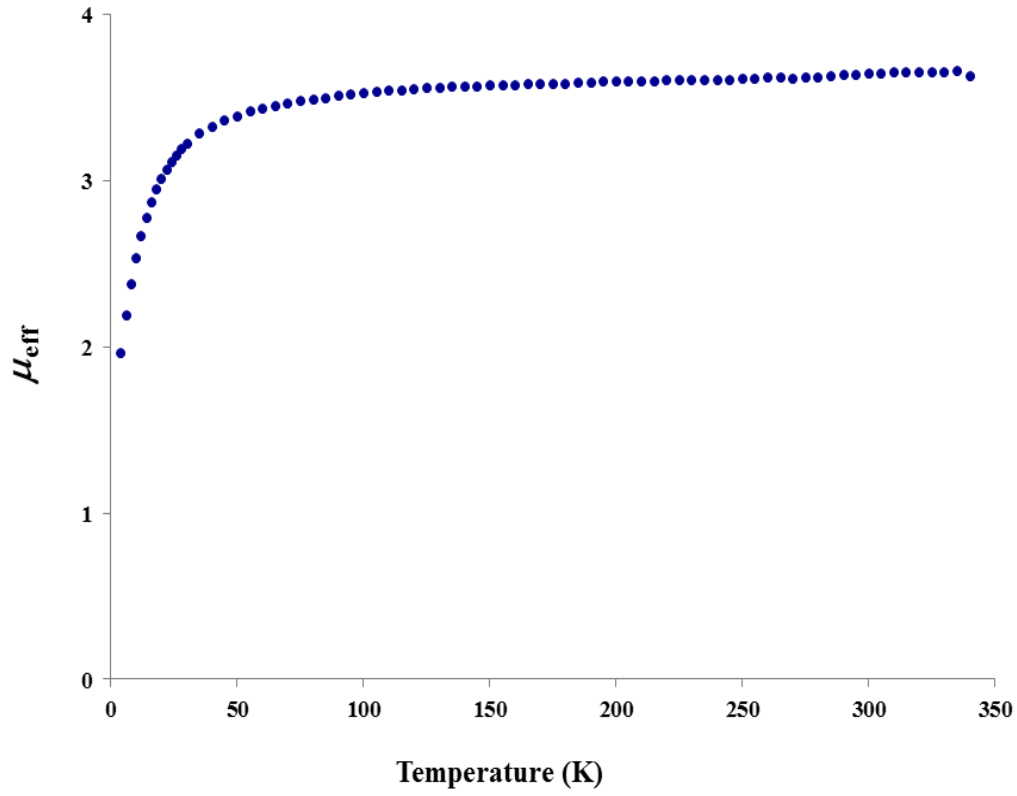

Figure A1.5: Temperature dependence of the magnetic susceptibility of [(TPB)Co][$BAr^F{}_4$] (**3**) as measured by SQUID magnetometry.

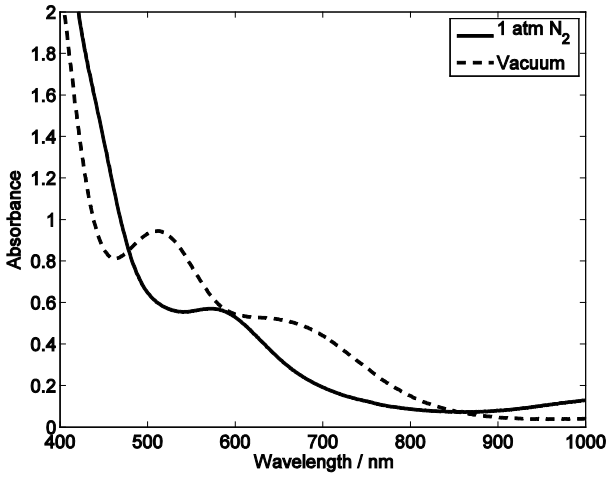

Figure A1.6: UV-Vis spectra of **6** under 1 atm N_2 and under static vacuum (after three freeze-pump-thaw cycles). Spectra collected of a 1 mM solution of **6** in THF at 298 K.

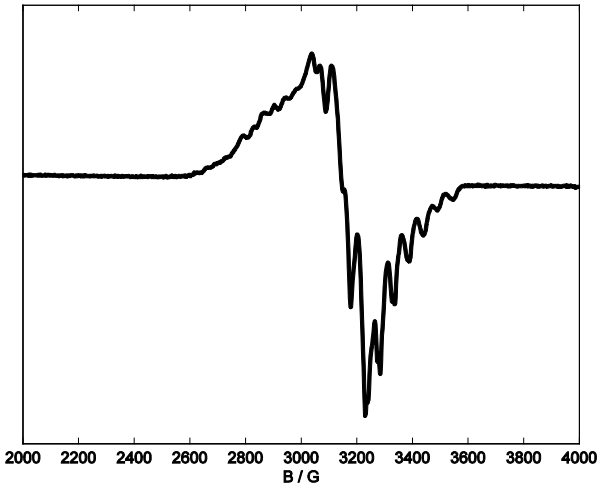

Figure A1.7: X-band EPR spectrum of **6** collected under 1 atm N_2 in 2-Me-THF at 80 K. No low-field features were detected.

A1.7 REFERENCES

1 Brookhart, M.; Grant, B.; Volpe Jr., A. F. *Organometallics* **1992**, *11*, 3920–3922.

2 Wietz, I. S.; Rabinovitz, M. J. *J. Chem. Soc., Perkin Trans.* **1993**, *1*, 117.

3 Suess, D. L. M.; Tsay, C.; Peters, J. C. *J. Am. Chem. Soc.* **2012**, *134*, 14158.

4 Whited, M. T.; Mankad, N. P.; Lee, Y.; Oblad, P. F.; Peters, J. C. *Inorg. Chem.* **2009**, *48*, 2507.

5 MacBeth, C. E.; Harkins, S. B.; Peters, J. C. *Can. J. Chem.* **2005**, *83*, 332.

6 Lin, T.-P.; Peters, J. C. *J. Am. Chem. Soc.* **2013**, *135*, 15310.

7 Creutz, S. E.; Peters, J. C. *J. Am. Chem. Soc.* **2014**, *136*, 1105.

8 Cotton, F. A.; Faut, O. D.; Goodgame, D. M. L.; Holm, R. H. *J. Am. Chem. Soc.* **1961**, *83*, 1780.

9 Evans, D. F. *J. Chem. Soc.* **1959**, 2003.

10 Nesse, F. *Comput. Mol. Sci.* **2012**, *2*, 73.

11(a) Hehre, W. J.; Ditchfield, R.; Pople, J. A. *J. Chem. Phys.* **1972**, *56*, 2257. (b) J. D.; Pople, J. A. *J. Chem. Phys.* **1975**, *62*, 2921. (c) Krishnan, R.; Binkley, J. S.; Seeger, R.; Pople, J. A. *J. Chem. Phys.* **1980**, *72*, 650. (d) McLean, A. D.; Chandler, G. S. *J. Chem. Phys.* **1980**, *72*, 5639. (e) Francl, M. M.; Pietro, W. J.; Hehre, W. J.; Binkley, J. S.; Gordon, M. S.; DeFrees, D. J.; Pople, J. A. *J. Chem. Phys.* **1982**, *77*, 3654. (f) Clark, T.; Chandrasekhar, J.; Schleyer, P. V. R. *J. Comp. Chem.* **1983**, *4*, 294. (g) Rassolov, V. A.; Pople, J. A.; Ratner, M. A.; Windus, T. L. *J. Chem. Phys.* **1998**, *109*, 1223.

12 Schaefer, A.; Horn, H.; Ahlrichs, R. *J. Chem. Phys.* **1992**, *97*, 2571.

13 Breneman, C. M.; Wiberg, K. B. *J. Comput. Chem.* **1990**, *11*, 361.

14 GaussView, Version 5, Dennington, Roy; Keith, Todd; Millam, John. Semichem Inc., Shawnee Mission, KS, 2009.

15 Weatherburn, M. W. *Anal. Chem.* **1967**, *39*, 971.

16 Watt, G. W.; Chrisp, J. D. *Anal. Chem.* **1952**, *24*, 2006.

Appendix 2

SUPPLEMENTARY INFORMATION FOR CHAPTER 3: A SYNTHETIC SINGLE-SITE FE NITROGENASE: HIGH TURNOVER, FREEZE-QUENCH ^{57}FE MÖSSBAUER DATA, AND A HYDRIDE RESTING STATE

Reproduced in part with permission from:

Del Castillo, T.; Thompson, N.; Peters, J. C.; *J. Am. Chem. Soc.*, **2016**, *138,* 5341-5350.

DOI: 10.1021/jacs.6b01706

A2.1 Experimental details

General considerations:

All manipulations were carried out using standard Schlenk or glovebox techniques under an N_2 atmosphere. Solvents were deoxygenated and dried by thoroughly sparging with N_2 followed by passage through an activated alumina column in a solvent purification system by SG Water, USA LLC. Nonhalogenated solvents were tested with sodium benzophenone ketyl in tetrahydrofuran (THF) in order to confirm the absence of oxygen and water. Deuterated solvents were purchased from Cambridge Isotope Laboratories, Inc., degassed, and dried over activated 3-Å molecular sieves prior to use.

KC_8,[1] [Na(12-crown-4)$_2$][P_3^BFe-N_2] (**1**),[2] [K(OEt_2)$_{0.5}$][P_3^CFe-N_2] (**2**),[3] [Na(12-crown-4)$_2$][P_3^{Si}Fe-N_2] (**3**),[4] (P_3^B)(μ-H)Fe(H)(N_2) (**4-N_2**),[5] (P_3^B)(μ-H)Fe(H)(N_2) (**4-H_2**),[5] [P_3^BFe-NH_3][$BAr^F{}_4$],[6] [P_3^BFe-N_2H_4][$BAr^F{}_4$],[6] P_3^BFe-NH_2,[6] [P_3^BFe][$BAr^F{}_4$],[6] P_3^BFe-NAd,[7] and [P_3^BFe-NAd][$BAr^F{}_4$][7] were prepared according to literature procedures. $NaBAr^F{}_4$ and [H(OEt_2)$_2$][$BAr^F{}_4$] ($HBAr^F{}_4$) were prepared and purified according to a procedure modified from the literature as described below. All other reagents were purchased from commercial vendors and used without further purification unless otherwise stated. Diethyl ether (Et_2O) and THF used NH_3 generation experiments were stirred over Na/K (≥ 2 hours) and filtered before use.

Physical Methods:

^{1}H chemical shifts are reported in ppm relative to tetramethylsilane, using ^{1}H resonances from residual solvent as internal standards. IR measurements were obtained as solutions or thin films formed by evaporation of solutions using a Bruker Alpha Platinum ATR spectrometer with OPUS software (solution IR collected in a cell with KBr windows and a 1 mm pathlength). Optical spectroscopy measurements were collected with a Cary 50 UV-vis spectrophotometer using a 1-cm two-window quartz cell. H_2 was quantified on an Agilent 7890A gas chromatograph (HP-PLOT U, 30 m, 0.32 mm ID; 30 °C isothermal; nitrogen carrier gas) using a thermal conductivity detector. Cyclic voltammetry measurements were carried out in a glovebox under an N_2 atmosphere in a one-compartment cell using a CH Instruments 600B electrochemical analyzer. A glassy carbon electrode was used as the working electrode and platinum wire was used as the auxiliary electrode. The reference electrode was Ag/AgOTf in Et_2O isolated by a CoralPor™ frit

(obtained from BASi). The ferrocene couple (Fc/Fc^+) was used as an external reference. Et_2O solutions of electrolyte (0.1 M $NaBAr^F{}_4$) and analyte were also prepared under an inert atmosphere.

Mössbauer Spectroscopy:

Mössbauer spectra were recorded on a spectrometer from SEE Co. (Edina, MN) operating in the constant acceleration mode in a transmission geometry. The sample was kept in an SVT-400 cryostat form Janis (Wilmington, MA). The quoted isomer shifts are relative to the centroid of the spectrum of a metallic foil of α-Fe at room temperature. Solid samples were prepared by grinding solid material into a fine powder and then mounted in to a Delrin cup fitted with a screw-cap as a boron nitride pellet. Solution samples were transferred to a sample cup and chilled to 77 K inside of the glovebox, and unless noted otherwise, quickly removed from the glovebox and immersed in liquid N_2 until mounted in the cryostat. Data analysis was performed using version 4 of the program WMOSS (www.wmoss.org) and quadrupole doublets were fit to Lorentzian lineshapes. See discussion below for detailed notes on the fitting procedure.

Ammonia Quantification:

Reaction mixtures are cooled to 77 K and allowed to freeze. The reaction vessel is then opened to atmosphere and to the frozen solution is slowly added a fourfold excess (with respect to acid) solution of a NaO^tBu solution in MeOH (0.25 mM) over 1–2 minutes. This solution is allowed to freeze, then the headspace of the tube is evacuated and the tube is sealed. The tube is then allowed to warm to RT and stirred at room temperature for 10

minutes. An additional Schlenk tube is charged with HCl (3 mL of a 2.0 M solution in Et_2O, 6 mmol) to serve as a collection flask. The volatiles of the reaction mixture are vacuum transferred into this collection flask. After completion of the vacuum transfer, the collection flask is sealed and warmed to room temperature. Solvent is removed in vacuo, and the remaining residue is dissolved in H_2O (1 mL). An aliquot of this solution (20–100 μL) is then analyzed for the presence of NH_3 (present as NH_4Cl) by the indophenol method.[8] Quantification is performed with UV−vis spectroscopy by analyzing absorbance at 635 nm.

A2.2 Synthetic Details:

Synthesis and Purification of $NaBAr^F_4$ and $[H(OEt_2)_2][BAr^F_4]$:

Crude $NaBAr^F_4$ was prepared according to a literature procedure.[9] The crude material, possessing a yellow-tan hue, was purified by a modification to the procedure published by Bergman,[10] as follows. The crude $NaBAr^F_4$ was ground into a fine powder and partially hydrated by exposure to air for at least 24 hours ($NaBAr^F_4$ is a hygroscopic solid and crystallizes as a hydrate containing between 0.5–3.0 equivalents of H_2O when isolated under air). This material was first washed with dichloromethane (~3 mL/g, in three portions), washing liberally with pentane between each portion of dichloromethane. The remaining solids were washed with boiling fluorobenzene (~1 mL/g, in three portions), to yield a bright white powder. Anhydrous $NaBAr^F_4$ was obtained by drying this material under vacuum at 100 °C over P_2O_5 for at least 18 hours. Note that additional $NaBAr^F_4$ may

be recrystallized from the fluorobenzene washings via slow diffusion of pentane vapors at room temperature, and further purified if necessary.

Crude $[H(OEt_2)_2][BAr^F{}_4]$ was prepared according to a literature procedure, using $NaBAr^F{}_4$ purified as described above.[11] The crude material was purified by iterative recrystallization from 4 mL/g Et_2O layered with an equivalent volume of pentane at -30 °C. The purity of the recrystallized $[H(OEt_2)_2][BAr^F{}_4]$ was assayed by collecting a UV-vis spectrum of a 10 mM solution in Et_2O, where the presence of yellow-brown impurities appears as a broad absorbance centered at ~330 nm (see Fig. S2.1). Typically 2–3 recrystallizations were required to obtain material of suitable purity for catalytic reactions.

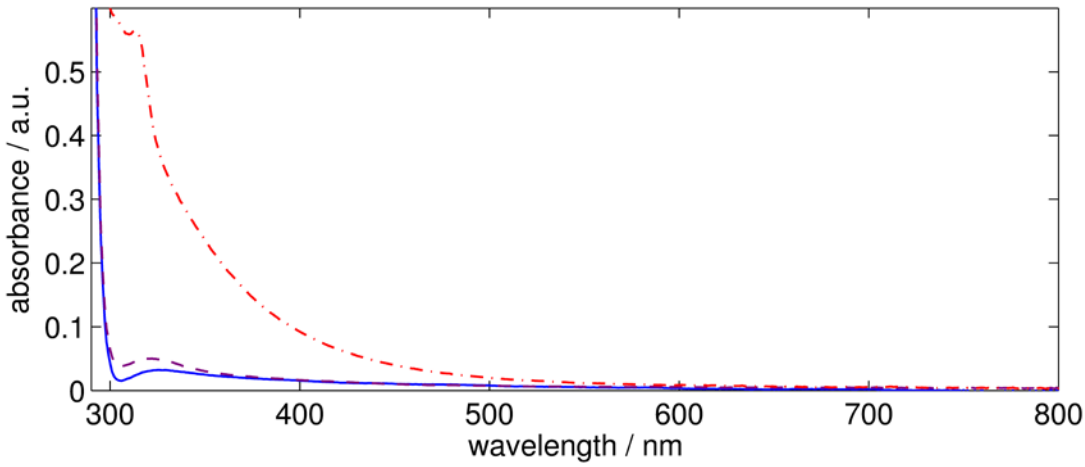

Figure A2.2.1: UV-vis traces of 10 mM solutions of $[H(OEt_2)_2][BAr^F{}_4]$ in Et_2O at various stages of purity. (Red dash-dotted trace) $[H(OEt_2)_2][BAr^F{}_4]$ prepared from crude $NaBAr^F{}_4$ without additional purification; (Purple dotted trace) $[H(OEt_2)_2][BAr^F{}_4]$ prepared from $NaBAr^F{}_4$ purified according to the above procedure, and recrystallized once; (Blue solid

trace) $[H(OEt_2)_2][BAr^F{}_4]$ prepared from $NaBAr^F{}_4$ purified according to the above procedure, and recrystallized twice.

Preparation of 10 wt% Na(Hg) shot:

In a three-neck round bottom flask equipped with a mechanical stirrer, reflux condenser, and a dropping funnel was added Na (0.5 g) and a sufficient volume of toluene to completely submerse the Na. The dropping funnel was charged with 5 grams of Hg. The toluene was brought to reflux and the molten Na was finely dispersed by rapid agitation with the mechanical stirrer, at which point the Hg was added in one shot. *Caution: upon contact with Na, the Hg vapors boil and there is a brief but intense exotherm.* The pelleted 10 wt% Na(Hg) immediately forms, at which point the toluene is decanted, and the shot is washed with Et_2O and pentane before being dried in vacuo. After breaking up coagulated pieces, this procedure yields somewhat uniform shot ranging 1–3 mm in diameter.

A2.3 Ammonia production and quantification studies

Standard NH_3 Generation Reaction Procedure with $[Na(12\text{-crown-}4)_2][P_3{}^BFe\text{-}N_2]$ (1):

All solvents are stirred with Na/K for ≥2 hours and filtered prior to use. In a nitrogen-filled glovebox, a stock solution of **1** in THF (9.5 mM) is prepared. Note that a fresh stock solution is prepared for each experiment and used immediately. An aliquot of this stock solution (50–200 μL, 0.47–1.9 μmol) is added to a Schlenk tube and evaporated to dryness under vacuum, depositing a film of **1**. The tube is then charged with a stir bar and cooled to 77 K in a cold well. To the cold tube is added a solution of $HBAr^F{}_4$ in Et_2O.

This solution is allowed to cool and freeze for 5 minutes. Then a suspension of KC_8 in Et_2O (1.2 equiv relative to $HBAr^F_4$) is added to the cold tube. The temperature of the system is allowed to equilibrate for 5 minutes and then the tube is sealed with a Teflon screw-valve. This tube is passed out of the box into a liquid N_2 bath and transported to a fume hood. The tube is then transferred to a dry ice/acetone bath where it thaws and is allowed to stir at -78 °C for the desired length of time. At this point the tube is allowed to warm to room temperature with stirring, and stirred at room temperature for 5 minutes. To ensure reproducibility, all experiments were conducted in 200 mL Schlenk tubes (51 mm OD) using 25 mm stir bars, and stirring was conducted at ~900 rpm.

Table A2.3.1: UV-vis quantification results for standard NH_3 generation experiments with **1**

Entry	**Total volume of Et_2O (mL)**	**1 µmol (mM)**	**$[H(OEt_2)_2][BAr^F_4]$ equiv (mM)**	**NH_4Cl (µmol)**	**Equiv NH_3/Fe**	**% Yield Based on H^+**
A	1.5	1.9 (1.3)	48 (63)	13.2	7.0	43.2
B	1.5	1.9 (1.3)	48 (63)	14.5	7.6	47.2
Avg.	—	—	—	—	7.3 ± 0.5	45 ± 3
C	3.0	1.9 (0.64)	97 (63)	22.1	11.6	35.9
D	3.0	1.9 (0.64)	97 (63)	25.1	13.2	40.8
Avg.	—	—	—	—	12 ± 1	38 ± 3

E	1.1	0.48 (0.43)	150 (63)	8.34	17.5	36.1
F	1.1	0.48 (0.43)	150 (63)	8.19	17.2	35.5
Avg.	—	—	—	—	17.4 ± 0.2	35.8 ± 0.4
G	5.5	0.48 (0.087)	730 (63)	23.3	48.9	20.2
H	5.5	0.48 (0.087)	730 (63)	20.3	42.5	17.6
I	5.5	0.48 (0.087)	730 (63)	19.1	40.2	16.6
J	1.4	0.12 (0.087)	730 (63)	4.82	40.5	16.7
Avg.	—	—	—	—	43 ± 4	18 ± 2
K	11.0	0.48 (0.043)	1500 (63)	28.4	59.5	12.3
L	11.0	0.48 (0.043)	1500 (63)	27.1	56.8	11.7
M	11.0	0.48 (0.043)	1500 (63)	22.9	48.1	9.9
N	11.0	0.48 (0.043)	1500 (63)	25.4	53.4	11.0

O		0.48				
	11.0	(0.043)	1500 (63)	30.2	63.5	13.1
P		0.12				
	2.8	(0.043)	1500 (63)	7.67	64.4	13.3
Q		0.12				
	2.8	(0.043)	1500 (63)	7.53	63.3	13.0
R		0.12				
	2.8	(0.043)	1500 (63)	7.67	64.4	13.3
S		0.12				
	2.8	(0.043)	1500 (63)	6.85	57.5	11.9
Avg.	—	—	—	—	59 ± 6	12 ± 1

Hydrazine was not detected in the catalytic runs using a standard UV-Vis quantification method.[12]

Standard NH_3 Generation Reaction Procedure with $[K(OEt_2)_{0.5}][P_3^CFe\text{-}N_2]$ (2):

The procedure was identical to that of the standard NH_3 generation reaction protocol with the changes noted. The precursor used was **2**.

Table A2.3.2: UV-vis quantification results for standard NH_3 generation experiments with **2**

Entry	Total volume of Et_2O (mL)	2 µmol (mM)	$[H(OEt_2)_2][BAr^F_4]$ equiv (mM)	NH_4Cl (µmol)	Equiv NH_3/Fe	% Yield Based on H^+
A*	2.5	2.5 (1.0)	37 (37)	—	4.6 ± 0.8	36 ± 6
B	1.1	0.63 (0.56)	110 (60)	6.66	10.7	29.7
C	1.1	0.63 (0.56)	110 (60)	7.41	11.9	33.0
Avg.	—	—	—	—	11.3 ± 0.9	31 ± 2
D	2.3	0.63 (0.28)	220 (60)	7.41	11.9	16.4
E	2.3	0.63 (0.28)	220 (60)	9.89	15.8	21.9
Avg.	—	—	—	—	14 ± 3	19 ± 4
F	2.0	0.16 (0.080)	750 (60)	2.49	15.6	6.2
G	2.0	0.16 (0.080)	750 (60)	3.50	21.9	8.8
Avg.	—	—	—	—	19 ± 4	7 ± 2
H	4.0	0.16 (0.040)	1500 (60)	7.46	46.8	9.3
I	4.0	0.16 (0.040)	1500 (60)	4.63	29.0	5.8
J	4.0	0.16 (0.040)	1500 (60)	5.82	36.5	7.3
K	4.0	0.16 (0.040)	1500 (60)	5.56	34.8	6.9
L	4.0	0.16 (0.040)	1500 (60)	5.13	32.1	6.4
Avg.	—	—	—	—	36 ± 7	7 ± 1

Hydrazine was not detected in the catalytic runs using a standard UV-Vis quantification method.[12]

* Data for entry A is an average of experiments described in reference 3.

Standard NH_3 Generation Reaction Procedure with $[Na(12\text{-crown-}4)_2][P_3^{Si}Fe\text{-}N_2]$ (3):

The procedure was identical to that of the standard NH_3 generation reaction protocol with the changes noted. The precursor used was **3**.

Table A2.3.3: UV-vis quantification results for standard NH_3 generation experiments with **3**

Entry	Total volume of Et_2O (mL)	3 µmol (mM)	$[H(OEt_2)_2][BAr^F_4]$ equiv (mM)	NH_4Cl (µmol)	Equiv NH_3/Fe	% Yield Based on H^+
A*	3.25	1.9 (0.58)	49 (28)	—	0.8 ± 0.5	5 ± 3
B	3.0	0.12 (0.039)	1500 (60)	0.516	4.4	0.9
C	3.0	0.12 (0.039)	1500 (60)	0.380	3.2	0.6
Avg.	—	—	—	—	3.8 ± 0.8	0.8 ± 0.2

Hydrazine was not detected in the catalytic runs using a standard UV-Vis quantification method.[12]

* Data for entry A is an average of experiments described in reference 13.

Standard NH_3 Generation Reaction Procedure with $(P_3^B)(\mu\text{-}H)Fe(H)(N_2)$ (4-N_2):

The procedure was identical to that of the standard NH_3 generation reaction protocol with the changes noted. The precursor used was **4-N2**. Note that **4-N_2** is not indefinitely stable in the solid state, even at -30 °C; accordingly **4-N_2** was used within 24 hours after isolation as a solid. The addition of toluene was necessary to load the precatalyst volumetrically. The final solvent composition for entries A and B was 3% toluene in Et_2O. The final solvent composition for entries C and D was 25% toluene in Et_2O.

Table A2.3.4: UV-vis quantification results for standard NH_3 generation experiments with **4-N_2**

Entry	**Total volume of (mL)**	**4-N_2 µmol (mM)**	**$[H(OEt_2)_2]$ $[BAr^F{}_4]$ equiv (mM)**	**NH_4Cl (µmol)**	**Equiv NH_3/Fe**	**% Yield Based on H^+**
A	1.1	0.48 (*)	150 (63)	0.582	1.19	2.56
B	1.1	0.48 (*)	150 (63)	0.490	1.00	2.15
Avg.	—	—	—	—	1.1 ± 0.1	2.4 ± 0.3
C	1.7	0.74 (0.44)	150 (63)	3.66	4.95	10.3
D	1.7	0.74 (0.44)	150 (63)	4.63	6.26	13.0
Avg.	—	—	—	—	5.6 ± 0.9	12 ± 2

Hydrazine was not detected in the catalytic runs using a standard UV-Vis quantification method.[12]

* **4-N_2** not fully soluble under these conditions.

NH_3 Generation Reaction Procedure with (1) with the inclusion of NH_3:

A standard catalytic reaction was prepared according to the procedure detailed in section 3.1. After the frozen Schlenk tube was removed from the glovebox, it was brought to a Schlenk line and attached to the line via a 0.31 mL calibrated volume (corresponding to 12.7 μmol gas when filled at 21 °C and 1 atm). The gas manifold of the line was first filled with N_2 by three pump-refill cycles, and subsequently sparged (through a mineral oil bubbler) with $NH_{3(g)}$ for 30 minutes, passing the $NH_{3(g)}$ through a -30 °C trap to remove adventitious water. At this point the calibrated volume was filled with $NH_{3(g)}$ via 5 pump-refill cycles, and then sealed from the gas manifold. The frozen Schlenk tube was opened and allowed to equilibrate with the calibrated volume for 1 hour before it was resealed, and the reaction carried out in the usual manner. As a control, several trials were conducted with only an 2.0 M ethereal solution of HCl frozen in the tube, and it assumed that the average amount of NH_3 recovered in those trials was added to the catalytic reactions.

Table A2.3.5: UV-vis quantification results for NH_3 generation experiments with **1** with the inclusion of NH_3

Entry	**Total volume of Et_2O (mL)**	**1 μmol (mM)**	**$[H(OEt_2)_2][BAr^F{}_4]$ equiv (mM)**	**NH_4Cl (μmol)**	**NH_4Cl due to Fe (μmol)**	**Equiv NH_3/Fe**
A	3.0	0	0	12.5	N/A	N/A
B	3.0	0	0	11.8	N/A	N/A
C	3.0	0	0	12.1	N/A	N/A
D	3.0	0	0	12.0	N/A	N/A

E	3.0	0	0	12.2	N/A	N/A
Avg.	—	—	—	12.1 (95 % of expected value)		
C	1.1	0.48 (0.43)	150 (63)	15.1	3.0	6.3
D	1.1	0.48 (0.43)	150 (63)	15.2	3.1	6.5
Avg.	—	—	—	—	—	6.4 ± 0.1

Hydrazine was not detected in the catalytic runs using a standard UV-Vis quantification method.[12]

Standard NH_3 Generation Reaction Procedure with 1 using Na(Hg) as the reductant:

The procedure was identical to that of the standard NH_3 generation reaction protocol with the changes noted. The precursor used was **1** and 10 wt% Na(Hg) shot of approximately 1–3 mm diameter was employed as the reductant (1900 Na atom equiv relative to catalyst).

Table A2.3.6: UV-vis quantification results for standard NH_3 generation experiments with **1** using Na(Hg) as the reductant

Entry	**Total volume of Et_2O (mL)**	**1 µmol (mM)**	**$[H(OEt_2)_2]$ $[BAr^F{}_4]$ equiv (mM)**	**NH_4Cl (µmol)**	**Equiv NH_3/Fe**	**% Yield Based on H^+**
A	1.1	0.48 (0.43)	150 (63)	2.45	5.15	10.6
B	1.1	0.48 (0.43)	150 (63)	2.30	4.84	9.97
Avg.	—	—	—	—	5.0 ± 0.2	10.3 ± 0.5

Hydrazine was not detected in the catalytic runs using a standard UV-Vis quantification method.[12]

A2.4 NH_3 Generation Reaction with Periodic Substrate Reloading, Procedure with 1:

All solvents are stirred with Na/K for ≥2 hours and filtered prior to use. In a nitrogen-filled glovebox, a stock solution of [Na(12-crown-4)$_2$][P_3^BFe-N_2] (**1**) in THF (9.5 mM) is prepared. Note that a fresh stock solution is prepared for each experiment and used immediately. An aliquot of this stock solution (50-200 μL, 0.47-1.9 μmol) is added to a Schlenk tube. This aliquot is evaporated to dryness under vacuum, depositing a film of **1**. The tube is then charged with a stir bar and cooled to 77 K in a cold well. To the cold tube is added a solution of $HBAr^F_4$ (48 equiv with respect to **1**) in Et_2O. This solution is allowed to cool and freeze for 5 minutes. Then a suspension of KC_8 (1.3 equiv with respect to $HBAr^F_4$) in Et_2O is added to the cold tube. The temperature of the system is allowed to equilibrate for 5 minutes and then the tube is sealed. The cold well cooling bath is switched from a $N_{2(l)}$ bath to a dry ice/acetone bath. In the cold well the mixture in the sealed tube thaws with stirring and is allowed to stir at -78 °C for 40 minutes. Then, without allowing the tube to warm above -78 °C, the cold well bath is switched from dry ice/acetone to $N_{2(l)}$. After ten minutes the reaction mixture is observed to have frozen, at this time the tube is opened. To the cold tube is added a solution of $HBAr^F_4$ (48 equiv with respect to **1**) in Et_2O. This solution is allowed to cool and freeze for 5 minutes. Then a suspension of KC_8 (1.3 equiv with respect to $HBAr^F_4$) in Et_2O is added to the cold tube. The temperature of the system is allowed to equilibrate for 5 minutes and then the tube is sealed. The cold well cooling bath is switched from a $N_{2(l)}$ bath to a dry ice/acetone bath. In the cold well the

mixture in the sealed tube thaws with stirring and is allowed to stir at -78 °C for 40 minutes. These last steps are repeated for the desired number of loadings. Then the tube is allowed to warm to RT with stirring, and stirred at RT for 5 minutes.

Table A2.4.1: UV-vis quantification results for NH_3 generation experiments with 1, with reloading

Entry	Number of Loadings	4-N_2 µmol	$[H(OEt_2)_2]$ $[BAr^F{}_4]$ equiv	NH_4Cl (µmol)	Equiv NH_3/Fe	% Yield Based on H^+
A	1	1.9	48	13.3	6.96	43.2
B	1	1.9	48	14.5	7.60	47.2
Avg.	—	—	—	—	7.3 ± 0.5	45 ± 3
C	2	0.95	96	9.56	10.0	31.5
D	2	0.95	96	10.3	10.9	34.0
Avg.	—	—	—	—	10.4 ± 0.6	33 ± 2
C	2	0.95	150	13.4	14.1	32.7
D	2	0.95	150	14.9	15.6	29.4
Avg.	—	—	—	—	15 ± 1	31 ± 2
C	2	1.0	190	18.4	17.6	29.0
D	2	1.0	190	18.4	17.6	29.0
Avg.	—	—	—	—	17.6	29

A2.5 General Procedure for Time-resolved NH_3 Quantification via Low-temperature Quenching:

A typical catalytic reaction is prepared according to the procedure described above. The timer is set to zero as soon as the frozen reaction mixture is transferred to the dry ice/acetone bath; note that the average thaw time is 2.0 ± 0.3 minutes (measured for a 1.1 mL solution of Et_2O over 8 trials). At the desired reaction time, the Schlenk tube is rapidly transferred to a liquid N_2 bath and the reaction mixture is allowed to freeze. Under N_2 counterflow, a solution of ^{t}BuLi (1.6 M in hexanes, 4 equiv with respect to $HBAr^F_4$ is added to the frozen reaction mixture. The Schlenk tube is then sealed, thawed to -78 °C, and stirred rapidly for 10 minutes. The Schlenk tube is transferred to a liquid N_2 bath and the reaction mixture is re-frozen. The reaction vessel is opened to atmosphere and to the frozen solution is slowly added a fivefold excess (with respect to $HBAr^F_4$) solution of a NaO^{t}Bu solution in MeOH (0.25 mM) over 1–2 minutes. This solution is allowed to freeze, then the headspace of the tube is evacuated and the tube is sealed. The tube is then allowed to warm to RT and stirred at room temperature for 10 minutes. At this point the reaction is quantified for the presence of NH_3 (*vide supra*).

As a control to determine that the action of ^{t}BuLi is sufficiently fast to enable rapid quenching of catalytic reactions at low temperature, we added ^{t}BuLi to reaction mixtures prepared as described above before allowing them to thaw to -78 °C for the first time (effectively at time 0, Table A2.5.1, Entry A) and observed no detectable NH_3 formation.

Table A2.5.1: Time profiles for NH_3 generation by **1**

Entry	Total volume of Et_2O (mL)	1 µmol (mM)	$[H(OEt_2)_2]$ $[BAr^F{}_4]$ equiv (mM)	Quench time (min)	$[NH_3]$ (mM)	Equiv NH_3/Fe
A	3.0	1.9 (0.64)	48 (31)	0	0	0
B	3.0	1.9 (0.64)	48 (31)	5	1.21	1.91
C	3.0	1.9 (0.64)	48 (31)	5	1.87	2.94
Avg.	—	—	—	5	1.5 ± 0.5	2.4 ± 0.2
D	3.0	1.9 (0.64)	48 (31)	10	4.36	6.86
E	3.0	1.9 (0.64)	48 (31)	10	3.66	5.76
Avg.	—	—	—	10	4.0 ± 0.5	6.3 ± 0.8
F	3.0	1.9 (0.64)	48 (31)	15	4.87	7.68
G	3.0	1.9 (0.64)	48 (31)	15	4.63	7.29
Avg.	—	—	—	15	4.8 ± 0.2	7.5 ± 0.3
H	3.0	1.9 (0.64)	48 (31)	25	4.40	6.93
I	3.0	1.9 (0.64)	48 (31)	25	4.79	7.54
Avg.	—	—	—	25	4.6 ± 0.3	7.2 ± 0.4
J	1.1	0.48 (0.43)	150 (63)	5	0.806	1.86
K	1.1	0.48 (0.43)	150 (63)	5	1.09	2.51
Avg.	—	—	—	5	0.9 ± 0.2	2.2 ± 0.5
L	1.1	0.48 (0.43)	150 (63)	10	2.08	4.81
M	1.1	0.48 (0.43)	150 (63)	10	2.74	6.33

Avg.	—	—	—	10	2.4 ± 0.5	6 ± 1
N	1.1	0.48 (0.43)	150 (63)	15	3.79	8.75
O	1.1	0.48 (0.43)	150 (63)	15	4.06	9.39
Avg.	—	—	—	15	3.9 ± 0.2	9.1 ± 0.4
P	1.1	0.48 (0.43)	150 (63)	25	5.73	13.2
Q	1.1	0.48 (0.43)	150 (63)	25	4.68	10.8
Avg.	—	—	—	25	5.2 ± 0.7	12 ± 2
R	1.1	0.48 (0.43)	150 (63)	35	6.11	14.1
S	1.1	0.48 (0.43)	150 (63)	35	5.51	12.7
Avg.	—	—	—	35	5.8 ± 0.4	13 ± 1
T	1.1	0.48 (0.43)	150 (63)	45	7.99	18.5
U	1.1	0.48 (0.43)	150 (63)	45	8.37	19.3
Avg.	—	—	—	45	8.2 ± 0.3	18.9 ± 0.6
V	1.1	0.48 (0.43)	150 (63)	55	7.18	16.6
W	1.1	0.48 (0.43)	150 (63)	55	7.94	18.3
Avg.	—	—	—	55	7.6 ± 0.5	17 ± 1

Hydrazine was not detected in the catalytic runs using a standard UV-Vis quantification method.[10]

Kinetic Study of NH_3 Generation by 1 via the Method of Initial Rates:

General procedure: Typical catalytic reactions were prepared at various concentrations of **1** and $HBAr^{F}_{4}$ (1.1 mL Et_2O total for each reaction). For each given

concentration of **1** and $HBAr^F_4$, the time profile of NH_3 generation was measured over the first 15 minutes by quenching reactions at 5, 10 and 15 minutes, as described above. The results of individual experiments are given in Table A2.5.2. The initial rate of NH_3 formation, $v_0 = \frac{d[NH_3]}{dt}(0)$ was measured as the slope of a least-squares linear regression for these data. For the cases where the timescale of the reaction was too fast to obtain pseudo-first-order behavior over the first 15 minutes, v_0 was approximated as the slope of the line between the yield of NH_3 at 5 minutes and a zero point at 2 minutes (the average thaw time for the reaction, *vide supra*); the results of this analysis are given in Table A2.5.3 and plotted in Figures A2.5.1 and A2.5.2. The reaction order in **1** and $HBAr^F_4$ was determined by applying a least-squares linear analysis to the initial rates determined for 5 different concentrations in each reagent, ranging over a factor of 16 (Table A2.5.4).

Table A2.5.2: Time resolved NH_3 quantification data used in initial rates analysis for NH_3 generation by **1**

Entry	**Total volume of Et_2O (mL)**	**1 µmol (mM)**	**$[H(OEt_2)_2][BAr^F_4]$ equiv (mM)**	**Quench time (min)**	**$[NH_3]$ (mM)**
A	1.1	0.12 (0.11)	560 (63)	5	0.268
B	1.1	0.12 (0.11)	560 (63)	5	0.273
Avg.	—	—	—	5	0.270 ± 0.004
C	1.1	0.12 (0.11)	560 (63)	10	0.225

D	1.1	0.12 (0.11)	560 (63)	10	0.338
Avg.	—	—	—	10	0.28 ± 0.08
E	1.1	0.12 (0.11)	560 (63)	15	0.747
F	1.1	0.12 (0.11)	560 (63)	15	1.27
Avg.	—	—	—	15	1.0 ± 0.4
G	1.1	0.24 (0.22)	290 (63)	5	0.538
H	1.1	0.24 (0.22)	290 (63)	5	0.763
Avg.	—	—	—	5	0.7 ± 0.2
I	1.1	0.24 (0.22)	290 (63)	10	1.81
J	1.1	0.24 (0.22)	290 (63)	10	1.29
Avg.	—	—	—	10	1.5 ± 0.4
K	1.1	0.24 (0.22)	290 (63)	15	3.47
L	1.1	0.24 (0.22)	290 (63)	15	2.23
Avg.	—	—	—	15	2.9 ± 0.9
M	1.1	0.95 (0.87)	73 (63)	5	1.98
N	1.1	0.95 (0.87)	73 (63)	5	1.64
Avg.	—	—	—	5	1.8 ± 0.2
O	1.1	0.95 (0.87)	73 (63)	10	5.36
P	1.1	0.95 (0.87)	73 (63)	10	4.20
Avg.	—	—	—	10	4.8 ± 0.8
Q	1.1	0.95 (0.87)	73 (63)	15	9.27
R	1.1	0.95 (0.87)	73 (63)	15	8.84

Avg.	—	—	—	15	9.1 ± 0.3
S	1.1	1.9 (1.7)	36 (63)	5	4.53
T	1.1	1.9 (1.7)	36 (63)	5	7.24
Avg.	—	—	—	5	6 ± 2
U	1.1	1.9 (1.7)	36 (63)	10	10.8
V	1.1	1.9 (1.7)	36 (63)	10	10.3
Avg.	—	—	—	10	10.5 ± 0.3
W	1.1	1.9 (1.7)	36 (63)	15	10.4
X	1.1	1.9 (1.7)	36 (63)	15	10.4
Avg.	—	—	—	15	10.44 ± 0.02
Y	1.1	0.48 (0.43)	35 (15)	5	1.06
Z	1.1	0.48 (0.43)	35 (15)	5	1.27
Avg.	—	—	—	5	1.2 ± 0.2
AA	1.1	0.48 (0.43)	35 (15)	10	1.33
BB	1.1	0.48 (0.43)	35 (15)	10	1.43
Avg.	—	—	—	10	1.38 ± 0.07
CC	1.1	0.48 (0.43)	35 (15)	15	1.26
DD	1.1	0.48 (0.43)	35 (15)	15	1.53
Avg.	—	—	—	15	1.4 ± 0.2
EE	1.1	0.48 (0.43)	68 (30)	5	1.23
FF	1.1	0.48 (0.43)	68 (30)	5	1.29
Avg.	—	—	—	5	1.26 ± 0.04

GG	1.1	0.48 (0.43)	68 (30)	10	3.22
HH	1.1	0.48 (0.43)	68 (30)	10	2.76
Avg.	—	—	—	10	3.0 ± 0.3
II	1.1	0.48 (0.43)	68 (30)	15	3.42
JJ	1.1	0.48 (0.43)	68 (30)	15	3.50
Avg.	—	—	—	15	3.46 ± 0.05
KK	1.1	0.48 (0.43)	290 (130)	5	0.736
LL	1.1	0.48 (0.43)	290 (130)	5	1.04
Avg.	—	—	—	5	0.9 ± 0.2
MM	1.1	0.48 (0.43)	290 (130)	10	4.11
NN	1.1	0.48 (0.43)	290 (130)	10	3.47
Avg.	—	—	—	10	3.8 ± 0.4
OO	1.1	0.48 (0.43)	290 (130)	15	6.24
PP	1.1	0.48 (0.43)	290 (130)	15	6.64
Avg.	—	—	—	15	6.4 ± 0.3
QQ	1.1	0.48 (0.43)	580 (250)	5	0.495
RR	1.1	0.48 (0.43)	580 (250)	5	1.13
Avg.	—	—	—	5	0.8 ± 0.5
SS	1.1	0.48 (0.43)	580 (250)	10	3.56
TT	1.1	0.48 (0.43)	580 (250)	10	2.50
Avg.	—	—	—	10	3.0 ± 0.8
UU	1.1	0.48 (0.43)	580 (250)	15	7.13

VV	1.1	0.48 (0.43)	580 (250)	15	7.40
Avg.	—	—	—	15	7.3 ± 0.2

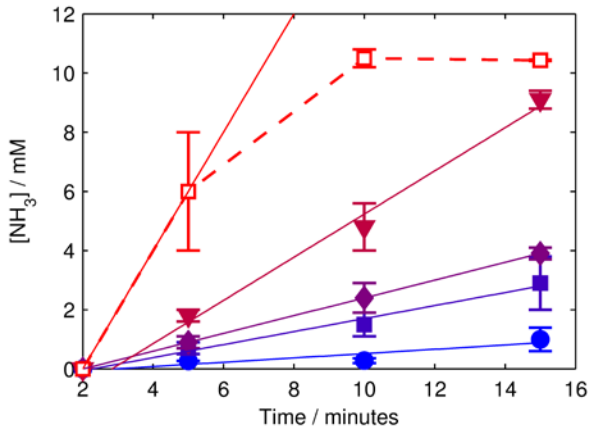

Figure A2.5.1: Time courses for NH_3 generation by **1** at varying concentrations of **1**. All reactions conducted in 63 mM $HBAr^F_4$ with 1.2 equiv KC_8 with respect to $HBAr^F_4$. (Blue circles) [**1**] = 0.11 mM; (Indigo squares) [**1**] = 0.22 mM; (purple diamonds) [**1**] = 0.43 mM; (maroon triangles) [**1**] = 0.87 mM; (red squares) [**1**] = 1.7 mM. Solid lines show the least-squares linear regression fit to the 5, 10 and 15 minute data, except for the [**1**] = 1.7 mM trace (red squares), which deviates from pseudo-first-order behavior; in this case, the line is fit from the data at 5 minutes to a zero point at t = 2 minutes.

Figure A2.5.2: Time courses for NH_3 generation by **1** at varying concentrations of $HBAr^F_4$. All reactions conducted in 0.43 mM **1** with 185 equiv KC_8 with respect to **1**. Left: (Blue circles) $[HBAr^F_4]$ = 15 mM; (Indigo squares) $[HBAr^F_4]$ = 30 mM. Right: (purple triangles) $[HBAr^F_4]$ = 63 mM; (maroon circles) $[HBAr^F_4]$ = 130 mM; (red diamonds) $[HBAr^F_4]$ = 250 mM. Left: Solid lines show the line connecting the 5 minute data with a zero point at t = 2 minutes. Right: solid lines show the least-squares linear regression fit to the 5, 10 and 15 minute data.

Table A2.5.3: Results of initial rates determination for NH_3 generation **1**

Entry	$[1]_0$ (mM)	$[[H(OEt_2)_2][BAr^F_4]]_0$ (mM)	v_0 (mM min^{-1})	r^2*
A				0.7
	0.11	63	0.07 ± 0.04	6

B				0.9
	0.22	63	0.22 ± 0.03	8
C	0.43	63	0.30	1.0
D				0.9
	0.87	63	0.73 ± 0.08	9
E	1.7	63	2.0 ± 0.9	N/A
F	0.43	15	0.4 ± 0.3	N/A
G	0.43	30	0.4 ± 0.2	N/A
H				0.9
	0.43	130	0.55 ± 0.02	9
I				0.9
	0.43	250	0.65 ± 0.1	7

* Coefficient of correlation for least-squares fits shown in Figures A2.5.1 and A2.5.2, where applicable.

Table A2.5.4: Least-squares analysis of log-transformed initial rates data from Table A2.5.3

Entry	**Data fit (from Table A2.5.3)**	**Optimal model**	r^2
A	A–E	$\log(v_0) = (-0.04 \pm 0.1) + (1.1 \pm 0.1) \cdot \log([\mathbf{1}]_0)$	0.98
B	C, F–I	$\log(v_0) = (-1.5 \pm 0.5) + (0.17 \pm 0.12) \cdot \log([\mathrm{H}^+]_0)$	0.42

A2.6 General Procedure for Time-resolved H_2 Quantification:

Inside of a nitrogen filled glovebox, the Fe precursor (**1** or **3**, 3.0 μmol) was added to a 500 mL round bottom flask as a solution in THF, and subsequently deposited as a thin film by removing the solvent in vacuo. To this flask was added solid $HBAr^F_4$ (0.44 mmol), KC_8 (0.56 mmol), and a stir bar. The flask was sealed with a septum at room temperature and subsequently chilled to -196 °C in the cold well of a nitrogen filled glovebox. Et_2O (7 mL) was added via syringe into the flask and completely frozen; the total volume of Et_2O was 7 mL, corresponding to a [Fe] = 0.43 mM and [$HBAr^F_4$] = 63 mM. The flask was passed out of the glovebox into a liquid N_2 bath, and subsequently thawed in a dry ice/acetone bath. The timer was set to zero as soon as the flask was transferred to the dry ice/acetone bath. The headspace of the reaction vessel was periodically sampled with a sealable gas sampling syringe (10 mL), which was immediately loaded into the GC, and analyzed for the presence of $H_{2(g)}$. From these data, the percent H_2 evolved (relative to $HBAr^F_4$) was calculated, correcting for the vapor pressure of Et_2O and the removed H_2 from previous samplings. Each time course was measured from a single reaction maintained at -78 °C. For the reaction using **1** as a precursor, the post-reaction material was analyzed for the presence of NH_3 via the methodology described above.

Table A2.6.1: Time profiles for the generation of H_2 in the presence of Fe precursors

Entry	Fe precursor	Time (min)	$H_{2(g)}$ (μmol)	% H_2 Based on H^+	% NH_3 Based on H^+
A	None	0	0	0	—
B		6	2.50	1.14	—
C		28	17.8	8.09	—
D		60	42.0	19.1	—
E		118	80.7	36.6	—
F		1039	169	76.7	—
G	**1**	0	0	0	—
H		5	8.63	3.92	—
I		25	53.5	24.3	—
J		45	72.4	32.9	—
K		66	74.0	33.6	—
L		118	78.2	35.5	—
M		1110	87.9	39.9	34
N	**3**	0	0	0	—
O		7.5	8.63	3.92	—
P		29	44.8	20.3	—
Q		60	133	60.6	—
R		119	190	86.0	—
S		945	195	88.4	—

A2.7 Solution IR calibration of [Na(12-crown-4)$_2$][P$_3^B$Fe-N$_2$] (1):

A series of dilutions of **1** in THF were prepared, their solution IR spectra collected, and the absorbance at 1918 cm^{-1} (υ_{NN}) recorded (Table A2.7.1). A least-squares linear regression provides a calibration curve relating [**1**] (mM) to the absorbance of the N—N stretching mode (Fig. S7.1).

Table A2.7.1: Results of solution IR calibration of **1**

Entry	**[1] (mM)**	**Abs @ 1918 cm^{-1} (a.u.)**
A	1.25	0.3225
B	1.25	0.2495
Avg.	—	0.29 ± 0.05
A	2.5	0.5748
B	2.5	0.5295
Avg.	—	0.55 ± 0.03
A	5	1.0937
B	5	1.0471
Avg.	—	1.07 ± 0.03
A	10	1.7906
B	10	2.0769
Avg.	—	1.9 ± 0.2

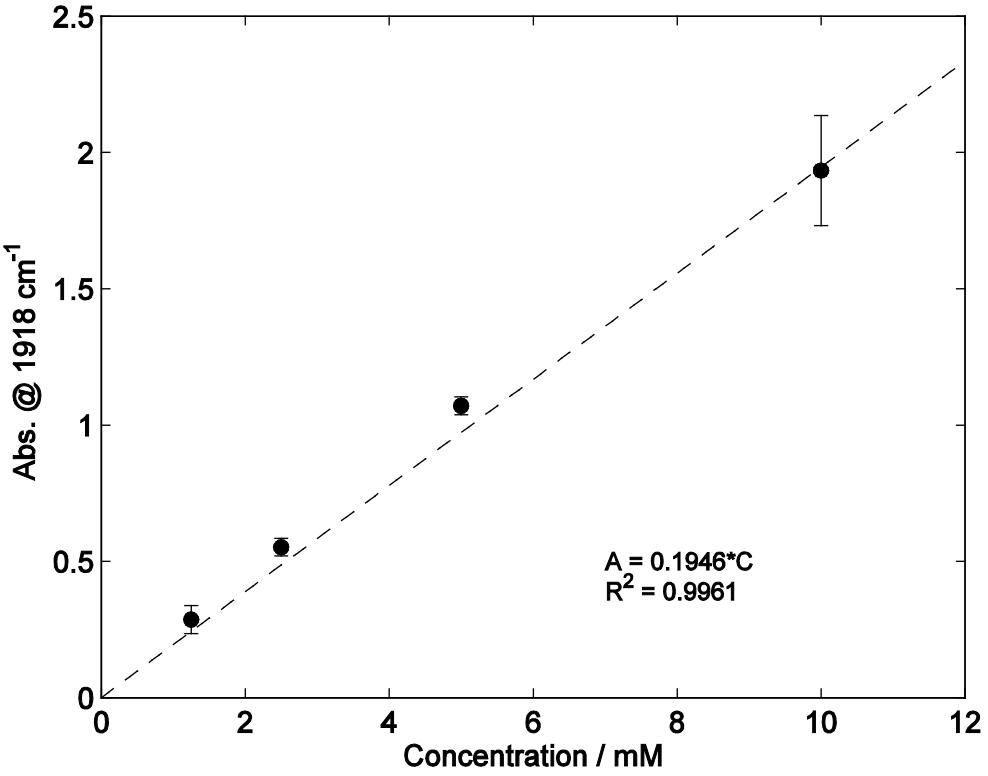

Figure A2.7.1: Solution IR calibration curve for **1**. Data for individual points are presented in Table A2.7.1

.

A2.8 Stoichiometric reaction of $(P_3^B)(\mu\text{-H})Fe(H)(N_2)$ (4-N_2) with $HBAr^F_4$ and KC_8:

Note that **4-N_2** is not indefinitely stable in the solid state, even at -30 °C; accordingly **4-N_2** was used within 24 hours after isolation as a solid

Reaction with $HBAr^F_4$ alone. To a solution of **4-N_2** (8 mg, 0.012 mmol) in 600 μL *d_8*-toluene was added a solution of $HBAr^F_4$ (12 mg, 0.012 mmol) in 100 μL Et_2O. This mixture was loaded into an NMR tube equipped with a J-Young valve and sealed. The tube was mixed over the course of 1.5 hrs with periodic monitoring by ^{1}H NMR (see Fig. S8.2). Over the course of this time the signals attributable to **4-N_2** slowly disappeared concomitant with the appearance of several new, paramagnetically-shifted resonances. An IR spectrum of the reaction material shows no characteristic resonances in the region from 1700–2500 cm^{-1} (except for a trace of residual **4-N_2** at 2070 cm^{-1}), suggesting the absence of terminally-coordinated N_2.

Sequential reaction with $HBAr^F_4$ and KC_8. A 20 mL scintillation vial was charged with a magnetic stir bar, **4-N_2** (5.0 mg, 0.0074 mmol), 0.75 mL of toluene and chilled to -78 °C in the cold well of a N_2 filled glove box. A solution of $HBAr^F_4$ (1.5 equiv, 11 mg, 0.011 mmol) was dissolved in 2.25 mL of Et_2O and similarly chilled. Subsequently, the ethereal $HBAr^F_4$ solution was added to the toluene solution of **4-N_2**, and the resultant mixture was stirred at low temperature for 1 hour, at which point it was pipetted into a pre-chilled vial containing solid KC_8 (6 equiv, 6.0 mg, 0.044 mmol). After stirring a low temperature for 30 minutes, this mixture was allowed to warm to room temperature for 15 minutes before all volatiles were removed in vacuo. The remaining solids were extracted with THF (2 x 1 mL) and filtered into a vial containing 6 μL of 12-crown-4. A sample of

this filtrate was loaded into a solution IR cell and its spectrum was collected. The sharp resonance characteristic of **1** was observed at 1918 cm^{-1} (υ_{NN}), with an absorbance of 0.23, corresponding to [**1**] = 1.2 mM (0.0024 mmol, 32% yield, see Fig. S8.1). In addition to this resonance, a sharp resonance at 2070 cm^{-1} was observed, characteristic of **4-N$_2$** (υ_{NN}).

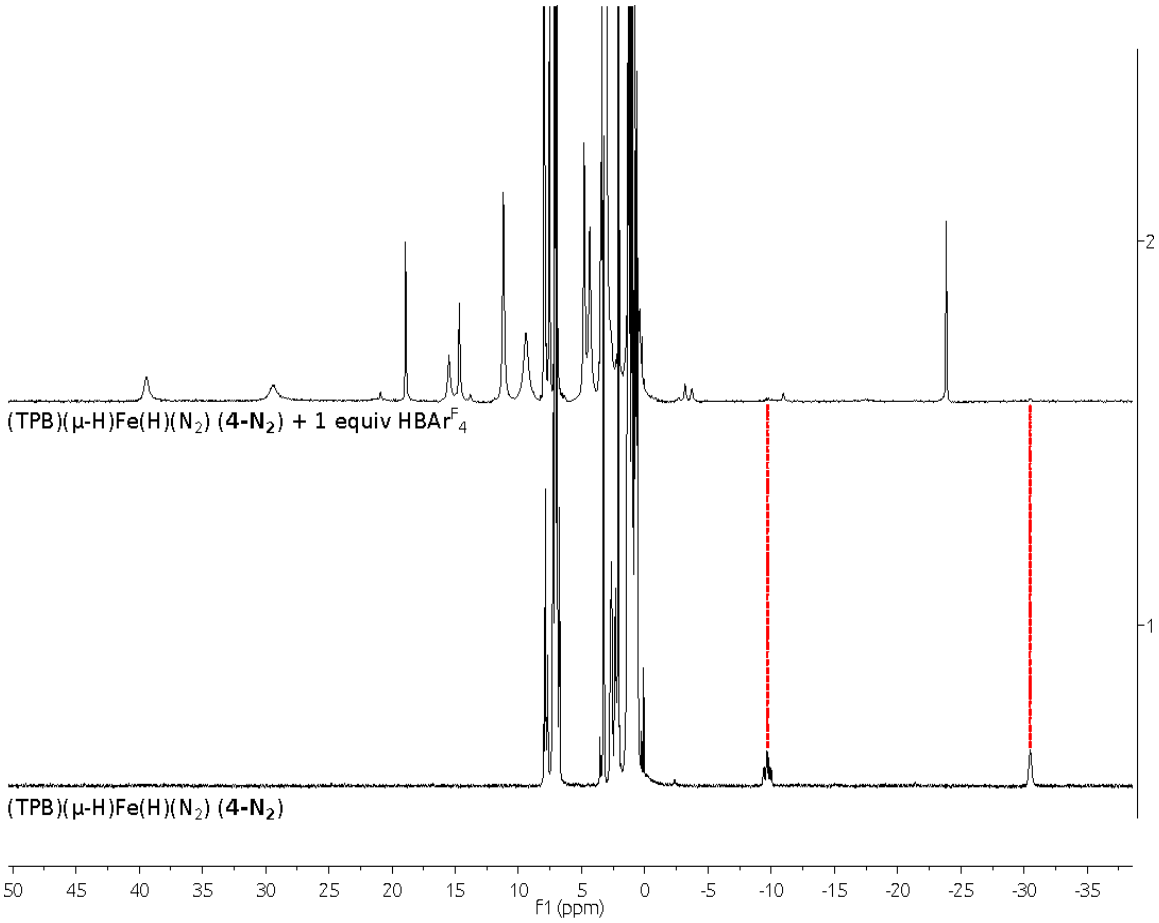

Figure A2.8.1: (Bottom) ^{1}H NMR spectrum of **4-N$_2$**, highlighting the characteristic hydride resonances appearing at ca. -10 and -30 ppm. (Top) Spectrum of the reaction between **4-N$_2$** and $HBAr^F_4$ in 6:1 *d*$_8$-toluene:Et_2O after 1.5 hrs of mixing at room temperature.

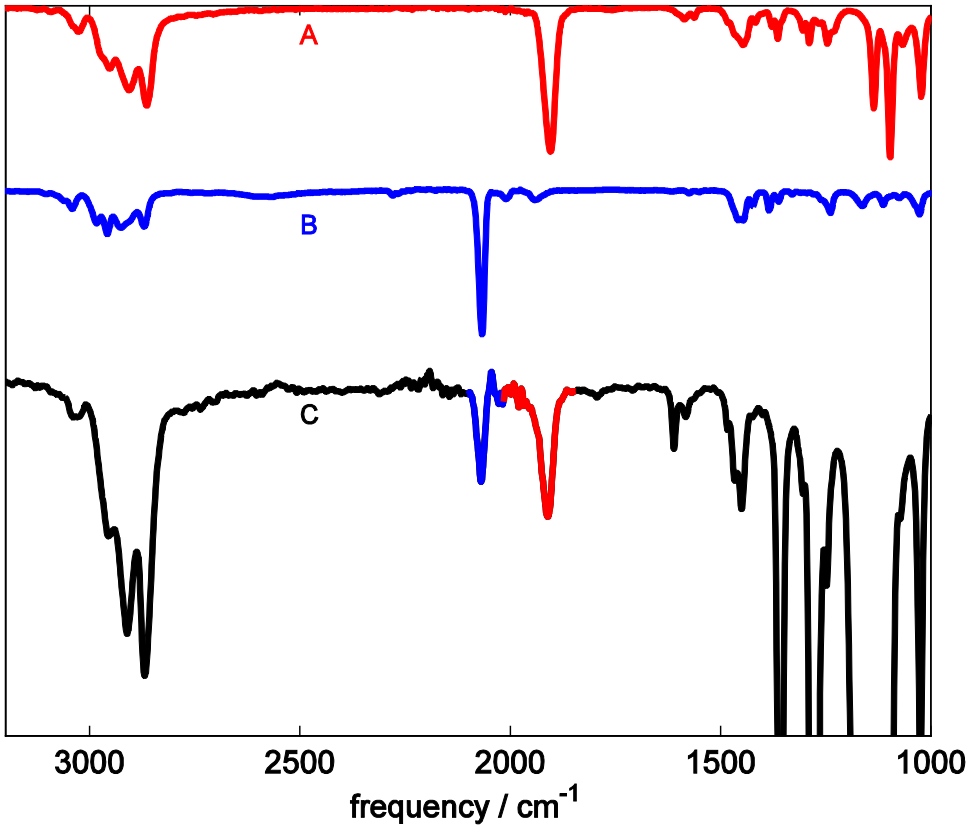

Figure A2.8.2: (A) Solid state IR spectrum of N_2 anion **1** deposited as a thin film from THF. (B) Solid state IR spectrum of hydride **4-N_2** deposited as a thin film from C_6D_6. (C) Solid state IR spectrum of the reaction mixture described in section 8 deposited as a thin film from THF.

A2.9 Mössbauer Spectra:

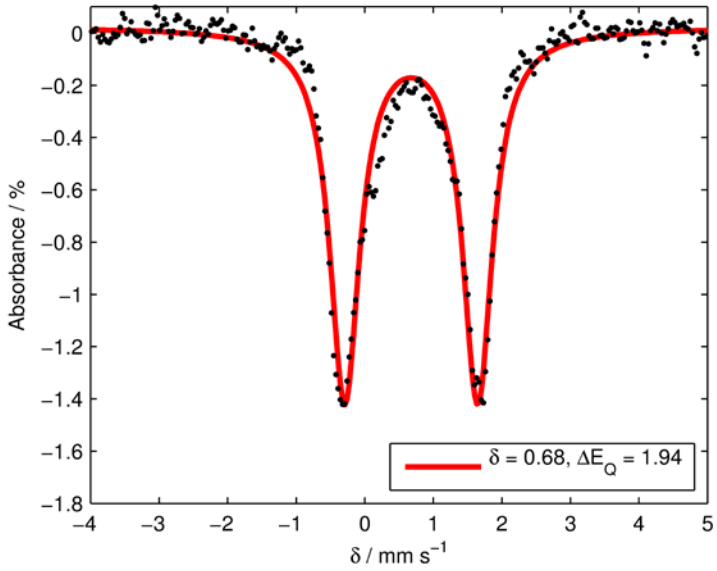

Figure A2.9.1: Zero field Mössbauer spectrum of [P_3^BFe-NH_3][BAr^F_4], prepared by the addition of an atmosphere of $NH_{3(g)}$ to a solution of [P_3^BFe][BAr^F_4] in 6:1 C_6D_6:THF. Raw data presented as black points, simulated data shown as a solid red line. Data collected on a frozen solution sample at 80 K.

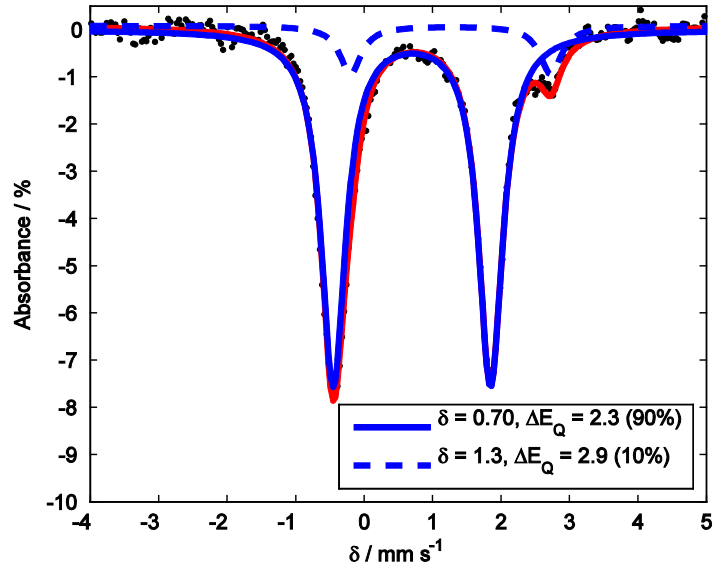

Figure A2.9.2: Zero field Mössbauer spectrum of $[P_3^BFe\text{-}N_2H_4][BAr^F_4]$, prepared by the addition of N_2H_4 to a solution of $[P_3^BFe][BAr^F_4]$ in 6:1 C_6D_6:THF. Raw data presented as black points, simulated data shown as a solid red line. The simulation is fit to two quadrupole doublets, that of $[P_3^BFe\text{-}N_2H_4][BAr^F_4]$ (solid blue line) and that of an unknown impurity (dashed blue line, < 10%). Data collected on a frozen solution sample at 80 K.

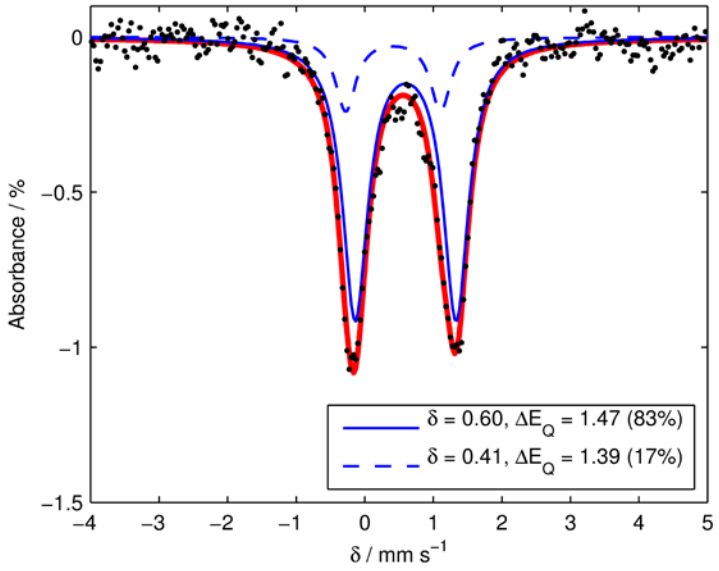

Figure A2.9.3: Zero field Mössbauer spectrum of $P_3^BFe\text{-}NH_2$, prepared by the addition $NaNH_2$ to a solution of $[P_3^BFe][BAr^F_4]$ in Et_2O. Raw data presented as black points, simulated data shown as a solid red line. The simulation is fit to two quadrupole doublets, that of $P_3^BFe\text{-}NH_2$ (solid blue line) and that of $P_3^BFe\text{-}OH$ (dashed blue line), resulting from NaOH contamination in $NaNH_2$. Data collected on a frozen solution sample at 80 K.

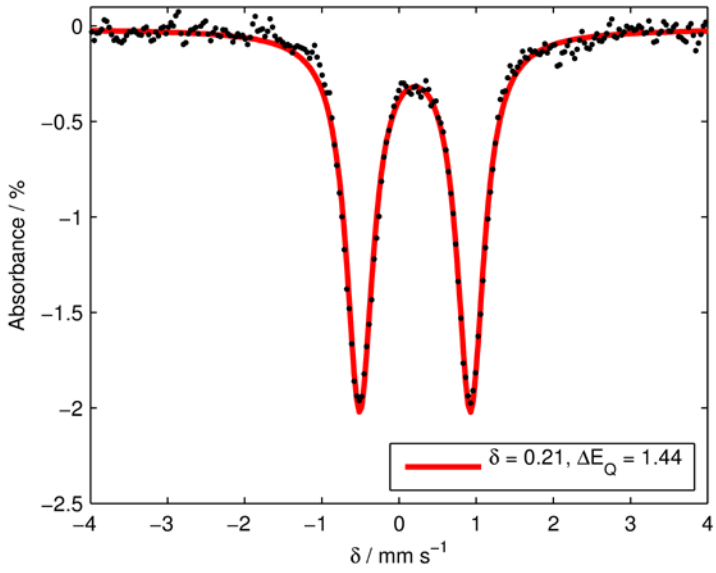

Figure A2.9.4: Zero field Mössbauer spectrum of (P_3^B)(μ-H)Fe(H)(N_2) (**4-N_2**), prepared by the addition of an H_2 atmosphere to a degassed solution of P_3^BFe-N_2 in C_6D_6, followed by removal of excess H_2 and mixing under an N_2 atmosphere overnight. Raw data presented as black points, simulated data shown as a solid red line. Data collected on a frozen solution sample at 80 K.

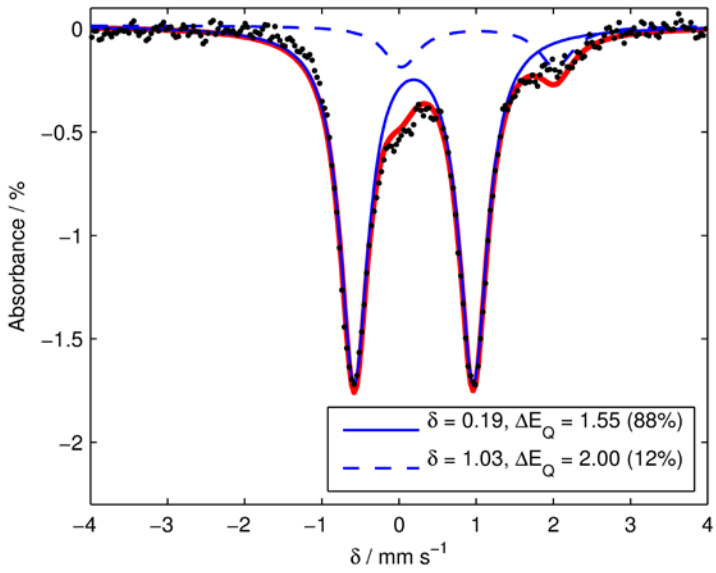

Figure A2.9.5: Zero field Mössbauer spectrum of (P_3^B)(μ-H)Fe(H)(H_2) (**4-H_2**), prepared by the addition of an H_2 atmosphere to a degassed solution of P_3^BFe-N_2 in C_6D_6. Raw data presented as black points, simulated data shown as a solid red line. The simulation is fit to two quadrupole doublets, that of **4-H_2** (solid blue line) and that of unknown decomposition product(s) (dashed blue line), likely resulting from B–C bond cleavage under excess H_2. Data collected on a frozen solution sample at 80 K.

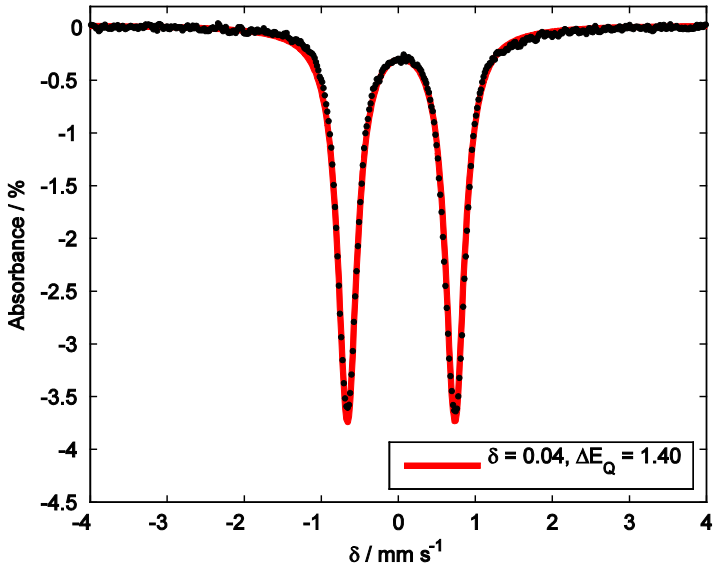

Figure A2.9.6: Zero field Mössbauer spectrum of P_3^BFe-NAd. Raw data presented as black points, simulated data shown as a solid red line. Data collected on a powder sample at 80 K.

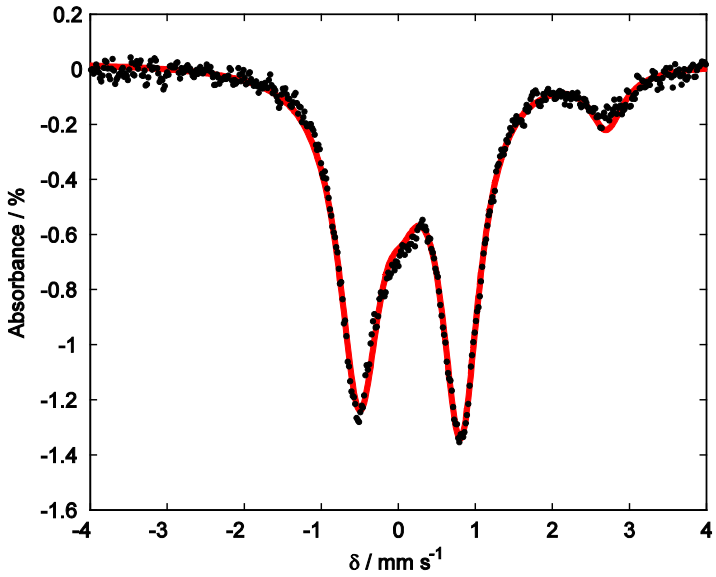

Figure A2.9.7: Zero field Mössbauer spectrum of [P_3^BFe-NAd][BAr^F_4]. Raw data presented as black points, simulated data shown as a solid red line. The simulation is fit to two quadrupole doublets, that of [P_3^BFe-NAd][BAr^F_4] (90%) and that of unknown high spin decomposition product (~10%). Data collected on a powder sample at 80 K in the presence of a 50 mT external magnetic field (parallel mode).

A2.10 Rapid-freeze-quench Mössbauer

General Procedure for Preparation of Rapid-freeze-quench Mossbauer Samples of Catalytic Reaction Mixtures using 1:

All manipulations are carried out inside of a nitrogen filled glovebox. Into a 150 mL Schlenk tube (51 mm OD) is deposited a film of $[Na(12\text{-crown-}4)_2][P_3^B{}^{57}Fe\text{-}N_2]$ from a freshly prepared stock solution in THF. The tube is charged with a 25 mm stir bar and chilled to -196 °C in dewar filled with liquid N_2. A solution of $HBAr^F{}_4$ in Et_2O is added to the chilled tube and allowed to freeze; subsequently a suspension of KC_8 in Et_2O is added and also allowed to freeze. The tube is sealed, and transferred to a pre-chilled cold well at -78 °C (the cold well temperature is monitored directly with a thermocouple). The timer is set to zero as soon as the stir bar is freed from the thawing solvent. At the desired time, the tube is opened, and ~1 mL of the well-stirred suspension is transferred to a Delrin cup pre-chilled to -78 °C using a similarly pre-chilled pipette. The sample in the Delrin cup is then rapidly frozen in liquid N_2. At this point the sample, immersed in liquid N_2, is taken outside of the glovebox and mounted in the cryostat.

General Procedure for Fitting of Rapid-freeze-quench Mössbauer Samples:

Data analysis was performed using version 4 of the program WMOSS (www.wmoss.org) and quadrupole doublets were fit to Lorentzian lineshapes. Simulations were constructed from the minimum number of quadrupole doublets required to attain a quality fit to the data (convergence of χ_R^2). Quadrupole doublets were

constrained to be symmetric, unless **1** was included in the model (the presence of **1** in samples was confirmed by comparison of zero-field spectra with spectra collected in an external 50 mT magnetic field, which dramatically sharpens the resonances attributable to **1**; see ref. 7). Using the non-linear error analysis algorithm provided by WMOSS, the errors in the computed parameters are estimated to be 0.02 mm s^{-1} for δ and 2% for ΔE_Q.

Details of Individual RFQ Mossbauer spectra:

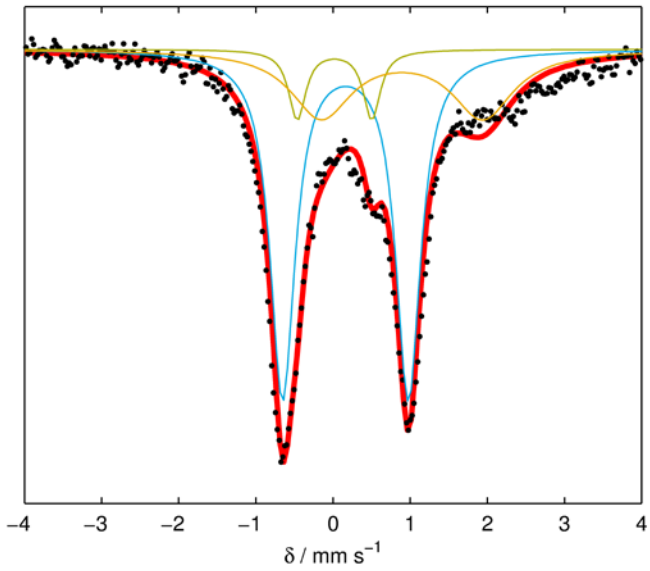

Figure A2.10.1: Mossbauer spectrum collected from a catalytic reaction quenched after 5 minutes. Conditions: [[Na(12-crown-4)$_2$][P_3^B ^{57}Fe-N_2]] = 0.64 mM, [[H(OEt_2)$_2$][$Bar^F{}_4$]] = 31 mM (48 equiv), 1.2 equiv KC_8 relative to [H(OEt_2)$_2$][$Bar^F{}_4$]. Raw data shown as black points, simulation as a solid red line, with components in blue, green, orange (see Table A2.10.1 for parameters). Collected at 80 K with a parallel applied magnetic field of 50 mT.

Fitting details for Figure A2.10.1: Three pairs of quadrupole doublets were found to be necessary to obtain an adequate simulation of these data. The simulation parameters are given in Table A2.10.1. The major component (shown in blue in Fig. S10.1) is the only species with resolved lineshapes, while the remaining components (shown in green and orange) were fit to the broad residual signal by least-squares refinement. While this fitting procedure is necessary to get an accurate integration of the major species, the Mossbauer parameters for the minor components should not be considered reliable. It is

possible that the broad residual signal arises from multiple minor components whose resonances are not well-resolved.

Table A2.10.1: Simulation parameters for Mossbauer spectrum in Figure A2.10.1

Component	**δ (mm s^{-1})**	**ΔE_Q (mm s^{-1})**	**Linewidths, Γ_L/ Γ_R (mm s^{-1})**	**Relative area**
A (blue)	0.16 ± 0.02	1.63 ± 0.03	0.39/0.39	0.61
B (green)	0.02 ± 0.02	0.97 ± 0.02	0.27/0.27	0.085
C (orange)	0.89 ± 0.02	2.10 ± 0.04	0.96/0.96	0.28

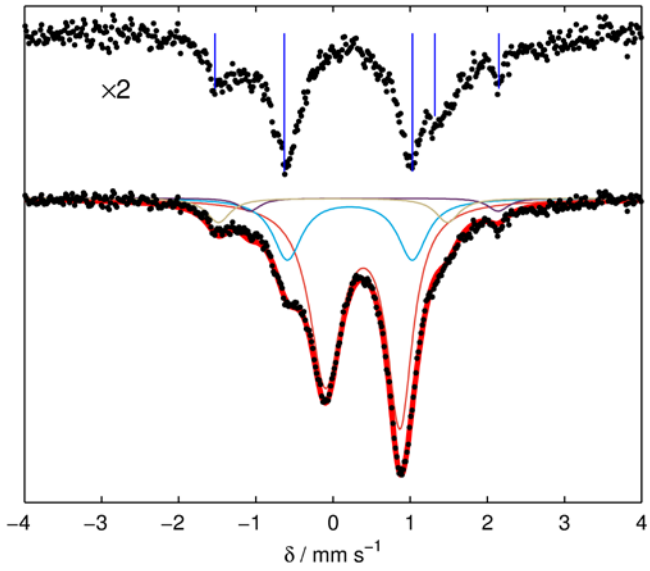

Figure A2.10.2: Mossbauer spectrum collected from a catalytic reaction quenched after 25 minutes. Conditions: [[Na(12-crown-4)$_2$][$P_3^{B\ 57}$Fe-N_2]] = 0.64 mM, [[H(OEt$_2$)$_2$][Bar$^F{}_4$]] = 31 mM (48 equiv), 1.2 equiv KC_8 relative to [H(OEt$_2$)$_2$][Bar$^F{}_4$]. (Bottom) Raw data shown as black points, simulation as a solid red line, with components in blue, red, tan, and purple (see Table A2.10.2 for parameters). (Top) Raw data after subtraction of major component, shown at twice the scale of the bottom spectrum for clarity. Collected at 80 K with a parallel applied magnetic field of 50 mT.

Fitting details for Figure A2.10.2: Four quadrupole doublets were found to be necessary to obtain an adequate simulation. The simulation parameters are given in Table A2.10.2. The major species present in this spectrum is well-simulated by the parameters of **1**. After subtraction of this component, the residual signal exhibits five resolved lines, indicating the presence of at least three quadrupole doublets (Fig. S10.2, Top). The most intense of these has parameters nearly identical to species A in Table A2.10.1. The remaining signal is well-simulated by two sharp quadrupole doublets, one with parameters nearly identical to those of P_3^BFe-N_2 (D, purple), and one novel species with an unusually low isomer shift (C, tan).

Table A2.10.2: Simulation parameters for Mossbauer spectrum in Figure A2.10.2

Component	**δ (mm s^{-1})**	**ΔE_Q (mm s^{-1})**	**Linewidths, Γ_L/ Γ_R (mm s^{-1})**	**Relative area**
A (blue)	0.22 ± 0.02	1.62 ± 0.03	0.46/0.46	0.22
B (red)	0.39 ± 0.02	0.97 ± 0.02	0.49/0.40	0.70
C (tan)	0.00 ± 0.02	2.97 ± 0.06	0.37/0.37	0.072
D (purple)	0.53 ± 0.02	3.22 ± 0.06	0.33/0.33	0.034

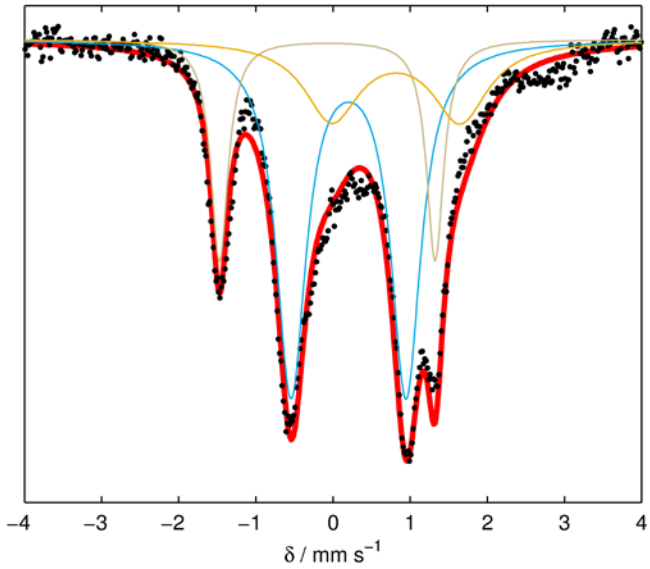

Figure A2.10.3: Mossbauer spectrum collected from a catalytic reaction quenched after 5 minutes. Conditions: [[Na(12-crown-4)$_2$][P_3^B ^{57}Fe-N_2]] = 0.43 mM, [[H(OEt$_2$)$_2$][Bar$^F_4$]] = 63 mM (150 equiv), 1.2 equiv KC_8 relative to [H(OEt$_2$)$_2$][Bar$^F_4$]. Raw data shown as black points, simulation as a solid red line, with components in blue, tan, and orange (see Table A2.10.3 for parameters). Collected at 80 K with a parallel applied magnetic field of 50 mT.

Fitting details for Figure A2.10.3: Four quadrupole doublets were found to be necessary to obtain an adequate simulation. The simulation parameters are given in Table A2.10.3. The major species present in this spectrum has parameters very similar to those of the major component in the spectrum in Figure A2.10.1 (Table A2.10.1, A); indeed, in both cases this species comprises approximately 60% of the signal. This spectrum also features a second well-resolved quadrupole doublet, which has parameters nearly identical to those of the novel minor component shown in tan in Figure A2.10.2 (Table A2.10.2, C). As with the spectrum in Figure A2.10.1, after fitting these two resolved

doublets there is a broad residual signal centered around 0.8 mm s^{-1}. Due to the broadness of this signal, the parameters for this component should not be considered reliable, but its inclusion in the simulation is required for accurate integration.

Table A2.10.3: Simulation parameters for Mossbauer spectrum in Figure A2.10.3

Component	**δ (mm s^{-1})**	**ΔE_Q (mm s^{-1})**	**Linewidths, Γ_L/ Γ_R (mm s^{-1})**	**Relative area**
A (blue)	0.20 ± 0.02	1.49 ± 0.03	0.47/0.47	0.61
B (tan)	-0.07 ± 0.02	2.80 ± 0.06	0.27/0.27	0.23
C (orange)	0.82 ± 0.02	1.67 ± 0.03	0.87/0.87	0.25

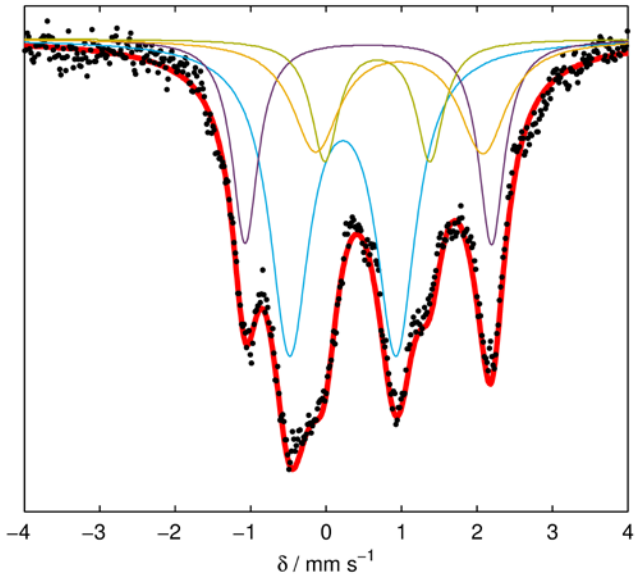

Figure A2.10.4: Mossbauer spectrum collected from a catalytic reaction quenched after 10 minutes. Conditions: [[Na(12-crown-4)$_2$][$P_3^{B\ 57}$Fe-N_2]] = 0.43 mM, [[H(OEt$_2$)$_2$][Bar$^F{}_4$]] = 63 mM (150 equiv), 1.2 equiv KC_8 relative to [H(OEt$_2$)$_2$][Bar$^F{}_4$]. Raw data shown as black points, simulation as a solid red line, with components in blue, purple, green, and orange (see Table A2.10.4 for parameters). Collected at 80 K with a parallel applied magnetic field of 50 mT.

Fitting details for Figure A2.10.4: Four quadrupole doublets were found to be necessary to obtain an adequate simulation. The simulation parameters are given in Table A2.10.4. The spectrum shown in Figure A2.10.4 exhibits six clearly resolved features, indicating at least three pairs of quadrupole doublets. The two most extreme resonances are well-modeled by the parameters for P_3^BFe-N_2. After fitting this component (purple), the residual signal shows a pair of nearly overlapping quadrupole doublets, as well as an additional broad baseline component centered around 1 mm s^{-1}. The resolved features fit to two species, one with parameters nearly identical to those of the major species show in

Figure A2.10.3 (Table A2.10.3, A), and another with parameters quite similar to those of $P_3^BFe\text{-}NH_2$ (green). As with previous spectra, a final component (orange) was included to model the broad residual baseline signal.

Table A2.10.4: Simulation parameters for Mossbauer spectrum in Figure A2.10.4

Component	**δ (mm s^{-1})**	**ΔE_Q (mm s^{-1})**	**Linewidths, Γ_L/ Γ_R (mm s^{-1})**	**Relative area**
A (blue)	0.22 ± 0.02	1.41 ± 0.03	0.64/0.64	0.50
B (purple)	0.56 ± 0.02	3.27 ± 0.07	0.41/0.41	0.22
C (green)	0.68 ± 0.02	1.40 ± 0.03	0.44/0.44	0.14
D (orange)	0.97 ± 0.02	2.22 ± 0.04	0.76/0.76	0.21

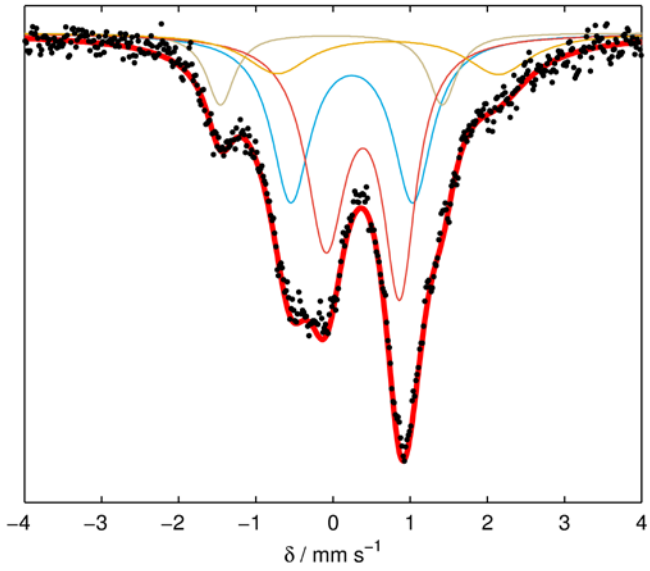

Figure A2.10.5: Mossbauer spectrum collected from a catalytic reaction quenched after 25 minutes. Conditions: [[Na(12-crown-4)$_2$][P_3^B ^{57}Fe-N_2]] = 0.43 mM, [[H(OEt$_2$)$_2$][Bar$^F{}_4$]] = 63 mM (150 equiv), 1.2 equiv KC_8 relative to [H(OEt$_2$)$_2$][Bar$^F{}_4$]. Raw data shown as black points, simulation as a solid red line, with components in blue, purple, green, and orange (see Table A2.10.5 for parameters). Collected at 80 K with a parallel applied magnetic field of 50 mT.

Fitting details for Figure A2.10.5: Four quadrupole doublets were found to be necessary to obtain an adequate simulation. The simulation parameters are given in Table A2.10.5. The spectrum shown in Figure A2.10.5 exhibits four clearly resolved features, the intensities of which indicate at least three pairs of quadrupole doublets. The major component is well modeled by the parameters for **1** (red). After subtraction of this

component, the residual signal exhibits two resolved quadrupole doublets in addition to a broad baseline signal centered around 0.7 mm s^{-1}. The two resolved species fit well to the two major components shown in Figure A2.10.3 (blue and tan), while the residual signal was fit to a broad quadrupole doublet for accurate integration.

Table A2.10.5: Simulation parameters for Mossbauer spectrum in Figure A2.10.5

Component	**δ (mm s^{-1})**	**ΔE_Q (mm s^{-1})**	**Linewidths, Γ_L/ Γ_R (mm s^{-1})**	**Relative area**
A (blue)	0.24 ± 0.02	1.58 ± 0.03	0.61/0.61	0.39
B (red)	0.39 ± 0.02	0.96 ± 0.02	0.63/0.51	0.49
C (tan)	-0.02 ± 0.02	2.88 ± 0.06	0.44/0.44	0.13
D (orange)	0.71 ± 0.02	2.87 ± 0.06	1.01/1.01	0.15

N.B. Note that the simulations of each of the spectra above were allowed to refine freely by a least-squares optimization model. Given that each spectrum reflects a mixture of species, some uncertainty in the fitting parameters is expected. Operating under the assumption that the signal assigned to species A in Tables A2.10.1–A2.10.5 is due to the same Fe compound, then we can estimate the uncertainty in the spectral simulations by the standard deviation in the optimized fits for each spectrum. We thus assign the parameters of A as $\delta = 0.21 \pm 0.03$ mm s^{-1} and $\Delta E_Q = 1.55 \pm 0.09$ mm s^{-1}. Performing the same analysis for the tan components in Tables A2.10.2, A2.10.3, and A2.10.5 yields parameters $\delta = -0.03 \pm 0.04$ mm s^{-1} and $\Delta E_Q = 2.88 \pm 0.09$ mm s^{-1}.

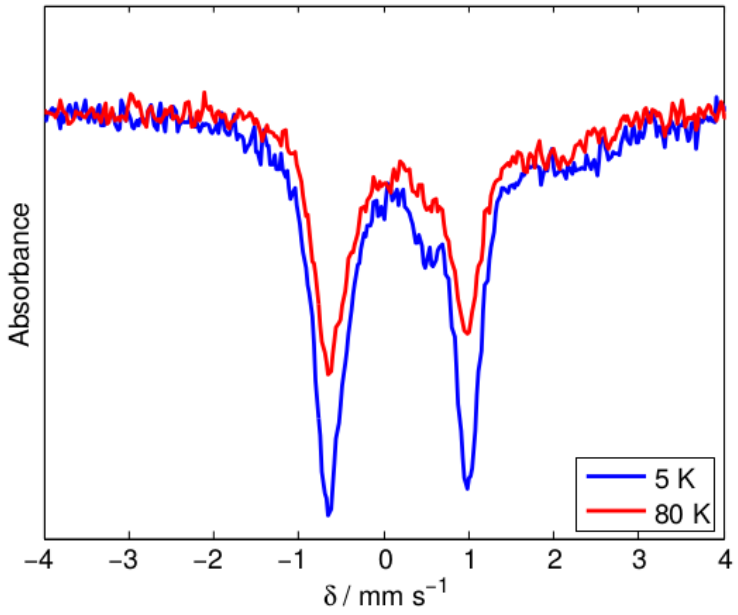

Figure A2.10.6: Low temperature Mossbauer spectrum of freeze-quenched catalytic reaction mixture. The sample is identical to that presented in Figure A2.10.1. Data collected in a 50 mT parallel magnetic field at 80 K (red trace) and 5 K (blue trace). The lack of magnetic hyperfine interactions in the 5 K spectrum of the major component strongly favors a non-Kramers spin system assignment.

A2.11 Controlled Potential Electrolysis of $[P_3^BFe][BAr^F{}_4]$ and $HBAr^F{}_4$

General considerations. All manipulations were carried out in an N_2 filled glove box. A sealable H-cell consisting of two compartments separated by a fine porosity sintered glass frit was charged with 15 mL (working chamber) and 7 mL (auxiliary chamber) of 0.1 M Na $BAr^F{}_4$ solution in Et_2O. The working chamber was outfitted with a reticulated vitreous carbon working electrode (100 pores per inch (ppi) grade obtained from K.R. Reynolds Company, prepared by holding the electrode at -3.0 V vs Fc/Fc^+ in a separate 0.1 M $NaBAr^F{}_4$ solution for 30 minutes and rinsing with Et_2O), the working electrode was rectangular prismatic in shape with dimensions of 10 mm x 6 mm and was submerged in the working chamber solution to a depth of ~2-3 mm. The working chamber also featured a $Ag/AgPF_6$ in Et_2O reference electrode isolated by a CoralPor™ frit (obtained from BASi) and referenced externally to Fc/Fc^+. The auxiliary chamber was outfitted with a Zn foil electrode of dimensions 21.5 cm x 1.5 cm. The cell was cooled to -45 °C in a cold well and then sealed before electrolysis. The cell was connected to a CH Instruments 600B electrochemical analyzer and controlled potential bulk electrolysis experiments were performed at -45 °C with stirring.

Electrolysis with 10 equiv $HBAr^F{}_4$ at -2.6 V vs Fc/Fc^+. To the working chamber was added 11.3 mg of $[P_3^BFe][BAr^F{}_4]$ (7.5 μmol), 76 mg of $HBAr^F{}_4$ (75 μmol), and a magnetic stir bar. The cell passed 5.85 C of charge over the course of 4.6 hours. After that time the potential bias was removed, the headspace of the cell was sampled with a sealable gas syringe (10 mL), which was immediately analyzed by GC for the presence of

$H_{2(g)}$. Then $HBAr^F_4$ solutions in Et_2O were injected through rubber septa into both chambers to sequester NH_3 as $[NH_4][BAr^F_4]$ (25 mg, 25 μmol for the working chamber and 10 mg, 10 μmol for the auxiliary chamber). The cell was allowed to stir at -45 °C for 10 minutes and then warmed to room temperature and stirred an additional 15 minutes. The contents of both chambers were then transferred to a Schlenk tube (cell washed with additional Et_2O) and this material was analyzed for NH_3 by base digestion, vacuum transfer of volatiles, and the indophenol method as described in section 1.4. The results of the two product analyses were that 3.5 μmol of NH_3 and 17.5 μmol of H_2 had been produced.

Electrolysis with 50 equiv $HBAr^F_4$ at -2.3 V vs Fc/Fc^+. To the working chamber was added 5.0 mg of $[P_3{}^BFe][BAr^F_4]$ (3.3 μmol), 170 mg of $HBAr^F_4$ (168 μmol), and a magnetic stir bar. The cell passed 8.39 C of charge over the course of 16.5 hours. After that time the potential bias was removed, the headspace of the cell was sampled with a sealable gas syringe (10 mL), which was immediately analyzed by GC for the presence of $H_{2(g)}$, and $HBAr^F_4$ solutions in Et_2O were injected through rubber septa into both chambers to sequester NH_3 as $[NH_4][BAr^F_4]$ (40 mg, 40 μmol for the working chamber and 20 mg, 20 μmol for the auxiliary chamber). The cell was allowed to stir at -45 °C for 10 minutes and then warmed to room temperature and stirred an additional 15 minutes. The contents of both chambers were then transferred to a Schlenk tube (cell washed with additional Et_2O) and this material was analyzed for NH_3 by base digestion, vacuum transfer of volatiles, and the indophenol method as described in section 1.4. The results of the two product analyses were that 7.3 μmol of NH_3 and 21.7 μmol of H_2 had been produced.

A2.12 REFERENCES

[1] Wietz, I. S.; Rabinovitz, M. J. *J. Chem. Soc., Perkin Trans.* **1993**, *1*, 117.

[2] Moret, M.-E.; Peters, J. C. *Angew. Chem. Int. Ed.* **2011**, *50*, 2063.

[3] Creutz, S. E.; Peters, J. C. *J. Am. Chem. Soc.* **2014**, *136*, 1105.

[4] Mankad, N. P.; Whited, M. T.; Peters, J. C. *Angew. Chem. Int. Ed.* **2007**, *46*, 5768.

[5] Fong, H.; Moret, M.-E.; Lee, Y.; Peters, J. C. *Organometallics* **2013**, *32*, 3053.

[6] Anderson, J. S.; Moret, M.-E.; Peters, J. C. *J. Am. Chem. Soc.* **2012**, *135*, 534.

[7] Anderson, J. S.; Cutsail, G. E. III; Rittle, J.; Connor, B. A.; Gunderson, W. A.; Zhang, L.; Hoffman, B. M.; Peters, J. C. *J. Am. Chem. Soc.* **2015**, *137*, 7803.

[8] Weatherburn, M. W. *Anal. Chem.* **1967**, *39*, 971.

[9] Reger, D. L.; Little, C. A.; Lamba, J. J. S.; Brown, K. J.; Krumper, J. R.; Bergman, R. G.; Irwin, M.; Fackler Jr., J. P. *Inorg. Synth.* **2004**, *34*, 5.

[10] Yakelis, N. A.; Bergman, R. G. *Organometallics* **2005**, *24*, 3579.

[11] Brookhart, M.; Grant, B.; Volpe Jr., A. F. *Organometallics* **1992**, *11*, 3920.

[12] Watt, G. W.; Chrisp, J. D. *Anal. Chem.* **1952**, *24*, 2006.

[13] Anderson, J. S.; Rittle, J.; Peters, J. C. *Nature* **2013**, *501*, 84.

Appendix 3

SUPPLEMENTARY INFORMATION FOR CHAPTER 4: CATALYTIC N_2-TO-NH_3 CONVERSION BY FE AT LOWER DRIVING FORCE: A PROPOSED ROLE FOR METALLOCENE-MEDIATED PCET

Reproduced in part with permission from:

Chalkley, M.; Del Castillo, T.; Matson, B.; Roddy, J.; Peters, J. C.; *ACS Central Science*, **2017**, 3, 217-223. **DOI:** 10.1021/acscentsci.7b00014

A3.1 Experimental details

General considerations:

All manipulations were carried out using standard Schlenk or glovebox techniques under an N_2 atmosphere. Solvents were deoxygenated and dried by thoroughly sparging with N_2 followed by passage through an activated alumina column in a solvent purification system by SG Water, USA LLC. Non-halogenated solvents were tested with sodium benzophenone ketyl in tetrahydrofuran (THF) in order to confirm the absence of oxygen and water. Deuterated solvents were purchased from Cambridge Isotope Laboratories, Inc., degassed, and dried over activated 3-Å molecular sieves prior to use.

Cp^*_2Co,[1] $[P_3^BFe][BAr^F_4]$,[2] $P_3^{Si}FeN_2$,[3] $[P_3^BCoN_2][Na(12\text{-crown-4})_2]$,[4] $P_3^{Si}CoN_2$,[5] $[P_3^BFeN_2][Na(12\text{-crown-4})_2]$,[6] and $[Ph_2{}^{15}NH_2][OTf]$[7,8] were prepared according to literature procedures. $Ph^{15}NH_2$ was obtained from Sigma-Aldrich, Inc. degassed, and

dried over activated 3-Å molecular sieves prior to use**.** All other reagents were purchased from commercial vendors and used without further purification unless otherwise stated. Diethyl ether (Et_2O) used in the experiments herein was stirred over Na/K (≥ 2 hours) and filtered or vacuum-transferred before use unless otherwise stated.

Physical Methods:

^1H chemical shifts are reported in ppm relative to tetramethylsilane, using ^1H resonances from residual solvent as internal standards. IR measurements were obtained as solutions or thin films formed by evaporation of solutions using a Bruker Alpha Platinum ATR spectrometer with OPUS software (solution IR collected in a cell with KBr windows and a 1 mm pathlength). H_2 was quantified on an Agilent 7890A gas chromatograph (HP-PLOT U, 30 m, 0.32 mm ID; 30 °C isothermal; nitrogen carrier gas) using a thermal conductivity detector.

Mössbauer Spectroscopy:

Mössbauer spectra were recorded on a spectrometer from SEE Co. (Edina, MN) operating in the constant acceleration mode in a transmission geometry. The sample was kept in an SVT-400 cryostat form Janis (Wilmington, MA). The quoted isomer shifts are relative to the centroid of the spectrum of a metallic foil of α-Fe at room temperature (RT). Solution samples were transferred to a sample cup and chilled to 77 K inside of the glovebox, and unless noted otherwise, quickly removed from the glovebox and immersed in liquid N_2 until mounted in the cryostat. Data analysis was performed using version 4 of

the program WMOSS (www.wmoss.org) and quadrupole doublets were fit to Lorentzian lineshapes. See discussion below for detailed notes on the fitting procedure.

Ammonia and Hydrazine Quantification:

Reaction mixtures are cooled to 77 K and allowed to freeze. The reaction vessel is then opened to atmosphere and to the frozen solution is slowly added an excess (with respect to acid) solution of a NaO^{t}Bu solution in MeOH (0.25 mM) over 1-2 minutes. This solution is allowed to freeze, then the headspace of the tube is evacuated and the tube is sealed. The tube is then allowed to warm to RT and stirred at RT for at least 10 minutes. An additional Schlenk tube is charged with HCl (3 mL of a 2.0 M solution in Et_2O, 6 mmol) to serve as a collection flask. The volatiles of the reaction mixture are vacuum transferred at RT into this collection flask. After completion of the vacuum transfer, the collection flask is sealed and warmed to RT. Solvent is removed in vacuo, and the remaining residue is dissolved in H_2O (1 mL). An aliquot of this solution (10–100 μL) is then analyzed for the presence of NH_3 (present as NH_4Cl) by the indophenol method.[9] A further aliquot of this solution is analyzed for the presence of N_2H_4 (present as N_2H_5Cl) by a standard colorimetric method.[10] Quantification is performed with UV−vis spectroscopy by analyzing absorbance at 635 nm. In this case of runs with [$PhNH_3$][OTf] we found that aniline in the form of anilinium chloride was present in the receiving vessels. The anilinium chloride interfered with the indophenol and hydrazine detection method. Therefore, quantification for NH_3 was performed by extracting the solid residue into 1 mL of DMSO-d_6 that has 20 mmol of trimethoxybenzene as an internal standard. Integration of the ^{1}H NMR peak observed for NH_4 was then integrated

against the two peaks of trimethoxybenzene to quantify the ammonium present. This ^{1}H NMR detection method was also used to differentiate [$^{14}NH_4$][Cl] and [$^{15}NH_4$][Cl] produced in the control reactions conducted with [$^{15}NPh_2H_2$][OTf].

EPR Spectroscopy

X-band EPR spectra were obtained on a Bruker EMX spectrometer. Samples were collected at powers ranging from 6-7 mW with modulation amplitudes of 2.00 G, modulation frequencies of 100.00 kHz, over a range of 1800 to 4500 Gauss. Spectra were baseline corrected using the algorithm in SpinCount.[11] EPR spectra were modeled using the easyspin program.[12]

Computational Methods

All stationary point geometries were calculated using DFT with an M06-L functional,[13] a def2-TZVP[14] basis set on transition metals (Stuttgart ECP[15] was used on Mo atoms) and a def2-SVP[14] basis set on all other atoms. Calculations were performed, in part, using Xtreme Science and Engineering Discovery Environment (XSEDE) resources.[16] Calculations were performed on the full P_3^EFe scaffolds. Calculations on the [HIPTN$_3$N]Mo system were performed on a truncated scaffold in which the isopropyl groups were removed (i.e. [{3,5-$(C_6H_4)_2C_6H_3NCH_2CH_2\}_3N]^{3-}$). Geometries were optimized using the NWChem 6.5 package.[17] All single point energy, frequency and solvation energy calculations were performed with the Gaussian09 package.[18] Frequency calculations were used to confirm true minima and to determine gas phase free energy

values (G_{gas}). Single point solvation calculations were done using an SMD solvation model with diethyl ether solvent and were used to determine solvated internal energy (E_{soln}). Free energies of solvation were approximated using the difference in gas phase internal energy (E_{gas}) and solvated internal energy ($\Delta G_{solv} \approx E_{soln} - E_{gas}$) and the free energy of a species in solution was then calculated using the gas phase free energy (G_{gas}) and the free energy of solvation ($G_{soln} = G_{gas} + \Delta G_{solv}$).[19,20,21] All reduction potentials were calculated referenced to $Fc^{+/0}$ using the standard Nernst relation $\Delta G = -nFE^0$.

Gas Chromatography

H2 was quantified on an Agilent 7890A gas chromatograph (HP-PLOT U, 30 m, 0.32 mm ID; 30 °C isothermal; nitrogen carrier gas) using a thermal conductivity detector. All measurements were taken using a 100 μL manual injection and the final value was obtained as an average of two runs.

A3.2 Synthetic Details:

General Procedure for the Synthesis of the Acids:

Prior to use the amine was purified (aniline by distillation and diphenylamine by recrystallization). To a 250 mL round bottom flask in the glovebox was added the amine which was subsequently dissolved in 100 mL of Et_2O (no additional drying with NaK). To this was added dropwise (1 equiv) of HOTf with stirring over five minutes. Immediate precipitation of white solid was observed and the reaction mixture was allowed to stir for one hour at RT. The reaction mixture was then filtered and the resulting white powder

was washed with Et_2O (50 mL), pentane (50 mL) and Et_2O again (50 mL). The resulting white microcrystalline material was then dried under vacuum. Yields of greater than 90% of microcrystalline material was obtained in this manner in all cases.

Procedure for Reaction of Cp^*_2Co with Acid:

A 1 mL solution of HOTf or DOTf (23 μL, 3.0 eq) in toluene and a 2 mL solution of Cp^*_2Co (40 mg, 1.0 eq) was chilled to -78 °C for ten minutes in a cold well. With strong stirring the Cp^*_2Co solution was added dropwise over ten minutes to the HOTf solution. Purple precipitate could be observed upon the addition of each drop. After the completion of the addition the reaction mixture was allowed to stir for 5 more minutes. The reaction was then vacuum filtered in the cold well through a medium porosity frit to yield a purple solid. This solid was then washed with toluene that had been prechilled to -78 °C (5 mL) and then likewise prechilled pentane (15 mL). After drying on the frit for ten minutes the solid was then transferred to a prechilled vial. The solid was then dried under vacuum for several hours at -78 °C. Exact yields were not obtained due to the solid retaining some solvent even after extended drying at these temperatures; however, the material isolated reproducibly represents > 75% of the expected chemical yield. All further spectroscopic and reactivity characterization of this material was carried out immediately after its synthesis and with the maintenance of the material at ≤ -78 °C except where specifically noted.

A3.3 Ammonia production and quantification studies

Standard NH_3 Generation Reaction Procedure:

All solvents are stirred with Na/K for ≥2 hours and filtered prior to use. In a nitrogen-filled glovebox, the precatalyst (2.3 μmol) was weighed into a vial.* The precatalyst was then transferred quantitatively into a Schlenk tube using THF. The THF was then evaporated to provide a thin film of precatalyst at the bottom of the Schlenk tube. The tube is then charged with a stir bar and the acid and reductant are added as solids. The tube is then cooled to 77 K in a cold well. To the cold tube is added Et_2O to produce a concentration of precatalyst of 2.3 mM. The temperature of the system is allowed to equilibrate for 5 minutes and then the tube is sealed with a Teflon screw-valve. This tube is passed out of the box into a liquid N_2 bath and transported to a fume hood. The tube is then transferred to a dry ice/acetone bath where it thaws and is allowed to stir at -78 °C for three hours. At this point the tube is allowed to warm to RT with stirring, and stirred at RT for 5 minutes. To ensure reproducibility, all experiments were conducted in 200 mL Schlenk tubes (51 mm OD) using 25 mm stir bars, and stirring was conducted at ~900 rpm.

* In cases where less than 2.3 μmol of precatalyst was used stock solutions were used to avoid having to weigh very small amounts.

Table A3.1: UV-vis quantification results for standard NH_3 generation experiments with $P_3^BFe^+$

Entry	$P_3^BFe^+$ (μmol)	Acid equiv	Cp^*_2Co equiv	NH_4Cl (μmol)	N_2H_5Cl (μmol)	Equiv NH_3/Fe	% Yield NH_3

							Based on e^-
A	2.3	108[a]	54	31.4	0.0	13.5	75.6
B	2.3	108[a]	54	28.5	0.0	12.3	68.6
C	2.3	108[a]	54	29.2	0.0	12.6	70.4
Avg.						12.8 ± 0.5	72 ± 3
D	2.3	322[a]	162	76.4	2.0	33.0	61.4
E	2.3	322[a]	162	80.0	0.7	34.5	64.2
Avg.						34 ± 1	63 ± 2
F	2.3	638[a]	322	60.4	0.5	26.0	24.3
G	2.3	638[a]	322	63.2	0.3	27.3	25.4
Avg.						26.7 ± 0.9	25 ± 1
H	1.1	108[b]	54	7.8	0.0	6.9	37.6
I	2.3	108[b]	54	19.2	0.0	8.3	46.3
Avg.						8 ± 1	42 ± 6
J	2.3	108[c]	54	17.7	N.D.	7.7	43.1
K	2.3	108[c]	54	13.8	N.D.	6.0	33.6
Avg.						7 ± 1	38 ± 7
L	2.3	322[c]	162	39.8	N.D.	17.3	32.0
M	2.3	322[c]	162	31.9	N.D.	13.9	25.7
Avg.						16 ± 3	29 ± 4

N.D. indicates the value was not determined [a]Acid used is $[Ph_2NH_2][OTf]$ [b]Acid used is $[Ph_2NH_2][BAr^F{}_4]$ [c]Acid used is $[PhNH_3][OTf]$

Table A3.2: UV-vis quantification results for standard NH_3 generation experiments with $P_3{}^{Si}FeN_2$

Entry	$P_3{}^{Si}FeN_2$ (µmol)	Acid equiv	Cp*$_2$Co equiv	NH_4Cl (µmol)	N_2H_5Cl (µmol)	Equiv NH_3/Fe	% Yield NH_3 Based on e^-
A	2.3	108[a]	54	6.6	0.0	1.7	9.3
B	2.3	108[a]	54	2.7	0.0	0.7	3.8
Avg.						1.2 ± 0.2	6.5 ± 0.3

[a]Acid used is $[Ph_2NH_2][OTf]$

Table A3.3: UV-vis quantification results for standard NH_3 generation experiments with $P_3{}^{B}CoN_2{}^-$

Entry	$P_3{}^{B}CoN_2{}^-$ (µmol)	Acid equiv	Cp*$_2$Co equiv	NH_4Cl (µmol)	N_2H_5Cl (µmol)	Equiv NH_3/Fe	% Yield NH_3 Based on e^-
A	2.3	108[a]	54	3.0	0.0	1.3	7.2
B	2.3	108[a]	54	1.8	0.0	0.8	4.4

Avg.	1.1 ± 0.4	6 ± 2

[a]Acid used is $[Ph_2NH_2][OTf]$

Table A3.4: UV-vis quantification results for standard NH_3 generation experiments with $P_3^{Si}CoN_2$

Entry	$P_3^{Si}CoN_2$ (μmol)	Acid equiv	Cp^*_2Co equiv	NH_4Cl (μmol)	N_2H_5Cl (μmol)	Equiv NH_3/Fe	% Yield NH_3 Based on e^-
A	2.3	108[a]	54	0.0	0.0	0.0	0.0
B	2.3	108[a]	54	0.0	0.0	0.0	0.0
Avg.						0.0	0.0

[a]Acid used is $[Ph_2NH_2][OTf]$

Ammonia production studies with $[Ph_2{}^{15}NH_2][OTf]$:

The procedure was the same as the general procedure presented in section 3.1 with 2.3 μmol of $P_3^BFe^+$ catalyst, 54 equiv Cp^*_2Co, and 108 equiv $[Ph_2{}^{15}NH_2][OTf]$. Product analyzed by ^1H NMR as described in section 1.4 and only the diagnostic triplet of $[^{14}NH_4][Cl]$ is observed.

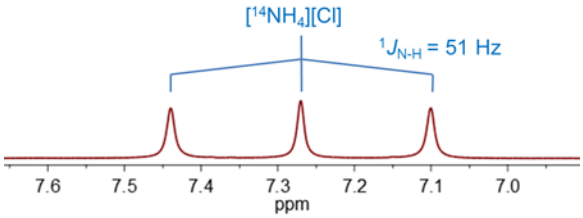

Figure A3.1. ^{1}H NMR spectrum (300 MHz, DMSO-d_6) of [^{14}NH$_4$][Cl] produced from catalytic N_2-to-NH_3 conversion conducted with $P_3^BFe^+$ catalyst, 54 equiv Cp^*_2Co, and 108 equiv [$Ph_2{}^{15}NH_2$][OTf] under an atmosphere of $^{14}N_2$.

A3.4 NH_3 Generation Reaction with Periodic Substrate Reloading – Procedure with $P_3^BFe^+$:

All solvents are stirred with Na/K for ≥2 hours and filtered prior to use. In a nitrogen-filled glovebox, the precatalyst (2.3 μmol) was weighed into a vial. The precatalyst was then transferred quantitatively into a Schlenk tube using THF. The THF was then evaporated to provide a thin film of precatalyst at the bottom of the Schlenk tube. The tube is then charged with a stir bar and the acid and reductant are added as solids. The tube is then cooled to 77 K in a cold well. To the cold tube is added 1 mL of Et_2O. The temperature of the system is allowed to equilibrate for 5 minutes and then the tube is sealed with a Teflon screw-valve. The cold well cooling bath is switched from a $N_{2(l)}$ bath to a dry ice/acetone bath. In the cold well the mixture in the sealed tube thaws with stirring and is allowed to stir at -78 °C for 3 hours. Then, without allowing the tube to warm above -78 °C, the cold well bath is switched from dry ice/acetone to $N_{2(l)}$. After fifteen minutes the reaction mixture is observed to have frozen, at this time the tube is opened. To the cold tube is added acid (324 equiv) and reductant (162 equiv) as solids.

To the tube then 1 additional mL of Na/K-dried Et_2O is added. The cold well cooling bath is switched from a $N_{2(l)}$ bath to a dry ice/acetone bath. In the cold well the mixture in the sealed tube thaws with stirring and is allowed to stir at -78 °C for 3 hours. These reloading steps are repeated the desired number of times. Then the tube is allowed to warm to RT with stirring, and stirred at RT for 5 minutes.

Table A3.5: UV-vis quantification results for NH_3 generation experiments with $P_3^BFe^+$, with reloading

Entry	Number of Loadings	$P_3^BFe^+$ (µmol)	Acid equiv	Cp*$_2$Co equiv	NH_4Cl (µmol)	N_2H_5Cl (µmol)	Equiv NH_3/Fe	% Yield Based on H^+
A	2	2.3	[322]x2[a]	[162]x2	115.0	0.1	49.6	46.2
B	2	2.3	[322]x2[a]	[162]x2	145.6	0.0	62.8	58.5
Avg.							56 ± 9	52 ± 9
C	3	2.3	[322]x3[a]	[162]x3	182.4	0.3	78.7	48.9
D	3	2.3	[322]x3[a]	[162]x3	207.3	0.1	89.5	55.5
Avg.							84 ± 8	52 ± 5

[a]Acid used is $[Ph_2NH_2][OTf]$

A3.5 Time-resolved H_2 quantification of background acid and Cp^*_2Co reactivity:

Inside of a nitrogen filled glovebox, solid acid (0.248 mmol) and Cp^*_2Co (0.124 mmol) are added to a 260 mL glass tube charged with a stir bar. The vessel is sealed with a septum at RT and subsequently chilled to -196 °C in a cold well in the nitrogen filled glovebox. Et_2O (1 mL) is added via syringe into the vessel and completely frozen. The vessel is passed out of the glovebox into a liquid N_2 bath, and subsequently thawed in a dry ice/acetone bath with stirring at ~900 rpm. The timer was started as soon as the vessel was transferred to the dry ice/acetone bath. The headspace of the reaction vessel was periodically sampled with a sealable gas sampling syringe (10 mL), which was loaded into a gas chromatograph, and analyzed for the presence of $H_{2(g)}$. From these data, the percent H_2 evolved (relative to Cp^*_2Co) was calculated, correcting for the vapor pressure of Et_2O and the removed H_2 from previous samplings. Each time course was measured from a single reaction maintained at -78 °C.

Table A3.6: Time-resolved H_2 quantification for the reaction of Cp^*_2Co and acid in Et_2O at -78 °C in the absence of an Fe precatalyst

Acid	Time (min)	$H_{2(g)}$ (µmol)	% H_2 Based on Cp^*_2Co
$[Ph_2NH_2][OTf]^a$	10	1.0 ± 0.4	1.6 ± 0.6
	60	2.1 ± 0.6	3 ± 1
$[Ph_2NH_2][BAr^F{}_4]^b$	10	3.7 ± 0.1	6.0 ± 0.2
	60	12.7 ± 0.8	21 ± 1

[a]Average of two experiments [b]Average of three experiments

A3.6 Time-resolved NH_3 quantification:

All solvents are stirred with Na/K for ≥2 hours and filtered prior to use. In a nitrogen-filled glovebox, the precatalyst (2.3 μmol) was weighed into a vial. The precatalyst was then transferred quantitatively into a Schlenk tube using THF. The THF was then evaporated to provide a thin film of precatalyst at the bottom of the Schlenk tube. The tube is then charged with a stir bar and diphenylammonium triflate (108 eq) and decamethylcobaltocene (54 eq) are added as solids. The tube is then cooled to 77 K in a cold well. To the cold tube is added Et_2O to produce a concentration of precatalyst of 2.3 mM. The temperature of the system is allowed to equilibrate for 5 minutes and then the tube is sealed with a Teflon screw-valve. This tube is passed out of the box into a liquid N_2 bath and transported to a fume hood.

For the control reaction at this point a 2.6 M heptane solution of ^{t}BuLi (2 eq with respect to the acid) was added to the tube under N_2 backflow and the headspace was evacuated. The tube was then allowed to warm to room temperature with stirring and then stirred for a further ten minutes at room temperature. At this point the normal procedure was used to quantify NH_3 and N_2H_4. No NH_3 or N_2H_4 was observed.

To test catalytic activity at five minutes, a tube prepared as described above was allowed to stir for five minutes at -78 °C. At five minutes the tube was frozen in a liquid N_2 bath and allowed to equilibrate for five minutes. Under N_2 backflow a 2.6 M heptane solution of ^{t}BuLi (2 eq with respect to the acid) was added to the tube. The tube was then sealed and the headspace was evacuated. The reaction mixture was then allowed to warm to room temperature with stirring and then stirred for a further ten minutes at room

temperature. At this point the normal procedure was used to quantify NH_3 and N_2H_4. Ammonia (1.2 ± 0.5 eq) was detected. No hydrazine was detected.

A3.7 Mössbauer spectra:

General procedure for preparation of rapid-freeze-quench Mössbauer samples of catalytic reaction mixtures using $P_3^BFe^+$:

All manipulations are carried out inside of a nitrogen filled glovebox. The precatalyst, $[P_3^B(^{57}Fe)][BAr^F_4]$, is weighed into a vial (3.5 mg, 2.3 μmol) and transferred using THF into a 150 mL Schlenk tube. The solvent is evaporated to form a thin film of the precatalyst and a stir bar is added. The $[Ph_2NH_2][OTf]$ (79.4 mg, 0.248 mmol) and Cp^*_2Co (40.3 mg, 0.124 mmol) are added to the Schlenk tube as solids. The Schlenk tube is then placed in $N_{2(l)}$ and the temperature is allowed to equilibrate. To the tube 1 mL of Et_2O is added. The tube is then sealed with a Teflon screw tap and transferred to a pre-chilled cold well at -78 °C. The timer is set to zero as soon as the stir bar is freed from the thawing solvent. At the desired time, the tube is opened and the well-stirred suspension is transferred to a Delrin cup pre-chilled to -78 °C using a similarly pre-chilled pipette. The sample in the Delrin cup is then rapidly frozen in $N_{2(l)}$. At this point the sample, immersed in $N_{2(l)}$, is taken outside of the glovebox and mounted in the cryostat.

General Procedure for Preparation of Rapid-freeze-quench Mössbauer Samples of the Reaction of $P_3^BFe^+$ with Reductants:

All manipulations are carried out inside of a nitrogen filled glovebox. The precatalyst, $[P_3^B(^{57}Fe)][BAr^F_4]$, is weighed into a vial (3.5 mg, 2.3 μmol) and .5 mL of THF is added. The solvent is then evaporated to provide a thin film of $[P_3^B(^{57}Fe)][BAr^F_4]$.

To this is added the desired reductant as a solid (46.0 μmol, 20 equiv). This vial is then placed in $N_{2(l)}$ and the temperature is allowed to equilibrate. To this is added 1 mL of NaK-dried Et_2O. The vial is then sealed with a cap and transferred to a pre-chilled cold well at -78 °C. The timer is set to zero as soon as the stir bar is freed from the thawing solvent. After five minutes using a pre-chilled pipette the well-stirred reaction mixture is transferred to a Delrin cup that has been pre-chilled to -78 °C. The sample in the Delrin cup is then rapidly frozen in $N_{2(l)}$. At this point the sample, immersed in $N_{2(l)}$, is taken outside of the glovebox and mounted in the cryostat.

General Procedure for Fitting of Rapid-freeze-quench Mössbauer Samples:

Data analysis was performed using version 4 of the program WMOSS (www.wmoss.org) and quadrupole doublets were fit to Lorentzian lineshapes. Simulations were constructed from the minimum number of quadrupole doublets required to attain a quality fit to the data (convergence of χ_R^2). Quadrupole doublets were constrained to be symmetric, unless $[P_3^BFe–N_2][Na(12\text{-crown-}4)_2]$ was included in the model. With $[P_3^BFe–N_2][Na(12\text{-crown-}4)_2]$ since it is known to have characteristic asymmetry we started with the observed linewidths in the authentic sample and allowed them to then relax. It is known that the exact linewidths are sensitive to the particular sample but the relative line breadth should be fairly constant. Using the non-linear error analysis algorithm provided by WMOSS, the errors in the computed parameters are estimated to be 0.02 mm s^{-1} for δ and 2% for Δ_{Eq}. We additionally note that in these spectra the exact percentage contributions given do not represent exact percentages.

Particularly for components that represent less than 10% of the overall spectrum, these values are subject to a high degree of uncertainty; however, all of the included components are necessary to generate satisfactory fits of the data and therefore are believed to be present in the reaction mixtures.

Details of Individual RFQ Mossbauer spectra:

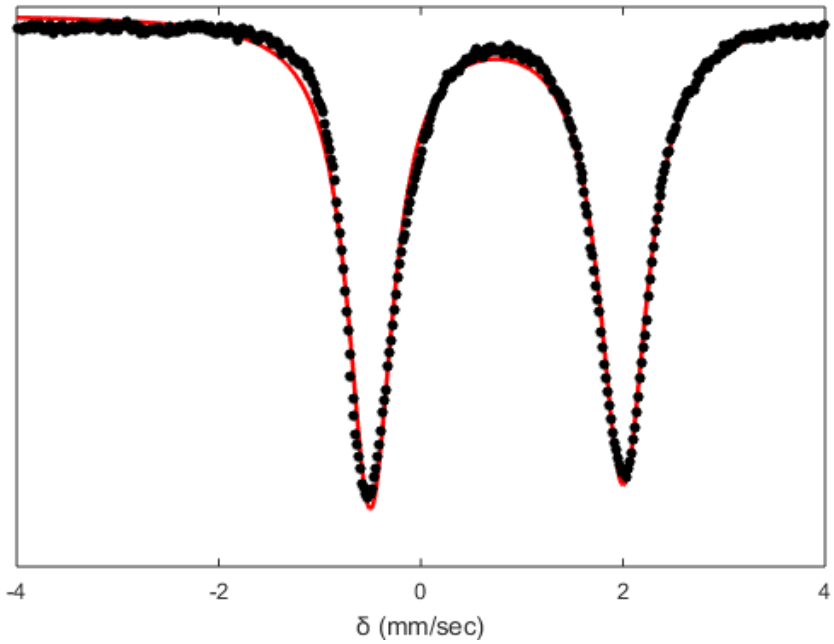

Figure A3.2. Mössbauer spectrum collected on $P_3^B(^{57}Fe)^+$ that was used for the Mössbauer experiments conducted in this paper. The parameters used to model this species are well within the experimental error of those used previously to model this species (δ = 0.75 mm/sec, Δ_{Eq} = 2.55 mm/sec, $\Gamma_r = \Gamma_l$ = 0.52 mm/sec).

Table A3.7: Fit parameters for ($P_3^BFe^+$)[22]

Component	δ (mm s^{-1})	ΔE_Q (mm s^{-1})	Linewidths, Γ_L/ Γ_R (mm s^{-1})
Fit	0.75 ± 0.02	2.50 ± 0.05	0.54/0.58

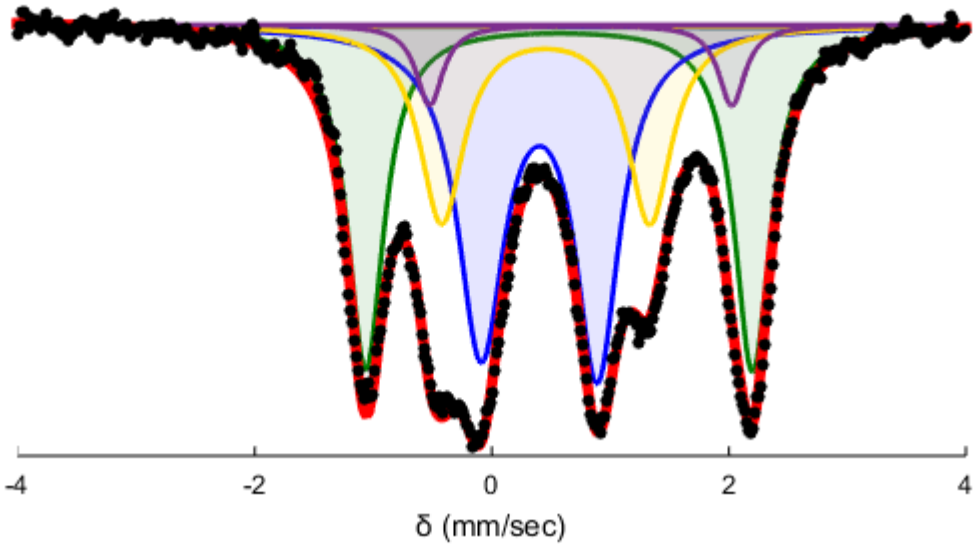

Figure A3.3. Mössbauer spectrum collected from a reaction freeze quenched after 5 minutes between $P_3^BFe^+$ and excess Cp^*_2Co (20 equiv). Raw data shown as black points, simulation as a solid red line, with components in green, blue, yellow, and purple (see Table A3.8 for parameters). The spectrum was collected at 80 K with a parallel applied magnetic field of 50 mT as a suspension in Et_2O.

Fitting details for Figure A3.3: Four quadrupole doublets were found to be necessary to obtain an adequate simulation. The simulation parameters are given in Table A3.8. The two major species in this spectrum are well simulated as $P_3^BFe–N_2$ and $P_3^BFe–N_2^-$. The residual signal exhibits only two well resolved absorbances but to obtain a good fit with symmetric lineshapes two additional quadrupole doublets were necessary. One of these can be identified as $[P_3^BFe]^+$ based on the asymmetry in the lineshape of the right feature of $P_3^BFe–N_2$. The similarity of the other two quadrupole doublets to those identified in the five-minute freeze quench make this a logically consistent fit but one that is not strictly required by the data.

Component	**δ (mm s^{-1})**	**ΔE_Q (mm s^{-1})**	**Linewidths, Γ_L/ Γ_R (mm s^{-1})**	**Relative area**
A (green)	0.57 ± 0.02	3.26 ± 0.06	0.29/0.29	0.33
B (purple)	0.75 ± 0.02	2.55 ± 0.05	0.27/0.27	0.06
C (yellow)	0.45 ± 0.02	1.76 ± 0.04	0.45/0.45	0.23
D (blue)	0.40 ± 0.02	0.98 ± 0.02	0.48/0.45	0.39

Table A3.8: **Simulation parameters for Mossbauer spectrum in Figure A3.3**

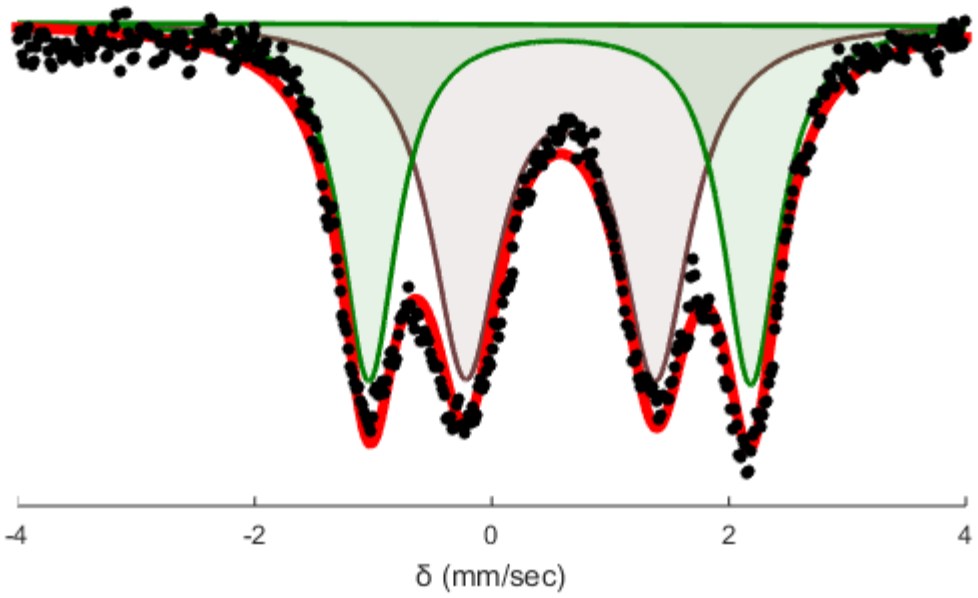

Figure A3.4: Mössbauer spectrum collected from a reaction freeze quenched after 5 minutes between $P_3^BFe^+$ and excess Cp^*_2Cr (20 equiv). Raw data shown as black points, simulation as a solid red line, with components in green and brown (see Table A3.9 for parameters). The spectrum was collected at 80 K with a parallel applied magnetic field of 50 mT as a suspension in Et_2O.

Fitting details for Figure A3.4: The two well-resolved quadrupole doublets can be simulated. The simulation parameters are given in Table A3.9. One of the two major species in this spectrum is well simulated as $P_3^BFe–N_2$. The other feature has a very similar isomer shift but a significantly narrower quadrupole splitting. Given the labile nature of the N_2 ligand this other species may represent a vacant neutral species or a dimeric N_2 bridged species.

Table A3.9: **Simulation parameters for Mossbauer spectrum in Figure A3.4**

Component	δ (mm s^{-1})	ΔE_Q (mm s^{-1})	Linewidths, Γ_L/ Γ_R (mm s^{-1})	Relative area
A (green)	0.57 ± 0.02	3.22 ± 0.06	0.29/0.29	0.46
B (brown)	0.58 ± 0.02	1.60 ± 0.05	0.71/0.71	0.54

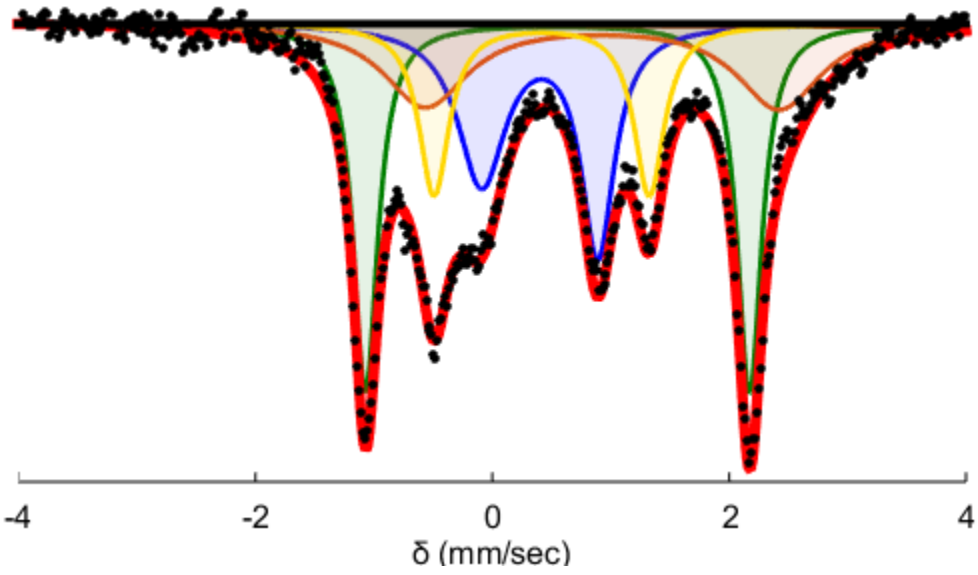

Figure A3.5: Mossbauer spectrum collected from a catalytic reaction freeze quenched after 5 minutes. Conditions: $[P_3^B(^{57}Fe)][BArF]$ = 0.23 mM, $[Ph_2NH_2][OTf]$ = 24.8 mM (108 equiv), and Cp^*_2Co 12.4 mM (54 equiv). Raw data shown as black points, simulation as a solid red line, with components in green, blue, yellow, and orange (see Table A3.10 for parameters). The spectrum was collected at 80 K with a parallel applied magnetic field of 50 mT.

Fitting details for Figure A3.5: Four pairs of quadrupole doublets were found to be necessary to obtain an adequate simulation of these data. The simulation parameters are given in Table A3.10. The outer pair of sharp features clearly belong to $P_3{}^BFeN_2$. The inner feature is highly suggestive of $P_3{}^BFeN_2^-$ the presence of which was confirmed by freeze-quench EPR. The residual then consists of two sharp features which were simulated with the quadrupole doublet in yellow and a broader residual feature that is captured by the quadrupole doublet in orange. The exact isomer shift and quadrupole splitting of orange is not determined by this model but the one here is representative.

Table A3.10: Simulation parameters for Mossbauer spectrum in Figure A3.5

Component	**δ (mm s^{-1})**	**ΔE_Q (mm s^{-1})**	**Linewidths, Γ_L/ Γ_R (mm s^{-1})**	**Relative area**
A (green)	0.55 ± 0.02	3.24 ± 0.06	0.25/0.25	0.32
B (blue)	0.40 ± 0.02	0.98 ± 0.02	0.49/0.34	0.26
C (yellow)	0.42 ± 0.02	1.82 ± 0.04	0.31/0.31	0.18
D (orange)	0.93 ± 0.02	2.99 ± 0.06	0.87/0.87	0.24

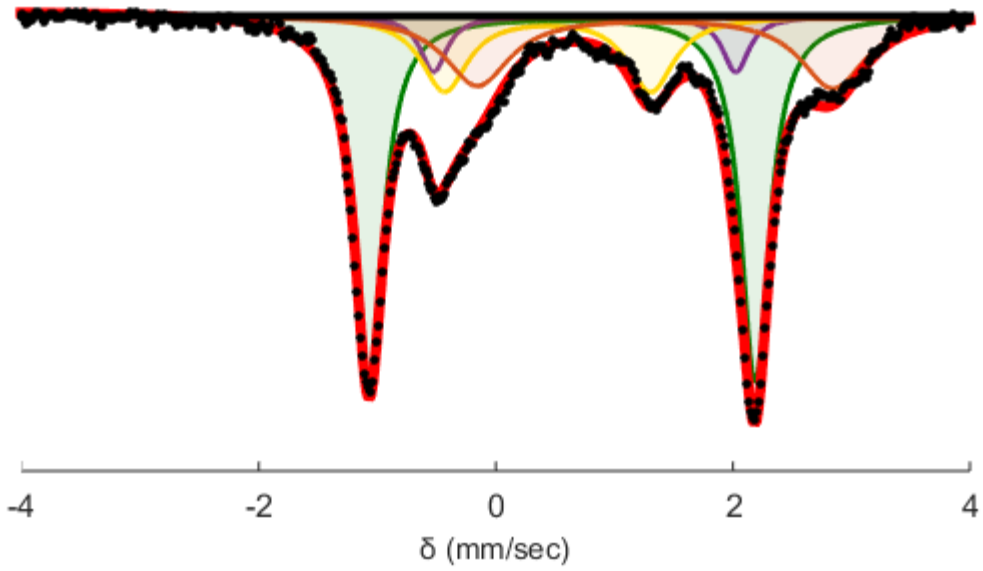

Figure A3.6: Mössbauer spectrum collected from a catalytic reaction freeze quenched after 30 minutes. Conditions: [$P_3^B(^{57}Fe)$][BArF] = 0.23 mM, [Ph_2NH_2][OTf] = 24.8 mM (108 equiv), and Cp^*_2Co 12.4 mM (54 equiv). Raw data shown as black points, simulation as a solid red line, with components in green, purple, yellow, and orange (see Table A3.11 for parameters). The spectrum was collected at 80 K with a parallel-applied magnetic field of 50 mT.

Fitting details for Figure A3.6: Four quadrupole doublets were found to be necessary to obtain an adequate simulation. The simulation parameters are given in Table A3.11. The major species in this spectrum is again well simulated as P_3^BFe–N_2. The residual signal exhibits only three well resolved absorbances. To obtain a good fit with symmetric lineshapes three additional quadrupole doublets were necessary. One of these can be identified as $[P_3^B Fe]^+$ based on the asymmetry in the lineshape of the right feature of P_3^BFe–N_2. The similarity of the other two quadrupole doublets to those identified in the

five-minute freeze quench make this a logically consistent fit but one that is not strictly required by the data.

Table A3.11: Simulation parameters for Mossbauer spectrum in Figure A3.6

Component	**δ (mm s^{-1})**	**ΔE_Q (mm s^{-1})**	**Linewidths, Γ_L/ Γ_R (mm s^{-1})**	**Relative area**
A (green)	0.55 ± 0.02	3.24 ± 0.06	0.29/0.29	0.53
B (purple)	0.75 ± 0.02	2.55 ± 0.05	0.27/0.27	0.08
C (yellow)	0.44 ± 0.02	1.74 ± 0.04	0.48/0.48	0.18
D (orange)	1.35 ± 0.02	3.00 ± 0.06	0.67/0.67	0.22

A3.8 EPR Spectra:

General Procedure for Preparation of Rapid-freeze-quench EPR Samples of Catalytic Reaction Mixtures using $P_3^BFe^+$:

All manipulations are carried out inside of a nitrogen filled glovebox. The precatalyst, [P_3^BFe][BAr^F_4], is weighed into a vial (3.5 mg, 2.3 μmol) and transferred using THF into a 150 mL Schlenk tube. The solvent is evaporated to form a thin film of the precatalyst and a stir bar is added. The [Ph_2NH_2][OTf] (79.4 mg, 0.248 mmol) and Cp^*_2Co (40.3 mg, 0.124 mmol) are added to the Schlenk tube as solids. The Schlenk tube is then placed in $N_{2(l)}$ and the temperature is allowed to equilibrate. To the tube 1 mL of Et_2O is added. The tube is then sealed with a Teflon screw tap and transferred to a pre-chilled cold well at -78 °C. The timer is set to zero as soon as the stir bar is freed from the thawing solvent. At the desired time, the tube is opened and the well-stirred suspension is transferred to an EPR tube that is prechilled to -78 °C using a pipette that has similarly been pre-chilled to -78 °C. The EPR sample is then rapidly frozen in $N_{2(l)}$. At this point the sample is quickly transferred out of the glovebox and put into $N_{2(l)}$ before it can warm.

General Procedure for Preparation of Rapid-freeze-quench EPR Samples of the Reaction of $P_3^BFe^+$ with Reductants:

All manipulations are carried out inside of a nitrogen filled glovebox. The precatalyst, [P_3^BFe][BAr^F_4], is weighed into a vial (3.5 mg, 2.3 μmol) and .5 mL of THF is added. The solvent is then evaporated to provide a thin film of [P_3^BFe][BAr^F_4]. To this is added (46.0 μmol, 20 equiv) of the desired reductant as a solid. This vial is then placed

in $N_{2(l)}$ and the temperature is allowed to equilibrate. To this is added 1 mL of NaK-dried Et_2O. The vial is then sealed with a cap and transferred to a pre-chilled cold well at -78 °C. The timer is set to zero as soon as the stir bar is freed from the thawing solvent. At the desired time, the tube is opened and the well-stirred suspension is transferred to an EPR tube that is prechilled to -78 °C using a pipette that has similarly been pre-chilled to -78 °C. The EPR sample is then rapidly frozen in $N_{2(l)}$. At this point the sample is quickly transferred out of the glovebox and put into $N_{2(l)}$ before it can warm.

General Procedure for Preparation of EPR Samples of Cp^*_2Co, $[P_3^BFe][BAr^F_4]$, and $[P_3^BFeN_2][Na(12\text{-crown-}4)_2]$:

The desired species was dissolved in 1 mL of Et_2O at RT and transferred to an EPR tube. The EPR tube was then chilled to -78 °C for five minutes. It was then rapidly frozen by transfer to a bath of $N_{2(l)}$.

Procedure for EPR Characterization of the Reaction of Cp^*_2Co with Acid:

The as isolated solid was added to a J-Young or septum-sealed X-Band EPR tube after prechilling both in the cold well to 77 K. Specific experimental details are listed with the accompanying spectra.

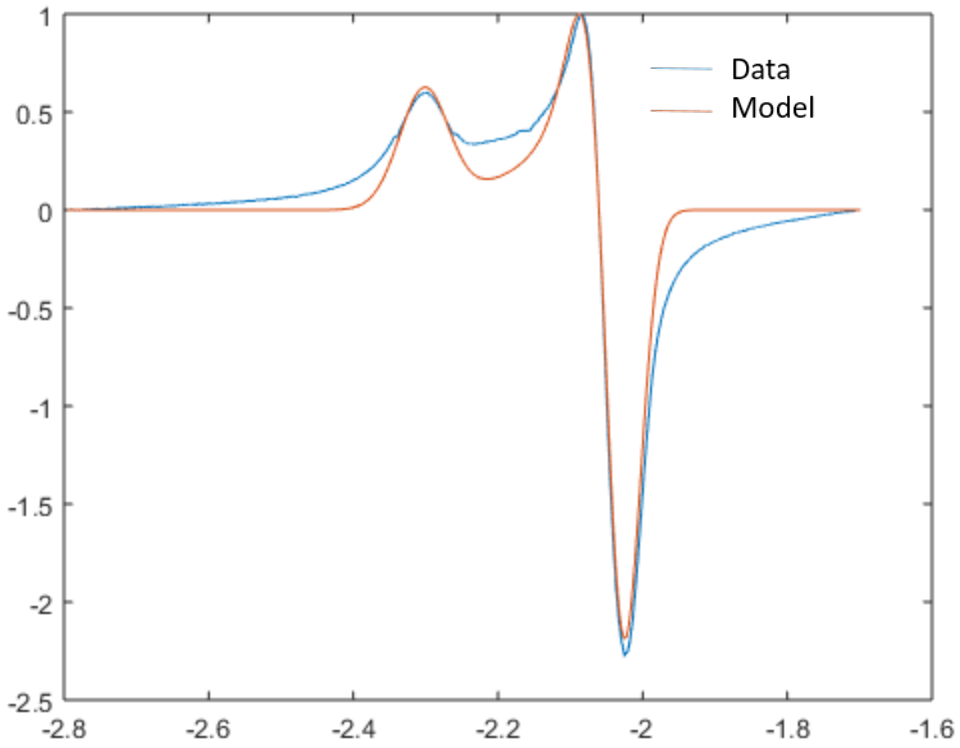

Figure A3.7: The X-band EPR spectrum in a 2-MeTHF glass of 2.3 mM [P_3^BFe–N_2][Na(12-crown-4)$_2$] at 77K. Note that the exceeding insolubility of these species when encapsulated in a crown salt prevented its measurement in ether. We note that this species has significantly different parameters than the species in which the Na is not encapsulated with a crown ether and is therefore interacting with the N_2 ligand. We think this species is more representative of what a hypothetical [P_3^BFe–N_2][Cp*$_2$Co] species would look like if isolated.

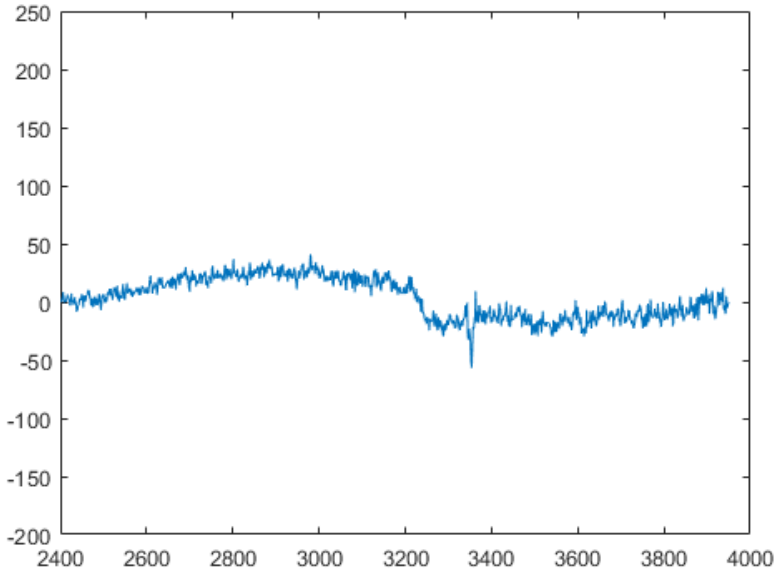

Figure A3.8: The X-band EPR spectrum in Et_2O of 2.3 mM $[P_3^BFe][BAr^F_4]$ at 77 K. Note this species is S = 3/2 and we have previously reported that this species is only observable at 10 K by X-band spectroscopy.[23] We attribute the extremely weak signal observed here to background signal from the cavity.

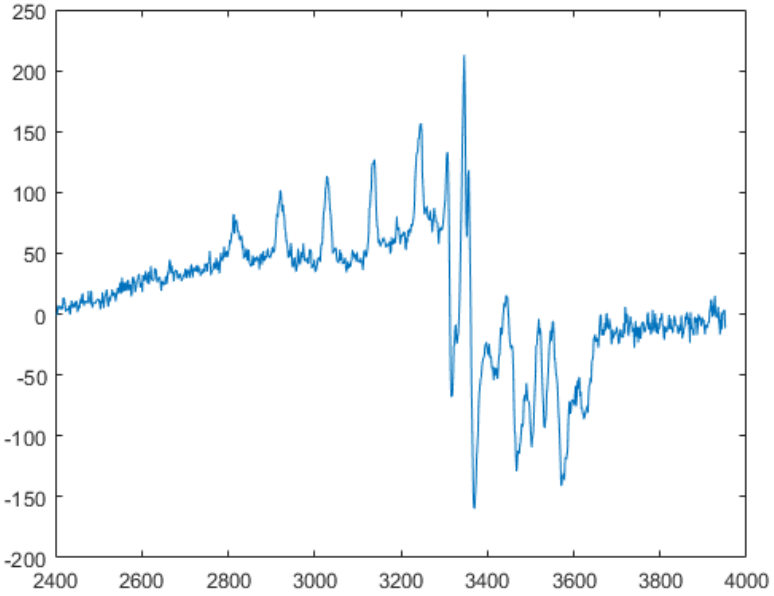

Figure A3.9: The X-band EPR spectrum in Et_2O of 46 mM Cp^*_2Co at 77K. Decamethylcobaltocene is known to be EPR silent at 77 K[24] but at these high concentrations it becomes apparent that there is a small S = ½ impurity present in this spectrum. This persistent impurity is observable in both freeze quenched reactions of this reductant with $[P_3^BFe][BAr^F_4]$ and in spectra of the freeze quenched catalytic reaction mixtures.

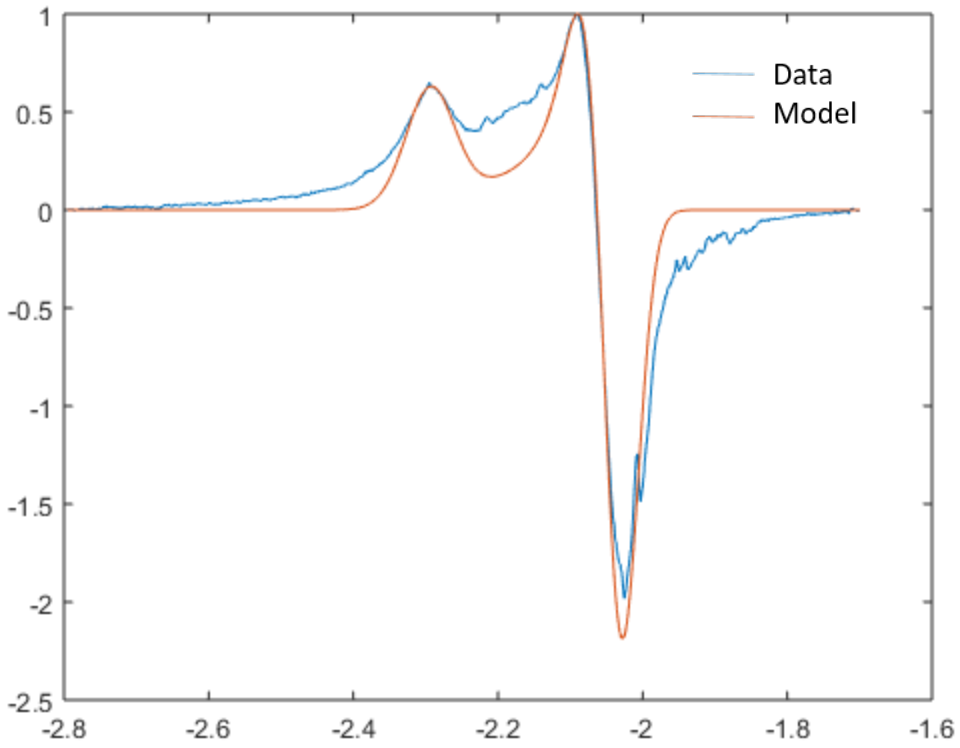

Figure A3.10: The X-band EPR spectrum in Et_2O (1 mL) of the reaction between $P_3^BFe^+$ (3.5 mg, 0.0023 mmol) and Cp^*_2Co (15.2 mg, 0.046 mmol) stirred for 5 minutes at -78 °C then rapidly frozen to 77 K.

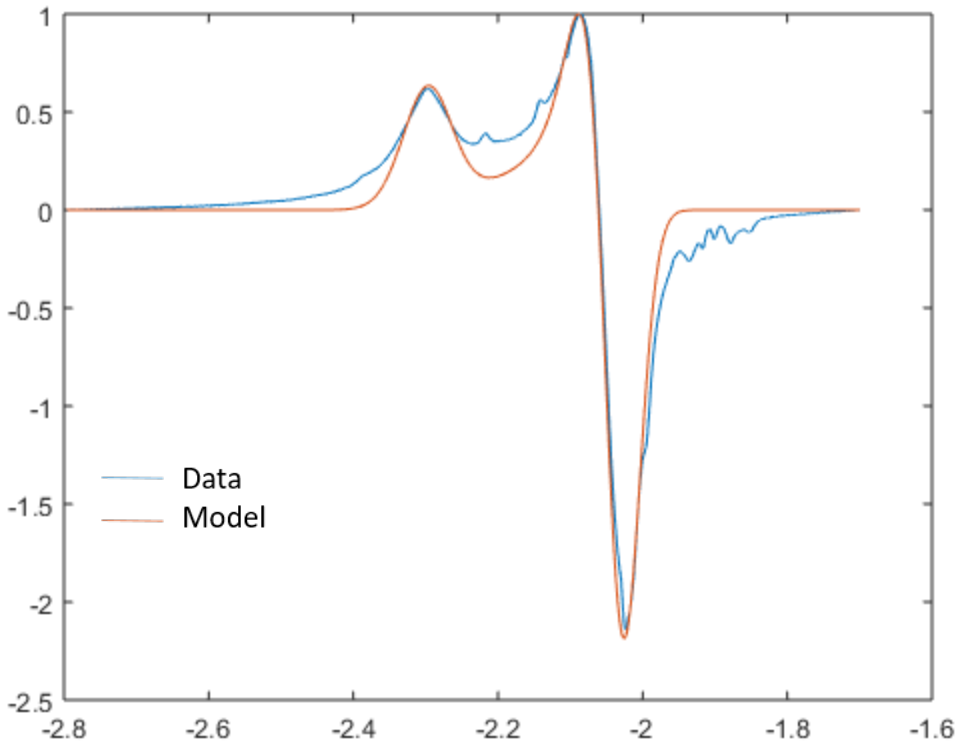

Figure A3.11: The X-band EPR spectrum in Et_2O (1 mL) of the reaction between $P_3{}^BFe^+$ (3.5 mg, 0.0023 mmol) and Cp^*_2Co (40.3 mg, 0.124 mmol) and $[Ph_2NH_2][OTf]$ (79.4 mg, 0.248 mmol) stirred for 5 minutes at -78 °C then rapidly frozen to 77 K.

Table A3.12: **A comparison of the best fitting parameters for the authentic sample of $P_3{}^BFeN_2^-$ (A), the freeze quench of the reaction with the reductant (B), the freeze quench of the catalytic reaction mixture (C)**

Reaction	g_x	g_y	g_z
A	2.304	2.048	2.032

B	2.295	2.048	2.032
C	2.298	2.048	2.032

Discussion of the EPR spectra obtained by reacting Cp^*_2Co with Acid:

Previous studies have demonstrated that the EPR signal for Cp^*_2Co is only apparent at temperatures below the 77 K used in this study. In line with this expectation the solution spectra of Cp^*_2Co at 77 K do not show any signal (Figure A3.12, green). The 77 K powder, X-band EPR spectrum obtained of the material isolated as described in SI 2.2 (Figure A3.12, red) demonstrates a signal with significant g-anisotropy and Co-hyperfine coupling. Although ^1H-hyperfine coupling is not resolved in this spectrum we believe that this is due to the large Co-hyperfine coupling and the significant linewidths observed (Figure A3.13). Attempts to obtain narrower linewidths by diluting the solid in KBr did not lead to any observable improvement. However, comparison of the spectrum obtained from reaction of Cp^*_2Co with HOTf and DOTf (Figure A3.14) strongly supports the hypothesis that this material represents a protonated Cp^*_2Co. In particular, the narrower lineshapes observed in the reaction with DOTf evidence both that the metallocene has been protonated but also that this proton is strongly coupled to the spin. The narrower line shapes manifest because of the lesser gyromagnetic ratio of ^2H compared to ^1H confirming that the linewidths in the reaction with HOTf are in part broadened by coupling to the added proton. That the appearance of the extra lines observed in the reaction with DOTf can be well-simulated simply by dividing the anisotropic strain parameter (HStrain in EasySpin) by the ratio of the ^1H gyromagnetic

ratio:^{2}H gyromagnetic ratio (~6.5) strongly supports this hypothesis (Figure A3.15). That two species are present (more obvious in the DOTf reaction due to the sharper lineshapes) is further evidence that these spectra represent *endo*- and *exo*-protonated decamethylcobaltocene ($Cp^*Co(\eta^4\text{-}C_5Me_5H)^+$, as we would expect both the *endo*- and *exo*-protonated isomers to be kinetically and thermodynamically accessible under these conditions, and they should manifest distinct EPR signatures. Although preliminary in nature the observed reactivity of these species (discussed in SI 9.1-9.3) is further evidence that this material is competent for PCET reactivity as predicted by DFT.

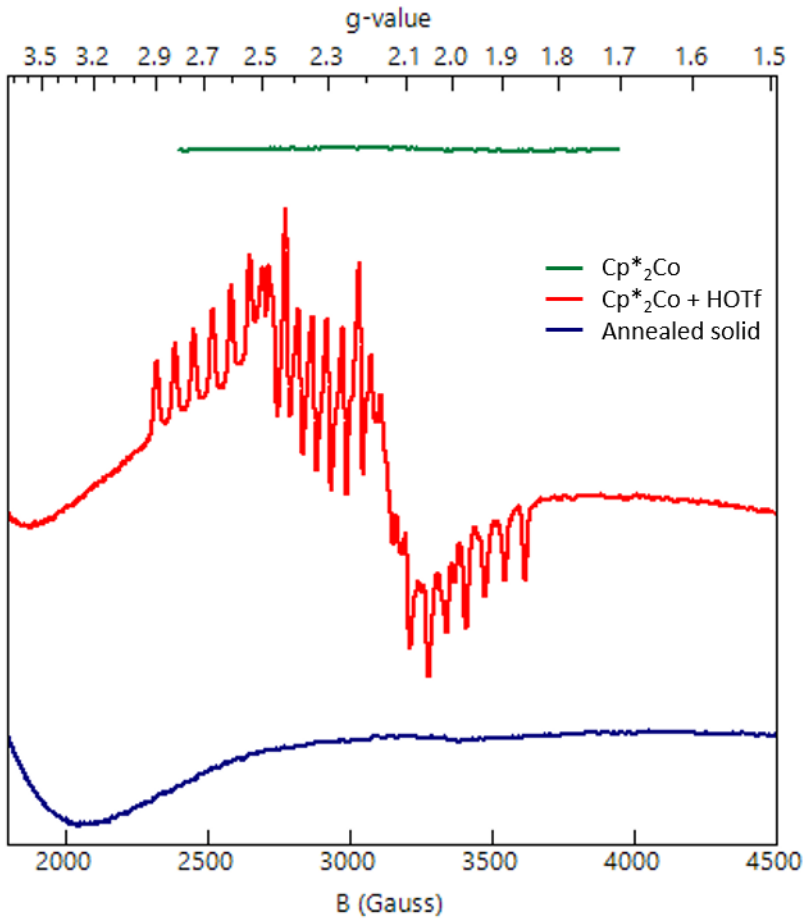

Figure A3.12: 77 K X-band EPR spectrum of a toluene solution of Cp^*_2Co (green), 77 K powder X-Band EPR spectrum of the purple solid isolated from the reaction of Cp^*_2Co and HOTf as described in SI 2.2 (red), and 77 K powder X-Band EPR spectrum after annealing the EPR tube RT for two hours (blue)

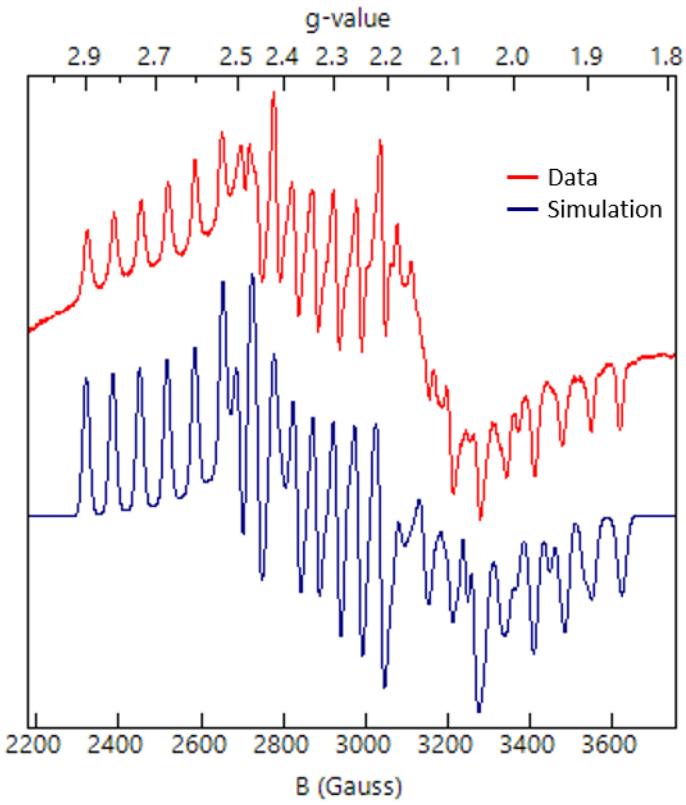

Figure A3.13: Powder EPR spectrum at 77 K for the reaction of HOTf and Cp^*_2Co and its simulation. Simulation parameters are g_1 = [2.63 2.345 1.984], $A_{1,Co}$ = [248 160 187], lw_1 = 1 MHz, $HStrain_1$ = [60 50 60], $Weight_1$ = 1; g_2 = [2.347 2.1 1.982], $A_{2,Co}$ = [200 50 110], lw_2 = 1, $HStrain_2$ = [40 40 40], $Weight_2$ = 0.2.

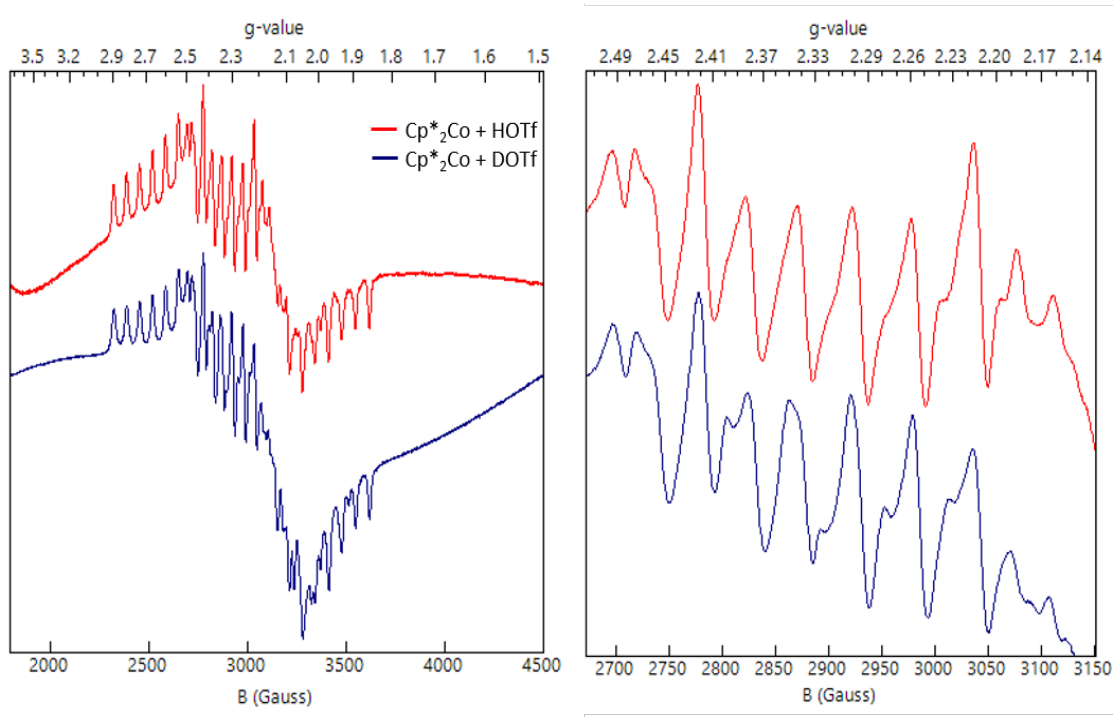

Figure A3.14: Comparison of the EPR spectra obtained using HOTf and DOTf in the reaction with Cp*$_2$Co. The zoomed in spectrum highlights the middle g-value where the differences are most apparent between the two reactions.

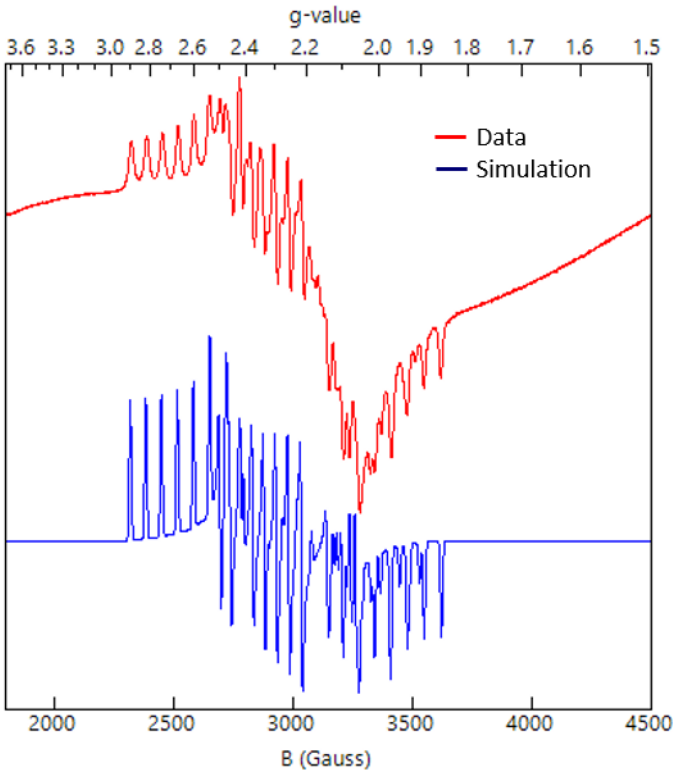

Figure A3.15: EPR spectrum obtained when reacting DOTf with Cp^*_2Co and its simulation. Simulation parameters are g_1 = [2.63 2.345 1.984], $A_{1,Co}$ = [248 160 187], lw_1 = 1 MHz, $HStrain_1$ = [9.2 7.7 9.2], $Weight_1$ = 1; g_2 = [2.347 2.1 1.982], $A_{2,Co}$ = [200 50 110], lw_2 = 1, $HStrain_2$ = [6.2 6.2 6.2], $Weight_2$ = 0.2.

A3.9 Reactivity of $Cp^*Co(\eta^4\text{-}C_5Me_5H)^+$

Annealing Purple Solid:

Purple solid isolated as described in SI 2.2 was placed in an X-band EPR tube at 77 K and sealed with a rubber septum. A 77 K, powder X-band EPR spectrum was then taken to confirm the presence of $Cp^*Co(\eta^4\text{-}C_5Me_5H)^+$. After two hours at room temperature a second 77 K, powder EPR spectrum was taken to confirm the quenching of $Cp^*Co(\eta^4\text{-}C_5Me_5H)^+$. At this point the headspace was analyzed for H_2 via GC (14% yield).

Annealing Suspension of Purple Solid in Toluene:

Into a 26 mL vial with a septum seal was loaded 2 mL of toluene which was frozen at 77 K. To this purple solid isolated as described in SI 2.2 was added along with a stir bar. The suspension was stirred for 1 hour at −78 °C and then warmed to room temperature and stirred for an additional 15 minutes. At this point the headspace was sampled for H_2 via GC (35% yield). The solvent was then removed and to the yellow residue was added 1,3,5-trimethoxybenzene (1 eq.). The solid was then extracted with d_6-acetone and ^1H NMR was obtained. $Cp^*_2Co^+$ was observed (___ % yield).

Upper Bound on Protonated Metallocene BDE

An upper bound for the BDE of the putative protonated metallocene was estimated using the literature BDE value for H_2 (105.8 kcal/mol) in MeCN, as well as the approximation for $T\Delta S_{H\bullet}$ (4.6 kcal/mol) in MeCN.[24] The maximum BDE was then approximated as follows:

$$\Delta G = \Delta H - T\Delta S < 0 \frac{\text{kcal}}{\text{mol}}$$

$$\Delta H = BDE_{H2} - 2 * BDE_{Cp*2CoH+} = 105.8 \frac{kcal}{mol} - 2 * BDE_{Cp*2CoH+}$$

$$T\Delta S = T\Delta S_{H\cdot} - 2 \cdot (T\Delta S_{H\cdot}) = -T\Delta S_{H\cdot} = -4.6 \frac{kcal}{mol}$$

$$105.8 \frac{kcal}{mol} - 2 * BDE_{Cp*2CoH+} + 4.6 \frac{kcal}{mol} < 0 \frac{kcal}{mol}$$

$$\therefore BDE_{Cp*2CoH+} < 50.6 \frac{kcal}{mol}$$

A3.10 Details on DFT Estimates of p*K*a and BDE

Computational Estimates of p*K*a in Et2O:

The pK_a values in diethyl ether were calculated referenced to $H(OEt_2)_2^+$ and were predicted on the basis of the free-energy change of the exchange reaction with $H(OEt_2)_2^+$ and application of Hess' law on the closed chemical cycle. The pK_a of $H(OEt_2)_2^+$ was defined as 0.0.

Computational Estimates of BDEs:

Bond dissociation enthalpies (BDE) of X–H bonds were calculated in the gas-phase using a series of known reference compounds containing M–OH, M–H and M–NH bonds.[20] The enthalpy difference between the H-atom donor/acceptor pair was calculated based on the thermochemical information provided by frequency calculations after

structure optimizations using the procedure described in the general computational section. A linear plot of ΔH *vs* BDE_{lit} was generated to form a calibration curve (Figure A3.12). BDE predictions were generated by application of the line of best fit to the calculated ΔH of the unknown species. Error were calculated by application of the trend line to the calculated enthalpies of known species and comparison to their literature BDE value.[23] Errors are reported as the average of BDE_{calc}-BDE_{lit} (mean signed error, MSE) and the average of the absolute values of BDE_{calc}-BDE_{lit} (mean unsigned error, MUE). The use of the Bordwell equation for bond dissociation enthalpies is well supported by small $\Delta S_{calc} = S(X^{\bullet}) - S(XH)$, as shown in Table A3.14.

Table A3.13: Calculated ΔH values and literature BDE values used for BDE calibration

Species	ΔH_{calc}	BDE_{lit}	BDE_{calc}	Notes
$Cr(H_2O)_5(OH)^{2+}$	97.735	89	90	ref 25
$Fe(H_2O)_6^{2+}$	77.985	77	75	ref 25
$Cr(H_2O)_5(OOH)^{2+}$	77.175	79	75	ref 25
$bimFeN_2^{2+}$	69.255	67	68	ref 25
$P_3^{Si}Fe\text{-}C{=}NH^{+}$	65.905	65	66	ref 26
$bipFeH_2^{2+}$	65.475	62	65	ref 25
$TrenFeOH^{2-}$	64.105	66	64	ref 25
$CpFe(CO)_2H$	57.455	56	59	ref 25
$[HIPTN_3N]Mo\text{-}N{=}NH$	47.715	49	51	Truncated; ref 27
$P_3^{Si}Fe\text{-}N{=}NMeH^{+}$	43.915	48	48	ref 25
$P_3^{Si}Fe\text{-}C{=}NH$	38.915	44	44	ref 25
$P_3^{Si}Fe\text{-}C{=}NMeH$	34.375	45	40	ref 25
$P_3^{Si}Fe\text{-}C{=}NMeH^{+}$	32.955	44	39	ref 25
			MSE	-0.9
			MUE	2.1

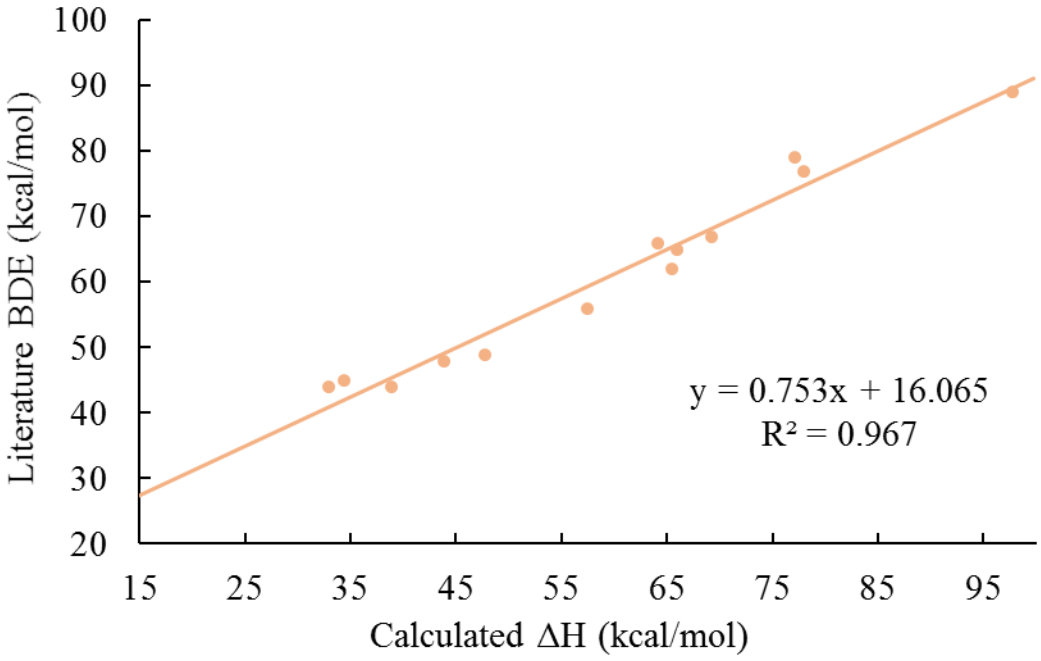

Figure A3.16: Calculated BDE vs literature BDE for the species shown in table A3.13.

Table A3.14: Calculated entropy (S) for selected XH and X• species

Species	S(X•) (cal/mol*K)	S(XH) (cal/mol*K)	ΔS (kcal/mol*K)
P_3^BFe-N=NH	271.6	268.9	$2.7x10^{-3}$
P_3^BFe=N-NH_2^+	266.3	273.1	$-6.8x10^{-3}$
P_3^BFe=N-NH_2	268.9	281.3	$-1.2x10^{-2}$
Cp*Co(η^4-C_5Me_5H)$^+$	168.8	162.0	$6.6x10^{-3}$
Cp*Cr(η^4-C_5Me_5H)$^+$	159.5	163.4	$-3.9x10^{-3}$

Estimation of PCET Activation Barriers:

Activation barriers were bracketed using the methods develop by the Hammes-Schiffer group. The inner sphere reorganization energy was estimated using force constants for normal modes in the Fe- and Co-coordination sphere.[28] The outer sphere reorganization energy (λ_{OS}) was estimated by calculating the outer sphere reorganization energy for a single ET in diethyl ether using the continuum solvation model[29] and assuming $\lambda_{OS,PCET} \leq \lambda_{OS,ET}$.[27] The activation barrier was plotted as a function of λ_{OS} (Figure A3.17) to determine a maximum and minimum barrier for each PCET reaction (Table A3.15).

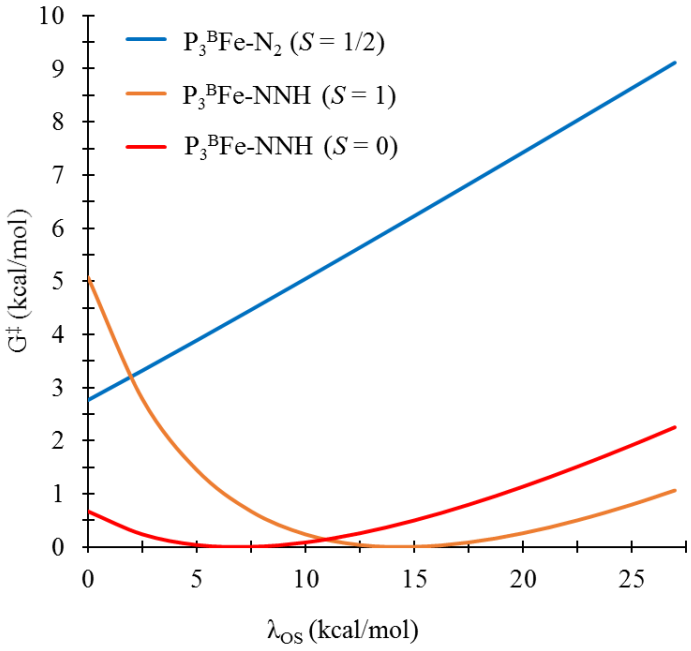

Figure A3.17: Activation barrier for PCET reactions between selected $P_3^BFe\text{-}N_xH_y$ species (as labeled, total spin-state of the surface in parenthesis) with $Cp^*Co(\eta^4\text{-}C_5Me_5H)^+$ as a function of outer-sphere reorganization energy.

Table A3.15: Calculated Reorganization Energies, Free-Energies of Reaction and Activation Barriers for Selected PCET Reactions

Acceptor	Spin State	Donor	λ_{tot} Range (kcal/mol)	ΔG_{rxn} (kcal/mol)	$G^‡$ Range (kcal/mol)
$P_3^BFe\text{-}N_2$	S = ½	$Cp^*Co(\eta^4\text{-}C_5Me_5H)^+$	26.1 - 53.5	-9.1	3 - 9
$P_3^BFe\text{-}NNH$	S = 0	$Cp^*Co(\eta^4\text{-}C_5Me_5H)^+$	17.7 – 45.1	-24.6	0 – 2
$P_3^BFe\text{-}NNH$	S = 1	$Cp^*Co(\eta^4\text{-}C_5Me_5H)^+$	10.2 – 37.6	-24.6	0 - 5

A3.11 REFERENCES

1 Robbins, J. L.; Edelstein, N.; Spencer, B.; Smart, J. C. Syntheses and Electronic Structures of Decamethylmetallocenes. *J. Am. Chem. Soc.* **1982**, *104*, 1882–1893.

2 Anderson, J. S.; Moret, M.-E.; Peters, J. C. Conversion of Fe–NH2 to Fe–N2 with Release of NH3. *J. Am. Chem. Soc.* **2013**, *135*, 534–537.

3 Mankad, N. P.; Whited, M. T.; Peters, J. C. Terminal Fe-N2 and FeII···H-C Interactions Supported by Tris(phosphino)silyl Ligands. *Angew. Chem. Int. Ed.* **2007**, *46*, 5768–5771.

4 Del Castillo, T. J.; Thompson, N. B.; Suess, D. L. M.; Ung, G.; Peters, J. C. Evaluating Molecular Cobalt Complexes for the Conversion of N2 to NH3. *Inorg. Chem.* **2015**, *54*, 9256–9262.

5 Suess, D. L. M.; Tsay, C.; Peters, J. C. Dihydrogen Binding to Isostructural S = 1/2 and S = 0 Cobalt Complexes. *J. Am. Chem. Soc.* **2012**, *134*, 14158–14164.

6 Moret, M.-E.; Peters, J. C. Terminal Iron Dinitrogen and Iron Imide Complexes Supported by a Tris(phosphino)borane Ligand. *Angew. Chem. Int. Ed.* **2011**, *50*, 2063–2067.

7 Melzer, M. M.; Mossin, S.; Dai, X.; Bartell, A. M.; Kapoor, P.; Meyer, K.; Warren, T. H. A Three-Coordinate Copper(II) Amide from Reductive Cleavage of a Nitrosamine. *Angew. Chem. Int. Ed.* **2010**, *49*, 904–907.

8 Vicente, J.; Chicote, M.-T.; Guerrero, R.; Jones, P. G. Synthesis of Complexes [Au(PPh3)L]+(L = Primary, Secondary or Tertiary Amine). Crystal Structure of [Au(PPh3)(NMe3)][ClO4]·CH2Cl2. *J. Chem. Soc., Dalton Trans.* **1995**,*8*, 1251–1254.

9 Weatherburn, M. W. Phenol-Hypochlorite Reaction for Determination of Ammonia. *Anal. Chem.* **1967**, *39*, 971–974.

10 Watt, G. W.; Chrisp, J. D. Spectrophotometric Method for Determination of Hydrazine. *Anal. Chem.* **1952**, *24*, 2006–2008.

11 The Spin Count program developed by the Hendrich group at Carnegie Mellon was used to convert them to the g-value and then baseline them.

12 Stoll, S.; Schweiger, A. EasySpin, a Comprehensive Software Package for Spectral Simulation and Analysis in EPR. *Journal of Magnetic Resonance* **2006**, *178*, 42–55.

13 Zhao, Y.; Truhlar, D. G. A New Local Density Functional for Main-Group Thermochemistry, Transition Metal Bonding, Thermochemical Kinetics, and Noncovalent Interactions. *J. Chem, Phys.* **2006**, *125*, 194101: 1-18.

14 Weigend, F.; Ahlrichs, R. Balanced Basis Sets of Split Valence, Triple Zeta Valence and Quadruple Zeta Valence Quality for H to Rn: Design and Assessment of Accuracy. *Phys. Chem. Chem. Phys.* **2005**, *7*, 3297–3305.

15 Andrae, D.; Häußermann, U.; Dolg, M.; Stoll, H.; Preuß, H. Energy-Adjusted Ab Initio Pseudopotentials for the Second and Third Row Transition Elements. *Theoret. Chim. Acta* **1990**, *77*, 123–141.

16 *John Towns, Timothy Cockerill, Maytal Dahan, Ian Foster, Kelly Gaither, Andrew Grimshaw, Victor Hazlewood, Scott Lathrop, Dave Lifka, Gregory D. Peterson, Ralph Roskies, J. Ray Scott, Nancy Wilkins-Diehr, "XSEDE: Accelerating Scientific Discovery", Computing in Science & Engineering, vol.16, no. 5, pp. 62-74, Sept.-Oct. 2014, doi:10.1109/MCSE.2014.80*

17 Valiev, M.; Bylaska, E. J.; Govind, N.; Kowalski, K.; Straatsma, T. P.; Van Dam, H. J. J.; Wang, D.; Nieplocha, J.; Apra, E.; Windus, T. L.; de Jong, W. A. NWChem: A Comprehensive and Scalable Open-Source Solution for Large Scale Molecular Simulations. *Comput. Phys. Commun.* **2010**, *181*, 1477–1489.

18 Gaussian 09, Revision **B.01**, Frisch, M. J.; Trucks, G. W.; Schlegel, H. B.; Scuseria, G. E.; Robb, M. A.; Cheeseman, J. R.; Scalmani, G.; Barone, V.; Mennucci, B.; Petersson, G. A.; Nakatsuji, H.; Caricato, M.; Li, X.; Hratchian, H. P.; Izmaylov, A. F.; Bloino, J.; Zheng, G.; Sonnenberg, J. L.; Hada, M.; Ehara, M.; Toyota, K.; Fukuda, R.; Hasegawa, J.; Ishida, M.; Nakajima, T.; Honda, Y.; Kitao, O.; Nakai, H.; Vreven, T.; Montgomery, J. A., Jr.; Peralta, J. E.; Ogliaro, F.; Bearpark, M.; Heyd, J. J.; Brothers, E.; Kudin, K. N.; Staroverov, V. N.; Kobayashi, R.; Normand, J.; Raghavachari, K.;

Rendell, A.; Burant, J. C.; Iyengar, S. S.; Tomasi, J.; Cossi, M.; Rega, N.; Millam, J. M.; Klene, M.; Knox, J. E.; Cross, J. B.; Bakken,V.; Adamo, C.; Jaramillo, J.; Gomperts, R.; Stratmann, R. E.; Yazyev, O.; Austin, A. J.; Cammi, R.; Pomelli, C.; Ochterski, J. W.; Martin, R. L.; Morokuma, K.; Zakrzewski, V. G.; Voth, G. A.; Salvador, P.; Dannenberg, J. J.; Dapprich, S.; Daniels, A. D.; Farkas, Ö.; Foresman, J. B.; Ortiz, J. V.; Cioslowski, J.; Fox, D. J. Gaussian, Inc., Wallingford CT, 2009.

19 Ribeiro, R. F.; Marenich, A. V.; Cramer, C. J.; Truhlar, D. G. Use of Solution-Phase Vibrational Frequencies in Continuum Models for the Free Energy of Solvation. *J. Phys. Chem. B* **2011**, *115*, 14556–14562.

20 Wang, T.; Brudvig, G.; Batista, V. S. Characterization of Proton Coupled Electron Transfer in a Biomimetic Oxomanganese Complex: Evaluation of the DFT B3LYP Level of Theory. *J. Chem. Theory Comput.* **2010**, *6*, 755–760.

21 Marten, B.; Kim, K.; Cortis, C.; Friesner, R. A.; Murphy, R. B.; Ringnalda, M. N.; Sitkoff, D.; Honig, B. New Model for Calculation of Solvation Free Energies: Correction of Self-Consistent Reaction Field Continuum Dielectric Theory for Short-Range Hydrogen-Bonding Effects. *J. Phys. Chem.* **1996**, *100*, 11775–11788.

22 Anderson, J. S.; Cutsail, G. E.; Rittle, J.; Connor, B. A.; Gunderson, W. A.; Zhang, L.; Hoffman, B. M.; Peters, J. C. Characterization of an Fe≡N–NH2 Intermediate Relevant to Catalytic N2 Reduction to NH3. *J. Am. Chem. Soc.* **2015**, *137*, 7803–7809.

23 Anderson, J. S.; Moret, M.-E.; Peters, J. C. Conversion of Fe−NH_2 to Fe−N_2 with release of NH_3. *J. Am. Chem. Soc.* **2013**, *135*, 534-537.

24 Robbins, J. L.; Edelstein, N.; Spencer, B.; Smart, J. C. Synthesis and Electronic Structure of Decamethylmetallocenes. *J. Am. Chem. Soc.* **1982**, *104*, 1882-1893.

25 Warren, J. J.; Tronic, T. A.; Mayer, J. M. Thermochemistry of Proton-Coupled Electron Transfer Reagents and Its Implications. *Chem. Rev.* **2010**, *110*, 6961–7001.

26 Rittle, J.; Peters, J. C. *Submitted Manuscript.*

27 Yandulov, D. V.; Schrock, R. R. Studies Relevant to Catalytic Reduction of Dinitrogen to Ammonia by Molybdenum Triamidoamine Complexes. *Inorg. Chem.* **2005**, *44*, 1103–1117.

28 Iordanova, N.; Decornez, H.; Hammes-Schiffer, S. Theoretical Study of Electron, Proton, and Proton-Coupled Electron Transfer in Iron Bi-Imidazoline Complexes. *J. Am. Chem. Soc.* **2001**, *123*, 3723–3733.

29 Marcus, R. A. On the Theory of Oxidation-Reduction Reactions Involving Electron Transfer. *J. Chem. Phys.* **1956**, *24*, 966–978.

Appendix 4

SUPPLEMENTARY INFORMATION FOR CHAPTER 5: FE-MEDIATED NITROGEN FIXATION WITH A METALLOCENE MEDIATOR: EXPLORING PK_A EFFECTS AND DEMONSTRATING ELECTROCATALYSIS

Reproduced in part with permission from:

Chalkley, M.; Del Castillo, T.; Matson, B.; Peters, J. C.; *J. Am. Chem. Soc.*, **2018**, submitted.

A4.1 Experimental Details

General Considerations

All manipulations were carried out using standard Schlenk or glovebox techniques under an N_2 atmosphere. Solvents were deoxygenated and dried by thoroughly sparging with N_2 followed by passage through an activated alumina column in a solvent purification system by SG Water, USA LLC. Non-halogenated solvents were tested with sodium benzophenone ketyl in tetrahydrofuran (THF) in order to confirm the absence of oxygen and water. Deuterated solvents were purchased from Cambridge Isotope Laboratories, Inc., degassed, and dried over activated 3-Å molecular sieves prior to use.

Cp^*_2Co,[1] $[P_3^BFe][BAr^F_4]$,[2] $[P_3^BFeN_2][Na(Et_2O)_3]$,[3] $[P_3^BFeN_2][Na(12\text{-crown-}4)_2]$,[3] $[H(OEt2)][BAr^F_4]$ ($HBAr^F_4$; BAr^F_4 = tetrakis- (3,5-bis(trifluoromethyl)phenyl)borate)[4],

sodium BAr^F_4 ($NaBAr^F_4$)[4], and ^{15}N-diphenylammonium triflate ($[Ph_2{}^{15}NH_2][OTf]$)[5,6] were prepared according to literature procedures. All other reagents were purchased from commercial vendors and used without further purification unless otherwise stated. Diethyl ether (Et_2O) used in the experiments herein was stirred over Na/K (≥ 2 hours) and filtered through celite before use.

Gas Chromatography

H_2 was quantified on an Agilent 7890A gas chromatograph (HP-PLOT U, 30 m, 0.32 mm ID; 30 °C isothermal; nitrogen carrier gas) using a thermal conductivity detector. A 10 mL manual injection was used and integration area was converted to percent H_2 composition by use of a calibration obtained from injection of H_2 solutions in N_2 of known concentration.

Mössbauer Spectroscopy

Mössbauer spectra were recorded on a spectrometer from SEE Co. (Edina, MN) operating in the constant acceleration mode in a transmission geometry. The sample was kept in an SVT-400 cryostat form Janis (Wilmington, MA). The quoted isomer shifts are relative to the centroid of the spectrum of a metallic foil of α-Fe at room temperature (RT). Solution samples were transferred to a sample cup and freeze-quenched with liquid nitrogen inside of the glovebox and then immersed in liquid N_2 until mounted in the cryostat. Data analysis was performed using version 4 of the program WMOSS (www.wmoss.org) and quadrupole doublets were fit to Lorentzian lineshapes. See discussion below for detailed notes on the fitting procedure.

Ammonia Quantification

Reaction mixtures are cooled to 77 K and allowed to freeze. The reaction vessel is then opened to atmosphere and to the frozen solution is slowly added a twofold excess (with respect to acid) solution of a NaO^{t}Bu solution in MeOH (0.25 mM) over 1-2 minutes. This solution is allowed to freeze and a Schlenk tube adapter is added and the headspace of the tube is evacuated. After sealing the tube is then allowed to warm to RT and stirred at RT for at least 10 minutes. An additional Schlenk tube is charged with HCl (3 mL of a 2.0 M solution in Et_2O, 6 mmol) to serve as a collection flask. The volatiles of the reaction mixture are vacuum transferred at RT into this collection flask. After completion of the vacuum transfer, the collection flask is sealed and warmed to RT and stirred vigorously for 10 minutes. Solvent is removed in vacuo, and the remaining residue is dissolved in DMSO-d_6 containing 20 mM 1,3,5-trimethoxybenzene as an internal standard. The ammonium chloride is quantified by integration relative to the 1,3,5-trimethoxybenzene internal standard.

Computational Methods

All stationary point geometries were calculated using DFT-D_3 (Grimmes D_3 dispersion correction[7]) with an TPSS functional,[8] a def2-TZVP[9] basis set on transition metals and a def2-SVP[7] basis set on all other atoms. Calculations were performed, in part, using Xtreme Science and Engineering Discovery Environment (XSEDE) resources.[10] Calculations were performed on the full P_3^BFe scaffold. Geometries were optimized using the NWChem 6.5 package.[11] All single point energy, frequency and solvation energy calculations were performed with the ORCA package.[12] Frequency calculations were used to confirm true minima and to determine gas phase free energy values (G_{gas}). Single point solvation calculations were done using an SMD solvation

model[13, 14] with diethyl ether solvent and were used to determine solvated internal energy (E_{soln}). Free energies of solvation were approximated using the difference in gas phase internal energy (E_{gas}) and solvated internal energy ($\Delta G_{solv} \approx E_{soln} - E_{gas}$) and the free energy of a species in solution was then calculated using the gas phase free energy (G_{gas}) and the free energy of solvation ($G_{soln} = G_{gas} + \Delta G_{solv}$).[15,16] All reduction potentials were calculated referenced to $Fc^{+/0}$ and using the standard Nernst relation $\Delta G = -nFE^0$.

A4.2 Synthetic Details:

General Procedure for the Synthesis of the Anilinium Triflates

Prior to use the amine was purified (aniline and 2,6-dimethylaniline by distillation and the remaining substituted anilines by sublimation). To a 100 mL round bottom flask in the glovebox was added the desired aniline which was subsequently dissolved in 50 mL of Et_2O (no additional drying with NaK). To this was added dropwise (1 equiv) of HOTf with stirring over five minutes. Immediate precipitation of white solid was observed and the reaction mixture was allowed to stir for thirty minutes. The reaction mixture was then filtered and the resulting white powder was washed with Et_2O (50 mL) and pentane (50 mL). The resulting white microcrystalline material was then dried under vacuum. Yields of greater than 90% of microcrystalline material was obtained in this manner in all cases.

4-methoxyanilinium triflate ([$^{4\text{-OMe}}PhNH_3$][OTf]): ^{1}H NMR (DMSO-*d*6, 400 MHz): 7.52 (m, 2 H), 7.28 (m, 2H), 4.30 (br, 3H).

anilinium triflate ([$PhNH_3$][OTf]): ^{1}H NMR (DMSO-*d*6, 400 MHz): 7.50 (m, 2 H), 7.41 (m, 1H), 7.34 (m, 2H).

2,6-dimethylanilinium triflate ([$^{2,6\text{-Me}}PhNH_3$][OTf]): ^{1}H NMR (DMSO-*d*6, 400 MHz): 7.14 (m, 3H), 2.32 (br, 6H).

2-chloroanilinium triflate ([$^{2\text{-Cl}}PhNH_3$][OTf]): ^{1}H NMR (DMSO-*d*6, 400 MHz): 7.32 (m, 1H), 7.15 (m, 1H), 7.02 (m, 1H), 6.82 (m, 1H).

2,5-chloroanilinium triflate ([$^{2,5\text{-Cl}}PhNH_3$][OTf]): ^{1}H NMR (DMSO-*d*6, 400 MHz): 7.19 (apparent d, 1H, ^{3}J(H-H) = 8.5 Hz), 6.83 (apparent dd, 1H, ^{3}J(H-H) = 2.5 Hz, 0.9 Hz), 6.56 (m, 1H).

2,6-chloroanilinium triflate ([$^{2,6\text{-Cl}}PhNH_3$][OTf]): ^{1}H NMR (DMSO-*d*6, 400 MHz): 7.22 (d, 2H, ^{3}J(H-H) = 8.0 Hz), 6.57 (t, 1H, ^{3}J(H-H) = 8.0 Hz).

2,4,6-chloroanilinium triflate ([$^{2,4,6\text{-Cl}}PhNH_3$][OTf]): ^{1}H NMR (DMSO-*d*6, 400 MHz): 7.37 (s, 2H).

Preparation of decamethylcobaltocenium tetrakis(3,5-bis(trifluoromethyl)phenyl)borate), [Cp*$_2$Co][BAr$^F_4$]

A RT solution of HBAr$^F_4$ (96.1 mg, 0.095 mmol) in Et_2O (6 mL) is added dropwise to a stirred, RT solution of Cp*$_2$Co (32.9 mg, 0.1 mmol) in Et_2O (6 mL). This mixture is allowed to stir 30 min and then reduced to dryness in vacuo. The resulting solid residue is washed with pentane (3 x 2 mL) to yield [Cp*$_2$Co][BAr$^F_4$] as a bright yellow solid (104 mg isolated, 92% yield).

^{1}H NMR (THF-*d*8, 300 MHz): δ 7.79 (8H, s, BAr^F_4), δ 7.58 (4H, s, BAr^F_4), δ 1.75 (30H, s, Cp^*_2Co).

A4.3 Ammonia Generation Details

Standard NH_3 Generation Reaction Procedure

All solvents are stirred with Na/K for ≥ 2 hours and filtered prior to use. In a nitrogen-filled glovebox, the precatalyst (2.3 μmol) was weighed into a vial. The precatalyst was then transferred quantitatively into a long tube with a female 24-40 joint at the top using THF. The THF was then evaporated to provide a thin film of precatalyst at the bottom of tube. The tube is then charged with a stir bar, the acid (108 equiv), and Cp^*_2Co (41.2 mg, 54 equiv) as solids. The tube is then sealed at RT with a septum that is secured with copper wire (this ensures a known volume of N_2 in the reaction vessel, which is important for H_2 detection). The tube is then chilled to 77 K and allowed to equilibrate for 10 minutes. To the chilled tube is added 1 mL of Et_2O. The temperature of the system is allowed to equilibrate for 5 minutes. This tube is passed out of the box into a liquid N_2 bath and transported to a fume hood. The tube is then transferred to a dry ice/acetone bath where it thaws and is allowed to stir at −78 °C for four hours. At this point the headspace of the tube is sampled with a 10 mL sealable gas syringe which is used to analyze for H_2 by GC. The tube is then allowed to warm to RT with stirring and then stirred at RT for a further ten minutes. At this point the previously described procedure for quantifying ammonia was employed. To ensure reproducibility, all experiments were conducted in 395 mL tubes (51 mm OD) using 25 mm stir bars and stirring was conducted at ~ 650 rpm.

Table A4.1: NMR quantification results for standard NH_3 generation experiments with $[P_3^BFe][BAr^F{}_4]$

Entry	Acid	Integration Relative to Internal Standard	% Yield NH_3 (error)	% Yield H_2 (error)
1	$[^{4\text{-OMe}}PhNH_3][OTf]$	0.01, 0.02	0.2 ± 0.1	89.1 ± 0.2
2	$[PhNH_3][OTf]$	3.42, 3.33	40.4 ± 0.5	48.6 ± 0.7
3	$[^{2,6\text{-Me}}PhNH_3][OTf]$	4.30, 3.63	47.5 ± 4.0	37.8 ± 0.2
4	$[^{2\text{-Cl}}PhNH_3][OTf]$	4.98, 4.92	59.3 ± 0.4	26.1 ± 1.9
5	$[^{2,5\text{-Cl}}PhNH_3][OTf]$	6.78, 6.15	77.5 ± 3.8	10.5 ± 1.1
6	$[^{2,6\text{-Cl}}PhNH_3][OTf]$	6.81, 6.00	76.7 ± 4.9	12.6 ± 2.5
7	$[^{2,6\text{-Cl}}PhNH_3][OTf]^*$	6.60, 5.81	74.4 ± 4.7	14.2 ± 3.4
8	$[^{2,6\text{-Cl}}PhNH_3][BAr^F{}_4]$	4.12, 3.0	42.7 ± 6.7	18.8 ± 0.8
9	$[^{2,4,6\text{-Cl}}PhNH_3][OTf]$	5.73, 6.10	70.9 ± 2.2	12.0 ± 0.8
10	pentachloroaniliniu m triflate ($[^{per\text{-Cl}}PhNH_3][OTf]$)	1.62, 1.70	19.9 ± 0.5	63.5 ± 1.1

*Run performed with $[P_3^BFeN_2][Na(Et_2O)_3]$ as the precatalyst.

A4.4 H_2 Monitoring Details

Standard Background Generation Reaction Procedure

All solvents are stirred with Na/K for ≥ 2 hours and filtered prior to use. In a nitrogen-filled glovebox, a long tube with a female 24-40 joint is charged with a stir bar, the acid (108 equiv) and Cp^*_2Co (41.2 mg, 54 equiv). The tube is then sealed at RT with a septum that is secured with copper wire. The tube is then chilled to 77 K and allowed to equilibrate for 10 minutes. To the chilled tube is added 1 mL of Et_2O. The temperature of the system is allowed to equilibrate for 5 minutes. This tube is passed out of the box into a liquid N_2 bath and transported to a fume hood. The tube is then transferred to a dry ice/acetone bath where it thaws and is allowed to stir at −78 °C for four hours. At this point the headspace of the tube is sampled with a 10 mL sealable gas syringe which is used to analyze for H_2.

Table A4.2: Data for Background H_2 Quantification Experiments

Acid	GC Integration for H_2	% Yield H_2
$[^{4\text{-OMe}}PhNH_3][OTf]$	49.8	31.5
$[PhNH_3][OTf]$	24.0	15.2
$[^{2,6\text{-Me}}PhNH_3][OTf]$	8.2	5.2
$[^{2\text{-Cl}}PhNH_3][OTf]$	47.2	29.9
$[^{2,5\text{-Cl}}PhNH_3][OTf]$	37.1	23.5

[$^{2,6\text{-Cl}}$PhNH$_3$][OTf]	77.8	49.2
[$^{2,4,6\text{-Cl}}$PhNH$_3$][OTf]	34.8	22.0
[$^{\text{per-Cl}}$PhNH$_3$][OTf]	98.3	62.3

H_2 Evolution Kinetics

All solvents are stirred with Na/K for ≥ 2 hours and filtered prior to use. For the catalyzed run, the precatalyst was then transferred quantitatively into a Schlenk tube using THF. The THF was then evaporated to provide a thin film of precatalyst at the bottom of the long tube with a female 24-40 joint. The tube is then charged with a stir bar and the [$^{2,6\text{-Cl}}$PhNH$_3$][OTf] (77.9 mg, 108 equiv) and Cp*$_2$Co (41.2 mg, 54 equiv) are added as solids. The tube is then sealed at RT with a septum that is secured with copper wire. The tube is then chilled to 77 K and allowed to equilibrate for 10 minutes. To the chilled tube is added 1 mL of Et_2O. The temperature of the system is allowed to equilibrate for 5 minutes. This tube is passed out of the box into a liquid N_2 bath and transported to a fume hood. The tube is then transferred to a dry ice/acetone bath where it thaws and is allowed to stir at −78 °C. As soon as the stir bar is freed from the frozen solution and stirring begins the timing is started. At the time points noted below the headspace was sampled for H_2 with a 10 mL sealable gas syringe.

Table A4.3: Time points for catalyzed H_2 evolution from 2,6-dichloroanlinium triflate and Cp*$_2$Co

Time (min)	GC Integration for H_2	% Yield H_2 (error)

5	3.8, 6.4	3.3 ± 0.9
15	11.6, 16.9	9.3 ± 1.8
25	14.7, 26.2	13.4 ± 3.8
35	22.5, 20.8	13.9 ± 0.5

Table A4.4. Time points for uncatalyzed H_2 evolution from 2,6-dichloroanlinium triflate and Cp^*_2Co

Time (min)	GC Integration for H_2	% Yield H_2 (error)
5	3.3, 2.9	2.0 ± 0.1
15	7.0, 6.2	4.3 ± 0.3
25	8.8, 11.1	6.3 ± 0.8
65	20.7, 27.0	14.5 ± 1.7

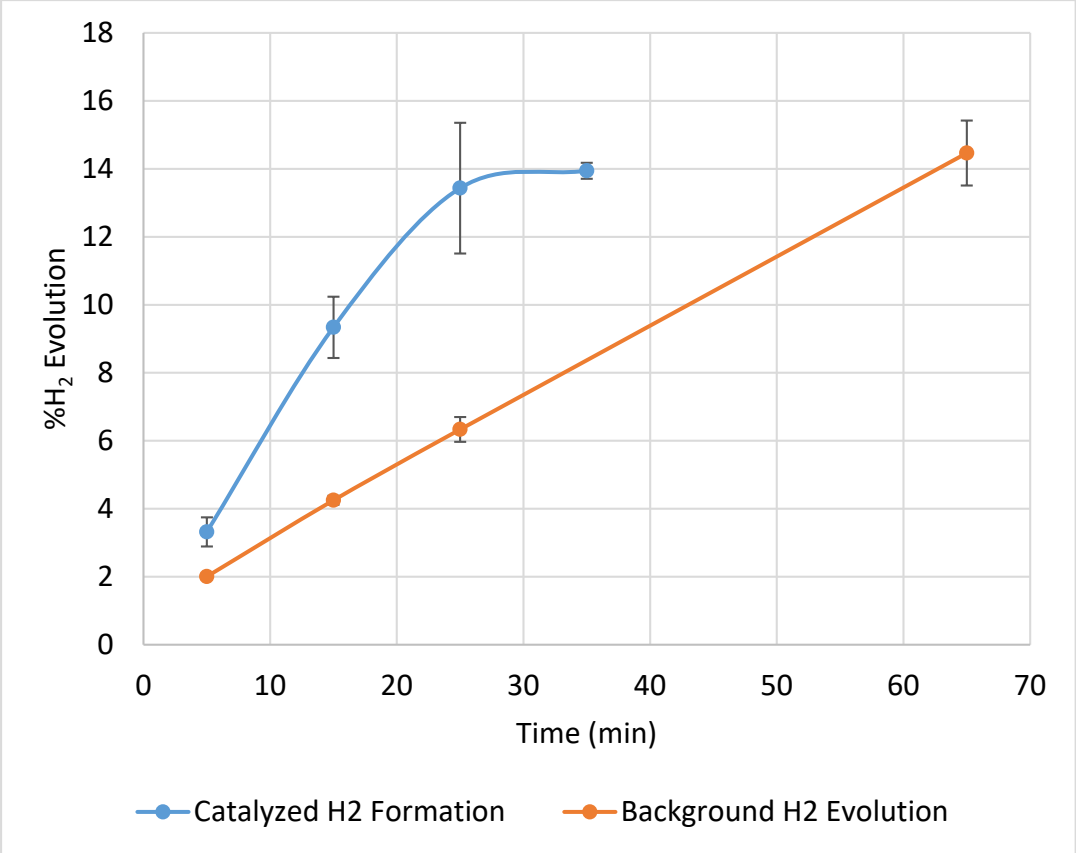

Figure A4.1. Comparison of catalyzed and uncatalyzed H_2 evolution from 2,6-dichloroanlinium triflate and Cp^*_2Co at early time points.

A4.5 Mössbauer Spectroscopy

General Procedure for Freeze-Quench Mössbauer Spectroscopy

All solvents are stirred with Na/K for ≥ 2 hours and filtered prior to use. In a nitrogen-filled glovebox, the desired ^{57}Fe species (0.0023 mmol) is quantitatively transferred using THF to a vial and then evaporated to yield a thin film. That vial is charged with a small stir bar and the other reagents as solids. The vial is then chilled to 77 K in a liquid nitrogen bath and allowed to equilibrate for five minutes. To the chilled tube is added 1 mL of Et_2O and this allowed to equilibrate for another five minutes. The

vial is then transferred to a cold well that has been pre-cooled for at least fifteen minutes to −78 °C with a dry ice/acetone bath. When the stir bar is freed from the frozen solvent and begins to stir the time is started. At the time noted the stirring is stopped and using a prechilled pipette the reaction mixture is transferred in one portion to a pre-chilled Mössbauer cup sitting in a vial. The vial is then placed in a liquid nitrogen bath causing the reaction mixture to freeze in approximately twenty seconds. The Mössbauer cup is then submerged in the liquid nitrogen and then removed from the glovebox and standard procedure is used to mount the sample on the Mössbauer spectrometer.

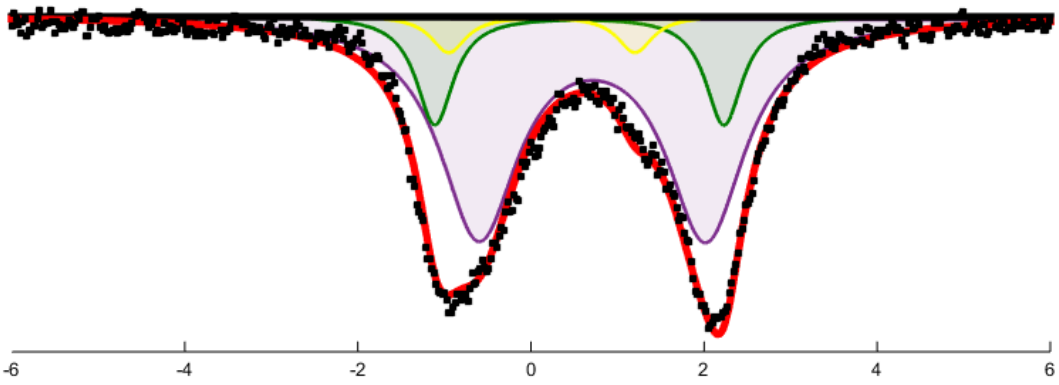

Figure A4.2. Mössbauer spectrum collected from a reaction freeze quenched after stirring for 5 minutes at −78 °C in 1 mL of Et_2O between $[P_3^B(^{57}Fe)N_2][Na(Et_2O)_3]$ and excess 2,6-$[^{2,6\text{-}Cl}PhNH_3][OTf]$ (50 equiv). Raw data shown as black points, simulation as a solid red line, with components in green, purple, and yellow (see Table A4.3 for parameters). The spectrum was collected at 80 K with a parallel applied magnetic field of 50 mT in Et_2O.

Fitting details for Figure A4.2: Three quadrupole doublets were found to be necessary to obtain an adequate simulation. Although a variety of parameters could potentially simulate the relatively broad absorptions observed here, previous reactivity of $P_3^BFeN_2^-$

with acid[19] suggested that $P_3^BFeN_2$ and $P_3^BFe^+$ were likely products. Satisfyingly if the known isomer shift and quadrupole splitting for one of those species was fixed during the fitting process and the other components were allowed to refine freely the other major component was found to be the complementary species.[19] The third species was always unchanged in these simulations and represents an unknown species. Its presence in the fit is demanded by the inflection point on the more negative side of the right-hand absorbance. Modeling this feature also helps to capture the asymmetry of the left-hand absorbance while using the symmetric line-shapes we expect for $P_3^BFeN_2$ (green) and $P_3^BFe^+$ (purple). The broad linewidths for $P_3^BFe^+$ have been observed previously and may be explained by the existence of unbound and bound varieties of the species with the reaction mixture providing potential ligands such as OTf^-, $^{2,6\text{-Cl}}PhNH_2$, and N_2.

Table A4.5: Simulation parameters for Mossbauer spectrum in Figure A4.2.

Component	δ (mm s^{-1})	ΔE_Q (mm s^{-1})	Linewidths, Γ_L/Γ_R (mm s^{-1})	Relative area
A (green)	0.58 ± 0.02	3.28 ± 0.07	0.52/0.52	0.26
B (purple)	0.76 ± 0.02	2.57 ± 0.05	1.10/1.10	0.63
C (yellow)	0.13 ± 0.02	2.24 ± 0.04	0.50/0.50	0.11

A4.6 EPR Spectroscopy

General Procedure for EPR Spectroscopy

All solvents are stirred with Na/K for ≥ 2 hours and filtered prior to use. In a nitrogen-filled glovebox, the desired Fe species (0.0023 mmol) is quantitatively transferred using THF to a vial and then evaporated to yield a thin film. That vial is charged with a small stir bar and the acid (0.116 mmol, 50 equiv) as solids ([$^{2,6\text{-Cl}}$PhNH$_3$][OTf] or [$^{2,6\text{-Cl}}$PhNH$_3$][BAr$^F{}_4$]). The vial is then chilled to 77 K in a liquid nitrogen bath and allowed to equilibrate for five minutes. To the chilled tube is added 1 mL of Et$_2$O (for HOTf 50 equiv have been dissolved in this 1 mL of Et$_2$O at RT) and this allowed to equilibrate for another five minutes. The vial is then transferred to a cold well that has been pre-cooled for at least fifteen minutes to −78 °C with a dry ice/acetone bath. When the stir bar is freed from the frozen solvent and begins to stir the time is started. The reaction mixture is stirred for five minutes and then stirring is stopped. Using a pre-chilled pipette approximately 0.5 mL of the reaction mixture is rapidly transferred to a pre-chilled X-band EPR tube. The X-band EPR tube is then placed in a liquid nitrogen bath causing the reaction mixture to freeze in approximately twenty seconds. The EPR tube is then sealed and removed from the glovebox in liquid nitrogen.

Comment on Stoichiometric Reactivity

In our attempt to model the catalytic reaction mixture we were interested in the reactivity of P$_3{}^B$FeN$_2{}^-$ (observed previously both from mixing [P$_3{}^B$Fe][BAr$^F{}_4$] with excess Cp*$_2$Co and under the catalytic reaction conditions) with acid. In order to achieve

this we wanted to prepare independently known $P_3^BFeN_2^-$ species to model the proposed catalytic intermediate $[P_3^BFeN_2][Cp^*_2Co]$. We chose $[P_3^BFeN_2][Na(Et_2O)_3]$ because we believed that its solubility in Et_2O likely modeled that of $[P_3^BFeN_2][Cp^*_2Co]$.

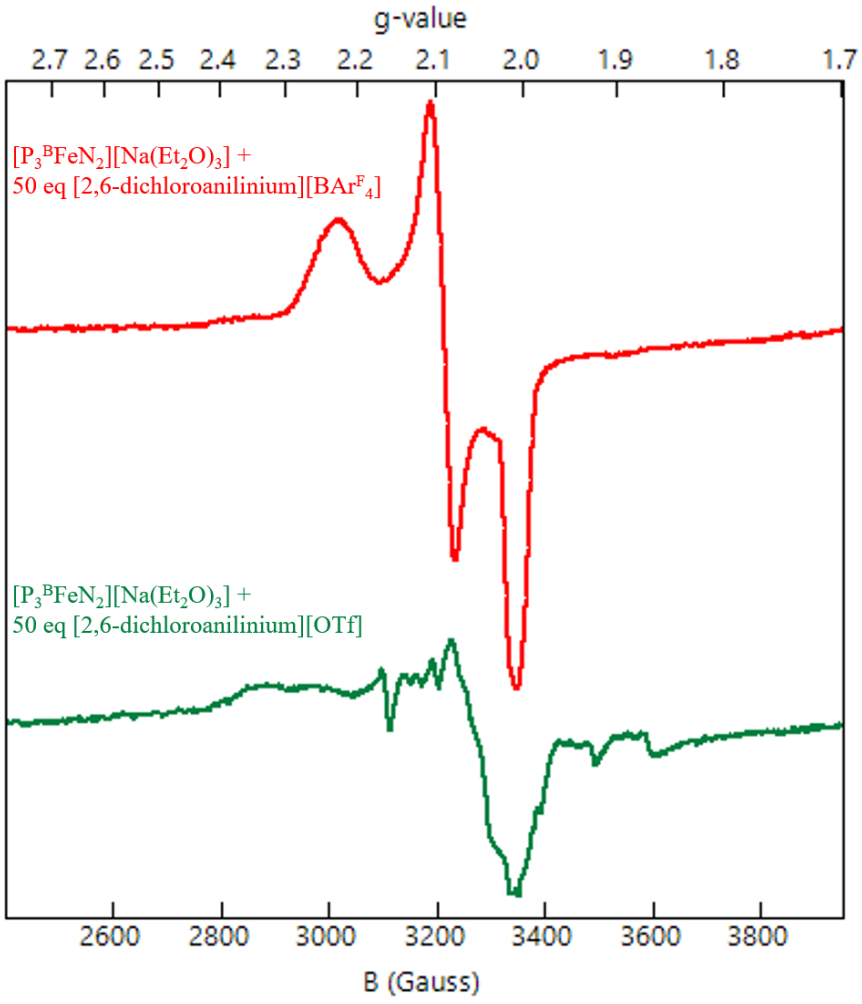

Figure A4.3. The continuous wave, X-band EPR at 77K in Et_2O of reaction mixtures freeze-quenched after five minutes. In red is the reaction of $[P_3^BFeN_2][Na(Et_2O)_3]$ with 50 equiv of $[^{2,6\text{-}Cl}PhNH_3][BAr^F_4]$ clearly demonstrating the formation of $[P_3^BFeNNH_2][BAr^F_4]$. In green is reaction of $[P_3^BFeN_2][Na(Et_2O)_3]$ with 50 equiv of [2,6-

^{Cl}PhNH$_3$][OTf] in which the small residual species is neither the starting material ([P-$_3^B$FeN$_2$][Na(Et$_2$O)$_3$]) or the desired product ([P$_3^B$FeNNH$_2$][OTf]). Although we do not know the chemical identity of this species we note that it is very similar to the EPR observed in the reaction of [P$_3^B$FeN$_2$][Na(12-crown-4)$_2$] with 1 equiv of HBAr$^F_4$.[19] We hypothesize therefore that it may represent a Fe–H side product.

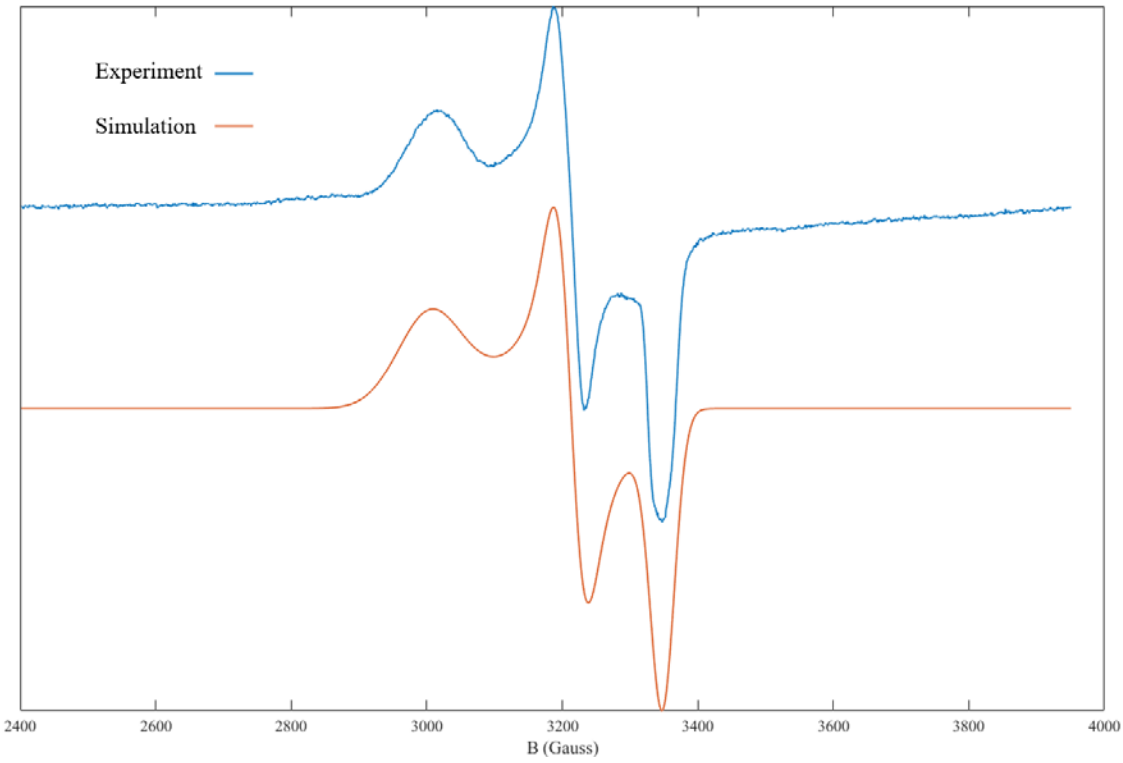

Figure A4.4. In blue is the continuous wave, X-band EPR spectrum at 77K of a reaction mixture of 50 equiv [$^{2,6\text{-Cl}}$PhNH$_3$][BAr$^F_4$] with [P$_3^B$FeN$_2$][Na(12-crown-4)$_2$] quenched with liquid nitrogen after 5 minutes. In orange is the simulation of this spectrum (fitting details below)

Fitting details for Figure A4.4: The parameters used to fit the spectrum were obtained using the esfit application in the easyspin program.[20] The fitting program obtains the best fit by minimizing the root mean square deviation from the data.

The data was fit with the following parameters: $g_1 = 2.23899$, $g_2 = 2.09189$, $g_3 = 2.00664$, and a line broadening of 323.8530, 71.2309, and 38.7902 MHz respectively. These parameters represent only a very small perturbation from those used previously to model $[P_3^BFeNNH_2][BAr^F_4]$: $g_1 = 2.222$, $g_2 = 2.091$, $g_3 = 2.006$ and a line broadening of 256, 113, and 41 MHz respectively.[19] The slightly broader spectrum observed here precludes resolution of the small phosphorus coupling on g_3. We believe that this broadening arises from either the use of a non-glassing solvent (Et_2O vs 2-MeTHF) or via small differences in hydrogen-bonding that arise from the presence of 2,6-dichloroaniline.

A4.7 Acid Quench of $P_3^BFeN_2^-$

Standard Acid Quench Procedure

All solvents are stirred with Na/K for ≥ 2 hours and filtered prior to use. In a nitrogen-filled glovebox, the desired Fe species (2.3 μmol) was weighed into a vial. The Fe species was then transferred quantitatively into a Schlenk tube using THF. The THF was then evaporated to provide a thin film of Fe species at the bottom of the Schlenk tube. The tube is then charged with a stir bar and acid (0.116 mmol, 50 equiv) as solids 9[$^{2,6\text{-Cl}}PhNH_3$][OTf] or [$^{2,6\text{-Cl}}PhNH_3$][BAr^F_4]) is added as a solid. The tube is then sealed at RT with a septum and a Konte's valve that is left partially open. The tube is then chilled to 77 K and allowed to equilibrate for 10 minutes. To the chilled tube is added 1 mL of Et_2O through the septum. The temperature of the system is allowed to equilibrate for 5 minutes and then the Konte's valve is sealed. This tube is passed out of the box into a liquid N_2 bath and transported to a fume hood. The tube is then transferred to a dry ice/acetone bath where it thaws and is allowed to stir at −78 °C for three hours. At the

end of the reaction the Konte's valve is opened and the reaction headspace is allowed to equilibrate. At this point the headspace of the tube is sampled with a 10 mL sealable gas syringe which is used to analyze for H_2. The tube is then allowed to warm to RT with stirring and then stirred at RT for a further ten minutes. At this point the previously described procedure for quantifying ammonia was employed.

Table A4.6. Comparative NH_3 and H_2 Yields for $[^{2,6\text{-}Cl}PhNH_3][OTf]$ and $[^{2,6\text{-}Cl}PhNH_3][BAr^F{}_4]$

Acid	Yield of NH_3 (equiv)	% Yield H_2
$[^{2,6\text{-}Cl}PhNH_3][OTf]$	0.0 ± 0.0	43.7 ± 4.6
$[^{2,6\text{-}Cl}PhNH_3][BAr^F{}_4]$	0.20 ± 0.03	37.8 ± 7.6

A4.8 Solubility Measurement

Procedure for Measuring Solubility of $Cp^*{}_2Co$:

All solvents are stirred with Na/K for ≥ 2 hours and filtered prior to use. In a nitrogen-filled glovebox, a Schlenk tube is charged with a stir bar and the $Cp^*{}_2Co$ (41.2 mg, 0.125 mmol) is added to the tube. The tube is then chilled to 77 K in a liquid nitrogen bath and allowed to equilibrate for 5 minutes. To the chilled tube is added 1 mL of Et_2O. The temperature of the system is allowed to equilibrate for 5 minutes and then the Schlenk tube is transferred to the cold well which has been prechilled to −78 °C for fifteen minutes. After five minutes of stirring at ~ 620 rpm, the stirring is stopped. With a prechilled pipette the entirety of the reaction mixture is transferred to a similarly prechilled celite pad for filtration. Filtration yielded a pale green solution that was then

warmed to RT and the solvent was removed under reduced pressure. The vial was then extracted with a 20 mM solution of 1,3,5-trimethoxybenzene in C_6D_6. The NMR was then measured and the Cp^*_2Co signal was integrated relative to the 1,3,5-trimethoxybenzene standard. The accuracy of this integration procedure was confirmed by performing this procedure on a sample of Cp^*_2Co that had simply been weighed into a vial. Repetition of this experiment resulted in Cp^*_2Co concentrations between 5-6 mM.

Procedure for Measuring Solubility of [$^{2,6\text{-Cl}}$PhNH$_3$][OTf]:

All solvents are stirred with Na/K for ≥ 2 hours and filtered prior to use. In a nitrogen-filled glovebox, a Schlenk tube is charged with a stir bar and the [$^{2,6\text{-Cl}}$PhNH$_3$][OTf] (77.9 mg, 0.250 mmol) is added to the tube. The tube is then chilled to 77 K in a liquid nitrogen bath and allowed to equilibrate for 5 minutes. To the chilled tube is added 1 mL of Et_2O. The temperature of the system is allowed to equilibrate for 5 minutes and then the Schlenk tube is transferred to the cold well which has been prechilled to −78 °C for fifteen minutes. After five minutes of stirring at ~ 620 rpm, the stirring is stopped. With a prechilled pipette the entirety of the reaction mixture is transferred to a similarly prechilled celite pad for filtration. Filtration yielded a colorless solution that was then warmed to RT and the solvent was removed under reduced pressure. The vial was then extracted with a 20 mM solution of 1,3,5-trimethoxybenzene in THF-d_8. The NMR was then measured and the two signals for [$^{2,6\text{-Cl}}$PhNH$_3$][OTf] were integrated relative to the 1,3,5-trimethoxybenzene standard. The result was a [$^{2,6\text{-Cl}}$PhNH$_3$][OTf] concentration of 0.4 mM.

A4.9 Controlled Potential Electrolysis (CPE) and Cyclic Voltammetry (CV) Details

General considerations:

All manipulations are carried out in an N_2-filled glove box. For CPE experiments a sealable H-cell consisting of two compartments separated by a fine porosity sintered glass frit is cooled to −35 °C in a cold well and charged with 4 mL (working chamber) and 4 mL (auxiliary chamber) of 0.1 M $NaBAr^F{}_4$ solution in Et_2O, the solutions are also cooled to −35 °C and the solution for the working chamber may contain additional chemical components as described below. The working chamber is outfitted with a glassy carbon working electrode, rectangular prismatic in shape with dimensions of 10 mm × 2 mm and submerged in the working chamber solution to a depth of ~ 10 mm. The working chamber is also equipped with a $Ag/AgPF_6$ in 0.1 M $NaBAr^F{}_4$ Et_2O reference electrode isolated by a CoralPor™ frit (obtained from BASi) and referenced externally to $Fc^{+/0}$. The auxiliary chamber is outfitted with a solid sodium auxiliary electrode (~ 5 mm × ~ 1 mm rectangular prism, submerged to ~ 5 mm). The cell is sealed before electrolysis. The cell is connected to a CH Instruments 600B electrochemical analyzer and controlled potential bulk electrolysis experiments were performed at −35 °C with stirring, cold well external bath temperature maintained by a SP Scientific FTS Systems FC100 immersion cooler.

CV experiments are conducted in a single compartment cell cooled to −35 °C in a cold well in 0.1 M $NaBAr^F{}_4$ Et_2O solution, again cold well external bath temperature maintained by a SP Scientific FTS Systems FC100 immersion cooler. The working electrode is a glassy carbon disk, the reference electrode is a $Ag/AgPF_6$ in 0.1 M $NaBAr^F{}_4$ Et_2O reference electrode isolated by a CoralPor™ frit (obtained from BASi)

and referenced externally to $Fc^{+/0}$, the auxiliary electrode is a platinum wire. Measurements conducted with a CH Instruments 600B electrochemical analyzer

General methodology for controlled potential electrolysis experiments:

To the working chamber is added 3 mg of $[P_3^BFe][BAr^F_4]$ (2 μmol), 100 μmol of acid (e.g. $[Ph_2NH_2][OTf]$), 0-23.8 mg of $[Cp^*_2Co][BAr^F_4]$ (0-20 μmol), and a magnetic stir bar. The cell is held at a working potential of −2.1 V vs $Fc^{+/0}$ until the current passed in the cell falls to 1% of the initial current pass or until 21.5 hours have passed. After that time the potential bias is removed, the headspace of the cell is sampled with a sealable gas syringe (10 mL), which is immediately analyzed by GC for the presence of H_2. Then an additional 100 μmol of acid in 2 mL 0.1 M $NaBAr^F_4$ solution in Et_2O is injected through rubber septa into both chambers to sequester NH_3 as $[NH_4][OTf]$. The cell is allowed to stir at −35 °C for 10 minutes and then warmed to RT. The contents of both chambers are then transferred to a Schlenk tube (cell washed with additional Et_2O) and this material is analyzed for NH_3 by base digestion, vacuum transfer of volatiles, and NMR integration as described in section S1.4

Methodology for controlled potential electrolysis experiments with reloading of substrate:

To the working chamber is added 3 mg of $[P_3^BFe][BAr^F_4]$ (2 μmol), 100 μmol of acid (e.g. $[Ph_2NH_2][OTf]$), 0-23.8 mg of $[Cp^*_2Co][BAr^F_4]$ (0-20 μmol), and a magnetic stir bar. The cell is held at a working potential of −2.1 V vs $Fc^{+/0}$ until the current passed in the cell falls to 1% of the initial current pass or until 21.5 hours have passed. After that

time the potential bias is removed. An additional 100 μmol of acid in 2 mL 0.1 M $NaBAr^{F}_{4}$ solution in Et_2O is then added to the working chamber of the cell via injection through a rubber septum. The cell is then held at a working potential of −2.1 V vs $Fc^{+/0}$ until the current passed in the cell falls to 1% of the initial current pass or until 21.5 hours have passed. After that time the potential bias is removed, the headspace of the cell is sampled with a sealable gas syringe (10 mL), which is immediately analyzed by GC for the presence of H_2. Then an additional 100 μmol of acid in 2 mL 0.1 M $NaBAr^{F}_{4}$ solution in Et_2O is injected through rubber septa into both chambers of the cell to sequester NH_3 as $[NH_4][OTf]$. The cell is allowed to stir at −35 °C for 10 minutes and then warmed to RT. The contents of both chambers are then transferred to a Schlenk tube (cell washed with additional Et_2O) and this material is analyzed for NH_3 by base digestion, vacuum transfer of volatiles, and NMR integration as described in section S1.4

Table A4.7. Controlled Potential Electrolysis Data.

Entry	Acid	Equiv [Cp*$_2$Co][BAr^{F}_{4}]	Time (h)	Charge Passed (C)	Yield of NH_3 (equiv per Fe)	FE NH_3 (%)	FE H_2[a] (%)
1	$[Ph_2NH_2][OTf]$	0	42	7.5	2.3	18	80
2	$[Ph_2NH_2][OTf]$	0	63	6.2	2.8	26	25
3	$[Ph_2NH_2]$	0	43	5.4	2.6	28	53

	[OTf]						
Avg					2.6 ± 0.3	24 ± 5	
4[b]	[Ph_2NH_2] [OTf]	0	43	7.5	2.2	17	67
5[b]	[Ph_2NH_2] [OTf]	0	43	9.0	3.0	19	22
Avg					2.6 ± 0.6	18 ± 1	
6	[Ph_2NH_2] [OTf]	1	17	8.1	4.4	31	56
7	[Ph_2NH_2] [OTf]	1	22	8.3	3.5	24	47
Avg					4.0 ± 0.6	28 ± 5	
8	[Ph_2NH_2] [OTf]	5	17	8.5	3.9	26	61
9	[Ph_2NH_2] [OTf]	5	21	9.1	3.5	22	57
10	[Ph_2NH_2] [OTf]	5	22	9.5	4.6	28	27

Avg					4.0 ± 0.6	25 ± 3	
11	$[Ph_2NH_2][OTf]$	10	21	9.4	3.0	19	64
12	$[Ph_2NH_2][OTf]$	10	10	10.2	5.1	29	47
Avg					4 ± 1	24 ± 7	
13	$[PhNH_3][OTf]$	5	15	9.0	1.2	8	48
14	$[PhNH_3][OTf]$	5	22	7.8	0.6	4	35
Avg					0.9 ± 0.4	6 ± 3	
15	$[^{2,6\text{-}Cl}PhNH_3][OTf]$	5	17	10.6	2.0	11	44
16	$[^{2,6\text{-}Cl}PhNH_3][OTf]$	5	17	10.7	1.7	9	41
Avg					1.9 ± 0.2	10 ± 1	
17[b]	$[Ph_2NH_2]$	5	32	17.3	6.1	20	43

	[OTf]						
18[b]	[Ph_2NH_2] [OTf]	5	22	18.7	6.7	21	32
19[b]	[Ph_2NH_2] [OTf]	5	37	13.7	4.7	20	38
20[b]	[Ph_2NH_2] [OTf]	5	41	15.3	4.8	18	52
21[b]	[Ph_2NH_2] [OTf]	5	43	17.8	5.4	18	31
Avg					5.5 ± 0.9	19 ± 1	
22A[c]	[Ph_2NH_2] [OTf]	5	21.5	9.5	4.6	28	27
22B[c]	[Ph_2NH_2] [OTf]	5	11.5	9.2	0.0	0	88
23[d]	[Ph_2NH_2] [OTf]	5	16	9.2	0.0	0	75
24[e]	[Ph_2NH_2] [OTf]	5	43	0.0	0.3	N/A	N/A
25[f]	[Ph_2NH_2]	Chemical	21.5	N/A	1.3	7.8 e^-	50 e^-

	[OTf]	runs					
26[f]	[Ph_2NH_2] [OTf]	Chemical runs	21.5	N/A	2.3	13.8 e^-	31 e^-
Avg					1.8 ± 0.7	11 ± 4	

[a]Some ports of the cell are sealed with septa and one of these is pierced before the electrolysis begins to pressure equilibrate the cell as it cools to −35 °C, we note therefore that H_2 gas may escape from the cell particular during long experiments, indeed a test of H_2 retention in the cell under equivalent conditions revealed leakage of H_2 (60% recovery), thus the detected % yield of H_2 reported here should be considered a lower limit. [b]These experiments were conducted using the reloading protocol as described above. [c]Electrode rinse test as described in main text. [d]Control experiment with no [P_3^BFe][BAr^F_4] included but including a typical loading of 11.9 mg (10 μmol) of [Cp^*_2Co][BAr^F_4]. [e]Control experiment in which the cell with all components, including the sodium auxiliary electrode, was assembled and stirred at −35 °C for 43 hours but neither a potential bias was applied, nor were the working and auxiliary electrodes externally connected. This experiment thus interrogates the ability of the sodium electrode to function as a chemical reductant for N_2RR under the CPE conditions. [f]Chemical catalysis runs at −35 °C in 0.1 M $NaBAr^F_4$ Et_2O solution with 50 equiv (100 μmol) of Cp^*_2Co included as a chemical reductant as well as [P_3^BFe][BAr^F_4] (2 μmol) and 100 μmol of acid ([Ph_2NH_2][OTf]).

Control experiment for the possibility of NH_3 being generated in a chemical rather than electrochemical process during acidic workup:

As per the general CPE methodologies described in S9.2 and S9.3, after electrolysis additional acid is added to the cell to sequester generated NH_3 as an ammonium salt to facilitate transfer of these materials to a Schlenk tube, ultimately allowing NH_3 quantitation via base digestion and vaccum transfer as described in S1.4. This presents the possibility that electrochemically reduced species formed during electrolysis (e.g., $P_3^BFeN_2^-$ and Cp^*_2Co) could react with this additional acid after the electrolysis was complete to generate NH_3 in a chemical reaction. A control experiment to determine the extent to which this type of reactivity might contribute to the total NH_3 yield observed from the CPE experiments was conducted. The H-cell is assembled via the standard methodology and charged with a typical loading of $[P_3^BFe][BAr^F_4]$ (2 μmol) and $[Cp^*_2Co][BAr^F_4]$ (10 μmol, 5 equiv) but without initial acid (i.e., no $[Ph_2NH_2][OTf]$). Electrolysis is then carried out at −2.1 V vs $Fc^{+/0}$ until the current pass in the cell falls to 1% of the initial current passed (in this case 1.12 C of charge were passed, corresponding to 11.6 μmol of reducing equivalents stored in the system, which approaches the theoretical limit of reducing equivalents that the loading of $[P_3^BFe][BAr^F_4]$ (2 μmol) and $[Cp^*_2Co][BAr^F_4]$ (10 μmol) could store) at this potential. This post electrolysis mixture is then treated with acid and analyzed for NH_3 via the standard methodology. This experiment yielded 0.2 equiv NH_3 (relative to Fe) indicating that chemical N_2RR between electrochemically reduced species during the acidic workup is very minor.

Additional CV data:

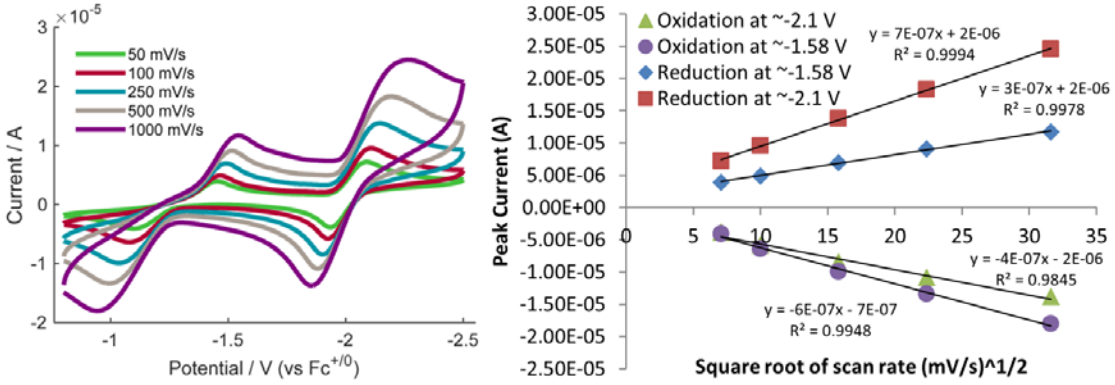

Figure A4.5. Cyclic voltammograms of 0.5 mM [P_3^BFe][BAr^F_4] at varied scan rates (left) and plot of peak current versus square root of scan rate for each feature (right) showing linear dependence in all cases. All spectra are collected in 0.1 M $NaBAr^F_4$ solution in Et_2O at −35 °C using a glassy carbon working electrode, and externally referenced to the $Fc^{+/0}$ couple.

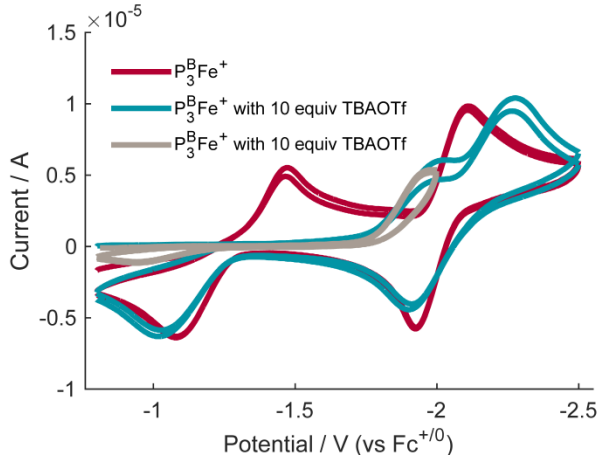

Figure A4.6. Cyclic voltammograms of 0.5 mM [P_3^BFe][BAr^F_4] (red trace) and [P_3^BFe][BAr^F_4] with 10 equiv of tetrabutylammonium trifluoromethanesulfonate

([TBA][OTf]) (blue and gray traces). The traces with [TBA][OTf] show disappearance of a wave corresponding to the $P_3^BFe^{+/0}$ couple at ~ −1.58 V (present in the red trace). This phenomenon, as in the case with acidic triflate sources as described in the main text, is likely due to triflate binding (to generate P_3^BFeOTf, thereby attenuating the wave associated with the reduction of $P_3^BFe^+$ and $P_3^BFeN_2^+$). If the scan is stopped and reversed at −2.0 (before the $P_3^BFeN_2^{0/-}$ couple) no reversibility is observed, consistent with a chemical step (dissociation of triflate) being coupled with this redox event. We note that in the presence of OTf^- it appears that the second reductive feature is also slightly anodically shifted. We believe this to be due to slow N_2 binding kinetics and thus this wave would represent a convolution of the 0/1− reduction processes for both a vacant and an N_2 bound P_3^BFe. All spectra are collected in 0.1 M $NaBAr^F_4$ solution in Et_2O at −35 °C using a glassy carbon working electrode, and externally referenced to the $Fc^{+/0}$ couple.

A4.10 Computational Details

Calculation of Acid Dissociation Constants

Acid dissociation constants (pK_a and pK_d) were performed were optimized and solvated as discussed in the general methods section. For pK_a values, the ΔG for the exchange of a proton (H^+) between the acid of interest and $^{2,6\text{-Cl}}PhNH_2/^{2,6\text{-Cl}}PhNH_3^+$. For pK_d values, the same approach was used except that the net exchange of a HOTf unit was calculated. In all cases the dissociation constant was reference to the literature value for the pK_a of $^{2,6\text{-Cl}}PhNH_3^+$ in THF.

Determination of PT, ET and PCET Kinetics

Kinetic barriers for reported for PT, ET and PCET were performed in one of two ways. Internal consistency between the methods was determined where possible. Values are summarized in Table A4.8.

Method A. Marcus Theory. Standard Marcus theory expressions[21] were used in method A. Inner sphere reorganization energies for PT or PCET were calculated using the method developed by the group of Hammes-Schiffer (Eq. S1) utilizing the force constants for the reactant (f_j^r) and product (f_j^p) species and the change in equilibrium bond length (Δq_j).[22]

$$\lambda_{is,PT/PCET} = \sum_j \frac{f_j^r f_j^p}{f_j^r + f_j^p} \Delta q_j{}^2 \qquad \text{(Eq. S1)}$$

Outer sphere reorganization energies were calculated using a continuum solvation model for the solvation of a point charge ($\lambda_{os,ET}$)[21] or a dipole ($\lambda_{os,PT}$).[22-24] The $\lambda_{os,PCET}$ was approximated using Eq. S2, where θ is the angle between the ET and PT vectors.[22] It was determined via analysis of the structure of a constrained optimization (in which the Fe−H–Co distance was kept constant) that θ is between 0 and 45º, a range which corresponds to an insignificant variation (less than 0.2 kcal mol^{-1}) in $\lambda_{os,PCET}$.

$$\lambda_{os,PCET} = \lambda_{os,PT} + \lambda_{os,ET} - (\lambda_{os,PT} * \lambda_{os,ET})\cos(\theta) \qquad \text{(Eq. S2)}$$

Relative rates for a bimolecular PT/ET vs PCET (k_{bi}) pathway for reaction shown in Table A4.8, Equation 6 were determined via the method outline by the group of Hammes-Schiffer in which the bimolecular rate constant for PT, ET or PCET is approximated by Eq. S3.

$k_{bi} = K_A * k_{uni}$ (Eq. S3)

K_A represents the pre-arrangement equilibrium constant and k_{uni} represents the unimolecular rate constant for PCET or ET.[25] Along an PT/ET pathway, the barriers calculated suggest that $k^{PT} > k^{ET}$. In approximating k_{uni} for PCET and ET, we made extensive use of the webPCET portal.[26] The electronic coupling for PCET and ET was assumed to be equal. In order to approximate a lower bound for k^{PCET}/k^{ET}, the pre-arrangement equilibrium (K_A) was also assumed to be equal for PCET and ET. We believe this represents a lower bound as the approximation for K_A does not include any hydrogen bonding interactions for a PCET pathway.

Method B. Optimization of a 1st Order Saddle Point. PT barriers for the protonation of Cp^*_2Co were also found by optimization of a 1st order saddle point. That the optimized structure represented a 1st order saddle point was confirmed with a frequency calculation, which showed only one imaginary frequency.

Table A4.8. Overview of Parameters Used to Calculate Kinetic Barriers

1. $[^{2,6\text{-Cl}}PhNH_3][OTf] + Cp^*_2Co \rightarrow Cp^*Co(exo\text{-}\eta^4\text{-}C_5Me_5H)\text{-}OTf + {}^{2,6\text{-Cl}}PhNH_2$
2. $[^{2,6\text{-Me}}PhNH_3][OTf] + Cp^*_2Co \rightarrow Cp^*Co(exo\text{-}\eta^4\text{-}C_5Me_5H)\text{-}OTf + {}^{2,6\text{-Me}}PhNH_2$
3. $[^{4\text{-OMe}}PhNH_3][OTf] + Cp^*_2Co \rightarrow Cp^*Co(exo\text{-}\eta^4\text{-}C_5Me_5H)\text{-}OTf + {}^{4\text{-OMe}}PhNH_2$
4. $P_3{}^BFeNNH + [Cp^*Co(exo\text{-}\eta^4\text{-}C_5Me_5H)][OTf] \rightarrow [P_3{}^BFeNNH_2][OTf] + Cp^*_2Co$
5. $[P_3{}^BFeNNH_2][OTf] + Cp^*_2Co \rightarrow P_3{}^BFeNNH_2 + [Cp^*_2Co][OTf]$

6. P_3^BFeNNH + [Cp*Co(*exo*-η^4-C_5Me_5H)][OTf] → $P_3^BFeNNH_2$+ [Cp*$_2$Co][OTf]				
Reaction	λ_{is}	λ_{os}	Barrier {k_{rel}}	Method
1	N/A	N/A	1.3 kcal mol^{-1}	A
1	7.5 kcal mol^{-1}	6.3 kcal mol^{-1}	1.3 kcal mol^{-1}	B
2	N/A	N/A	3.8 kcal mol^{-1}	A
2	7.5 kcal mol^{-1}	6.3 kcal mol^{-1}	3.6 kcal mol^{-1}	B
3	N/A	N/A	4.5 kcal mol^{-1}	A
3	7.5 kcal mol^{-1}	6.3 kcal mol^{-1}	4.8 kcal mol^{-1}	B
4	8.9 kcal mol^{-1}	6.3 kcal mol^{-1}	1.5 kcal mol^{-1}	A
5	8.9 kcal mol^{-1}	25.0 kcal mol^{-1}	4.1 kcal mol^{-1} {$k_{rel} \equiv 1$}	A[a]
6	13.7 kcal mol^{-1}	0-10 kcal mol^{-1}	0.2 – 0.6 kcal mol^{-1} {2000 – 4500}	A

[a] The barrier for $[P_3^BFeNNH_2][OTf]$ reduction was calculated assuming that rate-determining reduction to $[P_3^BFeNNH_2][OTf]^-$ precedes OTf^- release.

BDFE Calculations

Bond dissociation free energies (BDFE) of X–H bonds were calculated in the gas-phase using a series of known reference compounds.[27] The free-energy difference between the H-atom donor/acceptor pair was calculated based on the thermochemical information provided by frequency calculations after structure optimizations using the procedure described in the general computational section. A linear plot of ΔG vs $BDFE_{lit}$ was generated to form a calibration curve (Figure A4.7). BDFE predictions were generated by application of the line of best fit to the calculated ΔG of the unknown species.

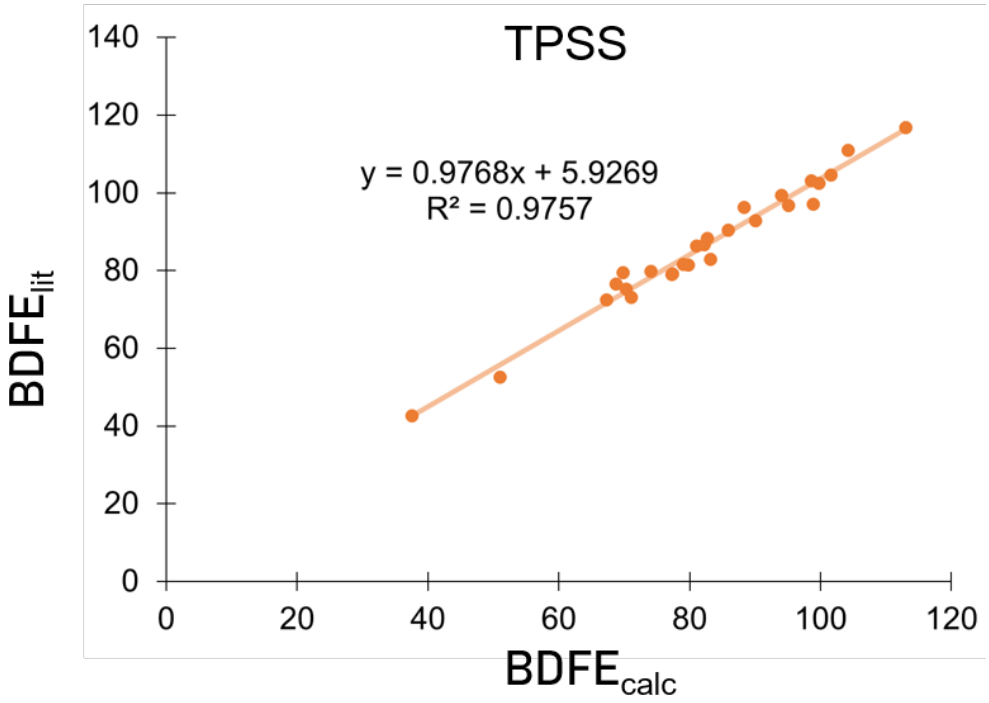

Figure A4.7. $BDFE_{calc}$ and $BDFE_{lit}$ plotted for species of known $BDFE_{E-H}$. Line of best fit is shown.

Table A4.9. Data used to generate the plot and line of best fit shown in Figure A4.5.

Species	ΔG (E-H) (kcal mol^{-1})	ΔG (E$^{\bullet}$) (kcal mol^{-1})	ΔG_{calc} (kcal mol^{-1})	$BDFE_{E-H}$ (kcal mol^{-1})
HOOH	−151.4	−150.8	69.8	79.7
MeOH	−115.6	−115.0	88.3	96.4
EtOOH	−230.0	−229.4	68.7	76.6
H_2O	−76.4	−75.7	104.2	111.0
NH_3	−56.5	−55.8	94.0	99.4
Me_3CH	−158.3	−157.6	82.7	88.3
PhOH	−307.2	−306.6	74.0	79.8
Et_2NH	−213.6	−212.9	81.0	86.4
NH_2NH_2	−111.8	−111.1	67.3	72.6
OH^-	−75.7	−75.0	98.6	103.1
PhSH	−630.2	−629.5	70.3	75.3
NH_4^+	−56.8	−56.1	113.0	116.9
Me_2CH_2	−119.0	−118.4	85.9	90.4

HC(O)OOH	−264.7	−264.1	82.2	86.8
OOH	−150.8	−150.2	37.5	42.7
C_6H_6	−232.1	−231.4	101.6	104.7
C_2H_4	−78.5	−77.8	99.7	102.5
C_2H_6	−79.7	−79.1	90.0	92.9
$PhCH_3$	−271.3	−270.7	79.0	81.6
CH_4	−40.5	−39.8	95.1	96.8
CpH	−193.9	−193.3	71.0	73.2
EtSH	−477.8	−477.2	77.2	79.1
MeSH	−438.6	−437.9	77.3	79.2
$PhNH_2$	−287.4	−286.7	79.8	81.5
NHNH	−110.6	−110.0	51.0	52.6
H_2S	−399.3	−398.7	83.1	83.0
H_2	−1.2	−0.5	98.8	97.2

Calculated Reduction Potentials for Selected $[Ar_nNH_{(4-n)}][OTf]$ and $Ar_nNH_{(3-n)}$

Table A4.10. Calculated Reduction Potentials of Selected Species

Species	E^o (V vs $Fc^{+/0}$)
$[^{4\text{-OMe}}PhNH_3][OTf]$	−3.8 V
$^{4\text{-OMe}}PhNH_2$	−3.4 V
$[^{2,6\text{-Me}}PhNH_3][OTf]$	−3.8 V
$[^{2,6\text{-Cl}}PhNH_3][OTf]$	−2.4 V
$[^{2,6\text{-Cl}}PhNH_3]^+$	−2.0 V
$[Ph_2NH_2]^+$	< −2.5 V[a]
Ph_2NH	−3.1 V
$[^{\text{per-Cl}}PhNH_3][OTf]$	−2.0 V
Cp^*_2Co	−2.2 V

[a] Potential for the formation of $Ph_2NH^\bullet$ + $H^\bullet$ is reported. No 'reversible' minima was found.

Discussion of the Anomalous Behavior of $[^{\text{per-Cl}}PhNH_3][OTf]$

Determining the reduction potential of the acids using electrochemical techniques is challenging due to the significant, electrode catalyzed HER observed upon scanning anodically (see Figure A4.8). However, as expected due to the lower pK_a of $[^{\text{per-Cl}}PhNH_3][OTf]$ compared to $[Ph_2NH_2][OTf]$ we see an earlier onset of the reduction potential and a higher current density. These processes are likely electrode-mediated and

thus do not reflect a pure reduction potential, so to better estimate the outer-sphere reduction potential of the acids employed we have used DFT (Table A4.10). In many cases, attempts to optimize the one electron reduced species results in a chemical step (*i.e.*, loss of Cl^- or H•) precluding determination of the reversible redox potential for the system. We are, however, able to find (*in silico*) a well-behaved reduction for [$^{per\text{-}Cl}PhNH_3$][OTf] of −2.0 V. As a comparison, the high efficiency acid, [$^{2,6\text{-}Cl}PhNH_3$][OTf], has a reduction potential of −2.4 V. This leads us to believe for [$^{per\text{-}Cl}PhNH_3$][OTf] rather than engaging in an inner-sphere proton transfer with Cp^*_2Co ($E^0_{calc}(Cp^*_2Co^{0/+})$ = −2.18 V) it is likely that an outer sphere electron transfer occurs first. This change in mechanism would explain the increased H_2 yields and the decreased N_2RR efficiency. In contrast, [$^{2,6\text{-}Cl}PhNH_3$][OTf] should be resistant to reduction and thus able to protonate the metallocene and engage in the mechanism discussed in the main text.

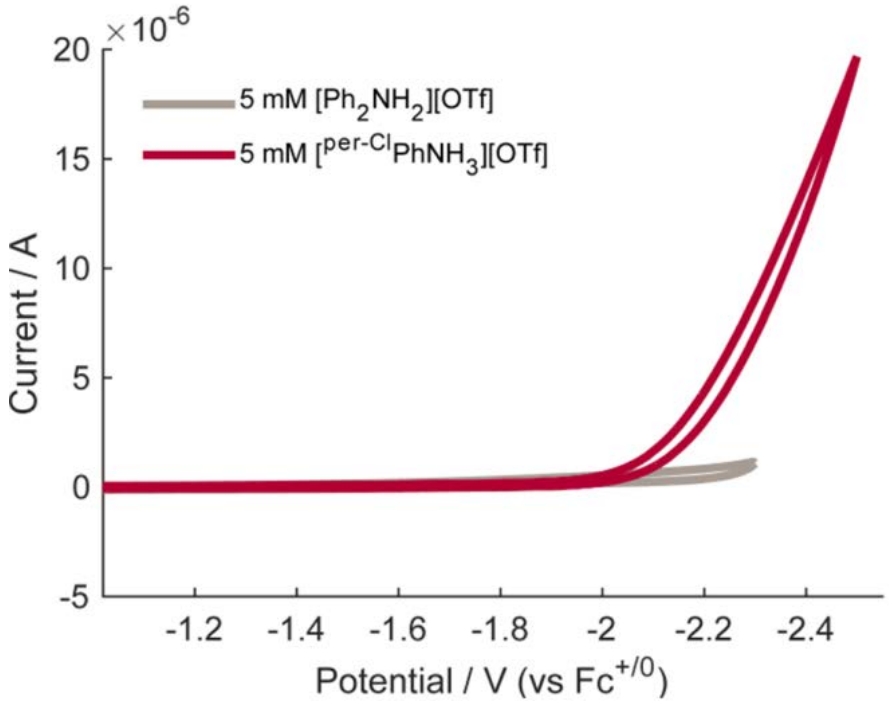

Figure A4.8. Cyclic voltammograms of 5 mM [Ph_2NH_2][OTf] (gray trace) and 5 mM [$^{per\text{-}Cl}PhNH_3$][OTf] (red trace). All spectra are collected in 0.1 M $NaBAr^F{}_4$ solution in Et_2O at −35 °C using a glassy carbon working electrode and externally referenced to the $Fc^{+/0}$ couple. Scan rate is 100 mV/s.

A4.11 X-ray Photoelectron Spectroscopy (XPS) details

The surface composition of the carbon electrode surface after a 15 hour bulk electrolysis in the presence of $[P_3^BFe][BAr^F_4]$, $[Cp^*_2Co][BAr^F_4]$, $[Ph_2NH_2][OTf]$ and N_2 was determined via XPS on a Kratos Axis Nova spectrometer with DLD (Kratos Analytical; Manchester, UK). The excitation source for all analysis was monochromatic Al $K\alpha_{1,2}$ ($h\nu$ = 1486.6 eV) operating at 10 mA and 15 kV. The X-ray source was directed at 54° with respect to the sample normal. A base pressure of 1×10^{-9} Torr is maintained in the analytical chamber, which rises to 5×10^{-9} Torr during spectral acquisition. All spectra were acquired using the hybrid lens magnification mode and slot aperture, resulting in an analyzed area of 700 μm × 400 μm. Survey scans were collected using 160 eV pass energy, while narrow region scans used 10 eV; charge compensation via the attached e^--flood source was not necessary in this study.

Subsequent peak fitting and composition analysis was performed using CasaXPS version 2.3.16 (Casa Software Ltd.; Teignmouth, UK). Energy scale correction for the survey and narrow energy regions was accomplished by setting the large component in the C 1s spectrum, corresponding to a C 1s C(=C) transition, to 284.8 eV. All components were fit using a Gaussian 30% Lorentzian convolution function. For quantification, Shirley baselines were employed where there was a noticeable change in CPS before and after the peak in the survey spectrum; otherwise, linear was chosen. Atomic percentages were calculated using the CasaXPS packages for regions and/or components and are reported herein. Calculations were performed using region or

component areas normalized to relative sensitivity factors specific to the instrument conditions with deconvolution from the spectrometer transmission function.

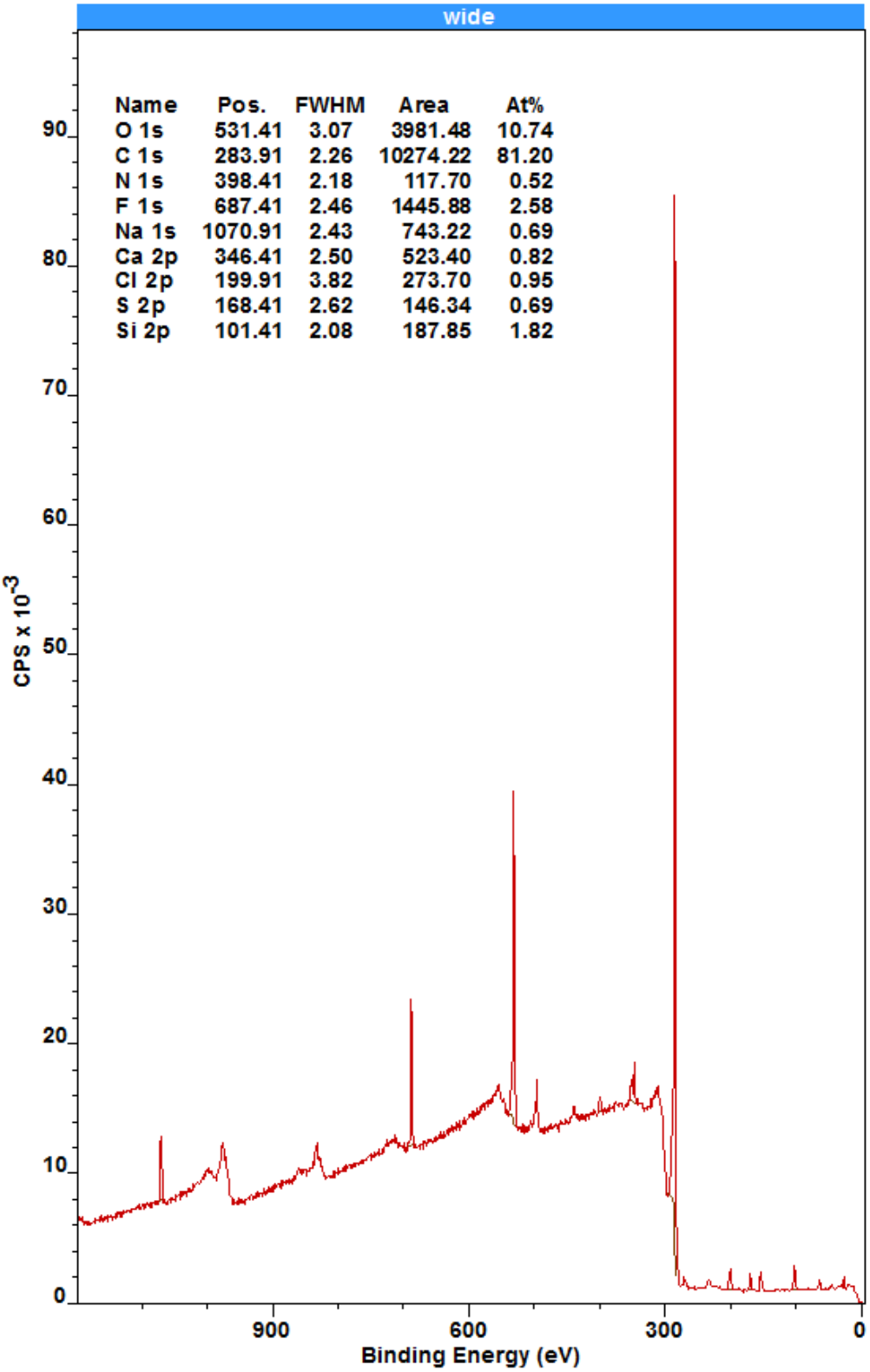
wide
Name Pos. FWHM Area At%
O 1s 531.41 3.07 3981.48 10.74
C 1s 283.91 2.26 10274.22 81.20
N 1s 398.41 2.18 117.70 0.52
F 1s 687.41 2.46 1445.88 2.58
Na 1s 1070.91 2.43 743.22 0.69
Ca 2p 346.41 2.50 523.40 0.82
Cl 2p 199.91 3.82 273.70 0.95
S 2p 168.41 2.62 146.34 0.69
Si 2p 101.41 2.08 187.85 1.82
CPS x 10-3
90
80
70
60
50
40
30
20
10
0
900
600
300
0
Binding Energy (eV)

Figure A4.9. XPS survey scan of a section of a glassy carbon plate which was not exposed to the working chamber solution during a 15 hour bulk electrolysis in the presence of $[P_3^BFe][BAr^F_4]$, $[Cp^*_2Co][BAr^F_4]$, $[Ph_2NH_2][OTf]$ and N_2 at −2.1 V (vs $Fc^{+/0}$). XPS and Auger peaks are assigned as labeled in the legend, which also includes atomic percentages calculated from component fits from scans of individual XPS regions. This material represents a baseline of the electrode surface composition resulting from cleaning, polishing, and handling prior to CPE experiments and is provided for comparison to a XPS survey scan of a section of the same glassy carbon plate which was exposed to the working chamber solution during a 15 hour bulk electrolysis in the presence of $[P_3^BFe][BAr^F_4]$, $[Cp^*_2Co][BAr^F_4]$, $[Ph_2NH_2][OTf]$ and N_2 at −2.1 V (vs $Fc^{+/0}$) presented in figure A4.10.

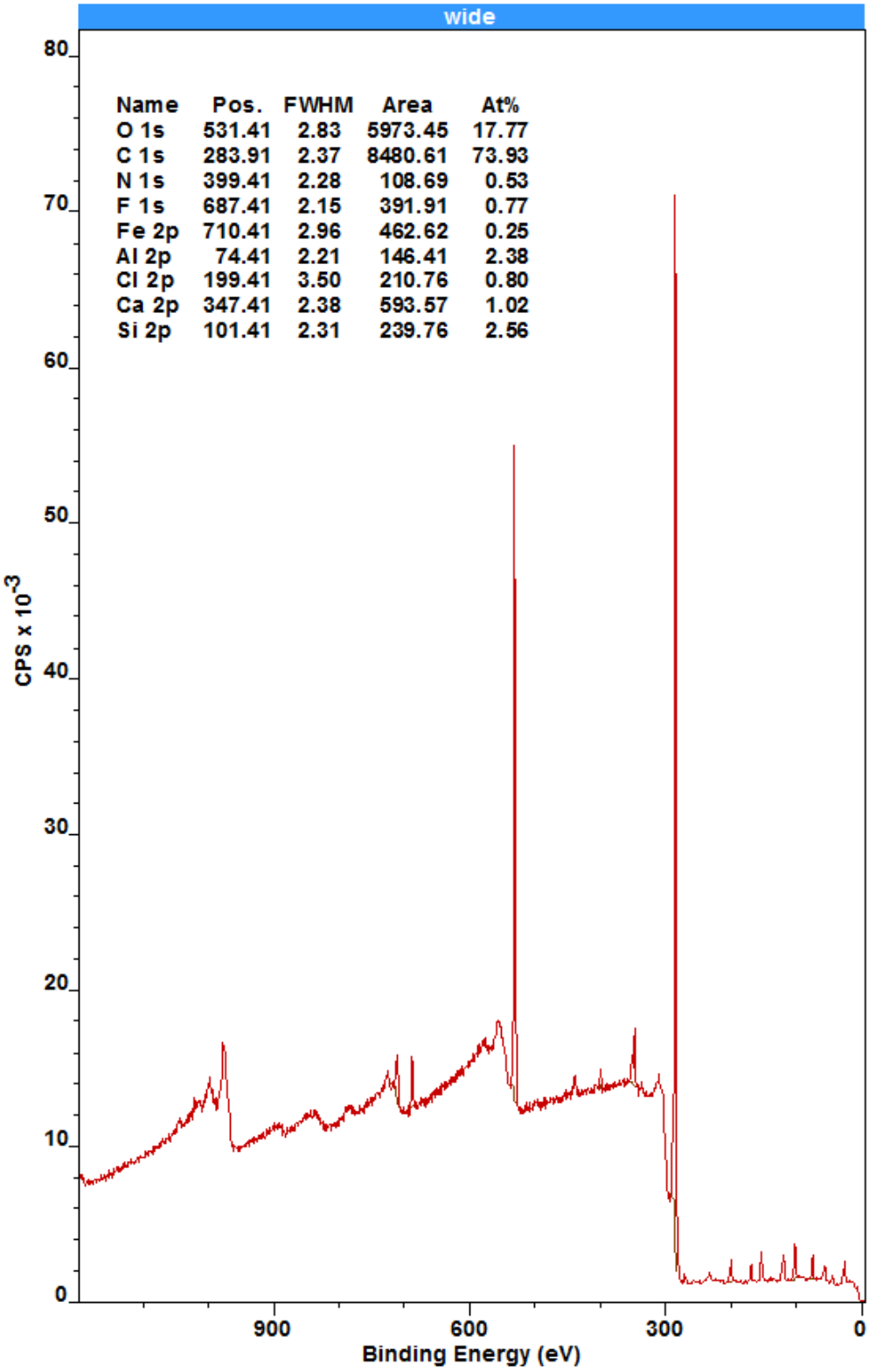
wide
Name Pos. FWHM Area At%
O 1s 531.41 2.83 5973.45 17.77
C 1s 283.91 2.37 8480.61 73.93
N 1s 399.41 2.28 108.69 0.53
F 1s 687.41 2.15 391.91 0.77
Fe 2p 710.41 2.96 462.62 0.25
Al 2p 74.41 2.21 146.41 2.38
Cl 2p 199.41 3.50 210.76 0.80
Ca 2p 347.41 2.38 593.57 1.02
Si 2p 101.41 2.31 239.76 2.56
CPS x 10^-3
80
70
60
50
40
30
20
10
0
900
600
300
0
Binding Energy (eV)

Figure A4.10. XPS survey scan of a section of a glassy carbon plate which was exposed to the working chamber solution during a 15 hour bulk electrolysis in the presence of $[P_3^BFe][BAr^F_4]$, $[Cp^*_2Co][BAr^F_4]$, $[Ph_2NH_2][OTf]$ and N_2 at −2.1 V (vs $Fc^{+/0}$). XPS and Auger peaks are assigned as labeled in the legend, which also includes atomic percentages calculated from component fits from scans of individual XPS regions. This material represents a post-electrolysis state of the electrode surface composition for comparison to a XPS survey scan of a section of the same glassy carbon plate which <u>was not</u> exposed to the working chamber solution during a 15 hour bulk electrolysis in the presence of $[P_3^BFe][BAr^F_4]$, $[Cp^*_2Co][BAr^F_4]$, $[Ph_2NH_2][OTf]$ and N_2 at −2.1 V (vs $Fc^{+/0}$) presented in figure A4.9. Notably this active surface scan reveals a small Fe signal, likely resulting from some degree of decomposition of the $[P_3^BFe][BAr^F_4]$ catalyst over the course of the 15 hour electrolysis; however it is also possible that this small Fe signal is the result of contamination during the handling of the sample. This Fe 2p signal occurs at 710.4 eV, but due to the weak signal intensity it is not possible to confidently assign its oxidation state. Although, the signal does not appear consistent with Fe(0) whose signal is typically around 707 eV; we would also note though that the handling process involves transferring the electrode quickly in air which could result in oxidation of Fe(0) that was present. Also notable is that no new Co signal is observed in the post-electrolysis scan suggesting that $[Cp^*_2Co][BAr^F_4]$ does not decompose to a surface bound Co species in detectable amounts during the electrolysis. Phosphorus is not detectable in the survey scan.

A4.12 pK_a Determination Strategy

Bosch et al. published a procedure for converting a pK_a in THF into the equivalent pK_a in different solvents.[28] Although not all of the pK_a values have been experimentally determined in THF the values obtained from converting from MeCN or H_2O into a THF value is quite accurate. So we have used these converted values in the text. Where available a number measured in THF has been used, if not the MeCN derived value is used. If neither is available then the H_2O derived value is used.

Solvent conversion equations:

$$pK_a(THF) = 0.78 \times pK_a(MeCN) - 0.52$$

$$pK_a(THF) = 1.19 \times pK_a(H_2O) + 2.13$$

Acid	pK_a in MeCN	pK_a in H_2O	Converted pK_a [a]	Experimental pK_a in THF
[$^{4\text{-OMe}}$PhNH$_3$][OTf]	11.86[29]	5.29[31]	8.8 (8.4)	8.8[28]
[PhNH$_3$][OTf]	10.62[29]	4.58[31]	7.8 (7.6)	8.0[28]
[$^{2,6\text{-Me}}$PhNH$_3$][OTf]	--	3.89[31]	-- (6.8)	
[$^{2\text{-Cl}}$PhNH$_3$][OTf]	7.86[29]	2.64[31]	5.6 (5.3)	6.0[28]

[$^{2,5\text{-Cl}}$PhNH$_3$][OTf]	6.21[30]	1.53[29]	4.3 (4.0)	4.5[28]
[$^{2,6\text{-Cl}}$PhNH$_3$][OTf]	5.06[29]	0.42[32]	3.4 (2.6)	
[$^{2,4,6\text{-Cl}}$PhNH$_3$][OTf]	--	−0.03[32]	-- (2.1)	
[$^{\text{per-Cl}}$PhNH$_3$][OTf]	2.35[30]	--	1.3 (--)	
collidinium triflate	14.98[29]	--	11.2 (--)	
benzylammonium triflate	--	9.34[33]	-- (13.2)	

[a]First is listed the value converted from THF and then in parentheses is the value converted from H_2O.

A4.13 References

[1] Robbins, J. L.; Edelstein, N.; Spencer, B.; Smart, J. C. *J. Am. Chem. Soc.* **1982**, *104*, 1882.

[2] Anderson, J. S.; Moret, M.-E.; Peters, J. C. *J. Am. Chem. Soc.* **2013**, *135*, 534.

[3] Moret, M.-E.; Peters, J. C. *J. Am. Chem. Soc.* **2011**, *133*, 18118.

[4] Del Castillo, T. J.; Thompson, N. B.; Peters, J. C. *J. Am. Chem. Soc.* **2016**, *138*, 5341.

[5] Melzer, M. M.; Mossin, S.; Dai, X.; Bartell, A. M.; Kapoor, P.; Meyer, K.; Warren, T. H. A *Angew. Chem. Int. Ed.* **2010**, *49*, 904.

[6] Vicente, J.; Chicote, M.-T.; Guerrero, R.; Jones, P. G. *J. Chem. Soc., Dalton Trans.* **1995**, *8*, 1251.

[7] Grimme, S.; Antony, J.; Ehrlich, S.; Krieg, H. *J. Chem. Phys.* **2010**, *132*, 154104.

[8] Tao, J.; Perdew, J. P.; Staroverov, V. N.; Scuseria, G. E. *Phys. Rev. Lett.* **2003**, *91*, 146401.

[9] Weigend, F.; Ahlrichs, R. *Phys. Chem. Chem. Phys.* **2005**, *7*, 3297.

[10] *John Towns, Timothy Cockerill, Maytal Dahan, Ian Foster, Kelly Gaither, Andrew Grimshaw, Victor Hazlewood, Scott Lathrop, Dave Lifka, Gregory D. Peterson, Ralph Roskies, J. Ray Scott, Nancy Wilkins-Diehr, "XSEDE: Accelerating Scientific Discovery", Computing in Science & Engineering, vol.16, no. 5, pp. 62-74, Sept.-Oct. 2014, doi:10.1109/MCSE.2014.80*

[11] Valiev, M.; Bylaska, E. J.; Govind, N.; Kowalski, K.; Straatsma, T. P.; Van Dam, H. J. J.; Wang, D.; Nieplocha, J.; Apra, E.; Windus, T. L.; de Jong, W. A. *Comput. Phys. Commun.* **2010**, *181*, 1477.

[12] Neese, F. *Wiley Interdiscip. Rev.: Comput. Mol. Sci.* **2012**, *2*, 73.

[13] Klamt, A.; Schüürmann, G. *J. Chem. Soc. Perkin Trans. 2*. **1993**, *2*, 799.

[14] Marten, B.; Kim, K.; Cortis, C.; Friesner, R. A.; Murphy, R. B.; Ringnalda, M. N.; Sitkoff, D.; Honig, B. *J. Phys. Chem.* **1996**, *100*, 11775.

[15] Ribeiro, R. F.; Marenich, A. V.; Cramer, C. J.; Truhlar, D. G. *J. Phys. Chem. B* **2011**, *115*, 14556.

[16] Wang, T.; Brudvig, G.; Batista, V. S. *J. Chem. Theory Comput.* **2010**, *6*, 755.

[17] Hamashima, Y.; Somei, H.; Shimura, Y.; Tamura, T.; Sodeoka, M. *Org. Lett.* **2004**, *6*, 1861.

[18] Anderson, L. L.; Arnold, J.; Bergman, R. G. *J. Amer. Chem. Soc.* **2005**, *127*, 14542.

[19] Anderson, J. S.; Cutsail, G. E., III; Rittle, J.; Connor, B. A.; Gunderson, W. A.; Zhang, L.; Hoffman, B. M.; Peters, J. C *J. Am. Chem. Soc.* **2015,** *137*, 7803.

[20] Stoll, S.; Schweiger, A. *J. Magn. Reson.* **2006**, *178*, 42.

[21] Marcus, R. A. I. *J. Chem. Phys.* **1956**, *24*, 966.

[22] Iordanova, N.; Decornez, H.; Hammes-Schiffer, S. *J. Am. Chem. Soc.* **2001**, *123*, 3723.

[23] Koper, M. T. M. *Chem. Sci.* **2013**, *4*, 2710.

[24] Onsager, L. *J. Am. Chem. Soc.* **1936**, *58*, 1486.

[25] Thoss, M.; Evers, F. *J. Chem. Phys.* **2018**, *148*, 030901.

[26] (a) *web*PCET Application Server, University of Illinois at Urbana-Champaign, http://webpcet.scs.uiuc.edu (2009) (b) Hammes-Schiffer, S.; Soudackov, A. V. *J. Phys. Chem. B* **2008**, *112*, 14108-14123.

[27] Warren, J. J.; Tronic, T. A.; Mayer, J. M. *Chem. Rev.* **2010**, *110*, 6961.

[28] Garrido, M. Rosés, C. Ràfols, E. Bosch *J. Soln. Chem.* 2008, *37*, 689.

[29] Kaljurand, I.; Kütt, A.; Sooväli, L.; Rodima, T.; Mäemets, V.; Leito, I.; Koppel, I. A. *J. Org. Chem.* **2005**, *70*, 1019.

[30] Haav, K.; Saame, J.; Kütt, A.; Leito, I. *Eur. J. Org. Chem.* **2012**, 2167.

[31] Pankratov, A. N.; Uchaeva, I. M.; Doronin, S. Y.; Chernova, R. K. *J. Struct. Chem.* **2001**, *42*, 739.

[32] Liao, K.; Pack, B. W.; Toltl, N. P. *J. Pharm. Biomed. Anal.* **2007**, *44*, 118.

[33] Hall, H. K. *J. Am. Chem. Soc.* **1957**, *79*, 5441.